Dissertation

submitted to the

Combined Faculties of the Natural Sciences and Mathematics
of the Ruperto-Carola University of Heidelberg, Germany

for the degree of

Doctor of Natural Sciences

Put forward by

Dipl.-Phys. Igor Böttcher

born in Karl-Marx-Stadt, German Democratic Republic

Oral examination: December 10, 2014

Dimensional BCS-BEC crossover in ultracold Fermi gases

Referees: Prof. Dr. Christof Wetterich
Prof. Dr. Manfred Salmhofer

Dimensioneller BCS-BEC-Crossover in ultrakalten Fermigasen

Wir untersuchen die Thermodynamik und Phasenstruktur ultrakalter Fermigase. Diese können mit modernen Fallentechniken im Labor realisiert und vermessen werden. Dabei nähern wir uns dem System sowohl vom theoretischen als auch experimentellen Standpunkt. Ein zentraler Punkt der Analyse ist der systematische Vergleich des BCS-BEC-Crossovers zweikomponentiger Fermionen in drei und zwei Dimensionen. Eine Reduktion der Dimensionalität lässt sich im Experiment mit stark anisotropen Fallen verwirklichen. Die Funktionale Renormierungsgruppe (FRG) erlaubt beide Fälle in einem einheitlichen theoretischen Rahmen zu beschreiben. In drei Dimensionen diskutieren wir mit der FRG den Einfluss von Teilchen mit hohem Impuls auf die Dichte, erweitern bisherige Zugänge zum unitären Fermigas um quantitative Präzision zu erreichen, und untersuchen den Zusammenbruch der Superfluidität aufgrund einer Asymmetrie in der Besetzung der zwei fermionischen Komponenten. In diesem Zusammenhang untersuchen wir auch die Stabilität der Sarmaphase. Für den Übergang zum zweidimensionalen System spielt die Streuphysik in reduzierter Dimension eine entscheidende Rolle. Wir legen theoretisch und experimentell relevante Aspekte dessen dar. Nach einer qualitativen Untersuchung des Phasendiagrams und der Zustandsgleichung in zwei Dimensionen mit der FRG, beschreiben wir die experimentelle Bestimmung des Phasendiagramms des zweidimensionalen BCS-BEC-Crossovers in Zusammenarbeit mit der Gruppe von S. Jochim am PI Heidelberg.

Dimensional BCS-BEC crossover in ultracold Fermi gases

We investigate thermodynamics and phase structure of ultracold Fermi gases, which can be realized and measured in the laboratory with modern trapping techniques. We approach the subject from a both theoretical and experimental perspective. Central to the analysis is the systematic comparison of the BCS-BEC crossover of two-component fermions in both three and two dimensions. A dimensional reduction can be achieved in experiments by means of highly anisotropic traps. The Functional Renormalization Group (FRG) allows for a description of both cases in a unified theoretical framework. In three dimensions we discuss with the FRG the influence of high momentum particles onto the density, extend previous approaches to the Unitary Fermi Gas to reach quantitative precision, and study the breakdown of superfluidity due to an asymmetry in the population of the two fermion components. In this context we also investigate the stability of the Sarma phase. For the two-dimensional system scattering theory in reduced dimension plays an important role. We present both the theoretically as well as experimentally relevant aspects thereof. After a qualitative analysis of the phase diagram and the equation of state in two dimensions with the FRG we describe the experimental determination of the phase diagram of the two-dimensional BCS-BEC crossover in collaboration with the group of S. Jochim at PI Heidelberg.

Contents

1 Introduction

Pushing the experimental frontier in physics has always refreshed and deepened our understanding of the fundamental laws of nature. With the achievement of quantum degeneracy in ultracold quantum gases (Anderson et al. [1995], Davis et al. [1995]) an exciting new chapter of research at the interface of few- and many-body quantum physics has been opened. Most characteristic for the corresponding experiments is an unprecedented degree of control and tunability of the atomic ensembles. This enables both a systematic study of the mechanisms governing these systems and a solid benchmarking of their theoretical description.

The big interest in ultracold quantum gases is twofold. First, anticipating the idea of Feynman [1982] of a quantum simulator, we can hope that the realization of atomic clouds in the laboratory will shed light on outstanding questions such as high temperature superconductivity in solid state materials, the properties of dense nuclear matter in neutron stars, thermalization in heavy-ion collisions, or particle production in the early universe. Second, and this will be the focus of this thesis, ultracold atoms as a new system in the field of condensed matter physics promise to reveal how the rich and often surprising macroscopic phenomenology of quantum few- and many-body systems emerges from a given, relatively simple Hamiltonian.

Typical ultracold quantum gases consist of $10^3 - 10^6$ alkali or earth alkali atoms trapped by electromagnetic fields (Ketterle et al. [1999], Dalfovo et al. [1999], Grimm et al. [2000]). With a succession of laser and evaporative cooling techniques it is possible to reach the sub-μK regime (Pethick and Smith [2002], Pitaevskii and Stringari [2003]). At those low temperatures the complex interatomic collisions can be described by effective contact interactions. Moreover, by diluting the ensemble it is possible to suppress three-body processes which would result in clustering of particles and eventually solidify the sample. As a consequence the low-energy physics of the gas, irrespective of its atomic details, is faithfully described by a simple many-body Hamiltonian with pointlike interactions between the particles (Bloch et al. [2008]). This model is often applied to other systems, where, however, it is only an approximation.

The artificial character of the systems just described is also their key feature. By modifying the preparation or trapping of the gas, experimentalists can nowadays engineer a large class of many-body systems which are of high general interest. The cold atoms tool box contains a variety of isotopes whose scattering properties are classified and well-understood. Interacting quantum gases with Fermi or Bose statistics, or mixtures thereof, can be designed by populating distinct hyperfine states of fermionic (e.g. ^{6}Li or ^{40}K) or bosonic atoms (e.g. ^{7}Li or ^{87}Rb). Ap-

plying an external magnetic field operated close to a Feshbach resonance of the trapped species (Chin et al. [2010]), the coupling constant between particles can be tuned almost at will, thereby connecting perturbative and nonperturbative regimes (Giorgini et al. [2008], Gurarie and Radzihovsky [2007]). Interference effects of the electromagnetic trapping fields can be employed to create effectively two- or one-dimensional systems, or to simulate Hubbard model physics in optical lattices (Jaksch and Zoller [2005], Lewenstein et al. [2006]).

In this work we will mainly be interested in the thermodynamic properties of interacting Fermi gases. However, many other promising directions in the field of cold atoms have appeared in the past two decades, out of which we want to present a small selection.

The study of finite quantum systems with a well-controlled particle number addresses fundamental questions concerning the transition from few- to many-body physics. Starting with three particles, where the famous Efimov-effect (Efimov [1970, 1973]) has been studied in detail (Ferlaino et al. [2011]), the subsequent adding of particles to the system (Serwane et al. [2011], Wenz et al. [2013]) allows to enter the mesoscopic regime, which is relevant, for instance, in nuclear physics. It is also possible to generate long-range interacting systems by trapping Rydberg atoms or polar molecules (Baranov [2008], Carr and Ye [2009], Saffman et al. [2010], Baranov et al. [2012]). Furthermore, there are many theoretical proposals on the implementation of SU(N) quantum magnetism or lattice gauge theories with ultracold atoms (Ye et al. [2008], Gorshkov et al. [2010], Daley [2011], Banerjee et al. [2013], Goldman et al. [2013], Celi et al. [2014]).

Another exciting direction is the study of systems out of thermal equilibrium. On the one hand, this comprises generic non-equilibrium phenomena in closed systems such as (pre-)thermalization (Berges et al. [2004], Gasenzer et al. [2005], Hofferberth et al. [2007], Cramer et al. [2008], Rigol et al. [2008]) or the response to parameter quenches (Greiner et al. [2002], Sadler et al. [2006], Calabrese and Cardy [2006], Kollath et al. [2007]). In particular, the interest in integrable one-dimensional systems was renewed with the experimental realization of cold atom ensembles in cigar shaped potentials. Cold atoms are also promising setups to investigate dynamical critical phenomena. On the other hand, ultracold quantum gases naturally represent open quantum systems. Whereas the loss of particles is often an unwanted effect, its influence can also be used to reveal interesting physics. By adjusting the pump of particles or energy into the system with the corresponding loss, such driven systems may eventually reach a non-equilibrium steady state (Diehl et al. [2008b], Verstraete et al. [2009], Diehl et al. [2010b], Dalla Torre et al. [2010]). Many interesting aspects of closed system like phase transitions or scaling phenomena are to a large part unexplored in open quantum systems.

Here we investigate the BCS-BEC crossover in two-component Fermi gases (Eagles [1969], Leggett [1980], Zwerger [2012], Randeria and Taylor [2014]). It describes the s-wave pairing of fermions with pointlike interactions in two distinct

hyperfine states, labelled $|1\rangle$ and $|2\rangle$. The nature of the pairs can be of very different form. In the BCS-limit, the system is fermionic and Cooper pairing between states on antipodal points of a sharp Fermi surface modify the low-energy physics on exponentially small scales. The theory of Bardeen, Cooper, and Schrieffer (BCS) for conventional superconductivity of weakly attractive fermions yields a good approximate account of the many-body state. In contrast, in the BEC-limit, every two fermions are bound into a diatomic molecule, and the fermion chemical potential is negative. The corresponding system of composite particles is well-described by a gas of weakly repulsive bosons, which may eventually form a Bose–Einstein condensate (BEC).

Remarkably, both limits can be connected continuously by varying the microscopic coupling strength. In the intermediate regime a strongly correlated superfluid emerges. At zero temperature the transition from the BCS- to the BEC-limit is a crossover, which explains the name of the system. In most systems where fermion pairing is relevant, such as superconductors or neutron stars, the pairing is, however, of one particular form. In those cases the corresponding microscopic coupling is fixed, and it determines the nature of the superfluid or superconductor under consideration. In contrast, for cold atoms the whole BCS-BEC crossover can be addressed by varying an external magnetic field in the vicinity of an interatomic Feshbach resonance. This allows in a unique fashion to experimentally study the transmutation from an atomic to a molecular superfluid by crossing the strongly correlated regime. At the same time this calls for a complete theoretical description which captures the rich phase diagram in all its facets.

Such a theoretical framework is offered by the Functional Renormalization Group (FRG) (Wetterich [1993], Berges et al. [2002], Pawlowski [2007], Gies [2012], Delamotte [2012], Kopietz et al. [2010], Metzner et al. [2012]). The method is built on the functional integral formulation of quantum field theory. In the cold atoms context we work with the coherent state path integral representation of the grand canonical partition function. A characteristic feature of the FRG is that it not only allows to resolve critical phenomena and scaling behavior, but also non-universal properties of a given Hamiltonian like phase diagrams or thermodynamic functions. During the renormalization group flow, the complexity of the many-body system is treated in a length scale resolved fashion: The impact of fluctuations on microscopic length scales is well-separated from the many-body effects and long-wavelength excitations on large length scales. In this way the often complicated substructure of correlation functions can be explained by the running of couplings and the decoupling of modes when going from microscopic to macroscopic scales.

The three-dimensional (3D) BCS-BEC crossover has been investigated extensively with the FRG after the seminal works by Birse et al. [2005] and Diehl et al. [2007a]. Landmarks are for instance the description of universality due to an ultraviolet fixed point (Diehl et al. [2007a,b]), the correct description of the second order superfluid phase transition in the whole crossover with critical ex-

ponents in the O(2) universality class, the inclusion of particle-hole fluctuations in the description of the strongly correlated regime (Floerchinger et al. [2008]), and a study of the influence of dimer-dimer- and dimer-atom-scattering onto the many-body system (Floerchinger et al. [2010]). The corresponding approach is technically parallel to FRG treatments of the quark-meson model (Berges et al. [2002], Schaefer and Wambach [2005, 2008]) or partially bosonized versions of the Hubbard model (Metzner et al. [2012]). This often leads to a fruitful mutual influence of these fields.

In this thesis we extend these earlier works in three directions. First we attempt to reach the level of quantitative precision which can compete with state-of-the-art experiments and theoretical methods such as Quantum Monte Carlo calculations or Luttinger–Ward approaches. This also aims at a solid benchmarking of our approach and at finding possible shortcomings or missing ingredients. Second we allow for an imbalance in chemical potential or population of $|1\rangle$- and $|2\rangle$-atom states. In this way it is possible to destroy superfluidity at zero temperature in either a first or second order phase transition. The qualitative resolution of this effect requires sophisticated methods for the computation of the effective potential of the system. Third we confine the system to two spatial dimensions (2D). This is experimentally relevant for cold atoms, as it can be emulated in highly anisotropic pancake traps, and may also shed light on unconventional superconductivity in solid state materials. Due to the enhanced role of fluctuations, the theoretical description of 2D systems is often plagued by infrared divergences. We show that those are absent in the FRG approach and apply the methods which have been successful in the investigation of the 3D system to the 2D BCS-BEC crossover.

In our quest for quantitative precision we mostly address the phase diagram and the equation of state of the system. The phase diagram consists in the critical temperature of superfluidity, $T_c(\mu, a)$ or $T_c(n, a)$, as a function of the chemical potential μ or density n, respectively, and the s-wave scattering length a. The latter fully characterizes the atomic interactions, which we assume to be of zero range. The thermodynamic information of the system is contained in the equation of state, which can be expressed in terms of the pressure as a function of the chemical potential and the temperature, $P(\mu, T, a)$. First or second order phase transitions manifest themselves as non-analyticities in the equation of state. Thus the knowledge of $P(\mu, T, a)$ allows to determine the phase diagram in those cases.

It is a beautiful and remarkably simple insight into thermodynamics in a large external potential that the equation of state of the homogeneous gas can be obtained from an in-situ density profile of the trapped gas (Ho and Zhou [2010]). For this to hold we have to assume that there exists a local equation of state for the gas at each point $\vec{r}$ in the trapping potential $V(\vec{r})$. We then find that the measured in-situ density at point $\vec{r}$ is given by $n(\mu_0 - V(\vec{r}), T, a)$, where μ_0 is the chemical potential in the center of the trap. Besides good statistics for the optical density, a precise measurement of the equation of state requires an accurate determination of μ_0 and T. This is a key challenge for experiments. There have been

equation of state measurements for the BCS-BEC crossover in both 3D (Horikoshi et al. [2010], Nascimbène et al. [2010], Navon et al. [2010], Ku et al. [2012]) and 2D (Makhalov et al. [2014]), which focus on different parameter regimes.

By introducing a chemical potential (or spin) imbalance $\delta\mu = (\mu_1 - \mu_2)/2$ between atoms in state $|1\rangle$ and $|2\rangle$, pairing becomes energetically less favourable. In particular, for a very large imbalance, the density of minority atoms vanishes. At zero temperature, this happens at the so-called polaron chemical potential. For intermediate values superfluidity breaks down at a critical imbalance $\delta\mu_c$. At this point, pairing is no longer related to a gain in energy, and thus the system enters a normal phase with unequal densities of $|1\rangle$- and $|2\rangle$-atoms. Within BCS-theory, the associated Chandrasekhar–Clogston limit appears for exponentially small mismatches of the Fermi spheres with $\mu_1 \neq \mu_2$ (Clogston [1962], Chandrasekhar [1962]). However, as we cross the resonance, the Fermi surfaces soften and superfluidity persists even for rather large imbalances.

From the mean field analysis of the spin-imbalanced BCS-BEC crossover, and also from experiments, it is apparent that the breakdown of superfluidity often manifests itself in a first order phase transition (Sheehy and Radzihovsky [2006], Parish et al. [2007], Navon et al. [2013]). A computation of the effective potential $U(\phi)$ of the pairing field ϕ thus has to account for the competition of local minima. In the FRG framework this can be resolved in several ways, e.g. by higher-order Taylor expansions of $U(\phi)$ beyond the ϕ^4-approximation, or by projecting $U(\phi)$ onto a complete function set like Chebyshev polynomials. Here we resolve the effective potential on a grid of typically 100 values of ϕ. The FRG analysis of the effective potential goes beyond the mean field approximation as it includes the feedback of $U(\phi)$ onto its own RG flow. This leads to a highly coupled set of equations, in sharp contrast to the mean field analysis, where the one-loop integral for the effective potential is readily integrated. We reproduce the correct perturbative limiting cases in the BCS-BEC crossover and find the transition of the Unitary Fermi Gas (UFG) to be of first order at zero temperature.

The breakdown of superfluidity due to a mismatch of Fermi surfaces is also of interest for neutron stars, where the imbalance between up- and down-quarks (due to an isospin chemical potential) results from a majority of neutrons over protons. Besides the relativistic dispersion relation of the fermions, the Lagrangian of the system and its mean field phase diagram are strikingly similar to those of the BCS-BEC crossover. Motivated by the finding that fluctuations beyond mean field theory induce a Sarma phase (Sarma [1963]) in the relativistic system (Kamikado et al. [2013], Boettcher et al. [2014b]), we search for the Sarma phase in the nonrelativistic setting. In the Sarma phase the system is a homogeneous superfluid with gapless fermionic excitations. Our analysis shows that in the 3D cold atoms case fluctuations rather destroy the parameter range which allows for a Sarma phase. Moreover, the Sarma phase only appears on the BEC-side of the crossover, where it describes a molecular BEC sprinkled with unpaired excess atoms.

The 2D BCS-BEC crossover (Randeria et al. [1989], Drechsler and Zwerger

[1992], Loktev et al. [2001], Iskin and de Melo [2009], Bertaina and Giorgini [2011], Bauer et al. [2014]) is similar to its 3D counterpart in the sense that it has a fermionic limit with sharp Fermi surfaces (called BCS side), and a bosonic limit of diatomic molecules with negative fermion chemical potential (called BEC side). Both regimes are connected by a strongly correlated superfluid. However, there are also inherent differences. Whereas a vacuum two-body bound state in 3D only exists on the BEC side, there is always such a bound state in 2D. From the corresponding binding energy ε_B it is then possible to define the 2D scattering length a according to $\varepsilon_\mathrm{B} = -\hbar^2/Ma^2$, where M is the mass of the atoms. The proper crossover parameter is given by $\log(k_\mathrm{F}a)$ with Fermi momentum $k_\mathrm{F} = (2\pi n)^{1/2}$. For $\log(k_\mathrm{F}a) = 0$ the interparticle spacing is of the same order as the interaction strength. Hence the system is strongly correlated. There is no nontrivial unitary regime in the 2D case (Nussinov and Nussinov [2006]).

The famous Mermin–Wagner theorem forbids long-range order in the 2D BCS-BEC crossover at nonzero temperature (Mermin and Wagner [1966], Hohenberg [1967]). For a trapped system this is only partially relevant due to the finite extent of the cloud. One then expects a nonzero condensate fraction which only vanishes logarithmically with the system size. But even in the truly 2D case there is still the possibility of a transition from a low-temperature superfluid phase to a high-temperature normal phase by means of the Berezinskii-Kosterlitz–Thouless (BKT) mechanism (Berezinskii [1972], Kosterlitz and Thouless [1973], José et al. [1977], Fröhlich and Spencer [1981]). Below the transition temperature phase correlations decay algebraically. It is thus in accordance with the Mermin–Wagner theorem. The decay exponent is related to the anomalous dimension, which is nonzero below the transition temperature.

We approach the 2D BCS-BEC crossover from both a theoretical and an experimental side. The theoretical description is performed with the FRG in close analogy to the 3D case. The beta functions governing the 2D system are the same as in 3D, however, with spatial dimension $d = 2$. Further modifications concern the initial conditions of the flow due to 2D scattering physics. For the experimental part there has been a close collaboration with the experimental group of Selim Jochim at PI Heidelberg, which realized the 2D BCS-BEC crossover using ^{6}Li-atoms in a highly anisotropic pancake trap. One of the experimental highlights is the determination of the phase diagram of the system. We outline the important steps which have been necessary for its extraction.

This thesis is organized as follows. In Sec. 2 we review the basics of ultracold atomic physics. In particular, after a discussion of Feshbach resonances we introduce the two-channel model for the BCS-BEC crossover which is employed throughout this thesis. In Sec. 3 we discuss functional approaches to interacting many-body systems with focus on applications to ultracold atoms. The framework of Functional Renormalization is then applied in Sec. 4 to the BCS-BEC crossover. We investigate the 3D and 2D BCS-BEC crossover in Secs. 5 and 6, respectively. In 3D we consider the Tan contact, the balanced Unitary Fermi Gas,

and the spin-imbalanced BCS-BEC crossover with the FRG. The discussion of the 2D system is based on a systematic comparison to the FRG-approach to the 3D system and the experimental realization of the setup using ^{6}Li-atoms. We draw our conclusions in Sec. 7, where we also indicate possible directions of future research.

The compilation of this thesis is solely to the author. The results and presentations have been obtained in collaboration with many other coworkers, which is highly appreciated by the author. Large parts of this thesis are published or available as preprint. The related works are:

- *Ultracold atoms and the Functional Renormalization Group*
  with S. Diehl and J. M. Pawlowski
  Nuclear Physics B - Proceedings Supplements **228** 63 - 135 (2012)

- *Tan contact and universal high momentum behavior of the fermion propagator in the BCS-BEC crossover*
  with S. Diehl, J. M. Pawlowski, and C. Wetterich
  Physical Review A **87** 023606 (2013)

- *Critical temperature and superfluid gap of the Unitary Fermi Gas from Functional Renormalization*
  with J. M. Pawlowski and C. Wetterich
  Physical Review A **89** 053630 (2014)

- *Phase structure of spin-imbalanced unitary Fermi gases*
  with J. Braun, T. K. Herbst, J. M. Pawlowski, D. Roscher, and C. Wetterich
  e-print available from arXiv:1409.5070 (2014)

- *Sarma phase in relativistic and non-relativistic systems*
  with T. K. Herbst, J. M. Pawlowski, N. Strodthoff, L. von Smekal, and C. Wetterich
  e-print available from arXiv:1409.5232 (2014)

- *Observation of pair condensation in a strongly interacting two-dimensional Fermi gas*
  with M. G. Ries, A. N. Wenz, G. Zürn, L. Bayha, D. Kedar, P. A. Murthy, M. Neidig, T. Lompe, and S. Jochim
  e-print available from arXiv:1409.5373 (2014)

2 Basics of ultracold atomic physics

2.1 Scales and interactions

The physics of ultracold quantum gases is governed by the interplay of several scales. Tuning their relative size, it is possible to access different regions of the phase diagram of the system, and thereby explore the underlying physics. In this section, we show which scales are relevant in the context of alkali atoms. In particular, we will discuss the conditions under which we have an ultracold quantum gas. These model-independent considerations will also reveal why it is possible to formulate a simple effective Hamiltonian, described by a few experimentally measurable parameters only, which governs all alkali (single valence electron) atoms.

Given a homogeneous gas of atoms with density n in d spatial dimensions, we may write

$$n = \ell^{-d}, \tag{2.1}$$

with ℓ being the *interparticle spacing*. Indeed, consider a homogeneous system in a box of volume V. We divide this volume into cells of size ℓ^d each. Putting exactly one atom into each cell, it is possible to distribute $N = V/\ell^d$ particles. Thus we arrive at the density $n = N/V = \ell^{-d}$. For two-component fermions it is common to associate a momentum scale $k_\mathrm{F} \propto \ell^{-1}$ to the density such that

$$k_\mathrm{F} = \begin{cases} (3\pi^2 n)^{1/3} & (d=3) \\ (2\pi n)^{1/2} & (d=2). \end{cases} \tag{2.2}$$

This quantity coincides with the Fermi momentum of a noninteracting system. For an interacting system $k_\mathrm{F} = k_\mathrm{F}(n)$ is still referred to as *Fermi momentum* for convenience, but it is not related to the presence of a Fermi surface. We also introduce the Fermi energy and Fermi temperature associated to the density by means of $\varepsilon_\mathrm{F} = \hbar^2 k_\mathrm{F}^2/2M$ and $T_\mathrm{F} = \varepsilon_\mathrm{F}/k_\mathrm{B}$, respectively.

Experiments on cold atoms are performed in either magnetic or optical traps, see e.g. Pethick and Smith [2002], Pitaevskii and Stringari [2003], Ketterle et al. [1999], Grimm et al. [2000] and references therein. As a consequence, the state of the many-body system is not homogeneous. In particular, the local density depends on the point in space. However, there are many cases where the picture of a locally homogeneous system is still valid and useful (Dalfovo et al. [1999]). In order to understand this, we consider a time-independent external trapping potential of harmonic shape. We have

$$V_\mathrm{ext}(\vec{x}) = \frac{M}{2}\omega_0^2 r^2 \tag{2.3}$$

with $r = |\vec{x}|$ and M being the mass of the atoms. The potential is characterized by the trapping frequency ω_0. Equivalently, we may write $V_{\text{ext}}(\vec{x}) = \frac{\hbar\omega_0}{2}(r/\ell_{\text{osc}})^2$ with the *oscillator length*

$$\ell_{\text{osc}} = \left(\frac{\hbar}{M\omega_0}\right)^{1/2}. \tag{2.4}$$

Thus, $\hbar\omega_0$ and ℓ_{osc} are the characteristic energy and length scales of the trap, respectively. We will later see that in a typical situation ℓ_{osc} constitutes the by far largest length scale in the system. (It will, however, act as an infrared (IR) cutoff for very long wavelength fluctuations present e.g. at a critical point.) Accordingly, $\hbar\omega_0$ usually provides the smallest energy scale of the problem.

If the physics under consideration takes place on much shorter distances than ℓ_{osc}, we can use this separation of scales to work with the so-called *local density approximation*: Consider the density at points $\vec{x}_1$ and $\vec{x}_2$, respectively. We can then expand $n(\vec{x}_1) = n(\vec{x}_2)(1+\mathcal{O}(|\vec{x}_1-\vec{x}_2|/\ell_{\text{osc}}))$. Obviously, for both points being close to each other we can neglect the correction and assume the density to be locally constant. In particular, for large values of ℓ_{osc} this may hold for subvolumes of the trapped cloud which contain many particles. The rules of thermodynamic equilibrium can then be applied to these small homogeneous subvolumes. We will come back to this point in the section on thermodynamics of cold quantum gases.

The statistical behavior of the trapped cloud is determined by the ratio between the interparticle spacing and the so-called *thermal* or *de Broglie wavelength*. To get an intuition for the latter quantity, consider a gas of atoms coupled to a heat bath of temperature T. The nonvanishing temperature induces a nonzero average kinetic energy $\langle p^2\rangle_T/2M$ per spatial direction of the particles. The thermal wavelength is the length scale associated to this energy according to $\lambda_T = h/\langle p^2\rangle_T^{1/2}$. More precisely, using $p = \hbar k = h/\lambda$, with k and λ being the wave number and length, respectively, we define λ_T as the de Broglie wavelength of a particle with kinetic energy $p^2/2M = \pi k_{\text{B}}T$. (The factor of π is purely conventional but standard.) This leads to

$$\lambda_T = \left(\frac{2\pi\hbar^2}{Mk_{\text{B}}T}\right)^{1/2}. \tag{2.5}$$

Note that $\lambda_T \sim T^{-1/2}$ becomes large for decreasing temperature. The quantities $\ell = \ell(n)$ and $\lambda_T = \lambda_T(T)$ constitute the many-body length scales of the system due to nonzero density and temperature, respectively.

Now we compare the length scales set by the interparticle spacing and the thermal wavelength. Thinking of particles as being represented by wave packets rather than pointlike objects, λ_T determines the spread of these lumps. The ratio ℓ/λ_T is large if the wave packets of the individual particles are widely separated and do not overlap. In this case the quantum nature of the particles does not play a role. Indeed, we may follow the trajectory of an individual particle by subsequent images, such that position and momentum are determined simultaneously, i.e. the gas can be described classically. However, for $\ell/\lambda_T \lesssim 1$, we are dealing with wave

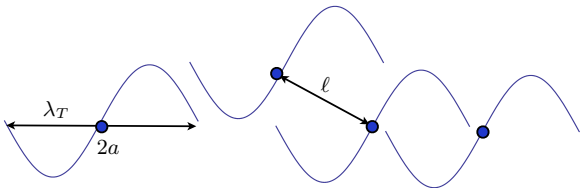

Figure 2.1: Quantum degeneracy is reached when the thermal wavelength λ_T is of the same order as the interparticle spacing $\ell = n^{-1/d}$. In this regime it is important for the statistics whether the particles are identical or not, leading to quantum many-body phenomena such as Bose condensation or Fermi surface formation. We also indicate a typical order of magnitude for the scattering length a, which, in the perturbative regime, roughly corresponds to the radius of equivalent hard-core particles with contact interactions and cross section $\sigma \propto a^2$. Figure taken from Boettcher et al. [2012].

packets which strongly overlap. The gas is then called *quantum degenerate*, or *ultracold*. Clearly, it is then no longer possible to distinguish the single atoms and their trajectories. In this case we rather have to deal with the whole many-body quantum system. The behavior is then determined by quantum mechanics, with statistics resulting from the spin of the constituents; ultracold atoms allow for exploring both degenerate Bose and Fermi gases.

The transition from the classical to the quantum degenerate regime occurs for $n\lambda_T^d \simeq 1$, i.e.

$$\ell/\lambda_T \simeq 1. \tag{2.6}$$

We visualize this situation in Fig. 2.1. The combination

$$\bar{\omega} = n\lambda_T^d = (\lambda_T/\ell)^d \tag{2.7}$$

is called the *phase space density*. It indicates the number of particles contained in a cube with linear extension set by the de Broglie wavelength. For two-component Fermi gases it is common to work with the ratio

$$\frac{T}{T_\mathrm{F}} = \begin{cases} 1.31(n\lambda_T^3)^{-2/3} & (d=3), \\ 2(n\lambda_T^2)^{-1} & (d=2), \end{cases} \tag{2.8}$$

which is small for large phase space density.

Interactions and effective Hamiltonian

So far our considerations did not depend on the interactions of the particles. The alkali atoms used in ultracold gas experiments are neutral and interact electromagnetically through van der Waals forces. A typical interaction potential $U(r)$ of two atoms separated by a distance r has a strongly repulsive part for small r. The

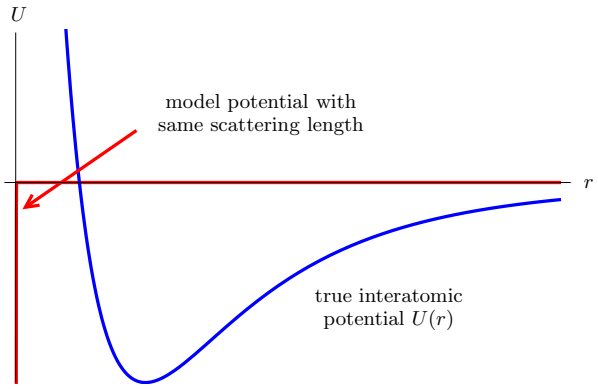

Figure 2.2: The interatomic potential $U(r)$ between two neutral atoms is of the Lennard–Jones type, with an attractive van der Waals tail $\sim 1/r^6$ at large separations. From $U(r)$ we can calculate the scattering length a, which is the only parameter relevant for low energy scattering. The δ-like potential from Eq. (2.16), which is shown here in red, is an equally good description (and more handy for practical calculations), as long as it has the same scattering length. The reason is that under ultracold conditions the short distance details of $U(r)$ are never resolved. Figure taken from Boettcher et al. [2012].

physical origin of the latter is Pauli's principle which forbids the electron clouds of the two atoms to overlap. This repulsive part can typically be modelled by a term $U(r) \sim 1/r^{12}$, but a hard-core repulsion with infinite strength works as well. For larger distances, two atoms experience an attraction due to mutual polarization of the electron clouds. Each atom then acts as a small induced dipole, and they attract each other according to a van der Waals interaction $U(r) \sim -1/r^6$. (We show the generic shape of the total interatomic potential, the Lennard–Jones potential, in Fig. 2.2.) We thus approximate the microscopic interaction potential to be

$$U_{\mathrm{vdW}}(r) = \begin{cases} \infty & (r \le r_0), \\ -C_4/r^6 & (r > r_0). \end{cases} \tag{2.9}$$

We can use this expression to construct a typical length scale, the *van der Waals length*, which characterizes the interatomic interactions. The typical length scale for zero energy scattering is obtained from equating the kinetic energy of a particle with momentum $p = \hbar/\ell_{\mathrm{vdW}}$ and reduced mass $M/2$, and the potential energy $U_{\mathrm{vdW}}(r = \ell_{\mathrm{vdW}})$. This results in

$$\ell_{\mathrm{vdW}} = \left(\frac{MC_6}{\hbar^2}\right)^{1/4}. \tag{2.10}$$

For typical values of C_6, we find that $\ell_{\mathrm{vdW}} = (50...200)a_0$ ($a_0 = 0.53 \times 10^{-10}$m the Bohr radius), which crucially is much smaller than the interparticle spacing

and the thermal wavelength (cf. Tab. 2.1):

$$\ell, \lambda_T \gg \ell_{\mathrm{vdW}}. \tag{2.11}$$

The many-body effects in an ultracold gas we are interested in thus never resolve physics beyond the van der Waals length. As a consequence, we will be able to specify an *effective low energy Hamiltonian*, valid on length scales $\gtrsim \ell_{\mathrm{vdW}}$, as the microscopic starting point of our calculations.

After indicating the rough scale associated to interactions, we now identify the relevant physical parameter which can be extracted from scattering experiments, the *scattering length*. This length scale characterizes two-body collisions and emerges universally as the *sole* parameter characterizing low energy collisions in potentials of sufficiently short range, such as $1/r^6$ as we deal with here. To see this, let us consider low energy elastic scattering of two particles in a quantum mechanical framework. (As we explain below, we can assume only elastic two-body processes to be relevant; further note that our meaning of "low energies" is quantified by Eq. (2.11).) Restricting ourselves to three dimensions for concreteness, the relative wave function of two quantum particles colliding along the z-axis in a short range potential can be written as

$$\psi_p(\vec{x}) = e^{\mathrm{i}pz/\hbar} + f(p,\theta)\frac{e^{\mathrm{i}pr/\hbar}}{r}. \tag{2.12}$$

The scattering amplitude $f(p,\theta)$ depends on the center of mass energy $p^2/2m_{\mathrm{r}}$ (m_{r} is the reduced mass) and the scattering angle θ. Solving the scattering problem for a particular potential $U(r)$ consists in determining $f(p,\theta)$ or, equivalently, all partial wave scattering amplitudes $f_l(p)$ in the expansion $f(p,\theta) = \sum_{l=0}^{\infty}(2l+1)f_l(p)P_l(\cos\theta)$ with Legendre polynomials P_l. A nonvanishing relative angular momentum l of the scattering particles introduces a centrifugal barrier term $\hbar^2 l(l+1)/2m_{\mathrm{r}}r^2$ in the Schrödinger equation of relative motion. As a lower estimate for the corresponding energy, we can replace $r^2 \to \ell_{\mathrm{vdW}}^2$ and find that this barrier is far too high for particles with energies $p^2/2m_{\mathrm{r}} \ll \hbar^2/\ell_{\mathrm{vdW}}^2$. Therefore, only isotropic s-wave-scattering ($l = 0$) occurs in ultracold alkali quantum gases.

With $p = \hbar k$, the low momentum expression of the s-wave scattering amplitude is given by

$$f_0(p) = \frac{1}{-\frac{1}{a} + \frac{1}{2}r_{\mathrm{e}}p^2 - \mathrm{i}p + \ldots}. \tag{2.13}$$

In this expansion, a is the scattering length anticipated above. It constitutes the most important parameter quantifying scattering in ultracold quantum gases in three dimensions. The coefficient r_{e} is referred to as effective range. It represents a correction which for the available p in ultracold gases is subleading, and thus we work with $f \simeq -a$. From Eq. (2.12) we then have $\psi(\vec{x}) \sim -a/r$ for large r and low momenta.

The limitation to s-wave scattering has drastic consequences for ultracold gases of identical fermions. They are necessarily noninteracting. Collisions would only

be possible in the p-wave or higher channels, but these cannot be reached due to the low energies. In order to have interactions between ultracold alkali fermions, we therefore always need at least two different species.

From a low energy expansion of the s-wave scattering amplitude in one and two dimensions, respectively, it is possible to derive parameters similar to a which quantify scattering in reduced dimensionality. Such low dimensional geometries can be designed in experiments by choosing a highly anisotropic harmonic potential with strong confinement in either two or one directions. We refer to Sec. 6.1.1 for scattering theory in two dimensions.

Let us briefly comment on the role of inelastic collisions. For collisions which do not change the spin of the particles, the most important inelastic mechanism is the formation of a molecule: If two atoms come close to each other, there may be energetically lower lying bound states and it is desirable for both atoms to build a molecule. However, without a third partner which allows for conservation of energy and momentum in this process, the excess energy from binding cannot go anywhere. Therefore, in two-body processes molecule formation is ruled out. If a third atom is involved, we end up with a high kinetic energy of both the third atom and the molecule. These fast particles are then expelled from the trap. This three-body loss results in a finite lifetime of the gas. Due to diluteness and the contact interaction nature of ultracold atoms, such processes are suppressed and we find stable gases even at extremely low temperatures, where solidification would be expected. Increasing the density, we have to ensure the typical time scale of three-body recombination to be much larger than the experimental time of observation.

Equipped with the length scale characterizing interactions, we give a concrete meaning to the notion of "weak" interactions by requiring the scattering length to be much smaller than the interparticle spacing in this case. This is equivalent to the *gas parameter* $|a|n^{1/3}$ being small. The criterion for weak interactions

$$|a|n^{1/3} \ll 1 \tag{2.14}$$

is often referred to as *diluteness condition*. This interpretation is motivated by the fact that the scattering length provides the typical extent of a particle as far as its collisional properties are concerned. We indicate this in Fig. 2.1. In the dilute regime it is possible to perform perturbation theory in the gas parameter.

For short range interaction potentials and low energy scattering, the s-wave scattering length can be calculated within the Born approximation. It is then given by the Fourier transform of the interaction potential at zero wave vector,

$$a = \frac{M}{4\pi\hbar^2} \int \mathrm{d}^3 x U(r). \tag{2.15}$$

In particular, this formula can be applied to the Lennard–Jones potential for cold atoms introduced above. Importantly, from Eq. (2.15) we learn (i) that value and sign of the scattering length may depend sensitively on the short distance

physics of the interatomic potential and (ii) that we do not need to know these details, since very different shapes of the interaction potential will have the *same* scattering length, i.e. the same low energy scattering behavior. Quite remarkably, it is therefore possible to replace the microscopic Lennard–Jones potential by any other model potential producing the same scattering length (cf. Fig. 2.2). For practical reasons, it is often convenient to work with completely local *contact potentials*

$$U_\Lambda(r) = g_\Lambda \delta(\vec{x}). \tag{2.16}$$

This simple model potential needs regularization at short distances and a subsequent renormalization procedure. We remind to this fact with the index referring to an ultraviolet cutoff Λ. The cutoff-independent renormalized coupling constant g is related to the physically measured scattering length by the simple formula

$$a = \frac{M}{4\pi\hbar^2} g. \tag{2.17}$$

The above considerations on ultracold atoms can be summarized in the *effective Hamiltonian*

$$\hat{H} = \int_{\vec{x}} \left(\hat{a}^\dagger(\vec{x}) \left(-\frac{\nabla^2}{2M} + V_{\text{ext}}(\vec{x}) \right) \hat{a}(\vec{x}) + g_\Lambda \hat{n}(\vec{x})^2 \right), \tag{2.18}$$

where the operators $\hat{a}^\dagger(\vec{x})$ and $\hat{a}(\vec{x})$ create and annihilate an atom at point $\vec{x}$, respectively, and $\hat{n}(\vec{x}) = \hat{a}^\dagger(\vec{x})\hat{a}(\vec{x})$ is the local particle density operator. Note that the power of two in the interaction term $\sim g\hat{n}^2$ stems from the fact that two particles have to meet at one point in order to interact. The trapping potential $V_{\text{ext}}(\vec{x})$ lifts the energy of the particles at the point $\vec{x}$ and thus this term is proportional to $\hat{n}(\vec{x})$. This rather universal Hamiltonian provides an accurate description for all ultracold alkali atoms.

It is a key feature of ultracold quantum gases that they are accurately described by effective microscopic Hamiltonians which depend only on a few system parameters. The latter can be measured in experiments to a high precision, e.g. by spectroscopic methods or by measurement of the collisional cross sections (Grimm et al. [2000]), without the need to resolve the full interatomic potentials. This situation is very distinct from condensed matter systems, where the underlying microscopic model is not known to such precision, and often has to be approximated by an educated guess. Moreover, realizations of ultracold quantum gases allow to change the system parameters continuously and thus to understand their influence on the many-body state.

In Table 2.1 and Fig. 2.3 we summarize our discussion by indicating the standard scale hierarchy, which is built up from the scattering length a, the interparticle distance (density) ℓ, the thermal wavelength (temperature) λ_T and the oscillator length ℓ_{osc}. Moreover, the system has a natural UV cutoff $\Lambda^{-1} \ll \ell_{\text{vdW}}$. Microscopic details on shorter length scales are irrelevant for our purposes because none of the many-body length scales can resolve the underlying physics.

Scattering length	Particle spacing	Th. wavelength	Trap size
a	ℓ	λ_T	$\ell_{\rm osc}$
$(3\ldots10)$nm	$(0.1\ldots1)\mu$m	$(0.5\ldots5)\mu$m	$(0.5\ldots20)\mu$m

Table 2.1: Standard scale hierarchy in ultracold quantum gases with typical values. The ratios of scales have the following physical meaning. $a/\ell \ll 1$: weakly interacting or dilute. $\ell/\lambda_T \ll 1$: ultracold. As long as $\ell_{\rm osc}$ is the largest length scale, the local density approximation is valid (except for long distance physics in the vicinity of a critical point). In order to simulate a 2D geometry, the transverse z-direction may be confined to $\ell_{{\rm osc},z} = 0.5\mu$m with a radial trapping $\ell_{{\rm osc},r} = 10\mu$m. This results in an aspect ratio $\eta = \omega_z/\omega_r = 400$.

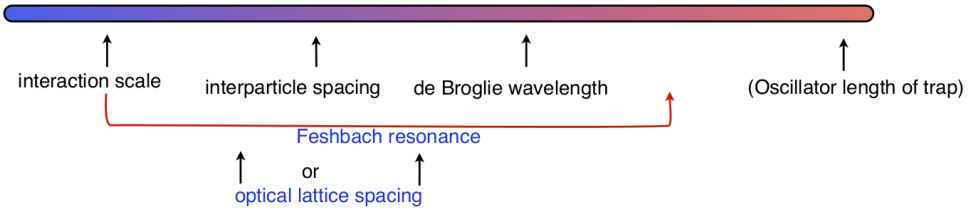

Figure 2.3: Violations of the scale hierarchy which do not invalidate the effective Hamiltonian since all length scales are still much larger than $\ell_{\rm vdW}$. Figure taken from Boettcher et al. [2012].

It is both experimentally and theoretically appealing that ultracold atoms can be tuned such that they *violate the scale hierarchy*, allowing to reach strongly interacting regimes – crucially, without loosing the validity of the above discussion. One way is provided by *Feshbach resonances* of the scattering length. Here, we can loosen the condition $|a| \ll \ell$ and explore new regimes of the many-body system which are not captured by mean field theory or perturbative expansions. Such resonances are realized in cold atoms if a bound state is located close to the zero energy scattering threshold, and is tuned to resonance due to the variation of an external magnetic field B. From this we infer that a Feshbach resonance is a result of a specific fine-tuning of the microphysics. The scattering length can then be parametrized according to

$$a(B) = a_{\rm bg}\left(1 - \frac{\Delta B}{B - B_0}\right), \tag{2.19}$$

where $a_{\rm bg}$, ΔB and B_0 are background scattering length, width and position of the resonance, respectively. Obviously, approaching B_0 we can obtain an anomalously large scattering length, meaning that, by virtue of fine-tuned microphysics, it

greatly exceeds the generic scale set by the van der Waals length,

$$|a| \gg \ell_{\mathrm{vdW}}. \tag{2.20}$$

We discuss Feshbach resonances in more detail in Sec. 2.4 when introducing our effective model for the BCS-BEC crossover.

Another way to reach an interaction dominated regime is by superimposing an *optical lattice* (Lewenstein et al. [2006], Bloch et al. [2008]). This is a standing wave of counterpropagating laser beams in each spatial direction, which provides a conservative periodic potential landscape for the atoms. Tuning the depth of the lattice wells via the laser intensity, we can withdraw the kinetic energy more strongly then the interaction energy and thus arrive at a strongly correlated system. The lattice spacing is related to the wavelength of the light used for the optical lattice. By engineering neighboring sites close to each other, we can reach high densities ("fillings"). Each of these effects enhances the correlations in the system.

Recall that the validity of the effective Hamiltonian in Eq. (2.18) is restricted to length scales sufficiently larger than ℓ_{vdW}. Since the mentioned scale violations happen at larger scales, the faithful microscopic modelling is not touched. Therefore, the pointlike description of the interactions is also applicable in the dense and strong coupling regimes.

For a more detailed presentation of low energy universality in atomic few-body systems and from the viewpoint of quantum field theory we refer to Braaten and Hammer [2006].

2.2 Thermodynamics

In this section we review a few thermodynamic concepts which are of relevance for experiments with ultracold atoms. We derive general thermodynamic statements, which hold independently of the particular system under consideration. We will see that the phase diagram and the equation of state encode important, experimentally accessible information about a many-body system and thus are desirable quantities to be computed from first principles. This also serves as one of the motivations to investigate cold atoms with the Functional Renormalization Group.

For thermodynamics to be applicable, we require the internal processes of a many-body system to be such that the system is in equilibrium on the time scale of observation. Strictly speaking, thermodynamic statements and, in particular, the theory of phase transitions are only valid in infinitely large systems. But this requirement is less severe as it might seem at first sight because any thermodynamic relation can be expressed in terms of intensive quantities only, like particle density, entropy density, or magnetization per particle. Taking these densities to be local quantities, we can apply the laws of thermodynamics locally for small *subsystems* of finite volume and particle number. This procedure works perfectly

at room temperature with large particle numbers $N \sim 10^{23}$, and is still justified for trapped gases with typically $N \sim 10^3 - 10^6$. In addition, systems with low atom loss rate and long lifetime can indeed be assumed to be thermodynamically equilibrated over the period of observation. Such a system is provided by two-component fermions in the BCS-BEC crossover.

We recall that the full thermodynamic information of a system is stored in the *equation of state* $P(\mu, T)$, which can be expressed in terms of the pressure as a function of chemical potential and temperature. Using the Gibbs–Duhem relations $\mathrm{d}P = n\mathrm{d}\mu + s\mathrm{d}T$ and $\varepsilon = Ts - P + \mu n$ we can calculate all other intensive thermodynamic quantities from the pressure. Here, $n = N/V$, $s = S/V$ and $\varepsilon = E/V$ are the densities of particle number, entropy and energy, respectively. The chemical potential μ is a parameter which determines the particle number $N(\mu)$ for a given temperature. Eliminating μ for the density $n(\mu, T)$, the equation of state can also be formulated in terms of the free energy density $f(n, T)$, which is the Legendre transform of the pressure according to $f = \mu n - P$.

In order to understand the influence of a trap, we consider a cloud in a time-independent external potential $V_{\mathrm{ext}}(\vec{x})$ which varies on much larger length scales than the typical atomic ones (e.g. interparticle spacing and scattering length). Picking two neighboring small but yet macroscopic subvolumes V_1 and V_2 of the cloud, thermal and chemical processes between them will result in the equality of their temperature and chemical potential. Since the subvolumes were arbitrary, we conclude that temperature and *full* chemical potential are constant inside the trap. However, from the Gibbs-Duhem relation we infer that the full chemical potential corresponds to the Gibbs free energy $G = F + PV$ per particle: $\mu = G/N$. The latter is spatially inhomogeneous due to the trap and we find $\mu = \mu_{\mathrm{hom}}(n(\vec{x}), T) + V_{\mathrm{ext}}(\vec{x}) = \text{const}$. In this formula, $\mu_{\mathrm{hom}}(n, T)$ is the internal chemical potential obtained from a calculation in a homogeneous setting, e.g. a box of volume V containing N particles.

We conclude that a system where the thermodynamic quantities are replaced according to

$$P(\mu, T) \to P(\mu - V_{\mathrm{ext}}(\vec{x}), T) \tag{2.21}$$

behaves like a system trapped in a potential of large spatial extent. This prescription is called *local density approximation* (LDA). The above derivation provides an intuitive understanding why this procedure should give reasonable results. Of course, if we cannot pick small, yet macroscopic subvolumes, the argument breaks down. The applicability of LDA is therefore limited to systems where the trap ℓ_{osc} provides the largest length scale. This agrees with our earlier considerations. From a field theory perspective it is very promising that properties of homogeneous systems can be obtained from trapped gases and, indeed, there have already been beautiful measurements of the equation of state of the BCS-BEC crossover to a high precision using LDA (Nascimbène et al. [2010], Navon et al. [2010], Ku et al. [2012]).

The equation of state also contains information about possible phase transi-

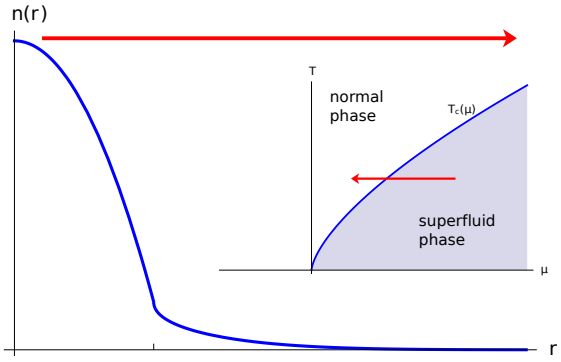

Figure 2.4: Within LDA, the inner regions of the trapped cloud correspond to higher local chemical potentials: $\mu_{\mathrm{loc}}(r) = \mu - V_{\mathrm{ext}}(r)$. We show here the density profile of a weakly interacting Bose gas in an external harmonic confinement. The inset shows a typical phase diagram in the (μ, T)-plane, where the blue region represents the superfluid phase. We cross the critical line of the superfluid phase transition for fixed temperature T at a certain chemical potential $\mu_{\mathrm{c}}(T)$. This corresponds to a kink in the density profile at a critical value $n_{\mathrm{c}}(T)$. Note, however, that LDA breaks down in the outer regions of the cloud, where the gas is extremely dilute. Figure taken from Boettcher et al. [2012].

tions appearing in the many-body system. Phases consist of extended parameter regimes which can be distinguished from each other by macroscopic observables. As an example, we consider the element iron. Despite the difference of solid, liquid and gaseous phase we can independently also distinguish the ferromagnetically from the antiferromagnetically ordered phase, or furthermore the crystal structures of γ-Fe and α-Fe. Phase transitions manifest themselves through kinks and jumps in the thermodynamic functions, typically in the higher derivatives of $P(\mu, T)$. These root in non-analyticities contained in the partition function. It is easy to see that true phase transitions need a continuum of degrees of freedom, i.e. occur only in the thermodynamic limit. Indeed, the partition function is $Z = \mathrm{Tr} e^{-\beta H} = \sum_n e^{-\beta E_n}$, E_n the eigenenergies of the system. Each of the contributions is analytic. Non-analyticities can only be generated in the case of infinitely many states entering the sum.

More formally, we distinguish two phases by an *order parameter* $\rho_0(\mu, T)$, which depends on the thermodynamic variables. In different phases, it is either zero or nonzero, which gives rise to the *phase diagram* in the (μ, T)-plane. For a fixed value of the chemical potential, we define the critical temperature $T_{\mathrm{c}}(\mu)$ at a second order phase transition via the relation $\rho_0(\mu, T_{\mathrm{c}}(\mu)) = 0^+$. Of course, we can also fix the density n to obtain the critical temperature $T_{\mathrm{c}}(n)$ as a function of n.

In the regime where LDA is applicable, the local chemical potential $\mu_{\mathrm{loc}}(\vec{x}) =$

$\mu - V_{\text{ext}}(\vec{x})$ has its largest value at the minima of the trapping potential. Accordingly, an increase of the potential reduces μ_{loc}. For this reason, we can *scan the phase diagram* over a certain region from a density image in a harmonic potential $V_{\text{ext}}(\vec{x}) = \frac{M}{2}\omega_0^2 r^2$, see Fig. 2.4. From our above considerations we conclude that the corresponding path in the (μ, T)-plane is an isothermal line. In particular, we may cross the phase boundary when the local chemical potential reaches the critical value $\mu_{\text{c}}(T)$. For this reason, we can have a superfluid gas in the inner regions of the cloud, whereas the outer shell is in its normal phase. The lobes in the phase diagram of the Bose-Hubbard model lead to a wedding cake structure of the density profile (Fölling et al. [2006]).

2.3 Noninteracting Bose and Fermi gases

After these general remarks on thermodynamics we turn our attention to degenerate, noninteracting Bose and Fermi gases. The notions of Bose–Einstein condensation and Fermi surfaces are introduced. They constitute the two cornerstones of quantum statistical phenomena and are crucial for understanding interacting gases.

The state of a single particle can be addressed by its momentum $\vec{p}$ and spin-projection σ. The corresponding occupation numbers $n_{\vec{p},\sigma}$ are restricted to $0, 1$ for fermions due to Pauli's principle, whereas they can have arbitrary integer values $0, 1, 2, \ldots$ for bosons. As is known from statistical mechanics, we then find for the equation of state

$$P(\mu, T) = \mp g k_{\text{B}} T \int \frac{\mathrm{d}^d p}{(2\pi\hbar)^d} \log\left(1 \mp e^{-\beta(\varepsilon_p - \mu)}\right), \tag{2.22}$$

where $\varepsilon_p = \vec{p}^2/2M$ and g is the spin degeneracy of the momentum states. We have $g = 1$ for spinless bosons considered here, and $g = 2$ for spin-1/2 fermions. The upper (lower) sign in Eq. (2.22) holds for bosons (fermions). As we will see below, for bosons, this expression is only valid in the absence of a condensate.

Free bosons and Bose–Einstein condensation

To understand the appearance of condensation as a purely quantum statistical effect, we consider an ideal gas of identical bosons. At zero temperature, we expect all bosons to be in the single particle state with energy $\varepsilon = 0$. In particular, this means that the occupation number N_0 of that state is extensive, $N_0 \sim V$. We say that the zero mode $\varepsilon = 0$ is occupied *macroscopically*. At low nonzero temperature some particles will be thermally excited into the higher states. At very high temperatures we approach the Boltzmann limit, where all occupation numbers are small (in particular, none of them is occupied macroscopically) and the distribution function $n(\varepsilon)$ is very broad. Therefore, there must be a critical temperature T_{c} below which macroscopic occupation of the single particle ground

state sets in. Since this particular behavior is due to quantum statistics and absent in a classical gas, we can estimate the critical temperature very roughly to satisfy $\lambda_{T_\mathrm{c}} \simeq \ell$.

We obtain the particle number in a three-dimensional box of volume V by virtue of a μ-derivative of Eq. (2.22) as

$$N(T,V,\mu) = \sum_{\vec{q}} \langle \hat{a}^\dagger_{\vec{q}} \hat{a}_{\vec{q}} \rangle = \frac{V}{\lambda_T^3} \frac{1}{\Gamma(3/2)} \int_0^\infty \frac{\mathrm{d}\varepsilon \sqrt{\varepsilon}}{e^{\varepsilon - \beta\mu} - 1}. \tag{2.23}$$

For fixed temperature and volume, this formula has a maximum N_max at $\mu = 0$. However, if we decide to put more than N_max particles into the box, the expression necessarily becomes invalid. The critical temperature $T_\mathrm{c}(n)$ where this happens is determined by the critical phase space density

$$\bar{\omega}_\mathrm{c} = n\lambda_{T_\mathrm{c}}^3 = (\lambda_{T_\mathrm{c}}/\ell)^3 \stackrel{!}{=} \zeta(3/2) \simeq 2.612, \tag{2.24}$$

i.e. $\lambda_{T_\mathrm{c}}/\ell$ is indeed of order unity as anticipated above.

Since our starting point was physically sound, but we ended up with an unphysical result, we must have made an error. This led Einstein and Bose to treating the zero momentum mode separately. Indeed, in Eq. (2.23) we did not appropriately incorporate the states with $\varepsilon = 0$: Replacing the quantized momenta of the finite system, $\vec{p}_{\vec{n}} = 2\pi\hbar\vec{n}/L$, in the naive continuum limit

$$\frac{1}{V} \sum_{\vec{n} \in \mathbb{Z}^3} \to \int \frac{\mathrm{d}^3 p}{(2\pi\hbar)^3} \sim \int_0^\infty \mathrm{d}\varepsilon \sqrt{\varepsilon}, \tag{2.25}$$

we multiply the contribution from the zero energy state with $\varepsilon = 0$ (or equivalently $p^2 = 0$). This corresponds to a vanishing occupation of the single particle ground state, which constitutes a bad approximation, as is apparent from our above considerations.

Therefore, the situation at temperatures $T < T_\mathrm{c}(n)$ is as follows. Formula (2.23) with $\mu = 0$ describes the excited particles in the states with $\varepsilon > 0$. The remaining $N_0(T) = N - N_\mathrm{ex}(T)$ particles are condensed to the zero energy state, leading to its macroscopic occupation. This resolves the puzzle from above. If we put more than N_max particles into the box, they will add to the condensate. The particle number below T_c is given by

$$N(T,V) = \langle \hat{a}^\dagger_{\vec{0}} \hat{a}_{\vec{0}} \rangle + \frac{gV}{\lambda_T^3} \zeta(3/2). \tag{2.26}$$

Obviously, $N_0(T) = \langle \hat{a}^\dagger_{\vec{0}} \hat{a}_{\vec{0}} \rangle \sim V$ is extensive. The condensate fraction $N_0(T)/N$ is an order parameter for the Bose–Einstein condensation phase transition. From Eq. (2.24) we conclude

$$\frac{N_0(T)}{N} = 1 - \left(\frac{T}{T_\mathrm{c}} \right)^{3/2} \quad \text{for } T \leq T_\mathrm{c}. \tag{2.27}$$

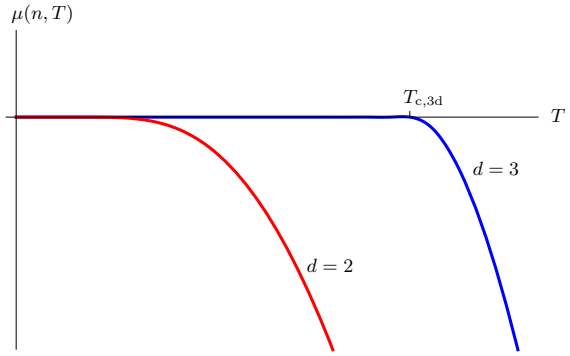

Figure 2.5: We plot the chemical potential $\mu(n,T)$ from Eq. (2.22) for an ideal Bose gas at fixed density n. In three spatial dimensions, the function hits zero at $T_c(n) > 0$. Since Eq. (2.22) cannot be applied for positive μ, the chemical potential remains zero and condensation sets in. In contrast, the chemical potential in two dimensions is negative for all $T > 0$ and thus there are always enough thermally excited states and condensation is absent. Figure taken from Boettcher et al. [2012].

It vanishes continuously for $T \to T_c$, which signals a second order phase transition.

In Eq. (2.25) we used the three-dimensional density of states $\rho(\varepsilon) \sim \sqrt{\varepsilon}$ to show why condensation appears. In d spatial dimension, we have $\rho(\varepsilon) \sim \varepsilon^{d/2-1}$ and the ground state contribution is not multiplied by zero for $d \leq 2$. Indeed, a similar calculation shows that for one- and two-dimensional systems the particle number $N(T,V,\mu)$ does not have a maximum at nonzero temperatures and thus Bose–Einstein condensation is absent. For $d = 1$ this also holds at zero temperature. In Fig. 2.5, we plot the chemical potential as a function of temperature. Whereas $\mu(T_c) = 0$ for a nonzero T_c in three dimensions, we find $T_c = 0$ for $d = 2$. Our finding for noninteracting particles is a special case of the generally valid *Mermin–Wagner theorem* (Mermin and Wagner [1966], Hohenberg [1967]), which states that there is no spontaneous breaking of a continuous symmetry in $d \leq 2$ (noncompact) dimensions. The ingredients to this theorem are the locality of the underlying Hamiltonian, and the universal relativistic long-wavelength form of the dispersion relation. The long-range order is then destroyed by fluctuations with very long wavelengths. However, in atomic gas experiments the trap provides the largest length scale ℓ_{osc}, such that these fluctuations are not present and condensation can be observed in lower-dimensional geometries.

Free fermions and Fermi surface

Whereas the appearance of a Bose–Einstein condensate is closely related to the fact that identical bosons can have arbitrarily large occupation numbers, the notion of a *Fermi surface* is a consequence of Pauli's principle for many-fermion systems.

To get an intuition, we consider an ideal gas of N identical fermions and ask: What is the ground state of the quantum many-body system? (This state is realized at zero temperature.) Obviously, each of the particles seeks to minimize its energy. But since every single particle state can only be occupied by at most one fermion, the ground state will be such that precisely the N energetically lowest lying states are occupied. Equivalently, due to rotation symmetry, all states with momenta inside a sphere of radius p_F in momentum space will be occupied. Restricting to three dimensions, we can count states by dividing the classical phase space into cells of volume h^3. This yields

$$N \stackrel{!}{=} \frac{gV}{(2\pi\hbar)^3}\frac{4\pi}{3}p_\mathrm{F}^3. \tag{2.28}$$

We call $p_\mathrm{F} = \hbar k_\mathrm{F}$ the Fermi momentum and deduce

$$k_\mathrm{F}(n) = (6\pi^2 n/g)^{1/3}. \tag{2.29}$$

From p_F we construct the *Fermi energy* and *temperature*, $\varepsilon_\mathrm{F} = \varepsilon_{p_\mathrm{F}} = p_\mathrm{F}^2/2M$ and $T_\mathrm{F} = \varepsilon_\mathrm{F}/k_\mathrm{B}$, respectively.

Our simple picture of the many-body ground state is correct, because from Eq. (2.22) we have

$$\begin{aligned} n = \frac{\partial P}{\partial \mu} &= g\int \frac{\mathrm{d}^3p}{(2\pi\hbar)^3}\frac{1}{e^{\beta(\varepsilon_p-\mu)}+1} \\ &\xrightarrow{T\to 0} g\int \frac{\mathrm{d}^3p}{(2\pi\hbar)^3}\theta(\mu-\varepsilon_p) = \frac{g}{6\pi^2\hbar^3}(2M\mu)^{3/2}. \end{aligned} \tag{2.30}$$

On the other hand, from the zero temperature limit of the Fermi–Dirac distribution we infer that the highest energy present in the system is $\varepsilon_\mathrm{F} = \mu$ and thus we find $p_\mathrm{F} = (2M\mu)^{1/2}$. As before, we eventually arrive at $k_\mathrm{F} = (6\pi^2 n/g)^{1/3}$. The Fermi–Dirac distribution at zero temperature is shown in Fig. 2.6.

What happens to this picture at nonzero temperature? The Fermi–Dirac distribution $n_\mathrm{F}(\varepsilon) = (e^{(\varepsilon-\mu)/k_\mathrm{B}T}+1)^{-1}$ is no longer a sharp step function but is rather smeared out around $\epsilon = \mu$. Nevertheless, the smeared out region is of order $k_\mathrm{B}T$, whereas the distance of the edge from $\varepsilon = 0$ is of order $\mu \simeq \varepsilon_\mathrm{F} = k_\mathrm{B}T_\mathrm{F}$. Therefore, as long as $T/T_\mathrm{F} \ll 1$, the distribution function looks approximately like a step function. We visualize this situation in Fig. 2.6. For $T > 0$, there are thermally excited particles with energies close to the chemical potential. We conclude that the low lying excitations of a Fermi gas are not at zero momentum but rather at momenta close to the Fermi surface, which consists of the momenta $|\vec{p}| = p_\mathrm{F}$.

2.4 Feshbach resonances and BCS-BEC crossover

In this section we introduce the BCS-BEC crossover of two-component ultracold fermions. For this purpose we discuss the underlying physics of a Feshbach resonance (FR), and then motivate the two-channel model for a field theoretical

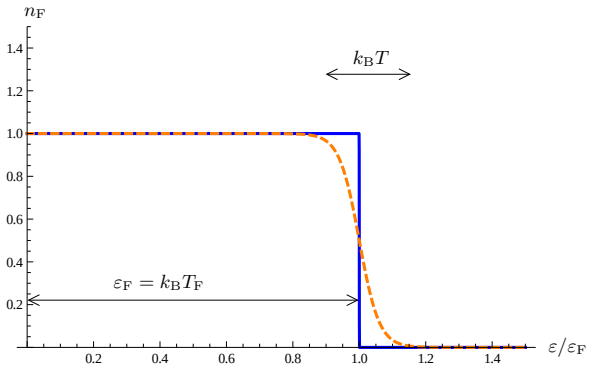

Figure 2.6: The Fermi–Dirac distribution at zero temperature (solid line) constitutes a step function. For $T > 0$ (dashed line), broadening appears in a region of width $k_B T$ around the Fermi edge located at $\varepsilon = \varepsilon_F = k_B T_F$. If the distance of the edge from the origin is much larger than the area of broadening, the distribution function still displays the characteristic step-like behavior. Clearly, this picture is valid for the dimensionless parameter T/T_F being small. Figure taken from Boettcher et al. [2012].

description of the BCS-BEC crossover. We also discuss its relation to the single-channel model in the case of a broad FR. We refer to Boettcher et al. [2012] for a pedagogical introduction to the BCS-theory of superfluidity and the Bogoliubov description of the BEC-limit.

Feshbach resonances and microscopic model

There are two cornerstones of quantum condensation phenomena in the weak coupling regimes: On the one hand, attractive interactions lead to superfluidity of two-component fermions via the formation of Cooper pairs. The momenta of two fermions constituting such a pair are located on opposite points of the Fermi surface. This locality in momentum space implies that the spacing between them may be large in position space. On the other hand, there is Bose condensation of weakly repulsive bosons, which are microscopically pointlike objects localized in position space. Such bosons could effectively be realized as tightly bound pairs of two fermions.

There exists an experimental knob to connect these two scenarios, the atomic FR (Grimm et al. [2000]), which allows to change the scattering length through the variation of an external magnetic field B. We write

$$a(B) = a_{\mathrm{bg}} \left(1 - \frac{\Delta B}{B - B_0} \right) , \tag{2.31}$$

where a_{bg}, ΔB and B_0 are parameters which can be determined experimentally. This formula is a decent parametrization in a range of order ΔB around $B \approx$

B_0. In particular, at $B = B_0$ the scattering length changes sign and becomes anomalously large, $|a| \gg \ell_{\mathrm{vdW}}$. Recall that this does not invalidate our effective Hamiltonian and the fact that scattering can be assumed to be pointlike, see the discussion at the end of Sec 2.1.

Sufficiently stable ultracold quantum gases of two-component fermions are built from either ^{6}Li or ^{40}K, which are alkali atoms. Their internal structure is relevant in order to have fermionic s-wave interactions at all, but also manifests itself in the appearance of Feshbach resonances. To understand this, we consider a single alkali atom. We can approximate the system to consist of an atomic core and a valence electron. The ground state of the system is given by the electron being in the s-orbital. Accordingly, the orbital angular momentum of the valence electron vanishes ($\ell = 0$) and thus a fine structure does not appear. However, the electron spin S couples to the spin of the nucleus I. The resulting quantum number F introduces a (tiny) hyperfine splitting of the ground state. Since $S = 1/2$, the value of F is given by $F = I \pm 1/2$. In addition, every hyperfine state has a $(2F + 1)$-fold degeneracy $m_F = -F, \ldots, F$. Thus, alkali atoms in their electronic ground state can be distinguished according to their hyperfine state $|F, m_F\rangle$.

Now suppose that two atoms in different hyperfine states scatter off each other. Due to the internal (spin) structure of the colliding partners, we call this a multichannel scattering process. The two-body system of atoms will be in a superposition of the singlet and the triplet state. Depending on the species of atoms, the former will have a higher or a lower energy than the latter, while the first option is more generic. Moreover, due to the hyperfine coupling there will in general be a mixing between both states. For our purpose it is enough to restrict our considerations to two relevant channels, an *open* and a *closed channel*, which have different magnetic moments. We normalize the potential such that two atoms in the open channel at infinite distance have zero energy; this sets the *scattering threshold*. The closed channel is separated from the open one by a large energy gap ΔE (cf. Fig. 2.7). It thus cannot be accessed by atoms in the lower channel. The relevant feature of the closed channel is a bound state lying close to the open channel scattering threshold. It is evident that this situation is not particularly generic since typical bound state level spacings are much larger than typical collision energies in ultracold gases, and thus requires specific, fine-tuned conditions.

Due to a difference in magnetic moment $\Delta\mu$, open and closed channel couple differently to an external magnetic field B. For this reason, the difference in energies between both channels can be tuned according to $\Delta E \to \Delta E + \Delta\mu \cdot B$. Consider a particular bound state from the closed channel. Its energetic distance from the scattering threshold $E = 0$ is called the *detuning*

$$\nu(B) = \Delta\mu \cdot (B - B_0)\,. \tag{2.32}$$

Due to second order processes, where two colliding atoms virtually enter the closed channel and then leave it again, a bound state with small ν affects the scattering properties of the alkali atoms. In particular, changing the magnetic field such

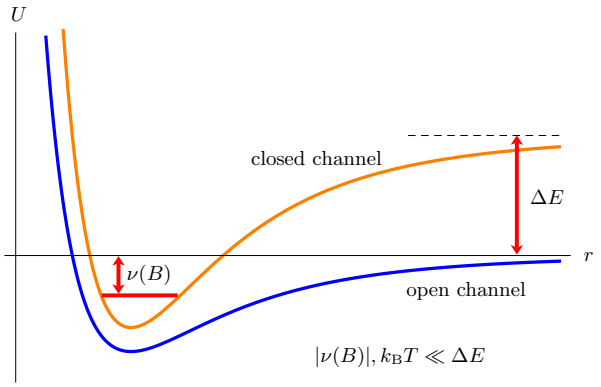

Figure 2.7: Interatomic potential U between two fermions in distinct hyperfine states separated by a distance r. The closed channel consists of bound states. Low energy scattering can only take place in the open channel. However, by changing the external magnetic field B, we can drive one of the bound states close to the scattering threshold at $U(r \to \infty) = 0$. The energy distance related to this particular bound state is denoted as $\nu(B) = \Delta\mu \cdot (B - B_0)$. The resulting scattering length $a = a(B)$ is parametrized according to Eq. (2.31). For $B \approx B_0$, it becomes anomalously large, and thus it can largely exceed the interparticle spacing: $|a| \gg \ell_{\mathrm{vdW}} \Rightarrow |(k_{\mathrm{F}} a)^{-1}| \lesssim 1$. Figure taken from Boettcher et al. [2012].

that $\nu \to 0$, both channels become resonant and we obtain a strongly interacting system.

We will see below that the scattering physics in the vicinity of a broad Feshbach resonance will effectively look like that of pointlike fermions, however, with a magnetic field dependent scattering length $a(B)$ as in Eq. (2.31). The scattering properties can thus be controlled by an external knob. This constitutes the most important application of Feshbach resonances in ultracold atomic physics. For more detailed discussions we refer to Chin et al. [2010].

We now incorporate the physics of a Feshbach resonance for two-component fermions on the level of the microscopic action. The action for a fermionic theory with pointlike interactions is given by

$$S_\psi[\psi^*, \psi] = \int_X \left(\psi^\dagger \left(\partial_\tau - \frac{\nabla^2}{2M} \right) \psi + \frac{\lambda_{\mathrm{bg}}}{2} (\psi^\dagger \psi)^2 \right), \tag{2.33}$$

with Grassmann fields $\psi = (\psi_1, \psi_2)$, see Eq. (2.18) and Sec. 3.1.1. Eq. (2.33) constitutes a single-channel model. To simplify notation we drop the dependence on the chemical potential in the following.

The closed channel can be included explicitly in terms of a microscopic bosonic field φ, which constitutes a composite degree of freedom resulting from the interconversion of two fermions into a closed channel molecule. The action for this

boson field is modelled as

$$S_\varphi[\varphi^*,\varphi] = \int_X \varphi^*\Big(\partial_\tau - \frac{\nabla^2}{4M} + \nu\Big)\varphi\,. \tag{2.34}$$

The most important term is the detuning ν, which acts as a mass term for the bosons. In addition, we allow for a Galilean invariant kinetic term, where the prefactor of $1/4M$ is related to the mass $2M$ of the composite object. As we will see in a moment, the microscopic kinetic term is, however, unimportant for the case of broad Feshbach resonances which are studied here, and could be equally well omitted. The full microscopic action from which we will extract the physics of the BCS-BEC crossover is then given by (Holland et al. [2001])

$$\begin{aligned} S[\psi^*,\psi,\varphi^*,\varphi] = \int_X \Bigg(&\psi^\dagger\Big(\partial_\tau - \frac{\nabla^2}{2M}\Big)\psi + \frac{\lambda_{\mathrm{bg}}}{2}(\psi^\dagger\psi)^2 \\ &+ \varphi^*\Big(\partial_\tau - \frac{\nabla^2}{4M} + \nu\Big)\varphi - h\big(\varphi^*\psi_1\psi_2 - \varphi\psi_1^*\psi_2^*\big)\Bigg). \end{aligned} \tag{2.35}$$

The Yukawa-type cubic coupling $\sim h\varphi^*\psi_1\psi_2$ (called *Feshbach coupling* in the cold atom context) allows for the interconversion of two fermions of opposite spin into one molecule.

The parameters λ_{bg}, ν and h of the microscopic action can be measured in experiment. We show here that they correspond to the three parameters in Eq. (2.31) for the scattering length $a(B)$ across a Feshbach resonance in the broad resonance limit. For this purpose, we consider the functional integral $Z = \int \mathrm{D}\varphi\mathrm{D}\psi\, e^{-S[\psi,\varphi]}$. For fixed ψ and ψ^*, we can perform the Gaussian integral in φ^* and φ. This is equivalent to the saddle-point approximation about the solution of the mean field equations of motion,

$$\frac{\delta S}{\delta\varphi^*} = 0 \quad\Rightarrow\quad \varphi = \frac{h}{\partial_\tau - \nabla^2/4M + \nu}\psi_1\psi_2\,. \tag{2.36}$$

As the action is quadratic in φ, the saddle-point approximation is exact. If we formally insert this into the partition function and integrate out the bosonic fields, we arrive at the action

$$S[\psi^*,\psi] = S_\psi + \int_X \psi_1\psi_2\frac{h^2}{\partial_\tau - \nabla^2/4M + \nu}\psi_1^*\psi_2^*\,, \tag{2.37}$$

with S_ψ from Eq. (2.33). We emphasize that the procedure described here corresponds to reversing a Hubbard–Stratonovich transformation for a slightly more complicated inverse boson propagator; this is possible due to the fact that in Eq. (2.34) we work with a quadratic bosonic action. We now take the *broad resonance limit*, where $h^2, \nu \to \infty$ with h^2/ν kept fixed. Then, we can neglect the derivatives corresponding to frequency and momentum dependence of the effective

four-fermion vertex. More precisely, we scale $\nu \sim h^2$ for $h \to \infty$, while leaving the derivative coefficients of order unity. We then obtain the action

$$S[\psi^*, \psi] = S_\psi[\psi^*, \psi] - \frac{1}{2}\frac{h^2}{\nu}\int_X (\psi^\dagger \psi)^2 \,. \tag{2.38}$$

Apparently, this coincides with a purely fermionic action with an effective coupling

$$\lambda_{\text{eff}} = \lambda_{\text{bg}} - \frac{h^2}{\nu} \,. \tag{2.39}$$

We conclude that in the broad resonance limit the two-channel and the single-channel model become equivalent (Diehl and Wetterich [2006, 2007], Gurarie and Radzihovsky [2007]). The single channel model, however, acquires an additional effective contribution to the coupling constant. The Feshbach resonances in ^{6}Li and ^{40}K are broad. The narrow resonance limit is conceptually interesting, as it can be solved exactly (Diehl and Wetterich [2006], Gurarie and Radzihovsky [2007]). Moreover, recently, examples of narrow resonances have been studied experimentally (Kohstall et al. [2012]). In an RG language, it corresponds to a Gaussian fixed point, while the broad resonances are governed by an interacting fixed point (Diehl et al. [2007b]). The broad resonance fixed point is characterized by a large degree of universality (Nikolić and Sachdev [2007], Diehl et al. [2007b]).

Assuming the couplings in Eq. (2.39) to be the renormalized ones, we can relate them to the scattering length according to $\lambda = 4\pi a/M$.[1] We find

$$a = \frac{M}{4\pi}\left(\lambda_{\text{bg}} - \frac{h^2}{\nu}\right) \,. \tag{2.40}$$

Comparing this to Eqs. (2.31) and (2.32), we find that indeed $\nu = \Delta\mu \cdot (B - B_0)$ corresponds to the detuning from resonance. The four-fermion coupling λ_{bg} is related to the background scattering length in the usual manner via $a_{\text{bg}} = M\lambda_{\text{bg}}/4\pi$. With $\Delta B = h^2\Delta\mu/\lambda_{\text{bg}}$, the Yukawa/Feshbach coupling h is seen to determine the *width of the resonance*. We also remark here that the sign of h is irrelevant.

For magnetic fields close to B_0, the scattering length becomes anomalously large and the background scattering length can be neglected. In what follows, we assume $a_{\text{bg}} = 0$ throughout the whole crossover.

As anticipated above, only the value of the scattering length plays the role of a relevant parameter for the crossover in the broad resonance limit. Given the density n of atoms, we build the dimensionless parameter $(k_{\text{F}}a)^{-1}$. Since the interparticle spacing is given by $\ell \approx k_{\text{F}}^{-1}$, we find the following scheme for the 3D BCS-BEC crossover:

1) $k_{\text{F}}a \to -\infty$: weakly interacting fermions,

[1] Note the difference in convention to identical bosons, where $\lambda = 8\pi a/M$.

2) $|(k_\mathrm{F}a)^{-1}| \leq 1$: strong interactions, dense regime,

3) $(k_\mathrm{F}a)^{-1} \to \infty$: weakly interacting molecules.

The regions $a < 0$ and $a > 0$ are called BCS and BEC side of the crossover, respectively. We call $(k_\mathrm{F}a)^{-1}$ the crossover parameter. An analogous classification scheme can be given in the 2D-case, where the crossover parameter $\log(k_\mathrm{F}a) = \frac{1}{2}\log(\varepsilon_\mathrm{F}/|\varepsilon_\mathrm{b})$ expresses the ratio of fermionic (ε_F) and bosonic ($\varepsilon_\mathrm{B} = -\hbar^2/Ma^2$) properties of the system.

The 3D system with $a^{-1} = 0$ is referred to as the *Unitary Fermi gas* (UFG). The origin of this term is the following. The cross section of two-body scattering in the s-wave channel is given by $\sigma_{l=0} = 4\pi|f_{l=0}|^2$. For the perturbative regions with $p|a| \ll 1$, where p is the relative momentum of scattering particles, we then find $\sigma = 4\pi a^2$. Naively extrapolating this to the resonance $|a|^{-1} \to 0$, this would imply a divergent cross section, which is excluded from the fact that the scattering matrix is unitary. Recalling however Eq. (2.13), we find in the latter limit that $\sigma \simeq 4\pi|(-1/a - \mathrm{i}p)|^{-2} \to 4\pi/p^2$. Since scattering is meaningful only for nonzero relative momenta, the expression on the right hand side constitutes the upper limit on possible s-wave scattering; in the UFG, the typical scale for the scattering momentum are $k_\mathrm{F}, \sqrt{T}$. This effect has been observed by Gupta et al. [2003]. We note that exactly at the unitary point, $a^{-1} = 0$, the scale associated to interactions drops out and the only remaining scales are interparticle spacing and temperature. This hints at highly universal properties in this regime (Ho [2004]) (distinct from the broad resonance universality described above). However, at this point and in its vicinity where $|k_\mathrm{F}a|^{-1} \ll 1$, the gas parameter Eq. (2.14) is large and cannot be used as a control parameter for systematic expansions. In this regime, where the interaction length scale greatly exceeds the interparticle spacing, we deal with a strongly coupled and dense quantum system.

Note that the crossover from the BCS- to the BEC side in 3D is driven by interactions, since only for $a > 0$ there is a two-particle bound state with energy $\varepsilon_\mathrm{B} = -\hbar^2/Ma^2$. This makes the BEC-side inaccessible to be reached by tuning many-body parameters such as k_F alone. One may also rephrase this in the observation that a sign-change of the crossover parameter $(k_\mathrm{F}a)^{-1}$ can only be achieved by changing the sign of a. In contrast, there always is a two-body bound state with binding energy $\varepsilon_\mathrm{B} = -\hbar^2/Ma^2$ in 2D. Hence the BCS- and BEC-sides are not qualitatively distinct in vacuum. In fact, the 2D crossover parameter $\log(k_\mathrm{F}a)$ can be tuned at will by changing the density of the sample. In this way the overlap between pairs can be increased, which makes the system atomic for sufficiently large n.

At zero temperature the system with equal number of $|1\rangle$- and $|2\rangle$-atoms is a homogeneous superfluid in both 3D and 2D. For sufficiently large nonzero temperature there is a second order transition to the disordered phase for all values of $k_\mathrm{F}a$. The value of the critical temperature $T_\mathrm{c}/T_\mathrm{F}$ as a function of $k_\mathrm{F}a$ is particularly interesting. In 3D in the deep BEC regime, we expect the noninteracting

formula (2.24) to hold, with a shift due to the small, but nonvanishing diluteness parameter $k_{\mathrm{F}}a$. On the BCS side, the BCS prediction for the critical temperature will turn out to be insufficient, because it is lowered by a factor of approximately two due to particle-hole fluctuations. One of the great challenges in many-body theory consists of the calculation of $T_{\mathrm{c}}/T_{\mathrm{F}}$ at unitarity from first principles and the determination of the phase diagram of the 2D BCS-BEC crossover.

3 Functional methods for ultracold atoms

3.1 Functional methods in quantum field theory

3.1.1 Functional integral and effective action

In this section, the quantum field theoretical formulation of interacting cold atoms is put forward. Starting from the functional integral representation of the quantum partition function $Z(\mu, T)$, we introduce the effective action Γ, which is a functional of the mean field. It stores the same information as the partition function or generating functional, however, in a way that is more intuitive. In particular, it naturally provides the classical limit. The effects of both quantum and thermal fluctuations on physical observables can be derived from it in the few- and many-body context. Moreover, it allows for a transparent discussion of spontaneous symmetry breaking, and allows to leverage the power of symmetry considerations from the classical action over to the full quantum theory. We set $\hbar = k_\mathrm{B} = 1$. For the moment, we keep the nonrelativistic mass M in our formulation, but later we will set $2M = 1$ in the same spirit as for the fundamental constants.

Functional integral

As we have shown in section 2.1, a system of ultracold atoms is accurately described by the effective Hamiltonian

$$\hat{H} = \int_{\vec{x}} \left(\hat{a}^\dagger(\vec{x}) \left(-\frac{\nabla^2}{2M} + V_\mathrm{ext}(\vec{x}) \right) \hat{a}(\vec{x}) + \frac{g}{2} \hat{n}(\vec{x})^2 \right), \tag{3.1}$$

where $\hat{a}^\dagger(\vec{x})$ and $\hat{a}(\vec{x})$ are operators which create and annihilate an atom at position $\vec{x}$, respectively. Depending on whether we consider bosons or fermions, these operators satisfy commutation or anti-commutation relations. The density operator is given by $\hat{n}(\vec{x}) = \hat{a}^\dagger(\vec{x})\hat{a}(\vec{x})$.

The Hamiltonian in Eq. (3.1) defines a quantum field theory with operators $\hat{a}$ and $\hat{a}^\dagger$ on each point of space. Physical observables are derived from expectation values of functions of these operators. However, the corresponding quantum field theory can also be formulated in terms of a functional integral. The latter does no longer depend on the notion of field operators. In the context of quantum many-body systems, a possible derivation starts from the grand canonical partition

function

$$Z(\mu, T) = \mathrm{Tr}\Big(e^{-\beta(\hat{H}-\mu\hat{N})}\Big), \tag{3.2}$$

where the trace is taken over Fock space. This trace can be represented in the basis of so-called coherent states, which are eigenstates of the annihilation operator $\hat{a}(\vec{x})$. We then obtain

$$Z(\mu, T) = \int \mathrm{D}\varphi^* \, \mathrm{D}\, \varphi e^{-S[\varphi^*, \varphi]}. \tag{3.3}$$

We call the expression in Eq. (3.3) a *functional* or *path integral*. It contains the microscopic action $S[\varphi^*, \varphi]$ of a field theory, which in our case is a nonrelativistic one.

The explicit construction of the functional integral representation of the partition function for a generic many-body Hamiltonian is carried out in Boettcher et al. [2012]. We summarize here the two main findings.

1) Bosonic atoms are represented by complex fields $\varphi(\tau, \vec{x})$, whereas fermions are described in terms of Grassmann valued fields $\psi(\tau, \vec{x})$.

2) The non-commutativity of operators introduces the *imaginary time* τ, which is restricted to the interval $[0, \beta]$. Bosonic fields are β-periodic in time, i.e. $\varphi(\beta, \vec{x}) = \varphi(0, \vec{x})$. In contrast, fermionic fields satisfy $\psi(\beta, \vec{x}) = -\psi(0, \vec{x})$.

The second property implies that the Fourier transform of the fields φ and ψ in imaginary time direction reduces to a Fourier series with discrete *Matsubara frequencies*

$$\omega_n = \begin{cases} 2\pi n T & \text{(bosons)} \\ 2\pi(n + 1/2)T & \text{(fermions)} \end{cases}, \qquad n \in \mathbb{Z}. \tag{3.4}$$

We say that the imaginary time direction is compactified to a torus of circumference β. In this way, introducing a chemical potential μ and compactifying the time direction to $0 \leq \tau \leq \beta$, we can describe the equilibrium properties of the quantum field theory at nonzero density and temperature. The action of the field theory is related to the normal ordered Hamiltonian $\hat{H} = H[\hat{a}^\dagger(\vec{x}), \hat{a}(\vec{x})]$ according to

$$S[\varphi^*, \varphi] = \int_0^\beta \mathrm{d}\tau \left(\int_{\vec{x}} \varphi^*(\tau, \vec{x})(\partial_\tau - \mu)\varphi(\tau, \vec{x}) + H[\varphi^*(\tau, \vec{x}), \varphi(\tau, \vec{x})] \right) \tag{3.5}$$

with inverse temperature $\beta = T^{-1}$. For the particular choice of the effective Hamiltonian in Eq. (3.1), we have

$$S[\varphi^*, \varphi] = \int_0^\beta \mathrm{d}\tau \int_{\vec{x}} \left(\varphi^*(\tau, \vec{x}) \Big(\partial_\tau - \frac{\nabla^2}{2M} - \mu \Big) \varphi(\tau, \vec{x}) + \frac{g}{2} (\varphi^*(\tau, \vec{x})\varphi(\tau, \vec{x}))^2 \right). \tag{3.6}$$

Generating functional and effective action

Starting from the functional integral representation for the partition function Z, we now construct the corresponding effective action. The procedure outlined here focuses on the application to systems of ultracold atoms. However, additional insights into these concepts can be obtained from a comparison to classical Ising magnets on a discrete lattice. We refer to Boettcher et al. [2012] for a comparison of the setup for classical magnets and ultracold atoms. Therein, the continuum limit is performed and the notions of functional differentiation and integration are reviewed. In our discussion of functional methods we mostly restrict to the bosonic case of a complex scalar field. There are only minor modifications for fermions, which are discussed at the end of the section.

The bosonic functional integral in Eq. (3.3) allows for the definition of a probability measure on the set of fields φ. Given an observable $\mathcal{O}(\{\varphi\})$ which depends on the field, we define

$$\langle \mathcal{O} \rangle = \frac{1}{Z} \int \mathrm{D}\,\varphi^* \mathrm{D}\varphi\, \mathcal{O}(\{\varphi\}) e^{-S[\varphi^*,\varphi]}. \tag{3.7}$$

Herein, the action S acts as a weight. For instance, from $\mathcal{O} = \varphi(X)$ or $\mathcal{O} = \varphi^*(X)\varphi(Y)$ we obtain the one- and two-point correlation functions of the theory, respectively. More generally, we obtain averages of observables by introducing a complex source field $j(X)$ according to

$$Z[j^*, j] = \int \mathrm{D}\varphi^*\, \mathrm{D}\varphi\, e^{-S[\varphi^*,\varphi] + \int_X j_X^* \varphi_X + \int_X \varphi_X^* j_X}. \tag{3.8}$$

We write $X = (\tau, \vec{x})$ and $\int_X = \int_0^\beta \mathrm{d}\tau \int_{\vec{x}}$. We call $Z[j^*, j]$ the *generating functional* and have

$$\phi(X) = \langle \varphi(X) \rangle_j = \frac{\delta \log Z}{\delta j^*(X)}, \tag{3.9}$$

$$\langle \varphi^*(X)\varphi(Y) \rangle_j = \frac{1}{Z} \frac{\delta^2 Z}{\delta j(X) \delta j^*(Y)}, \tag{3.10}$$

etc. The subscript j indicates that the external source is not yet set to zero. For a physical picture of this situation, the external source $j(X)$ can be thought of as a (static) pump or loss of atoms such that the mean field of atoms at position X is engineered to the particular value $\phi(X)$.

Generalizing Eqs. (3.9) and (3.10), we find the representation of a general expectation value to be

$$\langle \mathcal{O} \rangle_j = \frac{1}{Z} \mathcal{O}\Big(\Big\{ \frac{\delta}{\delta j} \Big\} \Big) Z[j^*, j]. \tag{3.11}$$

We conclude that all correlation functions of interest can be obtained from the generating functional Z or the *Schwinger functional*

$$W[j^*, j] = \log Z[j^*, j]. \tag{3.12}$$

The latter constitutes the generating functional of connected n-point functions. For instance, we find that the connected two-point function is related to W according to

$$W^{(2)}[j](X,Y) = \frac{\delta^2 W}{\delta j^*(X)\delta j(Y)} = \langle\varphi(X)\varphi^*(Y)\rangle_j - \phi(X)\phi^*(Y). \tag{3.13}$$

This object is also called (time-ordered) *Green's function* or *propagator* of the theory. Imposing time-ordering onto the propagators leads to general time-ordered correlation functions in Eq. (3.11).

The field expectation value carries a direct physical significance. For example, for a three-dimensional Bose gas $\phi(X)$ describes the condensate. Therefore, it seems desirable to implement it into the theory in a more direct way. In fact, this is possible by the aid of a Legendre transformation, which gives rise to the *effective action*. We introduce the latter as the generating functional which depends on the *mean field* ϕ defined by

$$\phi(X) = \langle\varphi(X)\rangle_j = \frac{\delta W}{\delta j^*(X)}. \tag{3.14}$$

Assume we have solved this equation for j and j^*. We can then construct the effective action according to the Legendre transformation

$$\Gamma[\phi^*,\phi] = \int_X (\phi_X^* j_X + j_X^*\phi_X) - W[j^*,j], \tag{3.15}$$

where j and j^* are defined implicitly by Eq. (3.14).[1] Note that while the active variable for the partition function is the source, $Z = Z[j]$, the active variable for the effective action is the field expectation value, $\Gamma = \Gamma[\phi]$. The effective action is thus parametrized directly in terms of a physical observable. Applying the chain rule for functional differentiation we find

$$\frac{\delta\Gamma}{\delta\phi(X)}[\phi^*,\phi] = j^*(X). \tag{3.16}$$

Technically speaking, the effective action is the generating functional of *one-particle irreducible (1PI) correlation functions*. They can be obtained from Γ by taking successive functional derivatives with respect to $\phi(X)$ and $\phi^*(X)$. Diagrammatically the 1PI correlation functions are given by all diagrams that cannot be split by cutting one (internal) line, hence the name. Often, we are mainly interested in the situation of vanishing source. Then, given the effective action, we have to solve the *equations of motion*

$$\frac{\delta\Gamma}{\delta\phi(X)}[\phi_0^*,\phi_0] = 0 \tag{3.17}$$

[1] More generally we define $\Gamma[\phi^*,\phi] = \sup_{j^*,j}(\int_X(\phi_X^* j_X + j_X^*\phi_X) - W[j^*,j])$, see Eq. (3.45) for the case of a real scalar.

to obtain the thermodynamic equilibrium state $\phi_0 = \langle\varphi\rangle_{j=0}$ of the theory. The reference to the external field is no longer present and also not needed, because it is already included in $\Gamma[\phi^*, \phi]$. Often, especially for the purposes of this thesis, the solution ϕ_0 to Eq. (3.17) is constant in space-time. This will be explained in more detail below Eq. (3.28). However, in general there also might be inhomogeneous solutions ϕ_0 to the nonlinear partial differential equation Eq. (3.17), such as instantons, vortices, or inhomogeneous pairing fields (see Sec. 3.1.2).

Higher derivatives of the effective action with respect to the fields ϕ, ϕ^*, denoted by $\Gamma^{(n)}$ for the nth derivative, provide the 1PI vertices. The second derivative of the effective action,

$$\Gamma^{(2)}(X,Y) = \frac{\delta^2\Gamma}{\delta\phi^*(X)\delta\phi(Y)}, \tag{3.18}$$

plays a special role, as it is the *inverse propagator*. This is easily proven by

$$\begin{aligned}\int_Z \Gamma^{(2)}(X,Z)W^{(2)}(Z,Y) &= \int_Z \left(\frac{\delta j^*(Z)}{\delta\phi^*(X)}\frac{\delta\phi^*(Y)}{\delta j^*(Z)} + \frac{\delta j(Z)}{\delta\phi^*(X)}\frac{\delta\phi^*(Y)}{\delta j(Z)}\right) \\ &= \delta(X-Y),\end{aligned} \tag{3.19}$$

where we have used (3.14), (3.16), and the completeness relation of derivatives with respect to $j\,, j^*$.

In principle, Eq. (3.16) can be taken as a starting point to calculate the effective action $\Gamma[\phi^*, \phi]$ in certain approximations. However, the definition of Γ implies an exact identity, which is equivalent to Eq. (3.16), but more useful. Applying Eqs. (3.15), (3.16) and $W = \log Z$, we arrive at

$$\begin{aligned} e^{-\Gamma[\phi^*,\phi]} &= e^{-\int_X (j^*\phi+\phi^* j)+W} = e^{-\int_X (j^*\phi+\phi^* j)} \int \mathrm{D}\varphi^*\mathrm{D}\varphi\, e^{-S[\varphi^*,\varphi]+\int_X (j^*\varphi+\varphi^* j)} \\ &= \int \mathrm{D}\varphi^*\,\mathrm{D}\varphi\, e^{-S[\varphi^*,\varphi]+\int_X (j^*(\varphi-\phi)+(\varphi^*-\phi^*)j)} \\ &= \int \mathrm{D}\varphi^*\,\mathrm{D}\varphi\, e^{-S[\varphi^*,\varphi]+\int_X (\frac{\delta\Gamma}{\delta\phi}[\phi]\cdot(\varphi-\phi)+(\varphi^*-\phi^*)\cdot\frac{\delta\Gamma}{\delta\phi^*}[\phi])}. \end{aligned} \tag{3.20}$$

This equation is called the *background field identity* for the effective action. For $\phi = \phi_0$ with ϕ_0 satisfying Eq. (3.17) we recover

$$Z(\mu,T) = e^{-\Gamma[\phi_0^*,\phi_0]}, \tag{3.21}$$

i.e. the effective action then corresponds to the grand canonical potential. Furthermore, by performing a shift of the integration variable, we rewrite Eq. (3.20) as

$$e^{-\Gamma[\phi^*,\phi]} = \int \mathrm{D}\delta\varphi^*\mathrm{D}\delta\varphi e^{-S[\phi^*+\delta\varphi^*,\phi+\delta\varphi]+\int_X (\frac{\delta\Gamma}{\delta\phi}[\phi]\cdot\delta\varphi+\delta\varphi^*\cdot\frac{\delta\Gamma}{\delta\phi^*}[\phi])}. \tag{3.22}$$

This functional integral representation of the effective action gives rise to the intuitive picture that the effective action encodes the complete information on the

euclidean field theory by means of summing over all possible field configurations $\delta\varphi$ deviating from the classical one (ϕ).

We now show that in the *classical limit*, the effective action and the classical action coincide. Reintroducing Planck's constant $\hbar$, we have $\Gamma/\hbar$ and $S/\hbar$ appearing in Eq. (3.22). The classical limit is obtained for $\hbar \to 0$ at fixed Γ. The integrand is then sharply peaked around the solution to the classical equations of motion $\delta S/\delta\varphi = 0$. This results in $\Gamma = S$, which physically is the *classical approximation*.

It is clear that the effective action lends itself ideally for semiclassical approximations, and also systematic improvements thereof. From Eqs. (3.20) or (3.22) we can easily go one step beyond the classical approximation by expanding the exponent in the functional integral around its minimum value φ_0 determined from

$$-\frac{\delta S}{\delta\varphi^*}[\varphi_0] + \frac{\delta\Gamma}{\delta\phi^*}[\phi] = 0 = -\frac{\delta S}{\delta\varphi}[\varphi_0] + \frac{\delta\Gamma}{\delta\phi}[\phi]. \tag{3.23}$$

For the particularly simple case where $\phi = \varphi_0$, the linear derivatives cancel and we obtain

$$e^{-\Gamma[\varphi_0]} \simeq e^{-S[\varphi_0]} \int \mathrm{D}\varphi^* \mathrm{D}\varphi e^{-\frac{1}{2}\int (\varphi,\varphi^*)\cdot S^{(2)}[\varphi_0]\cdot \binom{\varphi}{\varphi^*}} \tag{3.24}$$

with $S^{(2)}$ the second functional derivative of S with respect to φ, φ^*.

More generally, employing the rules of Gaussian integration to the functional integral, the Gaussian approximation to Eq. (3.22) can be evaluated at any field ϕ which ensures the path integral to be dominated by small fluctuations $\delta\varphi$. This leads to the so-called *one-loop formula*

$$\Gamma[\phi^*, \phi] \simeq S[\phi^*, \phi] + \frac{1}{2}\mathrm{Tr}\log S^{(2)}[\phi^*, \phi]. \tag{3.25}$$

In this order of approximation, the linear derivative terms cancel due to the tree level relation $\Gamma \simeq S$. Note that the effective action equals the classical action also in the case of a free, noninteracting theory. Expanding the Tr log expression in powers of the field, we generate one-loop perturbation theory. We may therefore expect Eq. (3.25) to give good results in the perturbative regime of small coupling.

Our considerations can easily be extended to fermions as well. We introduce independent Grassmannian source terms $\eta(X)$ and $\eta^*(X)$ into the generating functional $Z[j^*, j, \eta^*, \eta]$, which couple linearly to the fields $\psi^*(X)$ and $\psi(X)$, respectively. The effective action is defined in the same manner as before via the Legendre transformation of $\log Z$ with respect to the mean fields. The ground state of the theory necessarily satisfies $\langle\psi(X)\rangle_{\eta=0} = \langle\psi^*(X)\rangle_{\eta=0} = 0$, since Pauli's principle forbids macroscopic occupation of fermionic states. However, the generating functional Γ depends on nonvanishing fermionic "mean fields". Such fields $\bar{\psi}(X)$ can be constructed by applying a source $\eta(X) = \delta\Gamma/\delta\bar{\psi}(X)$. They must not be regarded as physical objects, but rather as bookkeeping parameters used to generate the 1PI correlation functions via Grassmannian functional differentiation.

Eq. (3.25) is also valid for fermionic fields, but with an additional minus sign in front of the trace. For a mixed theory of both bosons and fermions we employ the *supertrace*, STr, which takes into account the appropriate sign for fermionic loops. Thus we arrive at the one-loop formula

$$\Gamma[\phi,\bar{\psi}] \simeq S[\phi,\bar{\psi}] + \frac{1}{2}\mathrm{STr}\log S^{(2)}[\phi,\bar{\psi}]. \tag{3.26}$$

More detailed presentations on functional integrals, with emphasis on quantum many-body systems, can be found in Negele and Orland [1998], Altland and Simons [2010].

3.1.2 Effective potential and spontaneous symmetry breaking

In this section, we discuss how phase transitions and spontaneous symmetry breaking (SSB) find their natural description in terms of the effective potential $U(\rho)$. The latter is the part of the effective action which does not contain derivatives of the field. It includes both quantum and thermal fluctuations, and typically changes its shape by tuning the system parameters like temperature, chemical potential, or interaction strength. For parameter regions where the minimum of the effective potential is nonzero, small perturbations can drive the system into an equilibrium ground state which does not respect the symmetry of the underlying physical theory. The symmetry is then broken *spontaneously*. We exemplify this important concept of many-body physics on systems with $\mathbb{Z}_2$- and U(1)-symmetry, respectively.

An intuitive picture of SSB is provided by a simple daily life observation. Suppose a pencil is balanced on its tip to stand upright. Due to the cylindrical symmetry, the pencil should stay in this position. Indeed, the underlying physics, here given by the gravitational force pointing downwards, does not prefer any direction. However, if there is a small perturbation of this symmetry due to the environment, the pencil will immediately fall to the side and thereby minimize its energy. Even if the perturbation is removed now, the pencil will remain in the horizontal position.

Thermodynamics from the effective action

In order to study the properties of the thermodynamic equilibrium state we consider a system of bosons. We assume the trapping potential $V_{\mathrm{ext}}(\vec{x})$ to vanish and the external source to be constant, $j(X) = j$. Hence the setting is homogeneous in space-time. We learned in Eq. (3.21) that the grand canonical partition function $Z(\mu,T)$ is related to the effective action according to

$$\Gamma[\phi_0] = -\log Z(\mu,T). \tag{3.27}$$

Herein, the field expectation value $\phi_0(X)$ minimizes the effective action, as can be seen from Eqs. (3.15) and (3.17). The effective action $\Gamma[\phi]$ has the structure

$$\Gamma[\phi] = \int_X \Big(\text{terms containing derivatives}\Big) + \int_X U(\phi(X))\,. \tag{3.28}$$

If the part containing derivatives is minimal for constant fields, ϕ_0 is a constant field which additionally minimizes the *effective potential* $U(\phi)$ according to

$$U(\phi_0) = \min_{\phi}\Big[U(\phi)\Big]. \tag{3.29}$$

Since the effective potential depends on both the external parameters μ and T, the same will be true for the field expectation value: $\phi_0 = \phi_0(\mu, T)$. In the presence of a nonvanishing background source field, we also have an explicit dependence on j. Note that the above argument does not exclude the existence of inhomogeneous ground states as they result from a nontrivial structure of the derivative-term which favours nonconstant field configurations. The existence of such inhomogeneous ground states is common in low dimensions, in particular in 1+1 dimensions, see e.g. Thies and Urlichs [2003] for the class of models under discussion here.

Using Eq. (3.21) the effective potential at its minimum value is related to the pressure according to

$$P(\mu, T) = -U(\phi_0, \mu, T). \tag{3.30}$$

This constitutes the *equation of state* of the system. Often we are mainly interested in the density $n(\mu, T)$, which is found from $\mathrm{d}P = n\mathrm{d}\mu + s\mathrm{d}T$. The relevant thermodynamic information contained in the effective potential can thus be summarized in the two equations by Eps. (3.29) and (3.30). These equations are generally valid and constitute the main building blocks for the evaluation of the phase diagram of the many-body problem. In particular, the above discussion is not limited to bosons, but can be applied to an arbitrary many-body system or quantum field theory, since the effective action approach is applicable to all of these system. For instance, the field $\varphi(X)$ may as well describe the degrees of freedom in a Heisenberg ferromagnet with magnetic moments, $\vec{m}_i$ or $\vec{m}(\vec{x})$, on a lattice or in the continuum, respectively. However, in the following we keep denoting the fields by φ and ϕ.

Spontaneous symmetry breaking

As a preparation for the more formal discussion of SSB, we first relate symmetries of the microscopic action to those of the effective action. To this end, we recall the definition of the effective action to be

$$e^{-\Gamma[\phi]} = \int \mathrm{D}\varphi\, e^{-S[\varphi] + \int_X j[\phi]\cdot(\varphi - \phi)}. \tag{3.31}$$

Setting the external source j to zero, we see that any symmetry of the microscopic action which is respected by the functional measure, will also be a symmetry of the effective action. A nonvanishing source $j(X)$, instead, typically leads to terms in the effective action which *explicitly* break the microscopic symmetry. This is accompanied by a nonzero expectation value $\phi(X)$, because $j(X)$ either introduces a non-homogeneity in space-time or at least singles out a direction in field space φ.

Spontaneous breaking of a symmetry refers to a different scenario. In this case, the external source vanishes such that the effective action manifestly shares the symmetry of the microscopic action. Nevertheless, the ground state of the theory (or, more generally, the thermodynamic equilibrium state), may spontaneously break this symmetry due to a nonzero expectation value according to

$$\phi_0 = \langle\varphi\rangle_{j\to 0} \neq 0. \tag{3.32}$$

The symmetry is then broken because of the field expectation value transforming nontrivially under the symmetry transformation. Whenever the state of the system does not respect the symmetries of the underlying physics (i.e. effective action), we say that the symmetry is broken spontaneously.

We illustrate this discussion with examples. First, we consider classical Ising magnets on a lattice. The symmetry transformation exerted on the Ising variables m_i is a global reflection, $m_i \to -m_i$ for all i. The Hamiltonian $H[m] = -J\sum_i m_i m_{i+1}$ is reflection symmetric, meaning that

$$H[m] = H[-m]. \tag{3.33}$$

Since the functional measure $\int\prod_i \mathrm{d}m_i\delta(m_i^2-1)$ does not break this symmetry, we have for the effective action

$$\Gamma[\bar{m}] = \Gamma[-\bar{m}] \tag{3.34}$$

with mean field $\bar{m}_i = \langle m_i\rangle$. We call this a $\mathbb{Z}_2$-symmetry.

Analogously, the microscopic action of cold atomic bosons given in Eq. (3.6) has a global U(1)-symmetry, meaning that it is invariant under the following global transformation of the fields

$$\varphi \to \varphi' = e^{\mathrm{i}\alpha}\varphi, \qquad \varphi^* \to (\varphi^*)' = e^{-\mathrm{i}\alpha}\varphi^* \tag{3.35}$$

with real parameter α. In the basis of real fields, $\varphi = \varphi_1 + \mathrm{i}\varphi_2$, this corresponds to a rotation

$$\begin{pmatrix} \varphi_1'(\vec{x}) \\ \varphi_2'(\vec{x}) \end{pmatrix} = \begin{pmatrix} \cos\alpha & -\sin\alpha \\ \sin\alpha & \cos\alpha \end{pmatrix} \begin{pmatrix} \varphi_1(\vec{x}) \\ \varphi_2(\vec{x}) \end{pmatrix} \tag{3.36}$$

in field space. Since the functional measure $\int \mathrm{D}\varphi^*\mathrm{D}\varphi$ shares this symmetry, the effective action $\Gamma[\phi^*,\phi]$ possesses the global U(1)-symmetry as well.

By virtue of Noether's theorem, the global U(1)-symmetry in conjunction with a linearly appearing time derivative in the kinetic term of the microscopic action leads to the conservation of total particle number $N = \int_{\vec{x}} \langle \varphi^*(\vec{x})\varphi(\vec{x})\rangle$. This is a characteristic feature of nonrelativistic field theories. A brief review of Noether's theorem in the classical and quantum case is provided by Boettcher et al. [2012].

The above mentioned properties of the effective action for vanishing external source have a profound consequence for the effective potential U. Indeed, from Eq. (3.28) we deduce that the latter is not a function of the individual fields ϕ and ϕ^*, but we rather have

$$U = U(\rho), \tag{3.37}$$

where ρ is the most general combination of fields allowed by symmetry. For instance, we have

$$\rho = \begin{cases} \bar{m}^2 & (\mathbb{Z}_2 - \text{symmetry}), \\ \phi^*\phi & (\mathrm{U}(1) - \text{symmetry}). \end{cases} \tag{3.38}$$

We plot the effective potential $U(\rho)$ for a second and first order phase transition in Figs. 3.1 and 3.2, respectively. The critical temperature $T_c(\mu)$ is defined such that the location of the minimum $\rho_0(\mu, T)$ approaches zero – either continuously or discontinuously. In particular, for a second order phase transition we distinguish the following three cases:

(i) $\rho_0 \neq 0$, $U'(\rho_0) = 0$: phase with broken symmetry,

(ii) $\rho_0 = 0$, $U'(\rho_0) = 0$: critical point,

(iii) $\rho_0 = 0$, $U'(\rho_0) \neq 0$: symmetric phase.

In the broken phase, the location of the minimum ρ_0 of the effective potential does not necessarily completely determine the state of the system under consideration. In the case of magnets, we have $\bar{m}_0^2 \neq 0$ and thus there is still the freedom to choose the sign of $\bar{m}_0$, which is a $\mathbb{Z}_2$-transformation. For the case of bosons, the condition $|\phi_0|^2 \neq 0$ only fixes the amplitude of the complex field $\phi_0 = |\phi_0|e^{\mathrm{i}\theta}$, whereas the phase θ can still be chosen arbitrarily. In the latter case the possible nonequivalent choices are given by $\theta \in [0, 2\pi) \simeq \mathrm{U}(1)$. We say that the condition on ρ_0 singles out a manifold of possible ground states ϕ_0, which in our examples is given by $\mathbb{Z}_2$ and U(1), respectively. In the absence of explicit symmetry breaking terms, the precise choice of the ground state in the degenerate manifold indeed happens *spontaneously* – it is induced by fluctuations or perturbations due to the environment, which we can neither resolve nor control (Nambu [1960]). Nevertheless, this phenomenon is ubiquitously observed experimentally; for example, spontaneous phase symmetry breaking can be detected in BEC-interference experiments of initially disjunct condensates (Andrews et al. [1997]), or the Josephon effect in superconductor junctions.

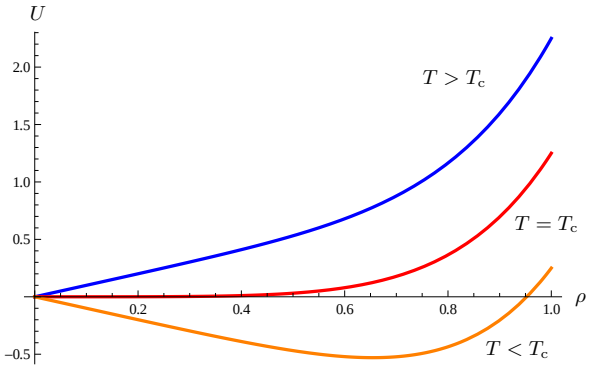

Figure 3.1: The effective potential $U(\rho)$ for vanishing external sources is a function of the symmetry invariant ρ. The latter is given by $\rho = \bar{m}^2$ or $\rho = |\phi|^2$ for magnets or ultracold bosons, respectively. Throughout a second order phase transition the location of the minimum of the effective potential changes from $\rho_0 = 0$ to $\rho_0 > 0$ in a continuous manner. We have chosen here the temperature to be the control parameter. However, since the effective potential depends on μ, T, and the microscopic parameters of the theory (e.g. coupling constants), we may also drive the phase transition differently. Figure taken from Boettcher et al. [2012]

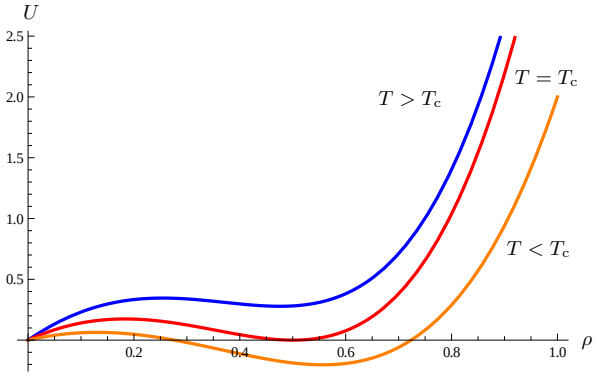

Figure 3.2: At a first order phase transition we find a jump in the order parameter ρ_0 as we cross $T = T_c$. From the plot of the effective potential we see how this discontinuous behavior can arise, although we smoothly vary the system parameters. Note that the effective potential is actual a convex function, as the effective action originates from the Legendre transform of the Schwinger functional. Therefore, the nonconvex parts should rather be replaced by straight lines according to the Maxwell construction, but this does not invalidate the overall picture of first order phase transitions. Figure taken from Boettcher et al. [2012].

In Fig. 3.3, we plot the boson effective action in the tree level approximation $\Gamma[\phi] \simeq S[\phi]$ for a constant field in the complex ϕ-plane. The microscopic action S is given in Eq. (3.6). For constant ϕ we have

$$U(\phi) = \frac{1}{\beta V}\Gamma[\phi] = -\mu|\phi|^2 + \frac{g}{2}|\phi|^4. \tag{3.39}$$

For obvious reasons $U(\phi)$ is called *Mexican hat potential*. Without loss of generality we assume the ground state ϕ_0 to be real, such that real and imaginary components of $\phi = \phi_1 + \mathrm{i}\phi_2$ are distinct directions in the complex plane. The ground state singles out the point $(\phi_0, 0)$. Now consider the field φ to be fluctuating around this point. We write

$$\varphi(\tau, \vec{x}) = \phi_0 + \delta\varphi(\tau, \vec{x}) \tag{3.40}$$

with $\langle\delta\varphi\rangle = 0$. The fluctuations $\delta\varphi$ are complex and can vary in both amplitude and phase of φ. However, the fluctuations which increase the amplitude away from ϕ_0 have to climb up the hill and thus are energetically unfavorable, i.e. they are suppressed in the functional integral by a term

$$\int \mathrm{D}\varphi_1 e^{-m_1^2\delta\varphi_1^2}. \tag{3.41}$$

We call them radial or gapped excitations. In contrast, fluctuations of the phase are not hindered energetically, i.e. "gapless", because they vary along the well of the Mexican hat.

The existence of a massless or gapless mode in a symmetry broken phase observed in the example above is a general phenomenon. In fact, it is an exact property of the full theory, as has been established by Goldstone [1961]. More precisely, Goldstone's theorem states that any spontaneous breaking of a continuous symmetry results in the appearance of gapless modes in the excitation spectrum of the system. The proof of Goldstone's theorem is very simple in the effective action framework. Since we are interested in a statement about the masses of the theory, i.e. properties of the system in the homogeneous limit of vanishing frequencies and momenta, we can restrict ourselves to the effective potential U. As we have seen above, $U(\rho)$ only depends on the symmetry invariant $\rho = |\phi|^2$. Consider the field equation $\frac{\delta\Gamma}{\delta\phi_1} = 0$ for the radial field. Since we assumed a homogeneous setting, this reduces to

$$0 = \frac{\partial U}{\partial\phi_1}(\phi_0) = \phi_0 U'(\rho_0) \overset{\text{SSB}}{\Longrightarrow} U'(\rho_0) = 0. \tag{3.42}$$

Here, a prime denotes differentiation with respect to ρ. The mass of the Goldstone mode $\delta\varphi_2$ is then found to be

$$\begin{aligned} m_2^2 = \frac{\partial^2 U}{\partial\phi_2^2}(\phi_0) &= \left(\frac{\partial^2\rho}{\partial\phi_2^2}U'(\rho) + \left(\frac{\partial^2\rho}{\partial\phi_2}\right)^2 U''(\rho)\right)\Big|_{\phi=\phi_0} \\ &= \Big(U'(\rho) + \phi_2^2 U''(\rho)\Big)\Big|_{\phi=\phi_0} = U'(\rho_0) = 0. \end{aligned} \tag{3.43}$$

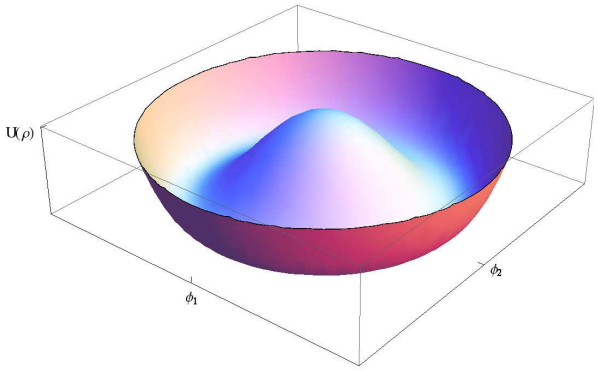

Figure 3.3: The Mexican hat potential from Eq. (3.39) only depends on the amplitude of the complex field $\phi = \phi_1 + \mathrm{i}\phi_2$. Thus it reflects the U(1)-symmetry of the bosonic theory, which is invariant under phase rotations $\phi \to e^{\mathrm{i}\alpha}\phi$. The ground state of the system will, however, spontaneously break this symmetry, e.g. by choosing $\phi_0 \in \mathbb{R}$. Figure taken from Boettcher et al. [2012].

We used the continuity of the symmetry by requiring ρ to depend smoothly on $\phi_{1,2}$. We have carried out the proof for the symmetry $\mathrm{U}(1) \simeq \mathrm{O}(2)$. The above steps can be performed analogously for larger symmetry groups such as $\mathrm{O}(N)$, leading to $N-1$ massless Goldstone modes. In the above case, the vanishing of the mass term allows for strong fluctuations of the phase field in the phase of broken symmetry. In particular, they question the assumption of small fluctuations $\delta\varphi$ in the functional integral, which lead to the one-loop formula given in Eq. (3.25).

3.2 Dyson–Schwinger equations

Dyson–Schwinger equations (DSE) are an exact rewriting of the generating functional $\log Z[J]$ in terms of an infinite hierarchy of equations for the n-point functions of the theory. They provide a solid starting point for physical approximations in terms of truncations of the set of equations. A diagrammatic representation of the DSE can be derived, with the characteristic feature that each diagram in a DSE contains exactly one microscopic vertex which is obtained from the classical action S. Here we give a self-contained derivation of the DSE for a real scalar field denoted by φ. In Sec. 5.1.2 we investigate the DSE for the fermion propagator in the BCS-BEC crossover.

Given the microscopic action $S[\varphi]$, the generating functional is given by

$$Z[J] = \int \mathrm{D}\varphi e^{-S[\varphi]+J\cdot\varphi}, \tag{3.44}$$

where $J \cdot \varphi = \int_X J_X \varphi_X = \int_Q J_{-Q} \varphi_Q$. The generating functional is a rather unintuitive object as it is parametrized in terms of the external source J. As a consequence, physically motivated approximations are difficult. We therefore introduce the effective action by a Legendre transform according to

$$\Gamma[\phi] = \sup_J \Big\{ J \cdot \phi - \log Z[J] \Big\}. \tag{3.45}$$

Assuming $\log Z[J]$ to depend smoothly on J, the optimal J_ϕ is found from

$$0 \stackrel{!}{=} \frac{\delta}{\delta J_X} \Big\{ J \cdot \phi - \log Z[J] \Big\}_{J_\phi} = \phi_X - \frac{\delta \log Z}{\delta J_X}[J_\phi] = \phi_X - \langle \varphi_X \rangle_{J_\phi}. \tag{3.46}$$

Here $\langle \dots \rangle_J$ denotes the average in the presence of the source J. Hence this equation states that the external field $J_\phi(X)$ is adjusted such that $\langle \varphi_X \rangle_{J_\phi} = \phi_X$ for a given ϕ_X. Taking a functional derivative of $\Gamma[\phi]$ with respect to ϕ_X we obtain

$$\begin{aligned} \frac{\delta \Gamma}{\delta \phi_X}[\phi] &= \frac{\delta}{\delta \phi_X} \Big\{ J_\phi[\phi] \cdot \phi - \log Z[J_\phi[\phi]] \Big\} \\ &= \frac{\delta J_\phi}{\delta \phi_X}[\phi] \cdot \phi + J_\phi[\phi]_X - \underbrace{\frac{\delta \log Z}{\delta J}[J_\phi]}_{\phi} \cdot \frac{\delta J_\phi}{\delta \phi_X}[\phi] = J_\phi[\phi]_X. \end{aligned} \tag{3.47}$$

This allows to eliminate J in Eq. (3.46) to arrive at

$$\phi_X = \langle \varphi_X \rangle_{J = \frac{\delta \Gamma}{\delta \phi}[\phi]}. \tag{3.48}$$

We write $\varphi = \phi + \delta\varphi$ with $\langle \delta\varphi \rangle_{J_\phi} = 0$.

We then have

$$Z[J_\phi[\phi]] = \int \mathrm{D}\varphi e^{-S[\varphi] + J_\phi[\phi] \cdot \varphi}, \tag{3.49}$$

$$e^{-\Gamma[\phi]} = Z[J_\phi[\phi]] e^{-J_\phi[\phi] \cdot \phi}. \tag{3.50}$$

Putting both expressions together we again arrive at the one-loop formula for the effective action,

$$e^{-\Gamma[\phi]} = \int \mathrm{D}\varphi e^{-S[\varphi] + J_\phi[\phi] \cdot (\varphi - \phi)} = \int \mathrm{D}\delta\varphi e^{-S[\phi + \delta\varphi] + \frac{\delta \Gamma}{\delta \phi}[\phi] \cdot \delta\varphi}. \tag{3.51}$$

To arrive at the DSE we take the functional derivative of this equation. We

then obtain

$$\begin{aligned}\frac{\delta\Gamma}{\delta\phi_X}[\phi] &= -\frac{e^{\frac{\delta\Gamma}{\delta\phi}[\phi]\cdot\phi}}{Z[J_\phi]}\frac{\delta}{\delta\phi_X}\int \mathrm{D}\delta\varphi e^{-S[\phi+\delta\varphi]+\frac{\delta\Gamma}{\delta\phi}[\phi]\cdot\delta\varphi} \\ &= \frac{e^{\frac{\delta\Gamma}{\delta\phi}[\phi]\cdot\phi}}{Z[J_\phi]}\int \mathrm{D}\delta\varphi\left(\frac{\delta S}{\delta\varphi_X}[\phi+\delta\varphi]-\frac{\delta^2\Gamma}{\delta\phi_X\delta\phi}[\phi]\cdot\delta\varphi\right)e^{-S[\phi+\delta\varphi]+\frac{\delta\Gamma}{\delta\phi}[\phi]\cdot(\varphi-\phi)} \\ &= \frac{1}{Z[J_\phi]}\int \mathrm{D}\varphi\Bigg(\frac{\delta S}{\delta\varphi_X}[\varphi]-\underbrace{\frac{\delta^2\Gamma}{\delta\phi_X\delta\phi}[\phi]\cdot\delta\varphi}_{\sim\langle\delta\varphi\rangle_{J_\phi}=0}\Bigg)e^{-S[\varphi]+\frac{\delta\Gamma}{\delta\phi}[\phi]\cdot\varphi}. \end{aligned} \tag{3.52}$$

The DSE or quantum equations of motion thus read

$$\frac{\delta\Gamma}{\delta\phi_X}[\phi] = \left\langle\frac{\delta S}{\delta\varphi_X}\right\rangle_{J_\phi=\frac{\delta\Gamma}{\delta\phi}[\phi]}. \tag{3.53}$$

3.3 Functional Renormalization Group

In this section we provide an introduction to the basic concepts of the FRG. It is based on the continuum version of Kadanoff's block-spinning transformations on the lattice (Kadanoff [1966]), and has been formulated for the continuum by Wilson [1971a,b]. Its modern functional form for the effective action used in the present work has been put forward by Wetterich [1993].

For the description of ultracold atom experiments, the action S derived from the Hamiltonian in Eq. (3.1) is a microscopic starting point. It is related to an ultraviolet momentum scale Λ. The relevant physics, however, takes place at momentum scales k far smaller than Λ, and the respective quantum and thermal fluctuations have to be included. In the FRG framework, these fluctuations are included successively at a given momentum scale k starting at Λ, with $\Gamma_\Lambda = S$, leading to the effective average action Γ_k. The latter already includes all quantum and thermal fluctuations above the momentum scale k. It can be interpreted as a microscopic action for the physics below the scale k in the very same way S has been introduced as the microscopic action of ultracold gases. After the inclusion of all fluctuations we arrive at the full effective action Γ:

$$\Gamma_{k=\Lambda} = S, \tag{3.54}$$

$$\Gamma_{k=0} = \Gamma. \tag{3.55}$$

The effective action Γ_k interpolates smoothly between the microscopic (or initial effective) action Γ_Λ and the full effective action $\Gamma = \Gamma_{k=0}$.

An infinitesimal change of the effective action with the scale k is described by a *flow equation* $\partial_k\Gamma_k$, which depends on the correlation functions of the theory at the scale k as well as the specific way the infrared modes with momenta smaller than k are suppressed. Such an RG-step has similarities to a coarse graining where

details on short distances are continuously washed out, the difference being that the effective action Γ_k still keeps the information about the fluctuations between Λ and k. At the end of the process, for $k \to 0$, we include fluctuations with large wavelength. These are the problematic modes which cause infrared divergences in other approaches. Due to the stepwise inclusion of fluctuations, the renormalization group procedure is not plagued by such divergences. In conclusion, a given initial effective action Γ_Λ and the flow equation (3.66) define the full quantum theory analogously to the setting with classical action and the path integral.

We derive the flow equation for Γ_k and discuss its practical solution. To that end we specify a suppression of low frequency and momentum fluctuations with $|q_0|, q^2 \leq k^2$. (In the following we write $q^2 = \vec{q}^2$.) This can be achieved via a mass-like infrared modification of the dispersion relation, while the ultraviolet modes remain unchanged: We add a *regulator* or *cutoff* term $\Delta S_k[\varphi]$ to the microscopic action $S[\varphi]$ which is quadratic in the fields,

$$S[\varphi] \to S[\varphi] + \Delta S_k[\varphi]. \tag{3.56}$$

The field φ is general and may be a collection of fields. For concreteness, we will use a notation analogous to ultracold bosons and write $\phi(X) = \langle \varphi(X) \rangle$. We have

$$\Delta S_k[\varphi] = \int_Q \varphi^*(Q)\, R_k(Q)\, \varphi(Q). \tag{3.57}$$

The requirement of the suppression of low momentum modes entails that $R_k(Q \to 0) \neq 0$. In turn, for large momenta (in comparison to k), the regulator has to vanish, $R_k(Q \to \infty) \to 0$. These properties can be summarized in the conditions

$$\lim_{q^2/k^2 \to 0} R_k(Q) = k^2\,, \qquad \lim_{q^2/k^2 \to \infty} R_k(Q) = 0\,. \tag{3.58}$$

For the sake of simplicity, we have restricted ourselves in Eq. (3.58) to regulators that only depend on q^2, and that have a standard normalization $R_k(0) = k^2$ in the infrared. The extension to general regulators is straightforward. In particular, in this thesis we will also apply regulators which depend on both q_0 and q^2.

If we interpret the action in Eq. (3.56) as the microscopic action of a physical theory, it has a trivial infrared sector: The fields are gapped with gap k^2. The generating functional of this theory is given by

$$Z_k[j] = \int \mathrm{D}\varphi\, e^{-S - \Delta S_k + \int j \cdot \varphi}\,. \tag{3.59}$$

From Eq. (3.58) we infer that $Z_{k=0}[j]$ is the full generating functional of the theory introduced in Eq. (3.3). For $k \to \Lambda$, the regulator term dominates the path integral as all physical scales are far smaller and we are left with a trivial Gaussian integral. Moreover, for a given k, the correlation functions $\langle \varphi(Q_1) \cdots \varphi(Q_n) \rangle$ tend towards the full correlation functions for $|q_{0,i}|, q_i^2 \gg k^2$ for all $i = 1, ..., n$. In turn, for $|q_{0,i}|, q_i^2 \ll k^2$, the correlation functions are trivial, as the fields are gapped.

For explicit computations, it is more convenient to deal with the effective average action Γ_k, which is obtained via a modified Legendre transform according to

$$\Gamma_k[\phi] = \int j \cdot \phi - \log Z_k[j] - \Delta S_k[\phi]\,, \tag{3.60}$$

where $j = j_k[\phi]$ satisfies $(\delta \log Z_k/\delta j)[j] = \phi$. We have already shown that the effective action has the simple physical interpretation of the grand canonical potential in a given background ϕ. Diagrammatically, it generates all one-particle irreducible diagrams. As in the case without regulator term, Γ_k satisfies a functional integro-differential equation similar to Eqs. (3.20), (3.22). Applying the definitions of Z_k and Γ_k we find

$$e^{-\Gamma_k[\phi]} = \int \mathrm{D}\varphi\, \exp\Big(-S[\phi+\varphi] - \Delta S_k[\varphi] + \int_X \frac{\delta\Gamma_k}{\delta\phi}[\phi]\cdot\varphi\Big), \tag{3.61}$$

where

$$j[\phi] = \frac{\delta(\Gamma_k + \Delta S_k)}{\delta\phi}, \tag{3.62}$$

following from the definition of the Legendre transform (3.60). Eq. (3.61) makes the suppression of the fluctuations even more apparent. Note first that the action S in the exponent depends on the sum $\phi+\varphi$, whereas the cutoff term only depends on the fluctuation φ. Hence, for large cutoff scales $k \to \Lambda$, the functional integral in Eq. (3.61) gets Gaussian and the effective action tends towards the microscopic action, $\Gamma_{k\to\Lambda} \to S$. For $k \to 0$, the regulator vanishes, $R_k \to 0$, and we are left with Eq. (3.22).

For a successive integration of momentum modes we need to know the "flow" $\partial_k\Gamma_k$. Applying the k-derivative to Eq. (3.60) leads to

$$\partial_k\Gamma_k[\phi] = -\partial_k\big|_j \log Z_k[j] - \partial_k\Delta S_k[\phi]. \tag{3.63}$$

The notation signals that j is k-dependent but the terms proportional to $\partial_k j$ cancel. We have $\partial_k\Delta S_k[\phi] = \int_Q \partial_k R_k(Q)\phi(Q)\phi^*(Q)$. The generating functional Z_k only depends on k via the cutoff term ΔS_k. Taking the k-derivative of Eq. (3.59), we can compute $\partial_k|_j \log Z_k$ to arrive at

$$\partial_k\Gamma_k[\phi] = \int_Q \partial_k R_k(Q)\left[\Big\langle \varphi(Q)\varphi^*(Q)\Big\rangle_k - \phi(Q)\phi^*(Q)\right]. \tag{3.64}$$

Herein, we have restricted ourselves to bosonic fields φ. In the case of fermions, a global minus sign occurs due to the Grassmann nature of the fermions. The expression in the square bracket in Eq. (3.64) is the full, field-dependent propagator, which reads in terms of the effective action

$$\Big\langle \varphi(Q')\varphi^*(Q)\Big\rangle_k - \phi(Q')\phi^*(Q) = \frac{1}{\Gamma_k^{(2)} + R_k}(Q',Q)\,. \tag{3.65}$$

In Eq. (3.65), we have used the property of Legendre transforms that the second derivatives of a functional and its Legendre transform are inversely related. In the present case, we note that the Legendre transform of $\log Z_k$ is $\Gamma_k + \Delta S_k$, as defined in Eq. (3.60). Hence, we are led schematically to $\delta^2 \log Z_k / \delta j^2 \cdot (\Gamma^{(2)} + R_k) = 1$, which we have used in Eq. (3.65).

The momentum integral in Eq. (3.64) can be conveniently written in terms of a trace. Including also the possibility of internal indices and different species of fields, we are led to the final expression for the flow equation for Γ_k,

$$\partial_t \Gamma_k = \frac{1}{2} \mathrm{STr} \left[\frac{1}{\Gamma_k^{(2)} + R_k} \, \partial_t R_k \right] , \tag{3.66}$$

the Wetterich equation. The supertrace includes the momentum integration and the summation over internal indices and field species. In Eq. (3.66) we have introduced the RG-time $t = \log k/k_0$ with some reference scale k_0, typically being either the ultraviolet scale, $k_0 = \Lambda$, or some physical scale. For a given quantity $\mathcal{O}_k$, the logarithmic scale derivative $\partial_t \mathcal{O}_k = k \partial_k \mathcal{O}_k$ has the same properties under RG-scaling as the quantity itself. It is also a convenient parametrization of the running of couplings as one usually integrates the flow over several orders of magnitude in the momentum scale k. Henceforth we shall use the standard choice $t = \log k/\Lambda$.

Above we have argued that regulators with the properties (3.58) lead to a suppression of the infrared physics of the theory. Moreover, since the finite initial effective action Γ_Λ at the initial scale Λ already includes all fluctuations of momentum modes with momenta larger than Λ, no ultraviolet divergences should be present. These properties have to be reflected in the flow equation (3.66): It has to be both infrared *and* ultraviolet finite. Here, we show this explicitly for the case of bosonic fields. For low momenta, the regulator adds a positive mass to $\Gamma_k^{(2)}$ in the denominator. The typical size of this mass is k^2, in Eq. (3.58) we have normalized it to k^2. For the sake of simplicity, consider a classical dispersion $\Gamma_k^{(2)} \simeq \mathrm{i}q_0 + q^2$ (with $2M = 1$) for small momenta which tends to zero for vanishing momentum. Schematically, we then have for small momenta

$$\frac{1}{\Gamma_k^{(2)}(Q) + R_k(Q)} \xrightarrow{Q \to 0} \frac{1}{\mathrm{i}q_0 + q^2 + k^2} , \tag{3.67}$$

which is finite for $Q \to 0$. For fermions, the infrared singularities arise close to the Fermi surface. Accordingly, the propagators have to be regularized there. In summary, this implies infrared safe flows.

In turn, for large momenta, the scale-derivative $\partial_t R_k(Q)$ vanishes due to Eq. (3.58). If this happens sufficiently fast,

$$\lim_{q^2/k^2 \to \infty} q^2 \partial_t R_k(Q) \to 0 , \tag{3.68}$$

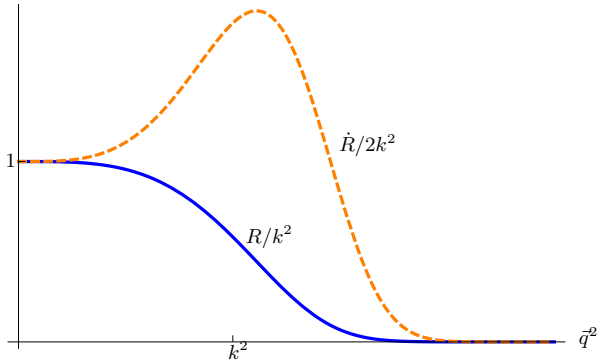

Figure 3.4: We plot a typical cutoff function $R_k(Q) = R_k(q^2)$, which only depends on the spatial momentum. The function is nonzero for $q^2 \lesssim k^2$ and thus provides an infrared cutoff for the propagators. For large momenta, it falls off rapidly, thus becoming inactive in the UV. The scale derivative $\dot{R}_k(Q) = k\partial_k R_k(Q)$ is sharply peaked at $q^2 \approx k^2$. For this reason, the loop integral on the right hand side of the flow equation is dominated by these modes. This provides the mechanism how momentum shells are successively integrated out in the FRG framework. Figure taken from Boettcher et al. [2012].

the momentum integral in Eq. (3.66) is finite. In the following, we shall show results for regulators that satisfy Eq. (3.68). We also remark that mass-like regulators, i.e. $R_k = k^2$, do not satisfy Eq. (3.68) and hence require UV renormalization. The related flows are functional Callan–Symanzik equations as first derived by Symanzik [1970]. They are sometimes used due to computational simplicity, see e.g. Diehl et al. [2007b]. The generic shape of a cutoff is shown in Fig. 3.4.

It is apparent from the derivation that $\Gamma_k[\phi]$ depends on the shape of the regulator. This regulator-dependence disappears for $k \to 0$, hence physical observables are independent of the choice of R_k, but the trajectory Γ_k from $k = \Lambda$ to $k = 0$ depends on R_k, see. Fig. 3.5. This leaves us with some freedom for the choice of the regulator. Indeed, its choice can be optimized to the approximation under investigation (Litim [2000, 2001b,a], Pawlowski [2007]). In general, such a choice is further guided by computational simplicity, as in complicated systems the computational costs can be high. Typical choices are functions $R_k(Q)$ which decay exponentially or even vanish identically for high Q. A slight complication for nonrelativistic system is provided by the fact that frequencies and spatial momenta appear differently. The Galilei symmetric combination is given by $\mathrm{i}q_0 + q^2$, in contrast to the O(4)-symmetric combination $q_\mu q_\mu = q_0^2 + q^2$ for relativistic systems. At nonvanishing temperature, Galilei symmetry is broken. In the Matsubara formulation used in the present work, the coupling to the heat bath leads to periodicity in the imaginary time τ with period β. Therefore, we may also

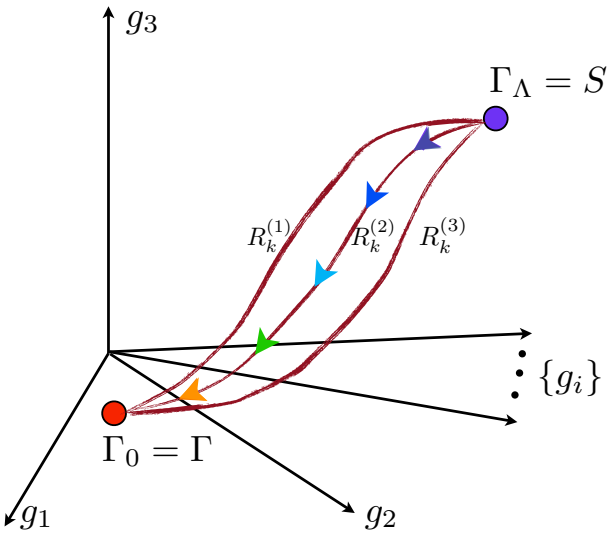

Figure 3.5: The flow of Γ_k connects the microscopic action to the effective action in the *theory space* of all possible action functionals. The latter is of infinite dimension since the effective action is characterized by an infinite set of couplings (or correlation functions). This is indicated here schematically by the couplings g_1, g_2, g_3 and $\{g_i\}$. For different choices of regulators, $R_k^{(i)}$, the trajectories in theory space differ, as is indicated in the figure. At $k = 0$, however, the particular paths merge again and eventually terminate at the full effective action. Figure taken from Boettcher et al. [2012].

choose a regulator which only depends on frequency or momentum space. Moreover, we may sacrifice Galilei symmetry in order to obtain simpler expressions for the flow equation.

Here briefly introduce a few common regulator choices for bosons with dispersion $\Gamma_k^{(2)}(Q) \sim \mathrm{i}q_0 + q^2$, and discuss their advantages and limitations.

For instance, exponential cutoffs are

$$R_k(Q) = \frac{k^2}{e^{(q^2/k^2)^n} + 1}, \quad \frac{k^2}{e^{(|q_0|/k^2)^n} + 1}. \tag{3.69}$$

The power of n can be chosen such that the cutoff falls off sufficiently fast for high Q. For $n = 1$ the cutoff insertion $\partial_t R_k(q^2)$ is not peaked at $q^2 \approx k^2$ but is a monotonously decaying function. Only for $n > 1$ we get peaked cutoff insertions. On the other hand, a rapid decay of R_k as a function of q_0 can pose problems for computing thermodynamic quantities. The best stability and quantitative precision in the context of Yang–Mills thermodynamics was found for $n = 2$ by Fister and Pawlowski [2011]. In this work we often employ the Q-exp cutoff

defined by

$$R_k(Q) = (\mathrm{i}q_0 + q^2)r\Big(\frac{q_0^2 + q^4}{k^4}\Big),\ r(Y) = \frac{1}{e^Y - 1}. \tag{3.70}$$

They provide regularization of both frequencies and momenta, and thus lead to particularly local Q-integrals contributing to beta functions. This is important for the success of a derivative expansion.

A particularly useful cutoff is the q^2-opt or Litim cutoff (Litim [2001b], Litim and Pawlowski [2006])

$$R_k(Q) = (k^2 - q^2)\theta(k^2 - q^2), \tag{3.71}$$

which effectively reduces the momentum integration to $q^2 \leq k^2$ and replaces q^2 by k^2. It facilitates the analytic derivation of flow equations for correlation functions in the derivative expansion, and hence leads to important computational simplifications. Its analytic property also allows an easy access to the structure and interrelation of the flows (and hence the correlation functions). These properties make it the standard choice within (lower orders of) the derivative expansion. Moreover, in three-dimensional theories, the cutoff in Eq. (3.71) provides an optimal choice (Litim [2000], Pawlowski [2007]) within the lowest order of the derivative expansion scheme.

A manifestly Galilei symmetric regulator is provided by

$$R_k(Q) = \frac{k^2}{1 + c\big(\frac{\mathrm{i}q_0 + q^2}{k^2}\big)^n}, \tag{3.72}$$

where n determines the algebraic decay for large momenta and c is a prefactor of order unity (Floerchinger [2014]). Eq. (3.72) can be extended to more general rational functions in the Galilei invariant $\mathrm{i}q_0 + q^2$. Its key advantages are its Galilei invariance as well as its analytic structure. The latter allows to continue the results to real time, and hence may give access to transport properties or more generally dynamics of ultracold gases. Similar choices in relativistic theories can be used for computing decay properties (Floerchinger [2012]).

Note that the flow equation (3.66) has a one-loop structure, which can be traced back to the quadratic form of the regulator in Eq. (3.57). Indeed, we may rewrite Eq. (3.66) as

$$\partial_t \Gamma_k[\phi] = \frac{1}{2}\mathrm{STr}\ \tilde{\partial}_t \log\Big(\Gamma_k^{(2)}[\phi] + R_k\Big), \tag{3.73}$$

where the derivative $\tilde{\partial}_t$ only acts on the k-dependence of the regulator, i.e. we have

$$\tilde{\partial}_t = \partial_t\Big|_{\Gamma_k^{(2)}}. \tag{3.74}$$

In Eq. (3.73), we identify the one-loop formula for the effective action (3.26) on the right hand side. Therein, we have to substitute $S^{(2)}$ with the full two-point function $\Gamma_k^{(2)} + R_k$.

Eq. (3.73) is a very convenient form of Eq. (3.66) for deriving the flows for correlation functions, e.g. $\partial_t \Gamma_k^{(n)}$. It also allows for an easy access to the fluctuation-dependence of specific correlation functions without performing any calculation. To see this we note that the flow equation for any correlation function (e.g. a coupling constant) can be obtained by deriving all one-loop diagrams which contribute to the expression, replace the propagators and vertices by the full regularized ones according to

$$\frac{1}{S^{(2)}} \to \frac{1}{\Gamma_k^{(2)} + R_k}\,, \qquad S^{(n>2)} \to \Gamma_k^{(n)}\,, \tag{3.75}$$

and then take the $\tilde{\partial}_t$-derivative. Remarkably, this renders the one-loop expression an exact (flow) equation. Note that this only holds true for additive IR regularizations of the one-loop formula for the effective action (3.26), see Litim and Pawlowski [2002]. Note also that one has to take into account perturbative one-loop diagrams where the involved vertices vanish classically, i.e. $S^{(n)} = 0$. Still this one-loop structure is very useful: If the loop expansion of a given correlation function does not exhibit a one-loop diagram, this correlation function is not sensitive to quantum fluctuations. This either happens due to internal symmetries or the pole structure of the diagrams. The latter is characteristic for nonrelativistic theories, and in the case of ultracold atoms it leads to strong simplifications for vacuum scattering properties in certain truncation schemes (Diehl et al. [2010a], Floerchinger [2014]).

The Wetterich equation (3.66) is an equation for a functional and thus may be evaluated for any (possibly inhomogeneous) mean field $\phi(X)$. It is a functional integro-differential equation and its full solution is, in most theories, beyond reach. Instead, one has to use approximation schemes to the full effective action Γ_k, which include the physics at hand already at a low order of the approximation. The systematics of a given approximation scheme and the control of the related systematic error is of chief importance when it comes to the discussion of the reliability of results. This point is tightly linked to the discussion of optimal choices of regulators mentioned above.

Here, we briefly discuss the most important approximation schemes which cover (in variations) all approximation schemes used in the literature. The most important scheme, which is partially behind all approximations used, is the *vertex expansion* about a specific background $\bar{\phi}$, schematically written as

$$\Gamma_k[\phi] = \sum_n \frac{1}{n!} \int \Gamma_k^{(n)}[\bar{\phi}](X_1, ..., X_N) \prod_{i=1}^{n} \Big[\phi(X_i) - \bar{\phi}(X_i)\Big]. \tag{3.76}$$

The information about the effective action is encoded in the vertices $\Gamma_k^{(n)}$. The

related flow can be derived from that of the effective action according to

$$\partial_t \Gamma_k^{(n)}[\bar{\phi}](X_1, \ldots, X_n) = \frac{\delta^n}{\delta\phi(X_1)\ldots\delta\phi(X_n)} \partial_t \Gamma_k[\bar{\phi}]. \tag{3.77}$$

On the right hand side, we have to take the nth derivative of the one-loop diagram in Eq. (3.66),

$$\frac{\delta^n}{\delta\phi(X_1)\ldots\delta\phi(X_n)} \frac{1}{2} \mathrm{STr}\left[\frac{1}{\Gamma_k^{(2)} + R_k}\, \partial_t R_k\right], \tag{3.78}$$

which produces all possible one-loop diagrams with cutoff insertions. Evidently, the diagrams for the flow of $\Gamma_k^{(n)}$ depend on $\Gamma_k^{(m)}$ with $m \leq n+2$. Hence, within the vertex expansion described above, we arrive at an infinite hierarchy of equations, because the flow equation for $\Gamma^{(n)}$ requires input from $\Gamma^{(n+1)}$ and $\Gamma^{(n+2)}$. The flow of the latter two quantities depends again on higher correlation functions and eventually the system never closes. We should not be surprised about this, as the effective action necessarily contains infinitely many independent terms, and we have just rewritten the functional integro-differential equation in terms of infinitely many partial integro-differential equations. In most interesting cases, it will not be possible to derive a closed expression for the functional $\Gamma[\phi]$. Practically, one *truncates* the hierarchy of flow equations at a given order n, i.e. approximates $\Gamma_k^{(m>n)} \approx 0$, and solves the restricted, finite set of partial integro-differential equations for $\Gamma_k^{(m\leq n)}(Q_1, ..., Q_m)$. Examples for this scheme can be found from e.g. Metzner et al. [2012], Benitez et al. [2012], Husemann et al. [2012], Fister and Pawlowski [2011], Dupuis [2009b,a], Sinner et al. [2009, 2010], Schmidt and Enss [2011]. The self-consistency of this approximation can be checked by computing the flow $\partial_t \Gamma_k^{(m>n)}$ as a function of $\Gamma_k^{(m\leq n)}$. This provides some error control.

A further important approximation scheme is the *derivative expansion*. Formulated in momentum space, it is an expansion of the vertices in powers of frequencies and momenta. Its nth order relates to the nth-order in $\mathrm{i}q_0 + q^2$. In contrast to the vertex expansion, all orders of vertices are present already at the lowest order of the derivative expansion. Here, we exemplify this expansion for the case of the effective action Γ_k of a Bose gas. An often used ansatz for this theory is provided by

$$\Gamma_k[\phi^*, \phi] = \int_X \Big(\phi^*(Z_k \partial_\tau - A_k \nabla^2)\phi + U_k(\phi^*\phi)\Big). \tag{3.79}$$

Herein, $U(\phi^*\phi)$ is the full effective potential. It is a general function of $\rho = \phi^*\phi$. Accordingly, we have $U^{(n)} \neq 0$ and thus vertices $\Gamma_k^{(n)}$ to all orders in n. For $Z_k = A_k \equiv 1$, the ansatz in Eq. (3.79) has the same momentum dependence as the classical action and is the lowest order in the derivative expansion. The derivative expansion, and, in particular, the above ansatz in Eq. (3.79) assumes lower orders of the differential operators to be more relevant than the higher ones.

In the presence of a mass gap m_{gap}, this is expected to be valid in the infrared, because

$$(\partial_\tau / m_{\text{gap}}^2)^n \sim (\nabla^2 / m_{\text{gap}}^2)^n \sim |q^2 / m_{\text{gap}}^2|^n \to 0. \tag{3.80}$$

Hence, within the derivative expansion, we make an expansion of the effective action about the low energy effective action. Besides the ansatz in Eq. (3.79), we also have to specify a projection description which determines the flow equations $\dot{Z}_k$, $\dot{A}_k$ and $\dot{U}_k(\rho)$ from Eq. (3.66). Examples for the full lowest order derivative expansion in bosonic as well as mixed fermionic-bosonic theories can be found from e.g. Berges et al. [2002], Schaefer and Wambach [2005, 2008].

Most applications to ultracold atoms discussed in the present work are done within low orders of the derivative expansion with or without an additional field expansion of the effective potential $U_k(\rho)$ up to the nth order of the fields. Of course, such an expansion can also be interpreted as the nth order of the vertex expansion with an additional expansion in powers of momenta and frequencies. Indeed, as has been mentioned before, any approximation scheme used in the literature can be seen as combination, deformation or further approximation of the vertex expansion and the derivative expansion. In any case, when using such an approximation, we restrict the space of functionals. For this reason, although we started from an exact flow equation, we may accumulate errors. In particular, given the exact flow equation, every regulator satisfying the mentioned properties should give the same result. But since we never integrate the full flow, we may end up at two different "effective actions" $\Gamma_{k=0}$ if we used two different regulators. This regulator dependence can be applied to partially test the stability of results, see e.g. the discussion in Schnoerr et al. [2013]. The approximate independence of the results at vanishing cutoff, $k = 0$, guarantees the self-consistency of the approximation. In turn, the independence of $\Gamma_{k=0}$ of the chosen regulator R_k or the chosen trajectory in theory space can be utilized for devising regulators that are best-suited (optimal) for the given order of a given approximation scheme at hand, see Liao et al. [2000], Latorre and Morris [2000], Litim [2000, 2001b,a], Canet et al. [2003], Pawlowski [2007], Salmhofer [2007].

In summary, the Functional Renormalization Group approach for the effective average action constitutes a fully *nonperturbative* approach to quantum field theory. It is neither restricted to small couplings nor to small amplitudes. For this reason, it can be applied to many strongly correlated systems such as quantum dots, the Hubbard model, graphene, QCD, quantum gravity, or – in our case – the Unitary Fermi Gas.

4 BCS-BEC Crossover from Functional Renormalization

4.1 Ansatz for the effective average action

Every truncation of the renormalization group flow can be characterized in terms of a set of running coupling $\{g_k\}$, accompanied by a corresponding set of beta functions $\{\beta_g\}$ and initial values $\{g_\Lambda\}$. The latter ensure $\Gamma_\Lambda = S$ in the beginning of the flow. Here, Λ is a large momentum cutoff scale. It has to be chosen much larger than the physical scales set by chemical potential, temperature, and scattering length. On the other hand, Λ has to be much smaller than the momentum scale where details of the atomic interactions are resolved, typically given by the inverse van-der-Waals length.

We present a systematic truncation scheme for the effective average action, starting with only a few running couplings which are necessary to describe the superfluid transition, then including more couplings which give subleading quantitative corrections. As the proposed set of improvements is based on a physical picture of the mechanisms in the crossover, the convergence of results verifies the corresponding intuition. Deviations, on the other hand, hint on missing ingredients, and can be employed for error estimates. The truncations described here are expected to work best for a sufficiently local RG flow, i.e. one-loop integrals which are peaked at scale k in *both* frequencies and momenta.

4.1.1 Truncation

Our ansatz for the effective average action Γ_k consists of a kinetic part, which comprises the fermion and boson dynamics, and an interaction part:

$$\Gamma_k = \Gamma_{\text{kin}} + \Gamma_{\text{int}}. \tag{4.1}$$

In terms of the renormalized fields $\psi = A_\psi^{1/2}\bar{\psi}$ and $\phi = A_\phi^{1/2}\bar{\phi}$, the kinetic part is given by

$$\Gamma_{\text{kin}}[\psi,\phi] = \int_X \left(\sum_{\sigma=1,2} \psi_\sigma^* \Big(S_\psi \partial_\tau - \nabla^2 + m_\psi^2 \Big) \psi_\sigma + \phi^* \Big(S_\phi \partial_\tau - V_\phi \partial_\tau^2 - \frac{1}{2}\nabla^2 \Big) \phi \right). \tag{4.2}$$

Here and in the following, the k-dependence of the couplings is understood implicitly. The coefficients of the gradient terms are normalized to constants by means

of the wave function renormalizations A_ψ and A_ϕ. The latter two quantities do not explicitly enter the RG flow, but rather appear via the anomalous dimensions

$$\eta_\psi = -k\partial_k \log A_\psi, \;\; \eta_\phi = -k\partial_k \log A_\phi. \tag{4.3}$$

In the following, unrenormalized quantities are denoted with an overbar, renormalized ones without an overbar.

Interactions are parametrized according to

$$\Gamma_{\mathrm{int}}[\psi,\phi] = \int_X \left(U(\phi^*\phi) - h\Big(\phi^*\psi_1\psi_2 - \phi\psi_1^*\psi_2^*\Big)\right). \tag{4.4}$$

The effective average potential $U(\rho)$ only depends on the U(1)-invariant $\rho = \phi^*\phi$. It describes higher order bosonic scattering processes. A nonzero minimum ρ_0 of $U_{k=0}(\rho)$ indicates the spontaneous breaking of U(1)-invariance, and, thus, superfluidity. In a Taylor expansion scheme we write

$$U(\rho) = m_\phi^2(\rho-\rho_0) + \frac{\lambda_\phi}{2}(\rho-\rho_0)^2 + \sum_{n=3}^{N} \frac{u_n}{n!}(\rho-\rho_0)^n, \tag{4.5}$$

where $\rho_{0,k} = 0$ in the symmetric regime of the flow ($m^2_{\phi,k} > 0$), and $m^2_{\phi,k} = 0$ for $\rho_{0,k} > 0$. A truncation of the effective potential to order N will be referred to as a ϕ^{2N}-truncation throughout this thesis. We always work at least with a ϕ^4-truncation.

It is important to note that, besides an ansatz for Γ_k, the truncation of the flow equation also consists in projection prescriptions for the running couplings. The corresponding equations are given in Sec. 4.2.

We can classify our truncations by means of the diagrams which are included on the right hand side of the flow equation. Those containing only fermionic (F) lines (or propagators) reproduce the mean field result. Including those with two bosonic (B) lines is important to resolve the impact of boson fluctuations on the critical temperature. The renormalization effects on the fermion propagator are given by mixed (M) diagrams with both boson and fermion lines. We visualize this hierarchy of diagrams in Fig. 4.1. By elaborating the truncation according to the inclusion F $\to$ FB $\to$ FBM, we successively incorporate higher order terms while keeping the physical content of the lower truncations in this hierarchy. Within a class of diagrams, we still have the freedom to keep several couplings at their classical level.

In this work we restrict to the following five truncation schemes:

- F: Fermion diagrams,
  Running couplings: $U(\rho), A_\phi$
- FB_0: Fermion and boson diagrams,
  Running couplings: $U(\rho), A_\phi, S_\phi$

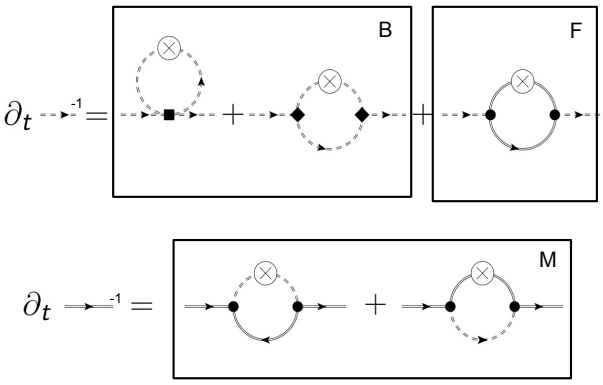

Figure 4.1: The truncations employed in this work can be classified according to the diagrams which appear on the right hand side of the flow equation. Here, as an example, we show the flow equations for the boson propagator (dashed line) and the fermion propagator (solid line), respectively. All lines and vertices are fully dressed. The cross indicates a regulator insertion $\dot{R}_k$. The particle-particle loop of fermionic (F) atoms corresponds to the F-truncation. Within the latter, the fermion propagator does not get renormalized. The same holds for the FB-truncations, where, in addition, purely bosonic diagrams (B) are also taken into account. Eventually, our highest truncations also include mixed diagrams (M) with both a fermion and a boson line. Figure taken from Boettcher et al. [2014c].

- FB: Fermion and boson diagrams,
  Running couplings: $U(\rho), A_\phi, S_\phi, V_\phi$

- FBM_0: Fermion, boson, and mixed diagrams,
  Running couplings: $U(\rho), A_\phi, S_\phi, V_\phi, m_\psi^2$

- FBM: Fermion, boson, and mixed diagrams,
  Running couplings: $U(\rho), A_\phi, S_\phi, V_\phi, m_\psi^2, A_\psi, h^2$.

The subscript 0 in the second and fourth truncation indicates that we leave out some running couplings which are included at a higher level of the truncation hierarchy with the same diagrams. For the last truncation we still keep $S_\psi = 1$. The effective potential $U(\rho)$ can be elaborated independently of the other running couplings. In the study of the spin-balanced BCS-BEC crossover we will mostly restrict to a ϕ^4- or ϕ^8-truncation, whereas this is inappropriate for the imbalanced system. In the latter case we resolve the effective potential on a grid of field values.

4.1.2 Regularization schemes

For choosing the cutoff function $R_k(Q)$ in the context of the BCS-BEC crossover, mainly two strategies can be applied. On the one hand, since the flow equation is valid for every appropriate regulator, one may choose a particularly simple function $R_k(Q)$ which is sufficient to yield finite loop-integrals. A convenient choice consists in the optimized cutoff, which only cuts off spatial momenta $q^2 = |\vec{q}|^2$. For bosons and fermions, respectively, it is given by

$$q^2\text{-opt:}$$

$$R_{\phi,k}(Q) = \Big(k^2 - \frac{q^2}{2}\Big)\theta\Big(k^2 - \frac{q^2}{2}\Big), \tag{4.6}$$

$$R_{\psi,k}(Q) = \Big[\mathrm{sgn}(q^2-\mu)k^2 - (q^2-\mu)\Big]\theta\Big(k^2 - |q^2-\mu|\Big), \tag{4.7}$$

where θ is the step function. (The notation q^2-opt shall indicate that this is a purely momentum cutoff.) The bosonic regulator R_ϕ takes into account that the boson mass is twice the fermion mass, whereas the fermionic function R_ψ regularizes around the Fermi surface. For a k-dependent running Fermi surface, one has to replace the chemical potential μ with a running coupling. In the spin-imbalanced case we employ either $R_{\psi\sigma,k}(Q) = R_{\psi,k}(Q)$ with $R_{\psi,k}$ from Eq. (4.7) and $\mu = (\mu_1+\mu_2)/2$ for the fermions in hyperfine state $|\sigma\rangle$ (symmetric scheme), or

$$R_{\psi\sigma,k}(Q) = \Big[\mathrm{sgn}(q^2-\mu_\sigma)k^2 - (q^2-\mu_\sigma)\Big]\theta\Big(k^2 - |q^2-\mu_\sigma|\Big) \tag{4.8}$$

(asymmetric scheme). For details we refer te the discussion in Sec. 5.3.2.

Whereas the q^2-opt regulators provide an efficient regularization of spatial momenta, they do not limit the range of summation for the Matsubara frequencies. Thus, at every scale k, both very large and very small frequencies contribute to the flow of Γ_k. This, however, spoils the separation of scales discussed above. As a result, the frequency and momentum structure of the k-dependent propagators is complicated. Precision then requires a sophisticated (numerical) treatment. For successful implementations with the nonperturbative RG in the context of the Kardar–Parisi–Zhang equation see Canet et al. [2010, 2011], Kloss et al. [2012].

A second possibility consists in the use of regulators which implement the idea of frequency and momentum shells, thereby depending on $Q = (q_0, \vec{q})$. In order to implement such regulators for a nonrelativistic system, we face the problem that the Galilean invariants for bosons and fermions are given by $\mathrm{i}q_0 + q^2/2$ and $\mathrm{i}q_0 + q^2 - \mu$, respectively. Due to the imaginary frequency dependence, the regulators frequently employed for Lorentz invariant relativistic systems cannot be applied

here. We choose the regulators

$$Q\text{-exp:}$$

$$R_{\phi,k}(Q) = \Big(\mathrm{i}q_0 + \frac{q^2}{2}\Big) r\Big(\frac{q_0^2 + q^4/4}{c_\phi k^4}\Big), \tag{4.9}$$

$$R_{\psi,k}(Q) = \Big(\mathrm{i}q_0 + q^2 - \mu\Big) r\Big(\frac{q_0^2 + (q^2-\mu)^2}{k^4}\Big), \tag{4.10}$$

with an exponential shape function

$$r(X) = (e^X - 1)^{-1}. \tag{4.11}$$

(The notation is again chosen to indicate that the R_k are now frequency and momentum cutoffs.) This particular choice respects all requirements on appropriate FRG regulators, cuts off frequencies efficiently, and has shown to be numerically convenient.

The relative cutoff scale c_ϕ in Eq. (4.9) allows to regularize bosons and fermions on slightly different scales $\sim k$. Given the different shapes of the dispersion relations and the somewhat arbitrary parametrization of the regulator functions, $c_\phi = 1$ is not necessarily a natural or distinguished choice. In particular, earlier works found rather strong dependences of observables on relative cutoff scales in two-species systems (Diehl et al. [2008a], Krippa et al. [2010], Birse et al. [2011]). Since exact results do not depend on c_ϕ, the residual dependence found with a given truncation gives some indication of the error due to the truncation, see e.g. Schnoerr et al. [2013]. For the truncations employed in this work with the Q-exp regulator we find that both Δ/μ and T_c/μ for the UFG show only 5%-variations with respect to $0.2 \leq c_\phi \leq 1$.

Regularized Loop Integrals

For spatial cutoffs which only depend on q^2, the Matsubara summation can be performed analytically. The remaining momentum integral can often be performed analytically for the q^2-opt regulator. This is outlined in Secs. 4.3.2 and 4.3.2. For frequency and momentum dependent regulators, however, the Q-integral has to be performed numerically. Here we discuss how this can be implemented in practice and how the cutoff substantially simplifies the integration. For concreteness we consider the Q-exp example relevant for the following analysis.

We consider the frequency and momentum regulator

$$\bar{R}^Q = A(\mathrm{i}q_0 + \xi_q) r(Y), \; Y = \frac{q_0^2 + \xi_q^2}{k^4}, \tag{4.12}$$

where $\xi_q = q^2/2$ for bosons and $\xi_q = q^2 + m_\psi^2$ for fermions. All one-loop integrals entering the beta functions become UV finite due to the insertion of

$$\dot{\bar{R}}^Q = A(\mathrm{i}q_0 + \xi_q)\Big[-\eta r(Y) - 4Y r'(Y)\Big] =: A(\mathrm{i}q_0 + \xi)\dot{r}(Y). \tag{4.13}$$

A typical diagram contributing to the flow has the form

$$\int_Q \frac{\dot{\bar{R}}^Q}{(P^Q + R^Q)^n} \propto \int_Q \frac{(\mathrm{i}q_0 + \xi_q)\dot{r}(Y)}{(\mathrm{i}q_0 + \xi_q)^n (1+r)^n} \sim \int_Q \frac{\dot{r}(Y)}{Y^{(n-1)/2}(1+r)^n}. \tag{4.14}$$

The integrand is cut off for a sufficiently large value of Y, such that only terms with $Y \leq N$ contribute, where N depends on the particular choice of the regulator. Accordingly, we find that the frequency and momentum integrals can be restricted to the domains

$$Y = \hat{q}_0^2 + \hat{\xi}_q^2 \leq N \;\Rightarrow \begin{cases} |\hat{q}_0| \leq N^{1/2},\ |\hat{q}^2 + \tilde{m}_\psi^2| \leq N^{1/2} & \text{(fermions)}, \\ |\hat{q}_0| \leq N^{1/2},\ |\hat{q}| \leq 2^{1/2} N^{1/4} & \text{(bosons)}. \end{cases} \tag{4.15}$$

Herein, $\hat{q}_0 = q_0/k^2$, $\tilde{\xi}_q = \xi_q/k^2$, $\hat{q}^2 = q^2/k^2$, and $\tilde{m}_\psi^2 = m_\psi^2/k^2$. For the Q-exp cutoff, we found that $N = 25$ is a good choice. Enlarging N allows for a check of the stability of the numerical integrations. For the fermions, the spatial condition translates to

$$q \in [K_{\psi,\min}, K_{\psi,\max}], \tag{4.16}$$

where

$$K_{\psi,\min} = \begin{cases} \sqrt{-(N^{1/2} + \tilde{m}_\psi^2)} & \text{if } N^{1/2} + \tilde{m}_\psi^2 < 0 \\ 0 & \text{else} \end{cases}, \tag{4.17}$$

$$K_{\psi,\max} = \begin{cases} \sqrt{N^{1/2} - \tilde{m}_\psi^2} & \text{if } N^{1/2} - \tilde{m}_\psi^2 > 0 \\ K_{\psi,\min} & \text{else} \end{cases}. \tag{4.18}$$

Finite temperature flow

At nonzero temperatures the loop integration over frequencies turns into an infinite Matsubara sum over frequencies $\omega_n = 2\pi(n + 1/2)T$ and $\omega_n = 2\pi n T$ for fermions and bosons, respectively. However, it is an interesting property of the renormalization group that, for large $k^2 \gg T$, the flow can be approximated by the zero temperature flow. In fact, the system at scale k can only resolve the actual value of the temperature once k^2 is comparable to T. We detail here how this feature is reflected in the flow equations and how it can be implemented numerically.

Given a function $f(\hat{q}_0) \propto \dot{\bar{R}}(Q)$ which has finite support due to the frequency and momentum regulator $\bar{R}(Q)$, the Matsubara summation is restricted to a finite domain according to

$$\tilde{T} \sum_{n=-\infty}^{\infty} f(\hat{\omega}_n) = \tilde{T} \sum_{n=-M}^{M} f(\hat{\omega}_n), \tag{4.19}$$

where the number M depends on the choice of the regulator and the value of $\tilde{T} = T/k^2$. With the choice of N from Eq. (4.15), the number of bins which are summed in Eq. (4.19) is given by

$$M(\tilde{T}) \simeq \frac{N^{1/2}}{\Delta\hat{\omega}_n} = \frac{N^{1/2}}{2\pi\tilde{T}} = \frac{k^2}{T}\mathcal{O}(1). \tag{4.20}$$

In particular, for large T or small k^2, we have

$$\tilde{T}\sum_{n=-\infty}^{\infty} f(\hat{\omega}_n) \overset{\tilde{T}\gg 1}{\longrightarrow} \begin{cases} \tilde{T}f(0) & \text{(bosons)} \\ 0 & \text{(fermions)} \end{cases}. \tag{4.21}$$

Our strategy is as follows: We search for the lowest number of bins $M(\tilde{T})$ such that the area of the Matsubara sum is still well approximated by the zero temperature integral. This will be the case in the early stages of the flow. Once the rescaled temperature $\tilde{T}$ gets too high, we evaluate the sum. However, due to the finite support of $\dot{\tilde{R}}(Q)$, this will involve only a few terms. Eventually, for $k^2 \to 0$, we only have to take into account the lowest modes, say $n = 0, \pm 1$.

We define a transition temperature $\tilde{T}_{\mathrm{tr}}$ such that

$$\tilde{T}\sum_n f(\hat{\omega}_0) = \begin{cases} \int_{-N^{1/2}}^{N^{1/2}} \frac{d\hat{q}_0}{2\pi} f(\hat{q}_0) & \tilde{T} \le \tilde{T}_{\mathrm{tr}} \\ \tilde{T}\sum_{n=-M(\tilde{T})}^{M(\tilde{T})} f(\hat{\omega}_n) & \tilde{T} > \tilde{T}_{\mathrm{tr}} \end{cases} \tag{4.22}$$

during the evolution of the flow, where

$$M(\tilde{T}) = \left[\frac{N^{1/2}}{2\pi\tilde{T}}\right] > 0. \tag{4.23}$$

Herein, $[x]$ defines the ceiling function, which maps x to the smallest integer not less than x. With this choice, we keep more terms than are actually necessary from the consideration in Eq. (4.21). For the Q-exp regulator $\tilde{T}_{\mathrm{tr}} = 0.01$ is a good choice. Thus we switch from an integration over continuous frequencies to a sum over finite frequencies once the number of Matsubara frequencies has decreased to $M(\tilde{T}_{\mathrm{tr}}) = 80$. By decreasing $\tilde{T}_{\mathrm{tr}}$ we can check for the stability of our numerical computations.

4.1.3 Physical content

We now discuss the physical content of the running couplings introduced above. The momentum dependence of the inverse bosons propagator

$$\bar{P}_\phi(Q) = A_\phi\Big(\mathrm{i}S_\phi q_0 + V_\phi q_0^2 + q^2/2\Big) \tag{4.24}$$

is generated during the early stages of the RG flow for a broad Feshbach resonance. It parametrizes the Q-dependence of the particle-particle channel of the four-fermion vertex. The coefficients A_ϕ, S_ϕ, and V_ϕ can be regarded as the expansion

coefficients of a derivative expansion of the boson self-energy for each scale k individually.

For large k and a sufficiently large initial Feshbach coupling h^2, the running of couplings is attracted to a universal vacuum fixed point with $\eta_{\phi\star} = 4 - d$. Then, A_ϕ in 3D scales as

$$A_{\phi,k} \sim k^{-\eta_{\phi\star}} \sim k^{-1}. \tag{4.25}$$

Accordingly, $A_{\phi,k} q^2 \simeq A_{\phi,q} q^2 \sim q$ in the early stages of the flow. In fact, the inverse boson propagator can be integrated analytically in this regime, yielding $\bar{P}_\phi(Q) \sim \sqrt{\mathrm{i}q_0/2 + q^2/4 - \mu}$, which indeed scales linear in q. We see that, although we pushed the truncation into a q^2-dependence of the propagator, the running couplings react in such a manner as to undo this forcing. The characteristic running of η_ϕ, S_ϕ, and V_ϕ in 3D is visualized in Fig. 4.2. In 2D the propagator in the scaling regime is given by $\bar{P}_\phi(Q) \sim \log(\mathrm{i}q_0/2 + q^2/4 - \mu)$, corresponding to an anomalous dimension of $\eta_{\phi\star} = 2$. To see this note that $(x^{d-2} - 1)/(d-2) \to \log(x)$ for $d \to 2$. The behavior of S_ϕ is very distinct in reduced dimension. We discuss this in more detail in Sec. 6.1.1, where we also derive the analytic expressions for the boson propagator in vacuum.

The quadratic frequency dependence $V_\phi q_0^2$ in the boson propagator constitutes the first nonvanishing frequency dependent term of the real part of the boson self-energy. Deep in the infrared Goldstone regime, it is expected to be dominant over the linear frequency term. This is well-known from purely bosonic systems, most pronounced in reduced dimensionality $d \leq 2$ (Wetterich [2008], Dupuis [2009b]). The V_ϕ-term is important for the two-dimensional BCS-BEC crossover. In 3D we find a rather mild dependence of the overall flow on the presence of V_ϕ for the Q-exp regulators. This indicates that the frequency and momentum regulators work sufficiently well, such that already the truncation without V_ϕ captures the leading frequency dependence. In contrast, for purely momentum regulators, the influence of V_ϕ turns out to be stronger.

In order to capture the physics of the second order superfluid phase transition, a Taylor expansion of the effective potential $U(\rho)$ needs to be at least of order ϕ^4. We start at large k with a non-vanishing boson "mass term" (or detuning) $m^2_{\phi,k} > 0$. The field expectation value is zero in this symmetric regime of the flow, $\rho_{0,k} = 0$. Scattering between bosons is described by the boson-boson coupling λ_ϕ, and n-boson scattering processes are encoded in u_n for $n \geq 3$. Due to a nonzero chemical potential, the boson mass term decreases during the flow and may reach zero for a nonzero symmetry breaking scale k_{sb}. This is equivalent to the Thouless criterion of a diverging four-fermion vertex, however, at a given scale k. Typically, the symmetry breaking scale is slightly above the chemical potential, $k^2_{\mathrm{sb}} \gtrsim \mu$. The origin of this divergence can be rooted in large contributions of fermion fluctuations due to an approximate zero of the inverse fermion propagator $\mathrm{i}q_0 + q^2 - \mu$, which occurs as soon as the typical momenta become of the order of the chemical potential. The flow of the boson-boson coupling λ_ϕ at $T = 0$ is displayed in Fig. 4.3.

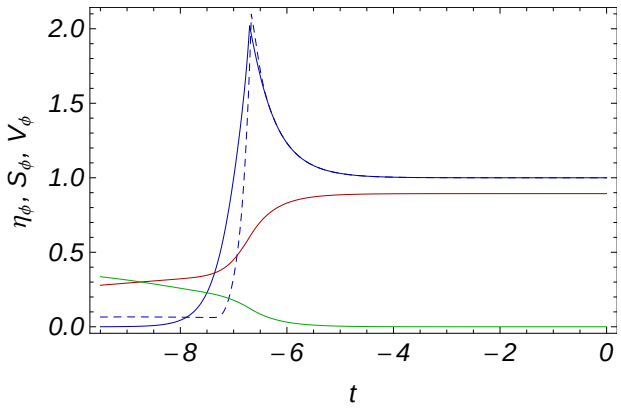

Figure 4.2: Typical running of the couplings which parametrize the boson propagator $P_\phi(Q)$, shown here for the spin-balanced UFG. Units are such that $\mu = 1$. From top to bottom we show the $t = \log(k/\Lambda)$-dependence of η_ϕ (blue, solid upper curve), S_ϕ (red middle curve), and V_ϕ (green lower curve) at $T = 0$. The initial values correspond to $t = 0$ ($k = \Lambda$), and the infrared regime is found for $t \to -\infty$ ($k \to 0$). Many-body effects strongly influence the flow at $k^2 \simeq \mu$, which corresponds to $t = -6.9$ in this plot. We also show the anomalous dimension η_ϕ for $T = T_c$ (blue, dashed), which does not vanish in the infrared but settles at the critical exponent $\eta = 0.05(1)$ for a ϕ^4-truncation. This value is expected in the O(2)-universality class within this order of the truncation. Figure taken from Boettcher et al. [2014c].

For $k < k_{sb}$ a nonzero expectation value $\rho_{0,k}$ of the boson field indicates local order on length scales $\sim k^{-1}$. Within our truncation, this results in an anomalous fermion self-energy

$$\Sigma_{an,k}(Q = 0) = \Delta_k = (h_k^2 \rho_{0,k})^{1/2}, \tag{4.26}$$

which enters the fermion propagator as a gap, hence removing the zero in the denominator. The fate of the k-dependent gap Δ_k depends on the temperature of the system. For $T = 0$ one finds a superfluid ground state with $\rho_0 \neq 0$ at $k = 0$ in the balanced case. For higher temperatures, thermal fluctuations may destroy the local order, such that $\rho_{0,k} > 0$ for some $k > 0$, but $\rho_{0,k=0} = 0$ at the end of the flow. We call this temperature range the precondensation region. The local expectation value $\rho_{0,k}$ of bosons can then be regarded as indicator for bosonic correlations on scales of order k, which do not yet suffice to produce a true long-range order. It is closely related to the notion of a pseudogap Δ_{pg}, see also the discussion in Sec. 5.3.2. We may use the nonvanishing value of $\rho_{0,k}$ at intermediate scales k to estimate roughly the size of the pseudogap according to $\Delta_{pg} = \max_k \Delta_k$ or $\Delta_{pg} = \Delta_{k=k_F}$. The former choice is illustrated in Fig. 4.4. A more accurate resolution of the size of the pseudogap can be obtained by computing the fermion

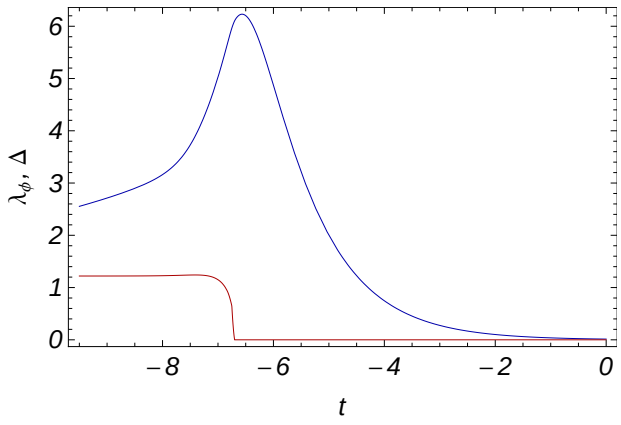

Figure 4.3: Zero temperature running of the boson-boson coupling λ_ϕ (blue, upper curve) for the UFG. We can clearly identify three regimes in the flow: For $t \simeq 0$ the coupling follows the scaling solution with constant $\tilde{\lambda}_\phi = k\lambda_\phi$. This behavior would continue in vacuum, where $\mu = T = 0$. For a nonzero $\mu > 0$, however, the flow is influenced by many-body effects at $k^2 \simeq \mu$ ($t \simeq -6.9$). For smaller scales, the flow enters the Goldstone regime, where all contributions to the running of couplings come from infrared Goldstone fluctuations, whereas the chemical potential μ/k^2 is gapped out due to $k \to 0$. The behavior exemplified here for λ_ϕ is found for all running couplings. We also show the running of $\Delta_k = (h^2\rho_0)^{1/2}$ in the red lower curve. It has a nonvanishing value below the symmetry breaking scale $t_{\rm sb} = -6.7$. Figure taken from Boettcher et al. [2014c].

spectral function from the full fermion propagator. For temperatures above the precondensation temperature, no local order emerges during the flow and we have $\rho_{0,k} = 0$ for all k.

The gap parameter is defined as

$$\Delta = \lim_{k\to 0} \Delta_k. \tag{4.27}$$

Superfluidity corresponds to $\rho_{0,k=0} > 0$, and thus is equivalent to a nonzero gap parameter in our truncation of the effective action. The critical temperature for the phase transition to superfluidity is defined as the highest temperature such that a precondensate $\rho_{0,k} > 0$ appearing during the flow survives at $k = 0$. In the BCS-limit, no precondensation occurs, and the rise of bosonic correlations is in one-to-one correspondence with bosonic condensation. On the BEC side, in contrast, the precondensation region is huge. The running of Δ_k for the balanced UFG is shown in Fig. 4.3. The continuous behavior of $\Delta(T)$ for all T is shown in Fig. 4.4. It indicates a second order phase transition.

Whereas the phase transition and thus the critical temperature is mainly driven

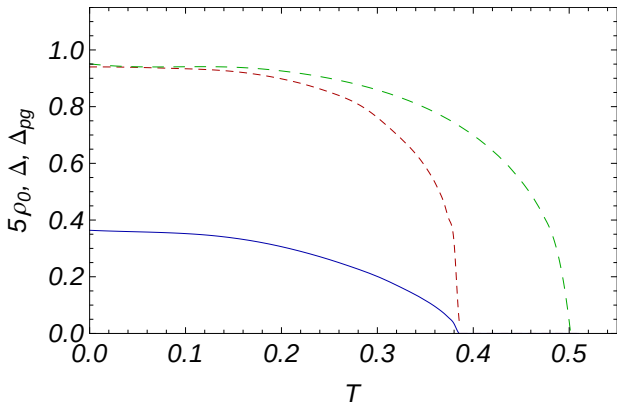

Figure 4.4: Temperature dependence of the minimum $\rho_0(T)$ of the effective potential $U(\rho)$ for the UFG within a FBM$_0$-truncation (blue solid curve, multiplied by a factor of 5 for better visibility). The continuous behavior of this order parameter at T_c is found for all of our truncations and results from the inclusion of bosonic fluctuations, which become dominant close to criticality. Units are such that $\mu = 1$. In our bosonized model we define the gap parameter according to $\Delta = \sqrt{h^2\rho_0}$ (red, dashed curve), where h^2 is the Yukawa coupling. The actual gap in the single-fermion spectrum persists even above the critical temperature, where it constitutes a pseudogap. Within our approach we observe the pseudogap behavior as a temperature region with $\rho_{0,k} \neq 0$ during the flow, but $\rho_0 = \rho_{0,k=0} = 0$ in the infrared. Here we estimate its value by $\Delta_{\mathrm{pg}} = \max_k \Delta_k$, shown in the green long-dashed curve. The pseudogap ceases to exist above $T_{\mathrm{pc}}/\mu = 0.50$ in this truncation. For zero temperature we have $\Delta = \Delta_{\mathrm{pg}}$. Figure taken from Boettcher et al. [2014c].

by the bosons, we expect the renormalization of the fermion propagator to be important for the density of the system due to the Tan contact effect, see Sec. 5.1. When employing purely momentum regulators, the diagrams renormalizing the fermion propagator vanish in vacuum. This is a result of the possibility to analytically perform the frequency integrations, which have all poles in the same half-plane. When employing frequency and momentum regulators, the fermion propagator gets renormalized in vacuum. This effect can be controlled by means of an appropriate vacuum renormalization of the initial "fermion mass term", $m^2_{\psi\Lambda}(\mu = 0) = C\Lambda^2$, where C is a regulator-dependent constant.

The physical many-body chemical potential $\mu_{\mathrm{mb}} = \mu - \varepsilon_{\mathrm{B}}/2$ vanishes in vacuum. The association of $\bar{m}^2_\psi - \bar{m}^2_{\psi,\mathrm{vac}}$ with μ_{mb} is only meaningful for a constant difference

$$\bar{m}^2_{\psi,k} - \bar{m}^2_{\psi,k,\mathrm{vac}} \simeq -\mu_{\mathrm{mb}} \tag{4.28}$$

in the early stages of the many-body flow, i.e. for large k. (The vacuum flow for the fermion mass term is given by the canonical running $m^2_{\psi,\mathrm{vac}} = Ck^2$ for the UFG.) If Eq. (4.28) is not satisfied, the relation between the chemical potential and the fermion mass term m^2_ψ is not obvious.

The Feshbach coupling h^2 receives small corrections in the ordered regime of the flow where $\rho_0 > 0$. We include this effect in our highest truncation. In this thesis we only employ truncations with $S_\psi = 1$.

4.1.4 Universality and initial conditions

To initialize the set of ordinary differential equations for the running couplings $\{g_k\}$, we have to equip the system with appropriate initial conditions $\{g_\Lambda\}$. This is particularly simple for the UFG, where the initial conditions for the running couplings are found as the zeros of the beta functions for the dimensionless renormalized running couplings.

The standard procedure for solving the flow equation for the effective average action consists in ensuring the initial Γ_Λ to agree with the microscopic action S. For instance, this would result in the initial values $A_\phi = S_\phi = V_\phi = 0$ for a single-channel model of the BCS-BEC crossover. The parameters of the microscopic action, here the boson and fermion mass terms $m^2_{\phi\Lambda}$ and $m^2_{\psi\Lambda}$, have to be chosen such that we arrive at the right vacuum scattering physics. In 3D we have

$$m^2_{\phi,k=0,\mathrm{vac}} = -\frac{h^2}{8\pi a}\theta(-a), \tag{4.29}$$

$$m^2_{\psi,k=0,\mathrm{vac}} = -\frac{1}{2}\varepsilon_\mathrm{B} = \frac{1}{a^2}\theta(a). \tag{4.30}$$

Accordingly, bosons (fermions) are gapped on the atomic (bosonic) side of the crossover in vacuum. In the unitary limit both masses vanish. Eqs. (4.29) and (4.30) are actually valid in both 3D and 2D, where a corresponds to the 3D and 2D scattering length, respectively. We refer to Sec. 6.1.1 for a detailed discussion of the corresponding scattering theory.

For a sufficiently broad Feshbach resonance, the running couplings are attracted to a scaling solution (Diehl et al. [2007a,b, 2010a]), for which the renormalized dimensionless couplings take constant values. The anomalous dimensions obey $4 - d - \eta_\phi - 2\eta_\psi = 0$, as for this choice $\partial_k \tilde{h}^2 = 0$ in our truncation. Depending on the deviation of the relevant boson and fermion mass terms from their UFG initial values, the system will stay sufficiently long (i.e. many k-steps) at this fixed point. At the fixed point, all other couplings acquire their corresponding fixed point values. We call this regime the scaling regime. For any nonzero a^{-1}, μ, or T, the system will eventually leave the scaling solution. However, memory of the precise initial condition is lost, as all couplings acquired their fixed point values. Accordingly, we might as well start directly at the scaling solution.

Due to this property, the initial conditions for the UFG can now be found for any given truncation-, regularization- and specification-prescription by simply solving

a fixed point equation. Indeed, for $a^{-1} = 0$, Eqs. (4.29) and (4.30) can be solved by ensuring the dimensionless boson and fermion mass terms to be constant and given by their fixed point values, $\tilde{m}_\phi^2 = m_\phi^2/k^2 = \tilde{m}_{\phi\star}^2$ and $\tilde{m}_\psi^2 = m_\psi^2/k^2 = \tilde{m}_{\psi\star}^2$. (Dimensionless running couplings, which are divided by their canonical power of k, will be denoted by a tilde. The subscript $\star$ indicates the fixed point.) We then trivially have $m_\phi^2, m_\psi^2 \sim k^2 \to 0$ for $k \to 0$. The other running couplings are attracted to their fixed point values. To simplify the ultraviolet flow, we let them start directly at the scaling solution: $\Gamma_\Lambda = \Gamma_\star$.

Thus, given a truncation in terms of a set of dimensionless running couplings $\{\tilde{g}_k\}$, the initial conditions for the UFG are found from the zeros $\tilde{g}_\star$ of the beta functions for the dimensionless running couplings in vacuum ($\mu = T = 0$). We set $T = 0$ in the following. For the UFG we then have

$$\dot{\tilde{g}}(\mu = 0) = \beta_{\tilde{g}}(\tilde{\mu} = 0) = 0 \tag{4.31}$$

for $g \neq m_\psi^2$, with $\tilde{\mu} = \mu/k^2$, and $m_{\psi\Lambda}^2 = \tilde{m}_{\psi\star}^2\Lambda^2 - \mu$. In the F, FB_0, and FB-truncations we have $\tilde{m}_{\psi\star}^2 = 0$. Away from unitarity, or in 2D, $m_{\phi\Lambda}^2$ and $m_{\psi\Lambda}^2$ have to be tuned such as to satisfy Eqs. (4.29) and (4.30). A finite scattering length or a nonzero $\mu_{\mathrm{mb}} = \mu - \varepsilon_{\mathrm{B}}/2$ define relevant perturbations which drive the system away from the fixed point. The initial scale Λ has to be chosen large enough such that many-body and interaction effects do not influence the ultraviolet flow.

The initial conditions for the running couplings except for $m_{\psi\Lambda}^2$ do not necessarily need a modification due to the chemical potential, as the corresponding terms are generated automatically during the ultraviolet flow. To simplify the latter for the numerically challenging analysis of the UFG with the Q-exp regulators, however, we choose them to be on their corresponding fixed point values as well. Thus we arrive at

$$\tilde{g}_\Lambda = \tilde{g}_\star + \tilde{g}_{\mu\star}\mu/\Lambda^2, \tag{4.32}$$

where the subscript μ indicates the μ-derivative of the respective running coupling, with $\tilde{m}_{\psi\mu}^2 = -1$.

For the sake of completeness we present here the rather technical way of obtaining the $\tilde{g}_{\mu\star}$ in Eq. (4.32) for the UFG. Upon introducing a chemical potential,

$$m_{\psi\Lambda}^2(\mu) = m_{\psi\star}^2 - \mu, \tag{4.33}$$

we slightly deviate from the fixed point in Eq. (4.31), and expect deviations from the scaling solution as soon as $k^2 \simeq \mu$. In terms of beta functions, the UV flow (large k) is governed by the set of equations

$$\dot{\tilde{g}}(\mu) = \beta_{\tilde{g}}(\tilde{\mu}) \simeq \frac{\partial\beta_{\tilde{g}}}{\partial\tilde{\mu}}(0)\cdot\tilde{\mu} + \cdots = \sum_i \frac{\partial\beta_{\tilde{g}}}{\partial\tilde{g}_i}(0)\cdot\tilde{g}_{i,\mu}\cdot\tilde{\mu} + \ldots \tag{4.34}$$

We used that the leading term vanishes and introduced the notation

$$g_\mu = \partial_\mu g. \tag{4.35}$$

The dimensionless running couplings $\tilde{g}_\mu$ are then found in the UV from the equations

$$\begin{aligned}\dot{\tilde{g}}_\mu &= \partial_t\Big(\frac{\partial\tilde{g}}{\partial\tilde{\mu}}\Big) = 2\tilde{g}_\mu + \sum_i \frac{\partial\beta_{\tilde{g}}}{\partial\tilde{g}_i}(0)\cdot\tilde{g}_{i,\mu}. \\ &\Rightarrow \dot{\tilde{g}}_{\mu,i} = A_{ij}\cdot\tilde{g}_{\mu,j}.\end{aligned} \tag{4.36}$$

The matrix

$$A = 2\cdot\mathbf{1} + \{\partial\beta/\partial\tilde{g}\} \tag{4.37}$$

is solely determined by the fixed point values $\tilde{g}_\star$. We will be interested in a situation where

$$\tilde{g}_\mu \simeq \tilde{g}_{\mu,\star} = \text{const. in the UV.} \tag{4.38}$$

Most importantly, we have to ensure

$$\alpha_\psi = \tilde{m}^2_{\psi\mu} = \frac{\partial m^2_\psi}{\partial\mu} \simeq -1 \text{ in the UV,} \tag{4.39}$$

because otherwise the value of the chemical potential loses its meaning due to an anomalous running in the UV.

The behavior of the set of equations (4.36) depends on whether we allow for a running fermion mass or not. If we allow for a running fermion mass, then α_ψ is a free parameter in (4.36), and, consequently, $\dot{\tilde{g}}_\mu = A\cdot\tilde{g}_\mu = 0$ will in general not have a nontrivial solution, as A has full rank: We have a homogeneous set of equations, with the only solution $\tilde{g}_{\mu,\star} = 0$. This conflicts $\alpha_\psi = -1$. In contrast, if we do not allow for a running fermion mass, thereby enforcing $\alpha_\psi = -1$ by hand, we find a scaling solution with fixed point values $\tilde{g}_{\mu,\star}$. The UV flow is then very simple:

$$\tilde{g}_k(\mu) \simeq \tilde{g}_\star + \tilde{g}_{\mu\star}\cdot\mu/k^2. \tag{4.40}$$

In particular, $\tilde{m}^2_\psi \simeq -\tilde{\mu}$ for large k.

In order to have $\alpha_\psi = -1$ in the UV, we need A not to be of full rank, i.e. A must have an eigenvalue 0. Then, the variables in $A\cdot\tilde{g}_\mu = 0$ are not independent, and there are nontrivial solutions. The matrix A is fully determined by the vacuum scaling values $\tilde{g}_\star$. The values of $\tilde{g}_\star$, however, depend on the regularization procedure. With the relative cutoff scale c_ϕ in Eq. (4.9), we have a knob to tune the behavior of the UV running of the couplings. In particular, we find that for $c_\phi = c_0 = 0.2454 \simeq 1/4$ we have a zero eigenvalue of A, and $m^2_\psi - m^2_{\psi,\star} \simeq -\mu$ in the UV.

4.2 Flow equations for general regulators

4.2.1 Flow equation building blocks

In this section we collect the building blocks which are required to efficiently compute beta functions within our truncation. The expressions derived in the following assume frequency and momentum independent vertices. They are independent of the regularization scheme and many assumptions on the boson and fermion dynamics. This section also introduces the notation used in the remainder of this thesis.

We generalize the ansatz for the kinetic part of the effective average action in Eq. (4.2) according to

$$\bar{\Gamma}_{\mathrm{kin}}[\bar{\psi},\bar{\phi}] = \int_X \left(\sum_{\sigma=1,2} \bar{\psi}_\sigma^* \bar{P}_{\psi\sigma}(\partial_\tau, -\mathrm{i}\nabla)\bar{\psi}_\sigma + \bar{\phi}^* \bar{P}_\phi(\partial_\tau, -\mathrm{i}\nabla)\bar{\phi} \right). \tag{4.41}$$

The inverse propagators $\bar{P}_{\psi\sigma}$ and $\bar{P}_\phi$ are assumed to be of the form

$$\bar{P}_{\psi\sigma}(\partial_\tau, -\mathrm{i}\nabla) = -A_{\psi\sigma}\nabla^2 + \ldots, \tag{4.42}$$

$$\bar{P}_\phi(\partial_\tau, -\mathrm{i}\nabla) = -A_\phi \frac{1}{2}\nabla^2 + \ldots, \tag{4.43}$$

such that the gradient coefficients $A_{\psi\sigma}$ and A_ϕ can be used to define renormalized fields via $\psi_\sigma = A_{\psi\sigma}^{1/2}\bar{\psi}_\sigma$ and $\phi = A_\phi^{1/2}\bar{\phi}$, respectively. This is in line with the truncation presented in Sec. 4.1.1 for a particular choice of $\bar{P}_\psi$ and $\bar{P}_\phi$. We then define renormalized couplings through an appropriate rescaling by powers of $A_{\psi\sigma}$ and A_ϕ such that

$$\bar{\Gamma}[\bar{\psi},\bar{\phi}] = \Gamma[\psi,\phi]. \tag{4.44}$$

This equation also allows to generate their RG-running from the flow of $\bar{\Gamma}_k$. In fact, the flow equation for the effective average action should be expressed in terms of $\bar{\Gamma}_k$, see Eq. (4.52) below. The flow of $\Gamma[\psi,\phi]$ receives additional terms proportional to the anomalous dimensions defined in Eq. (4.3). We indicate unrenormalized quantities by an overbar, renormalized ones are denoted without an overbar.

When evaluated for homogeneous mean fields, the n-th functional derivative $\bar{\Gamma}_k^{(n)}(X_1,\ldots,X_n)$ of the effective average action is proportional to n delta functions $\delta(X_1-X_2)\ldots\delta(X_1-X_n)$, where X_i is the argument of the i-th field derivative. Within the momentum representation of the fields,

$$\bar{\Psi}(P) = \int_X \bar{\Psi}(X)e^{-\mathrm{i}PX}, \tag{4.45}$$

the vertices transform according to

$$\bar{\Gamma}_k^{(n)}[\bar{\Psi}](P_1,\ldots,P_n) = \int_{X_1,\ldots,X_n} \bar{\Gamma}_k^{(n)}[\bar{\Psi}](X_1,\ldots,X_n)e^{\mathrm{i}P_1X_1}\ldots e^{\mathrm{i}P_nX_n}. \tag{4.46}$$

This results in an overall delta function $\delta(P_1+\cdots+P_n)$ for a homogeneous setting. We assume frequency and momentum independent vertices for $n > 2$, see Eq. (4.76) below. We denote 4-momenta as $Q = (q_0, \vec{q})$ with

$$\int_Q = T\sum_n \int_{\vec{q}} = T\sum_n \int \frac{\mathrm{d}^d q}{(2\pi)^d}. \tag{4.47}$$

The delta function $\delta(Q)$ is defined from $\int_Q \delta(Q) f(Q) = f(0)$ for any function $f(Q)$. We often denote the dependence on Q by a superscript, i.e. $f^Q := f(Q)$. The frequency q_0 is always understood as a Matsubara frequency with

$$q_0 = \begin{cases} 2\pi n T & \text{(bosons)} \\ 2\pi(n+1/2)T & \text{(fermions)} \end{cases} \tag{4.48}$$

for nonzero temperatures, and $q_0 \in \mathbb{R}$ for zero temperature. In the latter case we have

$$T\sum_n = \frac{2\pi T}{2\pi}\sum_n = \sum_n \frac{\Delta q_0}{2\pi} \overset{T\to 0}{\longrightarrow} \int \frac{\mathrm{d}q_0}{2\pi}. \tag{4.49}$$

We work with supermatrices according to the field vector

$$\bar{\Psi} = (\bar{\phi}_1, \bar{\phi}_2, \bar{\psi}_1, \bar{\psi}_2, \bar{\psi}_1^*, \bar{\psi}_2^*), \tag{4.50}$$

where the complex boson field is given in the real field basis according to $\bar{\phi} = \bar{\phi}_1 + \mathrm{i}\bar{\phi}_2$. Any supermatrix M can then be decomposed according to

$$M = \begin{pmatrix} M_{BB}^{2\times 2} & M_{BF}^{2\times 4} \\ M_{FB}^{4\times 2} & M_{FF}^{4\times 4} \end{pmatrix}, \ \mathrm{str} M = \mathrm{tr} M_{BB} - \mathrm{tr} M_{FF}, \tag{4.51}$$

where (s)tr denotes a (super)trace. For an introduction to the notions of superalgebra we refer to Zinn-Justin [1993]. The flow equation for the effective average action in this notation is given by

$$\partial_t \bar{\Gamma}[\bar{\phi}, \bar{\psi}] = \frac{1}{2}\mathrm{STr}\left[\begin{pmatrix} \bar{\Gamma}^{(2)}_{BB}[\bar{\phi}, \bar{\psi}] + \bar{R}_\phi & \bar{\Gamma}^{(2)}_{BF}[\bar{\phi}, \bar{\psi}] \\ \bar{\Gamma}^{(2)}_{FB}[\bar{\phi}, \bar{\psi}] & \bar{\Gamma}^{(2)}_{FF}[\bar{\phi}, \bar{\psi}] + \bar{R}_\psi \end{pmatrix}^{-1} \begin{pmatrix} \dot{\bar{R}}_\phi & 0 \\ 0 & \dot{\bar{R}}_\psi \end{pmatrix}\right]. \tag{4.52}$$

The mean fields $\bar{\phi}_X$ and $\bar{\psi}_X$ have to be arbitrary and $\bar{\Gamma}_{BF}, \bar{\Gamma}_{FB} \neq 0$ in order to derive flow equations for higher n-point functions.

The effective average potential $U_k(\rho) = \bar{U}_k(\bar{\rho})$ is defined by $\bar{\Gamma}_k[\bar{\phi}] = \beta V \cdot U_k(\rho)$ for a constant field ϕ. Herein, V is the d-dimensional volume. The inverse propagators $\bar{G}_\phi^{-1}(Q)$, $\bar{G}_\psi^{-1}(Q)$ are found from

$$\bar{\Gamma}^{(2)}_{\bar{\phi}_i\bar{\phi}_j}(X, Y, \bar{\rho}) = \frac{\delta^2\bar{\Gamma}}{\delta\bar{\phi}_i(X)\delta\bar{\phi}_j(Y)}[\bar{\phi}], \tag{4.53}$$

$$\bar{\Gamma}^{(2)}_{\bar{\psi}_\alpha^{(*)}\bar{\psi}_\beta^{(*)}}(X, Y, \bar{\rho}) = \frac{\overrightarrow{\delta}}{\delta\bar{\psi}_\alpha^{(*)}(X)}\bar{\Gamma}\frac{\overleftarrow{\delta}}{\delta\bar{\psi}_\beta^{(*)}(Y)}[\bar{\phi}] \tag{4.54}$$

for an arbitrary constant background field $\rho = \phi^*\phi = \frac{1}{2}\phi_1^2$. We assume the boson background field ϕ to be real-valued. In momentum representation we have

$$\bar{\Gamma}^{(2)}_{BB}(Q', Q) = \delta(Q' + Q)\bar{G}_\phi^{-1}(Q), \tag{4.55}$$

$$\bar{\Gamma}^{(2)}_{FF}(Q', Q) = \delta(Q' + Q)\bar{G}_\psi^{-1}(Q). \tag{4.56}$$

We first consider the spin-balanced case with $\mu_1 = \mu_2$. The modifications for the imbalanced case are presented below. For the above ansatz (4.41) for the effective average action we find

$$\bar{G}_\phi^{-1}(Q) = A_\phi G_\phi^{-1}(Q) = A_\phi \begin{pmatrix} P_\phi^{S,Q} + U' + 2\rho U'' & \mathrm{i}P_\phi^{A,Q} \\ -\mathrm{i}P_\phi^{A,Q} & P_\phi^{S,Q} + U' \end{pmatrix}, \tag{4.57}$$

$$\bar{G}_\psi^{-1}(Q) = A_\psi G_\psi^{-1}(Q) = A_\psi \begin{pmatrix} -h\phi\varepsilon & -P_\psi^{-Q}\mathbb{1} \\ P_\psi^{Q}\mathbb{1} & h\phi\varepsilon \end{pmatrix}. \tag{4.58}$$

Herein, $\mathbb{1} = ((1,0),(0,1))$ and $\varepsilon = ((0,1),(-1,0))$, and primes denote derivatives with respect to ρ. Moreover, for a given function $f(Q)$ we define the symmetrized and anti-symmetrized components, respectively, according to

$$f^{S,A}(Q) = \frac{1}{2}\Big(f^Q \pm f^{-Q}\Big). \tag{4.59}$$

Note that $f^Q f^{-Q} = f^S(Q)^2 - f^A(Q)^2$. The regulators read

$$\bar{R}_\phi^Q = A_\phi R_\phi^Q = A_\phi \begin{pmatrix} R_\phi^S(Q) & \mathrm{i}R_\phi^A(Q) \\ -\mathrm{i}R_\phi^A(Q) & R_\phi^S(Q) \end{pmatrix}, \tag{4.60}$$

$$\bar{R}_\psi^Q = A_\psi R_\psi^Q = A_\psi \begin{pmatrix} 0 & -R_\psi^{-Q}\mathbb{1} \\ R_\psi^Q\mathbb{1} & 0 \end{pmatrix}. \tag{4.61}$$

The regularized propagators are given by

$$G_\phi^Q = A_\phi \bar{G}_\phi^Q = \frac{1}{\det_B^Q} \begin{pmatrix} L_\phi^{S,Q} + U' & -\mathrm{i}L_\phi^{A,Q} \\ \mathrm{i}L_\phi^{A,Q} & L_\phi^{S,Q} + U' + 2\rho U'' \end{pmatrix}, \tag{4.62}$$

$$G_\psi^Q = A_\psi \bar{G}_\psi^Q = \frac{1}{\det_F^Q} \begin{pmatrix} h\phi\varepsilon & L_\psi^{-Q}\mathbb{1} \\ -L_\psi^{Q}\mathbb{1} & -h\phi\varepsilon \end{pmatrix}, \tag{4.63}$$

where we introduce the notation

$$L_\psi^Q = P_\psi^Q + R_\psi^Q, \tag{4.64}$$

$$L_\phi^Q = P_\phi^Q + R_\phi^Q + U'(\rho) + \rho U''(\rho), \tag{4.65}$$

$$\det{}_F^Q = L_\psi^Q L_\psi^{-Q} + h^2\rho, \tag{4.66}$$

$$\det{}_B^Q = L_\phi^Q L_\phi^{-Q} - (\rho U'')^2. \tag{4.67}$$

We do not distinguish in our notation between the regularized and non-regularized propagators, i.e. $(\Gamma^{(2)}+R_k)^{-1}$ and $(\Gamma^{(2)})^{-1}$, since it will always be clear from the context what is meant.

The boson propagator can also be represented in the *conjugate field basis* $\{\phi,\phi^*\}$. The corresponding matrix will be denoted by a widehat, i.e.

$$M_{BB}=\begin{pmatrix}M_{\phi_1\phi_1} & M_{\phi_1\phi_2}\\ M_{\phi_2\phi_1} & M_{\phi_2\phi_2}\end{pmatrix},\qquad \widehat{M}_{BB}=\begin{pmatrix}M_{\phi\phi} & M_{\phi\phi^*}\\ M_{\phi^*\phi} & M_{\phi^*\phi^*}\end{pmatrix}. \tag{4.68}$$

We can change bases according to the transformation

$$\widehat{G}^{-1}=UG^{-1}U^t \tag{4.69}$$

with

$$U=\frac{1}{\sqrt{2}}\begin{pmatrix}1 & -\mathrm{i}\\ 1 & \mathrm{i}\end{pmatrix},\qquad U^t=\frac{1}{\sqrt{2}}\begin{pmatrix}1 & 1\\ -\mathrm{i} & \mathrm{i}\end{pmatrix}. \tag{4.70}$$

This is inverted by

$$G^{-1}=U^\dagger\widehat{G}^{-1}U^* \tag{4.71}$$

with

$$U^\dagger=U^{-1}=\frac{1}{\sqrt{2}}\begin{pmatrix}1 & 1\\ \mathrm{i} & -\mathrm{i}\end{pmatrix},\qquad U^*=(U^t)^{-1}=\frac{1}{\sqrt{2}}\begin{pmatrix}1 & \mathrm{i}\\ 1 & -\mathrm{i}\end{pmatrix}. \tag{4.72}$$

In this way we obtain

$$\widehat{G}_\phi^{-1}(Q)=\begin{pmatrix}\rho U''(\rho) & L_\phi^{-Q}\\ L_\phi^{Q} & \rho U''(\rho)\end{pmatrix},\qquad \widehat{R}_\phi(Q)=\begin{pmatrix}0 & R_\phi^{-Q}\\ R_\phi^{Q} & 0\end{pmatrix}. \tag{4.73}$$

The propagator becomes

$$\widehat{G}_\phi(Q)=\frac{1}{\det{}_B(Q)}\begin{pmatrix}-\rho U''(\rho) & L_\phi^{-Q}\\ L_\phi^{Q} & -\rho U''(\rho)\end{pmatrix}. \tag{4.74}$$

Higher n-point functions are represented by supermatrices with additional external indices, i.e. each $\Gamma^{(n\geq 2)}$ is either BB, BF, FB, FF, and carries further indices. We introduce a vertical bar, $|$, to separate those fermion derivatives which act from the left from those which act from the right, e.g.

$$\left(\bar\Gamma^{(5)}_{\bar\psi_1^*\bar\psi_3 F|F\bar\phi_1}(X_1,\dots,X_5)\right)_{AB}=\frac{\overrightarrow{\delta}^3}{\delta\bar\psi_1^*(X_1)\delta\bar\psi_3(X_2)\delta\bar\psi_A(X_3)}\bar\Gamma\frac{\overleftarrow{\delta}^2}{\delta\bar\psi_B(X_4)\delta\bar\phi_1(X_5)}. \tag{4.75}$$

For bosons the order of the functional derivatives does not play a role. In our truncation we assume momentum independent vertices. We write

$$\bar{\Gamma}^{(n>2)}(Q_1,\dots,Q_n) = \bar{\gamma}^{(n)}\delta(Q_1+\cdots+Q_n). \tag{4.76}$$

The boson matrices can be given either in the real field basis $\{\bar{\phi}_1,\bar{\phi}_2\}$ or in the conjugate field basis $\{\bar{\phi},\bar{\phi}^*\}$. We again label the latter case with a widehat. For a constant real background field $\phi=\sqrt{\rho}$ we have

$$\begin{aligned}
\bar{\gamma}^{(3)}_{\bar{\phi}_1 BB} &= A_\phi^{3/2}\begin{pmatrix} u^{(3)}_{111} & 0\\ 0 & u^{(3)}_{122}\end{pmatrix},\ \bar{\gamma}^{(3)}_{\bar{\phi}_2 BB} = A_\phi^{3/2}\begin{pmatrix} 0 & u^{(3)}_{122}\\ u^{(3)}_{122} & 0\end{pmatrix},\\
\bar{\gamma}^{(4)}_{\bar{\phi}_1\bar{\phi}_1 BB} &= A_\phi^{2}\begin{pmatrix} u^{(4)}_{1111} & 0\\ 0 & u^{(4)}_{1122}\end{pmatrix},\ \bar{\gamma}^{(4)}_{\bar{\phi}_1\bar{\phi}_2 BB} = A_\phi^{2}\begin{pmatrix} 0 & u^{(4)}_{1122}\\ u^{(4)}_{1122} & 0\end{pmatrix},\\
\bar{\gamma}^{(4)}_{\bar{\phi}_2\bar{\phi}_2 BB} &= A_\phi^{2}\begin{pmatrix} u^{(4)}_{1122} & 0\\ 0 & u^{(4)}_{2222}\end{pmatrix},\\
\bar{\gamma}^{(3)}_{\bar{\phi}_1 F|F} &= A_\psi A_\phi^{1/2}\frac{h}{\sqrt{2}}\begin{pmatrix} -\varepsilon & 0\\ 0 & \varepsilon\end{pmatrix},\ \bar{\gamma}^{(3)}_{\bar{\phi}_2 F|F} = A_\psi A_\phi^{1/2}\frac{\mathrm{i}h}{\sqrt{2}}\begin{pmatrix} \varepsilon & 0\\ 0 & \varepsilon\end{pmatrix},\\
\bar{\gamma}^{(3)}_{\bar{\phi} F|F} &= A_\psi A_\phi^{1/2} h\begin{pmatrix} 0 & 0\\ 0 & \varepsilon\end{pmatrix},\ \bar{\gamma}^{(3)}_{\bar{\phi}^* F|F} = A_\psi A_\phi^{1/2} h\begin{pmatrix} -\varepsilon & 0\\ 0 & 0\end{pmatrix},
\end{aligned} \tag{4.77}$$

with

$$\begin{aligned}
u^{(3)}_{111} &= 3(2\rho)^{1/2}U'' + (2\rho)^{3/2}U^{(3)},\ u^{(3)}_{122} = (2\rho)^{1/2}U'',\\
u^{(4)}_{1111} &= 3U'' + 12\rho U^{(3)} + (2\rho)^2 U^{(4)},\ u^{(4)}_{1122} = U'' + 2\rho U^{(3)},\ u^{(4)}_{2222} = 3U''.
\end{aligned}$$

The mixed diagrams read

$$\begin{aligned}
\bar{\gamma}^{(3)}_{\bar{\psi}_1^* B|F} &= A_\psi A_\phi^{1/2}\frac{h}{\sqrt{2}}\begin{pmatrix} 0 & 0 & 0 & 1\\ 0 & 0 & 0 & \mathrm{i}\end{pmatrix},\ \bar{\gamma}^{(3)}_{BF|\bar{\psi}_1} = A_\psi A_\phi^{1/2}\frac{h}{\sqrt{2}}\begin{pmatrix} 0 & 1 & 0 & 0\\ 0 & -\mathrm{i} & 0 & 0\end{pmatrix},\\
\bar{\gamma}^{(3)}_{\bar{\psi}_1 B|F} &= A_\psi A_\phi^{1/2}\frac{h}{\sqrt{2}}\begin{pmatrix} 0 & -1 & 0 & 0\\ 0 & \mathrm{i} & 0 & 0\end{pmatrix},\ \bar{\gamma}^{(3)}_{BF|\bar{\psi}_2} = A_\psi A_\phi^{1/2}\frac{h}{\sqrt{2}}\begin{pmatrix} -1 & 0 & 0 & 0\\ \mathrm{i} & 0 & 0 & 0\end{pmatrix},
\end{aligned} \tag{4.78}$$

and

$$\begin{aligned}
\bar{\gamma}^{(3)}_{F|B\bar{\psi}_1} &= A_\psi A_\phi^{1/2}\frac{h}{\sqrt{2}}\begin{pmatrix} 0 & 0\\ 1 & -\mathrm{i}\\ 0 & 0\\ 0 & 0\end{pmatrix},\ \bar{\gamma}^{(3)}_{\bar{\psi}_1^* |FB} = A_\psi A_\phi^{1/2}\frac{h}{\sqrt{2}}\begin{pmatrix} 0 & 0\\ 0 & 0\\ 0 & 0\\ 1 & \mathrm{i}\end{pmatrix},\\
\bar{\gamma}^{(3)}_{F|B\bar{\psi}_2} &= A_\psi A_\phi^{1/2}\frac{h}{\sqrt{2}}\begin{pmatrix} -1 & \mathrm{i}\\ 0 & 0\\ 0 & 0\\ 0 & 0\end{pmatrix},\ \bar{\gamma}^{(3)}_{\bar{\psi}_1 |FB} = A_\psi A_\phi^{1/2}\frac{h}{\sqrt{2}}\begin{pmatrix} 0 & 0\\ -1 & \mathrm{i}\\ 0 & 0\\ 0 & 0\end{pmatrix}.
\end{aligned} \tag{4.79}$$

We also give the purely bosonic vertices in terms of the conjugate field basis $(\bar{\phi}, \bar{\phi}^*)$. We have

$$\hat{\bar{\gamma}}^{(3)}_{\bar{\phi}_i BB} = U\bar{\gamma}^{(3)}_{\bar{\phi}_i BB}U^t,\ \hat{\bar{\gamma}}^{(4)}_{\bar{\phi}_i\bar{\phi}_j BB} = U\bar{\gamma}^{(4)}_{\bar{\phi}_i\bar{\phi}_j BB}U^t,\ \hat{\bar{\gamma}}^{(3)}_{\bar{\phi}^{(*)}BB} = \hat{\bar{\gamma}}^{(3)}_{\bar{\phi}_1 BB} \pm \mathrm{i}\hat{\bar{\gamma}}^{(3)}_{\bar{\phi}_2 BB}. \tag{4.80}$$

We conclude that

$$\begin{aligned}
\hat{\bar{\gamma}}^{(3)}_{\bar{\phi}_1 BB} &= A_\phi^{3/2}\begin{pmatrix} u^{(3)}_{1\phi\phi} & u^{(3)}_{1\phi\phi^*} \\ u^{(3)}_{1\phi\phi^*} & u^{(3)}_{1\phi\phi}\end{pmatrix},\ \hat{\bar{\gamma}}^{(3)}_{\bar{\phi}_2 BB} = A_\phi^{3/2}\begin{pmatrix} u^{(3)}_{2\phi\phi} & 0 \\ 0 & -u^{(3)}_{2\phi\phi}\end{pmatrix}, \\
\hat{\bar{\gamma}}^{(4)}_{\bar{\phi}_1\bar{\phi}_1 BB} &= A_\phi^{2}\begin{pmatrix} u^{(4)}_{11\phi\phi} & u^{(4)}_{11\phi\phi^*} \\ u^{(4)}_{11\phi\phi^*} & u^{(4)}_{11\phi\phi}\end{pmatrix},\ \hat{\bar{\gamma}}^{(4)}_{\bar{\phi}_1\bar{\phi}_2 BB} = A_\phi^{2}\begin{pmatrix} u^{(4)}_{12\phi\phi} & 0 \\ 0 & -u^{(4)}_{12\phi\phi}\end{pmatrix}, \\
\hat{\bar{\gamma}}^{(4)}_{\bar{\phi}_2\bar{\phi}_2 BB} &= A_\phi^{2}\begin{pmatrix} u^{(4)}_{22\phi\phi} & u^{(4)}_{22\phi\phi^*} \\ u^{(4)}_{22\phi\phi^*} & -u^{(4)}_{22\phi\phi}\end{pmatrix},
\end{aligned} \tag{4.81}$$

with

$$\begin{aligned}
u^{(3)}_{1\phi\phi} &= (2\rho)^{1/2}U'' + \rho(2\rho)^{1/2}U^{(3)},\ u^{(3)}_{1\phi\phi^*} = 2(2\rho)^{1/2}U'' + \rho(2\rho)^{1/2}U^{(3)}, \\
u^{(3)}_{2\phi\phi} &= -\mathrm{i}(2\rho)^{1/2}U'',\ u^{(4)}_{11\phi\phi} = U''(\rho) + 5\rho U^{(3)} + 2\rho^2 U^{(4)}, \\
u^{(4)}_{11\phi\phi^*} &= 2U'' + 7\rho U^{(3)} + 2\rho^2 U^{(4)},\ u^{(4)}_{12\phi\phi} = -\mathrm{i}U'' - \mathrm{i}2\rho U^{(3)}, \\
u^{(4)}_{22\phi\phi} &= -U'' + \rho U^{(3)},\ u^{(4)}_{22\phi\phi^*} = 2U'' + \rho U^{(3)}.
\end{aligned} \tag{4.82}$$

Moreover, for external indices $\bar{\phi}$ or $\bar{\phi}^*$ we find

$$\begin{aligned}
\hat{\bar{\gamma}}^{(3)}_{\bar{\phi}BB} &= A_\phi^{3/2}\begin{pmatrix} u^{(3)}_{\phi\phi\phi} & u^{(3)}_{\phi\phi\phi^*} \\ u^{(3)}_{\phi\phi\phi^*} & u^{(3)}_{\phi\phi\phi^*}\end{pmatrix},\ \hat{\bar{\gamma}}^{(3)}_{\bar{\phi}^*BB} = A_\phi^{3/2}\begin{pmatrix} u^{(3)}_{\phi\phi\phi^*} & u^{(3)}_{\phi\phi\phi^*} \\ u^{(3)}_{\phi\phi\phi^*} & u^{(3)}_{\phi\phi\phi}\end{pmatrix}, \\
\hat{\bar{\gamma}}^{(4)}_{\bar{\phi}\bar{\phi}BB} &= A_\phi^{2}\begin{pmatrix} u^{(4)}_{\phi\phi\phi\phi} & u^{(4)}_{\phi\phi\phi\phi^*} \\ u^{(4)}_{\phi\phi\phi\phi^*} & u^{(4)}_{\phi\phi\phi^*\phi^*}\end{pmatrix},\quad \hat{\bar{\gamma}}^{(4)}_{\bar{\phi}\bar{\phi}^*BB} = A_\phi^{2}\begin{pmatrix} u^{(4)}_{\phi\phi\phi\phi^*} & u^{(4)}_{\phi\phi\phi^*\phi^*} \\ u^{(4)}_{\phi\phi\phi^*\phi^*} & u^{(4)}_{\phi\phi\phi\phi^*}\end{pmatrix}, \\
\hat{\bar{\gamma}}^{(4)}_{\bar{\phi}^*\bar{\phi}^*BB} &= A_\phi^{2}\begin{pmatrix} u^{(4)}_{\phi\phi\phi^*\phi^*} & u^{(4)}_{\phi\phi\phi\phi^*} \\ u^{(4)}_{\phi\phi\phi\phi^*} & u^{(4)}_{\phi\phi\phi\phi}\end{pmatrix},
\end{aligned} \tag{4.83}$$

with

$$\begin{aligned}
u^{(3)}_{\phi\phi\phi} &= \rho^{3/2}U^{(3)},\ u^{(3)}_{\phi\phi\phi^*} = 2\rho^{1/2}U'' + \rho^{3/2}U^{(3)},\ u^{(4)}_{\phi\phi\phi\phi} = \rho^2 U^{(4)}, \\
u^{(4)}_{\phi\phi\phi\phi^*} &= 3\rho U^{(3)} + \rho^2 U^{(4)},\ u^{(4)}_{\phi\phi\phi^*\phi^*} = 2U'' + 4\rho U^{(3)} + \rho^2 U^{(4)}.
\end{aligned}$$

4.2.2 Constitutive equations

In order to solve the flow equation for the effective average action in practice, we need to translate it to a set of coupled equations for correlation functions, which

is then truncated in a suitable manner. A convenient way of organizing this procedure is to start from a few *constitutive or master equations* which describe the flow of the effective potential, the inverse fermion and bosons propagator, and the Feshbach coupling, respectively. Those equations can be expressed in closed form with very few assumptions on the form of the effective action, and they hold for every choice of regulator. With appropriate projection descriptions we then arrive at flow equations for the individual running couplings $\{g_k\}$.

We start with the spin-balanced equations. The flow equation for the effective average potential $\bar{U}_k(\bar{\rho}) = \bar{\gamma}_k^{(0)}(\bar{\rho})$ takes the simple form

$$\begin{aligned}\dot{\bar{U}}_k(\bar{\rho}) &= \frac{1}{2}\mathrm{tr}\int_Q \bar{G}_\phi^Q \dot{\bar{R}}_\phi^Q - \frac{1}{2}\mathrm{tr}\int_Q \bar{G}_\psi^Q \dot{\bar{R}}_\psi^Q \\ &= \frac{1}{2}\int_Q \frac{1}{A_\phi}\frac{L_\phi^Q \dot{\bar{R}}_\phi^{-Q} + L_\phi^{-Q}\dot{\bar{R}}_\phi^Q}{\det{}_B^Q} - \int_Q \frac{1}{A_\psi}\frac{L_\psi^Q \dot{\bar{R}}_\psi^{-Q} + L_\psi^{-Q}\dot{\bar{R}}_\psi^Q}{\det{}_F^Q}. \end{aligned} \tag{4.84}$$

We write

$$\dot{\bar{U}}(\bar{\rho}) = \dot{U}^{(B)}(\rho) + \dot{U}^{(F)}(\rho) \tag{4.85}$$

to indicate the contributions from bosonic (B) and fermionic (F) diagrams, see Fig. 4.1. The flow of the renormalized effective average potential defined from $U(\rho) = \bar{U}(\bar{\rho})$ reads

$$\dot{U}(\rho) = \eta_\phi \rho U'(\rho) + \dot{U}^{(B)}(\rho) + \dot{U}^{(F)}(\rho). \tag{4.86}$$

The flow of the inverse boson propagator (assuming frequency and momentum independent vertices) reads

$$\begin{aligned}\dot{\bar{G}}^{-1}_{\bar{\phi}_i\bar{\phi}_j}(P) = &\frac{1}{2}\mathrm{tr}\int_Q \bar{G}_\phi(Q)\bar{\gamma}^{(3)}_{\bar{\phi}_i BB}\bar{G}_\phi(Q+P)\bar{\gamma}^{(3)}_{\bar{\phi}_j BB}\bar{G}_\phi(Q)\dot{\bar{R}}_\phi(Q) \\ &+ \frac{1}{2}\mathrm{tr}\int_Q \bar{G}_\phi(Q)\bar{\gamma}^{(3)}_{\bar{\phi}_j BB}\bar{G}_\phi(Q-P)\bar{\gamma}^{(3)}_{\bar{\phi}_i BB}\bar{G}_\phi(Q)\dot{\bar{R}}_\phi(Q) \\ &- \frac{1}{2}\mathrm{tr}\int_Q \bar{G}_\phi(Q)\bar{\gamma}^{(4)}_{\bar{\phi}_i\bar{\phi}_j BB}\bar{G}_\phi(Q)\dot{\bar{R}}_\phi(Q) \\ &- \frac{1}{2}\mathrm{tr}\int_Q \bar{G}_\psi(Q)\bar{\gamma}^{(3)}_{\bar{\phi}_i F|F}\bar{G}_\psi(Q+P)\bar{\gamma}^{(3)}_{\bar{\phi}_j F|F}\bar{G}_\psi(Q)\dot{\bar{R}}_\psi(Q) \\ &- \frac{1}{2}\mathrm{tr}\int_Q \bar{G}_\psi(Q)\bar{\gamma}^{(3)}_{\bar{\phi}_j F|F}\bar{G}_\psi(Q-P)\bar{\gamma}^{(3)}_{\bar{\phi}_i F|F}\bar{G}_\psi(Q)\dot{\bar{R}}_\psi(Q), \end{aligned} \tag{4.87}$$

or, in the conjugate field variables,

$$\begin{aligned}\dot{\bar{G}}^{-1}_{\bar{\phi}^*\bar{\phi}}(P) = &\frac{1}{2}\mathrm{tr}\int_Q \bar{G}_\phi(Q)\bar{\gamma}^{(3)}_{\bar{\phi}^*BB}\bar{G}_\phi(Q+P)\bar{\gamma}^{(3)}_{\bar{\phi}BB}\bar{G}_\phi(Q)\dot{\bar{R}}_\phi(Q)\\ &+\frac{1}{2}\mathrm{tr}\int_Q \bar{G}_\phi(Q)\bar{\gamma}^{(3)}_{\bar{\phi}BB}\bar{G}_\phi(Q-P)\bar{\gamma}^{(3)}_{\bar{\phi}^*BB}\bar{G}_\phi(Q)\dot{\bar{R}}_\phi(Q)\\ &-\frac{1}{2}\mathrm{tr}\int_Q \bar{G}_\phi(Q)\bar{\gamma}^{(4)}_{\bar{\phi}^*\bar{\phi}BB}\bar{G}_\phi(Q)\dot{\bar{R}}_\phi(Q)\\ &-\frac{1}{2}\mathrm{tr}\int_Q \bar{G}_\psi(Q)\bar{\gamma}^{(3)}_{\bar{\phi}^*F|F}\bar{G}_\psi(Q+P)\bar{\gamma}^{(3)}_{\bar{\phi}F|F}\bar{G}_\psi(Q)\dot{\bar{R}}_\psi(Q)\\ &-\frac{1}{2}\mathrm{tr}\int_Q \bar{G}_\psi(Q)\bar{\gamma}^{(3)}_{\bar{\phi}F|F}\bar{G}_\psi(Q-P)\bar{\gamma}^{(3)}_{\bar{\phi}^*F|F}\bar{G}_\psi(Q)\dot{\bar{R}}_\psi(Q).\end{aligned} \tag{4.88}$$

Analogous to Eq. (4.85) we split the flow into bosonic and fermionic contributions according to

$$\dot{\bar{G}}^{-1}_{\bar{\phi}_i\bar{\phi}_j} = \dot{\bar{G}}^{-1,(B)}_{\bar{\phi}_i\bar{\phi}_j} + \dot{\bar{G}}^{-1,(F)}_{\bar{\phi}_i\bar{\phi}_j}. \tag{4.89}$$

The flow of the inverse fermion propagator is given by

$$\begin{aligned}\dot{\bar{G}}^{-1}_{\bar{\psi}_A\bar{\psi}_B}(P) = &\frac{1}{2}\mathrm{tr}\int_Q \bar{G}_\phi(Q)\bar{\gamma}^{(3)}_{\bar{\psi}_AB|F}\bar{G}_\psi(Q+P)\bar{\gamma}^{(3)}_{F|B\bar{\psi}_B}\bar{G}_\phi(Q)\dot{\bar{R}}_\phi(Q)\\ &-\frac{1}{2}\mathrm{tr}\int_Q \bar{G}_\phi(Q)\bar{\gamma}^{(3)}_{BF|\bar{\psi}_B}\bar{G}_\psi(Q-P)\bar{\gamma}^{(3)}_{\bar{\psi}_A|FB}\bar{G}_\phi(Q)\dot{\bar{R}}_\phi(Q)\\ &-\frac{1}{2}\mathrm{tr}\int_Q \bar{G}_\psi(Q)\bar{\gamma}^{(3)}_{\bar{\psi}_A|FB}\bar{G}_\phi(Q+P)\bar{\gamma}^{(3)}_{BF|\bar{\psi}_B}\bar{G}_\psi(Q)\dot{\bar{R}}_\psi(Q)\\ &+\frac{1}{2}\mathrm{tr}\int_Q \bar{G}_\psi(Q)\bar{\gamma}^{(3)}_{F|B\bar{\psi}_B}\bar{G}_\phi(Q-P)\bar{\gamma}^{(3)}_{\bar{\psi}_AB|F}\bar{G}_\psi(Q)\dot{\bar{R}}_\psi(Q).\end{aligned} \tag{4.90}$$

We split the flow equation in a Tan (T) and Hartree (H) contribution via

$$\dot{\bar{G}}^{-1}_{\bar{\psi}_A\bar{\psi}_B} = \dot{\bar{G}}^{-1,(T)}_{\bar{\psi}_A\bar{\psi}_B} + \dot{\bar{G}}^{-1,(H)}_{\bar{\psi}_A\bar{\psi}_B}. \tag{4.91}$$

Here the Tan and the Hartree diagram are the loops where the regulator insertion appears in the boson and fermion line, respectively. This labelling indicates their contribution to the characteristic shape of the fermion self-energy given by the Tan contact and the Hartree shift, see the discussion in Sec. 5.1.

The flow equations for the inverse boson and fermion propagators are then most

easily parametrized by introducing

$$X_\psi^Q = \frac{(h^2\rho)^{1/2}}{A_\psi}\Big(L_\psi^Q \dot{\bar{R}}_\psi^{-Q} + L_\psi^{-Q}\dot{\bar{R}}_\psi^Q\Big), \tag{4.92}$$

$$Y_\psi^Q = \frac{1}{A_\psi}\Big((L_\psi^Q)^2 \dot{\bar{R}}_\psi^{-Q} - h^2\rho\dot{\bar{R}}_\psi^Q\Big), \tag{4.93}$$

$$X_\phi^Q = \frac{-\rho U''}{A_\phi}\Big(L_\phi^Q \dot{\bar{R}}_\phi^{-Q} + L_\phi^{-Q}\dot{\bar{R}}_\phi^Q\Big), \tag{4.94}$$

$$Y_\phi^Q = \frac{1}{A_\phi}\Big((L_\phi^Q)^2 \dot{\bar{R}}_\phi^{-Q} + (\rho U'')^2\dot{\bar{R}}_\phi^Q\Big), \tag{4.95}$$

such that

$$\bar{G}_\phi^Q \dot{\bar{R}}_\phi^Q \bar{G}_\phi^Q = \frac{1}{A_\phi}\frac{1}{\det_B^2(Q)}\begin{pmatrix} X_\phi^Q & Y_\phi^{-Q} \\ Y_\phi^Q & X_\phi^Q \end{pmatrix}, \tag{4.96}$$

$$\bar{G}_\psi^Q \dot{\bar{R}}_\psi^Q \bar{G}_\psi^Q = \frac{1}{A_\psi}\frac{1}{\det_F^2(Q)}\begin{pmatrix} X_\psi^Q\varepsilon & Y_\psi^{-Q}\mathbb{1} \\ -Y_\psi^Q\mathbb{1} & -X_\psi^Q\varepsilon \end{pmatrix}. \tag{4.97}$$

The flow of the fermion self-energy reads

$$\dot{\bar{G}}^{-1}_{\psi_1^*\psi_1}(P) = -A_\psi h^2 \int_Q \frac{Y_\phi^Q L_\psi^{Q+P}}{(\det_B^Q)^2\det_F^{Q+P}} - A_\psi h^2 \int_Q \frac{Y_\psi^Q L_\phi^{Q-P}}{(\det_F^Q)^2\det_B^{Q-P}}, \tag{4.98}$$

and the anomalous fermion self-energy flow is given by

$$\begin{aligned}\dot{\bar{G}}^{-1}_{\psi_1\psi_2}(P) = A_\psi(h^2\rho)^{3/2}U''\Bigg(&\int_Q \frac{1}{A_\phi}\frac{L_\phi^Q\dot{\bar{R}}_\phi^{-Q} + L_\phi^{-Q}\dot{\bar{R}}_\phi^Q}{(\det_B^Q)^2\det_F^{Q+P}} \\ &+ \int_Q \frac{1}{A_\psi}\frac{L_\psi^Q\dot{\bar{R}}_\psi^{-Q} + L_\psi^{-Q}\dot{\bar{R}}_\psi^Q}{(\det_F^Q)^2\det_B^{Q+P}}\Bigg).\end{aligned} \tag{4.99}$$

The flow of the Feshbach coupling $\bar{h}$ is given by

$$\dot{\bar{h}} = -A_\psi A_\phi^{1/2} h^3 U''\rho\left(\int_Q \frac{1}{A_\phi}\frac{L_\phi^Q\dot{\bar{R}}_\phi^{-Q} + L_\phi^{-Q}\dot{\bar{R}}_\phi^Q}{(\det_B^Q)^2\det_F^Q} + \int_Q \frac{1}{A_\psi}\frac{L_\psi^Q\dot{\bar{R}}_\psi^{-Q} + L_\psi^{-Q}\dot{\bar{R}}_\psi^Q}{(\det_F^Q)^2\det_B^Q}\right). \tag{4.100}$$

For the flow of the inverse boson propagator we turn to the real $(\bar{\phi}_1, \bar{\phi}_2)$-basis. The advantage of this choice is explained below. We have

$$\begin{aligned}\dot{\bar{G}}^{-1}_{\phi_2\phi_2}(P) = &-A_\phi\frac{1}{2}\int_Q \frac{(2U'' + \rho U^{(3)})(Y_\phi^Q + Y_\phi^{-Q})}{\det_B^2(Q)} \\ &+ A_\phi 2\rho(U'')^2\int_Q \frac{2\rho U'' X_\phi^Q + L_\phi^{-(Q+P)}Y_\phi^Q + L_\phi^{Q+P}Y_\phi^{-Q}}{(\det_B^Q)^2\det_B^{Q+P}} \\ &+ A_\phi h^2\int_Q \frac{2(h^2\rho)^{1/2}X_\psi^Q + L_\psi^{-(Q+P)}Y_\psi^Q + L_\psi^{Q+P}Y_\psi^{-Q}}{(\det_F^Q)^2\det_F^{Q+P}}\end{aligned} \tag{4.101}$$

for the 22-component. The tadpole diagram in the first line is momentum independent due to our choice of momentum independent vertices. The first line corrects the tadpole contribution in Eq. (B18) in Boettcher et al. [2014c]. For the 12-component we find

$$\begin{aligned}\dot{\tilde{G}}^{-1}_{\phi_1\phi_2}(P) = 2\mathrm{i}A_\phi \rho U'' \int_Q \frac{1}{(\det{}^Q_B)^2 \det{}^{Q+P}_B} \\ \times \Big[-L_\phi^{Q+P}\Big((2U''+\rho U^{(3)})X_\phi^Q + (U''+\rho U^{(3)})Y_\phi^{-Q}\Big) \\ + L_\phi^{-(Q+P)}\Big((2U''+\rho U^{(3)})X_\phi^Q + (U''+\rho U^{(3)})Y_\phi^{Q}\Big) \\ - \rho U''(2U''+\rho U^{(3)})\Big(Y_\phi^Q - Y_\phi^{-Q}\Big)\Big] \\ - \mathrm{i}A_\phi h^2 \int_Q \frac{Y_\psi^{-Q} L_\psi^{Q+P} - Y_\psi^Q L_\psi^{-(Q+P)}}{(\det{}^Q_F)^2 \det{}^{Q+P}_F}. \end{aligned} \tag{4.102}$$

We remark that for *both* the F- and B-contributions to the inverse boson propagator we have

$$\dot{\tilde{G}}^{-1}_{\phi_1\phi_2}(P) = \frac{\mathrm{i}}{2}\Big(\dot{\tilde{G}}^{-1}_{\phi^*\phi}(P) - \dot{\tilde{G}}^{-1}_{\phi^*\phi}(-P)\Big), \tag{4.103}$$

$$\dot{\tilde{G}}^{-1}_{\phi_2\phi_2}(P) = \frac{1}{2}\Big(\dot{\tilde{G}}^{-1}_{\phi^*\phi}(P) + \dot{\tilde{G}}^{-1}_{\phi^*\phi}(-P)\Big) - \frac{1}{2}\Big(\dot{\tilde{G}}^{-1}_{\phi\phi}(P) + \dot{\tilde{G}}^{-1}_{\phi\phi}(-P)\Big), \tag{4.104}$$

We now derive the constitutive equations for the effective potential and the inverse boson propagator in the presence of spin-imbalance $\delta\mu = (\mu_1 - \mu_2)/2$. Of course, the bosonic diagrams remain unchanged. We assume $A_{\psi 1} = A_{\psi 2} = A_\psi$ to keep the overall renormalization constants in the diagrams simple. We have

$$R_\psi(Q) = \begin{pmatrix} 0 & -R_\psi^{-Q} \\ R_\psi^Q & 0 \end{pmatrix} = \begin{pmatrix} 0 & 0 & -R_{\psi 1}^{-Q} & 0 \\ 0 & 0 & 0 & -R_{\psi 2}^{-Q} \\ R_{\psi 1}^Q & 0 & 0 & 0 \\ 0 & R_{\psi 2}^Q & 0 & 0 \end{pmatrix}, \tag{4.105}$$

and

$$G_\psi(Q) = \frac{1}{\det{}^Q_F}\begin{pmatrix} A & B \\ C & D \end{pmatrix} \tag{4.106}$$

with

$$A = h\phi \begin{pmatrix} 0 & \det{}^Q_{F12} \\ -\det{}^{-Q}_{F12} & 0 \end{pmatrix},\ B = \begin{pmatrix} L_{\psi 2}^{-Q}\det{}^Q_{F12} & 0 \\ 0 & L_{\psi 1}^{-Q}\det{}^{-Q}_{F12} \end{pmatrix}, \tag{4.107}$$

$$C = \begin{pmatrix} -L_{\psi 2}^{Q}\det{}^{-Q}_{F12} & 0 \\ 0 & -L_{\psi 1}^{Q}\det{}^{Q}_{F12} \end{pmatrix},\ D = h\phi \begin{pmatrix} 0 & -\det{}^{-Q}_{F12} \\ \det{}^{Q}_{F12} & 0 \end{pmatrix}. \tag{4.108}$$

We introduce the abbreviations

$$\det{}^{Q}_{F12} = L^{-Q}_{\psi 1} L^{Q}_{\psi 2} + h^2\rho,\ \det{}^{Q}_{F} = \det{}^{Q}_{F12}\det{}^{-Q}_{F12}. \tag{4.109}$$

Note that $\det{}^{-Q}_{F} = \det{}^{Q}_{F}$, but $\det{}^{-Q}_{F12} \neq \det{}^{Q}_{F12}$. In the following we will often drop the subscripts 'ψ' and 'F' to shorten the expressions.

For the flow of the effective potential we have

$$\begin{aligned}
\dot{U}^{(F)}(\rho) &= -\frac{1}{2}\mathrm{Tr}\Big(\dot{\bar{R}}_\psi \bar{G}_\psi\Big) \\
&= -\frac{1}{2}\int_Q \frac{1}{A_\psi}\frac{1}{\det{}^{Q}_{F,12}\det{}^{-Q}_{F,12}}\mathrm{tr}\begin{pmatrix} 0 & -\dot{\bar{R}}^{-Q}_{\psi} \\ \dot{\bar{R}}^{Q}_{\psi} & 0 \end{pmatrix}\begin{pmatrix} A & B \\ C & D \end{pmatrix} \\
&= -\int_Q \frac{1}{A_\psi}\frac{L^{-Q}_1 \dot{\bar{R}}^{Q}_2 + L^{Q}_2 \dot{\bar{R}}^{-Q}_1}{\det{}^{Q}_{F,12}}.
\end{aligned} \tag{4.110}$$

The derivatives are given by

$$\dot{U}^{(n),(F)}(\rho) = -n!(-h^2)^n \int_Q \frac{1}{A_\psi}\frac{L^{-Q}_1 \dot{\bar{R}}^{Q}_2 + L^{Q}_2 \dot{\bar{R}}^{-Q}_1}{(\det{}^{Q}_{F,12})^{n+1}}. \tag{4.111}$$

For the flow of the boson propagator we need the product $\bar{G}^{Q}_{\psi}\dot{\bar{R}}^{Q}_{\psi}\bar{G}^{Q}_{\psi}$. Analogous to the balanced case we define

$$X^{Q}_{\psi,12} = \frac{(h^2\rho)^{1/2}}{A_\psi}\Big(L^{Q}_{\psi 1}\dot{\bar{R}}^{-Q}_{\psi 2} + L^{-Q}_{\psi 2}\dot{\bar{R}}^{Q}_{\psi 1}\Big), \tag{4.112}$$

$$Y^{Q}_{\psi,12} = \frac{1}{A_\psi}\Big((L^{Q}_{\psi 1})^2\dot{R}^{-Q}_{\psi 2} - h^2\rho\dot{\bar{R}}^{Q}_{\psi 1}\Big), \tag{4.113}$$

$$Y^{Q}_{\psi,21} = \frac{1}{A_\psi}\Big((L^{Q}_{\psi 2})^2\dot{\bar{R}}^{-Q}_{\psi 1} - h^2\rho\dot{\bar{R}}^{Q}_{\psi 2}\Big). \tag{4.114}$$

We then arrive at

$$\begin{aligned}
\bar{G}^{Q}_{\psi}\dot{\bar{R}}^{Q}_{\psi}\bar{G}^{Q}_{\psi} &= \frac{1}{A_\psi}\frac{1}{(\det{}^{Q}_{12}\det{}^{-Q}_{12})^2} \\
&\times \begin{pmatrix} 0 & X^{Q}_{12}(\det{}^{Q}_{12})^2 & Y^{-Q}_{21}(\det{}^{Q}_{12})^2 & 0 \\ -X^{-Q}_{12}(\det{}^{-Q}_{12})^2 & 0 & 0 & Y^{-Q}_{12}(\det{}^{-Q}_{12})^2 \\ -Y^{Q}_{21}(\det{}^{-Q}_{12})^2 & 0 & 0 & -X^{-Q}_{12}(\det{}^{-Q}_{12})^2 \\ 0 & -Y^{Q}_{12}(\det{}^{Q}_{12})^2 & X^{Q}_{12}(\det{}^{Q}_{12})^2 & 0 \end{pmatrix}.
\end{aligned} \tag{4.115}$$

For the flow of the boson propagator we find

$$\begin{aligned}
\dot{\bar{G}}^{-1,(F)}_{\phi_2\phi_2}(P) &= -A_\phi\frac{1}{2}\mathrm{tr}\int_Q \frac{\mathrm{i}h}{\sqrt{2}}\begin{pmatrix}\varepsilon & 0 \\ 0 & \varepsilon\end{pmatrix} G^{Q+P}_{\psi}\frac{\mathrm{i}h}{\sqrt{2}}\begin{pmatrix}\varepsilon & 0 \\ 0 & \varepsilon\end{pmatrix}\frac{1}{A_\psi}G^{Q}_{\psi}\dot{\bar{R}}^{Q}_{\psi}G^{Q}_{\psi} \\
&\quad + \{P \to -P\} \\
&= A_\phi\frac{h^2}{2}\int_Q \frac{2h\phi X^{-Q}_{12} + Y^{Q}_{21}L^{-(Q+P)}_1 + Y^{-Q}_{12}L^{Q+P}_2}{(\det{}^{Q}_{12})^2\det{}^{Q+P}_{12}} + \{P \to -P\}.
\end{aligned} \tag{4.116}$$

In the balanced limit we reproduce the fermionic contribution in Eq. (4.101) due to $X_\psi^Q = X_\psi^{-Q}$ and $\det_F^Q = \det_F^{-Q}$. For the off-diagonal contribution we find

$$\begin{aligned}\dot{\tilde{G}}^{-1,(F)}_{\phi_1\phi_2}(P) &= -A_\phi \frac{1}{2}\mathrm{tr}\int_Q \left[\frac{h}{\sqrt{2}}\begin{pmatrix}-\varepsilon & 0\\ 0 & \varepsilon\end{pmatrix} G_\psi^{Q+P}\frac{\mathrm{i}h}{\sqrt{2}}\begin{pmatrix}\varepsilon & 0\\ 0 & \varepsilon\end{pmatrix}\right.\\ &\quad \left. + \frac{\mathrm{i}h}{\sqrt{2}}\begin{pmatrix}\varepsilon & 0\\ 0 & \varepsilon\end{pmatrix} G_\psi^{Q-P}\frac{h}{\sqrt{2}}\begin{pmatrix}-\varepsilon & 0\\ 0 & \varepsilon\end{pmatrix}\right]\frac{1}{A_\psi} G_\psi^Q \dot{\bar{R}}_\psi^Q G_\psi^Q\\ &= -A_\phi \frac{\mathrm{i}h^2}{2}\int_Q \frac{L_2^{Q+P}Y_{12}^{-Q} - L_1^{-(Q+P)}Y_{21}^Q}{(\det_{12}^Q)^2 \det_{12}^{Q+P}} - \{P\to -P\}. \end{aligned} \tag{4.117}$$

In the balanced limit we recover the fermion part of Eq. (4.102). Again we used the symmetry $\det_F^Q = \det_F^{-Q}$.

4.2.3 Derivative expansion

Given the constitutive or master equations, the flow of running couplings is obtained through suitable projection prescriptions. Here we derive the flow of the expansion coefficients of the effective potential and a apply derivative expansion of the inverse fermion and boson propagator according to

$$\bar{P}_{\psi\sigma}(Q) = Z_{\psi\sigma}\mathrm{i}q_0 + A_{\psi\sigma}q^2 + \bar{m}^2_{\psi\sigma} = A_{\psi\sigma}\Big(S_{\psi\sigma}\mathrm{i}q_0 + q^2 + m^2_{\psi\sigma}\Big), \tag{4.118}$$

$$\bar{P}_{\phi}(Q) = Z_{\phi}\mathrm{i}q_0 + \bar{V}_\phi q_0^2 + A_\phi\frac{1}{2}q^2 = A_\phi\Big(S_\phi \mathrm{i}q_0 + V_\phi q_0^2 + \frac{1}{2}q^2\Big). \tag{4.119}$$

Typically, there are several candidates for these projection of running couplings, which superficially seem equivalent within a truncation, but result in distinct flow equations. The reason for this ambiguity is that the flow equation incorporates all terms in the full effective average action, in particular all higher order terms. Therefore, when specifying a particular projection procedure, we always neglect certain higher order couplings in a particular way. The dependence of the running of couplings on the projection can be used to estimate the accuracy of a given truncation. Within a truncation which includes the most important effects, the precise projection should only result in minor modifications of observables. A strong dependence, however, signals a shortcoming of a particular truncation.

In the following derivation we assume that

$$A_{\psi 1} = A_{\psi 2} = A_\psi,\ S_{\psi 1} = S_{\psi 2} = S_\psi. \tag{4.120}$$

This is valid in the spin-balanced case and still a reasonable approximation for the slightly imbalanced case. However, for the strongly imbalanced regime (e.g. polaron physics), the propagator of the majority atoms will not be renormalized, whereas we have strong fluctuation effects on the minority species. However, we will mostly be interested in a perturbative fermion propagator with $S_\psi = A_\psi = 1$

anyway. Furthermore, our detailed presentation should allow for an extension to the more complicated scheme in a straightforward fashion.

Within a Taylor expansion scheme for the effective potential, we project the corresponding flow equation (4.84) onto the coefficients in an expansion

$$U_k(\rho) = m_\phi^2(\rho - \rho_0) + \frac{\lambda_\phi}{2}(\rho - \rho_0)^2 + \sum_{n>2} \frac{u_n}{n!}(\rho - \rho_0)^n. \tag{4.121}$$

In the symmetric regime of the flow we have $\dot{\bar{m}}_\phi^2 = \dot{\bar{U}}'(0)$. This flow equation is replaced by $\dot{\bar{\rho}}_0 = -\dot{\bar{U}}'(\bar{\rho}_0)/\bar{\lambda}_\phi$ in the ordered regime. We write $u_2 = \lambda_\phi$. We have $\bar{u}_n = \bar{U}_k^{(n)}(\bar{\rho}_{0,k})$. Accordingly, for $n \geq 2$,

$$\dot{\bar{u}}_n = \partial_t\Big(\bar{U}_k^{(n)}(\bar{\rho}_{0,k})\Big) = \dot{\bar{U}}_k^{(n)}(\bar{\rho}_0) + \bar{u}_{n+1}\dot{\bar{\rho}}_0. \tag{4.122}$$

The second term is important to obtain quantitative precision of the results. The flow of the renormalized couplings

$$m_\phi^2 = \frac{\bar{m}_\phi^2}{A_\phi},\ \rho_0 = A_\phi \bar{\rho}_0,\ u_n = \frac{\bar{u}_n}{A_\phi^n} \tag{4.123}$$

is given by

$$\dot{m}_\phi^2 = \eta_\phi m_\phi^2 + \frac{\dot{\bar{m}}_\phi^2}{A_\phi},\ \dot{\rho}_0 = -\eta_\phi \rho_0 + A_\phi \dot{\bar{\rho}}_0,\ \dot{u}_n = n\eta_\phi u_n + \frac{\dot{\bar{u}}_n}{A_\phi^n}. \tag{4.124}$$

The running couplings entering the fermion propagator are projected according to

$$\dot{\bar{m}}_{\psi\sigma}^2 = \dot{\bar{G}}^{-1}_{\psi_\sigma^*\psi_\sigma}(P, \rho_0)\Big|_{P=0,}, \tag{4.125}$$

$$\dot{Z}_\psi = \frac{1}{\mathrm{i}}\frac{\partial}{\partial p_0}\dot{\bar{G}}^{-1}_{\psi_1^*\psi_1}(P, \rho_0)\Big|_{P=0}, \tag{4.126}$$

$$\dot{A}_\psi = \frac{\partial}{\partial p^2}\dot{\bar{G}}^{-1}_{\psi_1^*\psi_1}(P, \rho_0)\Big|_{P=0} = \frac{1}{2}\frac{\partial^2}{\partial p^2}\dot{\bar{G}}^{-1}_{\psi_1^*\psi_1}(P, \rho_0)\Big|_{P=0}. \tag{4.127}$$

Similar to the expansion coefficients of the effective potential, one could first start from $\bar{m}_{\psi\sigma}^2 = \bar{G}^{-1}_{\psi_\sigma^*\psi_\sigma}(0, \bar{\rho}_0)$ and then take the t-derivative of this expression. In addition to Eq. (4.125), this generates a term proportional to $\dot{\bar{\rho}}_0$ in the ordered regime. However, we will neglect such contributions in this work. The flow of the renormalized couplings $m_{\psi\sigma}^2 = \bar{m}_{\psi\sigma}^2/A_\psi$, $S_\psi = Z_\psi/A_\psi$ reads

$$\dot{m}_{\psi\sigma}^2 = \eta_\psi m_{\psi\sigma}^2 + \frac{\dot{\bar{m}}_{\psi\sigma}^2}{A_\psi},\ \dot{S}_\psi = \eta_\psi S_\psi + \frac{\dot{Z}_\psi}{A_\psi}. \tag{4.128}$$

We write

$$\eta_\psi = \eta_\psi^{(T)} + \eta_\psi^{(H)}, \tag{4.129}$$

$$\dot{m}^2_{\psi\sigma} = \eta_\psi m^2_{\psi\sigma} + \dot{m}^{2(T)}_{\psi\sigma} + \dot{m}^{2(H)}_{\psi\sigma}, \tag{4.130}$$

$$\dot{S}_\psi = \eta_\psi S_\psi + \dot{S}_\psi^{(T)} + \dot{S}_\psi^{(H)} \tag{4.131}$$

in generalization of Eq. (4.91).

For our parametrization of the boson dynamics we employ

$$\dot{Z}_\phi = -\frac{\partial}{\partial p_0}\dot{\bar{G}}^{-1}_{\phi_1\phi_2}(P,\rho_0)\Big|_{P=0}, \tag{4.132}$$

$$\dot{\bar{V}}_\phi = \frac{\partial}{\partial p_0^2}\dot{\bar{G}}^{-1}_{\phi_2\phi_2}(P,\rho_0)\Big|_{P=0} = \frac{1}{2}\frac{\partial^2}{\partial p_0^2}\dot{\bar{G}}^{-1}_{\phi_2\phi_2}(P,\rho_0)\Big|_{P=0}, \tag{4.133}$$

$$\dot{A}_\phi = 2\frac{\partial}{\partial p^2}\dot{\bar{G}}^{-1}_{\phi_2\phi_2}(P,\rho_0)\Big|_{P=0} = \frac{\partial^2}{\partial p^2}\dot{\bar{G}}^{-1}_{\phi_2\phi_2}(P,\rho_0)\Big|_{P=0}. \tag{4.134}$$

The renormalized couplings $S_\phi = Z_\phi/A_\phi$ and $V_\phi = \bar{V}_\phi/A_\phi$ evolve according to

$$\dot{S}_\phi = \eta_\phi S_\phi + \frac{\dot{Z}_\phi}{A_\phi},\ \dot{V}_\phi = \eta_\phi V_\phi + \frac{\dot{\bar{V}}_\phi}{A_\phi}. \tag{4.135}$$

We again write

$$\eta_\phi = \eta_\phi^{(B)} + \eta_\phi^{(F)}, \tag{4.136}$$

$$\dot{S}_\phi = \eta_\phi S_\phi + \dot{S}_\phi^{(B)} + \dot{S}_\phi^{(F)}, \tag{4.137}$$

$$\dot{V}_\phi = \eta_\phi V_\phi + \dot{V}_\phi^{(B)} + \dot{V}_\phi^{(F)} \tag{4.138}$$

to distinguish bosonic from fermionic contributions within our notation.

The reason for choosing the $(\bar{\phi}_1, \bar{\phi}_2)$-basis of $\dot{\bar{G}}_\phi^{-1}$ to project onto the boson coefficients consists in the following. To be consistent with our truncation of $\bar{\rho}$-independent couplings $Z \in \{Z_\phi, \bar{V}_\phi, A_\phi\}$, we have to project them such that terms which arise from $Z'(\bar{\rho})$ are absent. In fact, if we would include the latter, we should also incorporate momentum dependent vertices which are proportional to $Z'(\bar{\rho})$. To this see let us start from the more general ansatz

$$\bar{\Gamma}_{\rm kin}[\bar{\phi}] = \int_X \frac{1}{2} Z(\bar{\rho})\Big(\bar{\phi}^* P_\phi(\partial_\tau, -\mathrm{i}\nabla)\bar{\phi} + \bar{\phi} P_\phi(-\partial_\tau, \mathrm{i}\nabla)\bar{\phi}^*\Big) \tag{4.139}$$

for the kinetic term of the bosons, where $P_\phi(Q) = \mathrm{i}q_0, q_0^2, q^2, \ldots$ is some monomial in Q. For the second functional derivative of Eq. (4.139) we obtain

$$\widehat{\bar{G}}_\phi^{-1,\{\phi,\phi^*\}}(Q,\bar{\rho}) = \begin{pmatrix} \bar{\rho}Z'(\bar{\rho})P_\phi^S(Q) & \Big(Z(\bar{\rho}) + \bar{\rho}Z'(\bar{\rho})\Big)P_\phi(-Q) \\ \Big(Z(\bar{\rho}) + \bar{\rho}Z'(\bar{\rho})\Big)P_\phi(Q) & \bar{\rho}Z'(\bar{\rho})P_\phi^S(Q) \end{pmatrix} \tag{4.140}$$

in the $(\bar{\phi}, \bar{\phi}^*)$-basis, and

$$\bar{G}_\phi^{-1,\{\phi_1,\phi_2\}}(Q,\bar{\rho}) = \begin{pmatrix} \Big(Z(\bar{\rho}) + 2\bar{\rho}Z'(\bar{\rho})\Big)P_\phi^S(Q) & \mathrm{i}\Big(Z(\bar{\rho}) + \bar{\rho}Z'(\bar{\rho})\Big)P_\phi^A(Q) \\ -\mathrm{i}\Big(Z(\bar{\rho}) + \bar{\rho}Z'(\bar{\rho})\Big)P_\phi^A(Q) & Z(\bar{\rho})P_\phi^S(Q) \end{pmatrix} \tag{4.141}$$

in the $(\bar{\phi}_1, \bar{\phi}_2)$-basis. Herein, $P_\phi^{S,A}(Q) = \frac{1}{2}(P_\phi^Q \pm P_\phi^{-Q})$ are the symmetrized and anti-symmetrized kinetic terms, respectively, see Eq. (4.59). Since the terms proportional to $Z'(\bar{\rho})$ are included in the full flow equation, they appear on the right hand side of the flow equation for $\bar{\Gamma}_k^{(2)} \sim \bar{G}_\phi^{-1}$. To avoid their influence on the beta functions, we project the coefficients $\bar{V}_\phi$, A_ϕ of the even functions $P_\phi^S(Q) = q_0^2, q^2$ from the 22-component of Eq. (4.141). Equivalently, as can be seen from Eq. (4.104), we may define them from the symmetrized part of $\bar{G}_{\phi^*\phi}$ and subtract $\bar{G}_{\phi\phi}$. The situation is less simple for Z_ϕ, which appears as the coefficient of $P_\phi^A(Q) = \mathrm{i}q_0$. No projection is preferred in this case, and we choose the 12-component. Since the overall impact of S_ϕ on the flow is rather small in 3D, this only results in small quantitative deviations. In 2D, instead, we found that changes in the projection of S_ϕ induce substantial (though only quantitative) changes.

The regulators in this work are chosen such that $\bar{R}_\phi$ depends on A_ϕ, and $\bar{R}_\psi$ is both A_ψ- and m_ψ^2-dependent. This dependence is necessary to account for the right scaling of correlation functions and to regularize around a flowing Fermi surface. Moreover, it provides for an efficient resummation of flow equations.

If we incorporate the flow of A_ψ and m_ψ^2, the fermionic regulator insertion $\dot{\bar{R}}_\psi/A_\psi$ depends linearly on both η_ψ and $\dot{m}_\psi^2$. Hence, we arrive at a set of equations

$$\begin{pmatrix} \eta_\phi \\ \dot{m}_\psi^2 \\ \eta_\psi \end{pmatrix} = \begin{pmatrix} A_0 \\ B_0 \\ C_0 \end{pmatrix} + \begin{pmatrix} A_1 & A_2 & A_3 \\ B_1 & B_2 & B_3 \\ C_1 & C_2 & C_3 \end{pmatrix} \begin{pmatrix} \eta_\phi \\ \dot{m}_\psi^2 \\ \eta_\psi \end{pmatrix}, \tag{4.142}$$

where the coefficients are one-loop integrals which depend on the remaining running couplings. The linear set is solved by

$$\begin{pmatrix} \eta_\phi \\ \dot{m}_\psi^2 \\ \eta_\psi \end{pmatrix} = \begin{pmatrix} 1-A_1 & -A_2 & -A_3 \\ -B_1 & 1-B_2 & -B_3 \\ -C_1 & -C_2 & 1-C_3 \end{pmatrix}^{-1} \begin{pmatrix} A_0 \\ B_0 \\ C_0 \end{pmatrix}. \tag{4.143}$$

The need for evaluating more one-loop integrals numerically makes an inclusion of even more couplings into $\bar{R}_\phi$ and $\bar{R}_\psi$ (e.g. S_ϕ, S_ψ, V_ψ) less attractive, although promising a further improved resummation of diagrams.

4.3 Flow equations for optimized regulators

In this section we derive the flow equations in the F, FB_0, and FB-truncations for q^2-opt regulator, both for the spin-balanced and spin-imbalanced case.

4.3.1 Derivative expansion

For purely spatial cutoffs, i.e. cutoffs which only depend on $q^2 = \vec{q}^2$, the Matsubara summation in the constitutive equations can be performed analytically. However, by interchanging the derivative projection with the Matsubara summation in those cases, the expressions become much simpler. We explain here how this particular feature can be implemented in practice, and derive the corresponding loop integral expressions for the boson propagator within the derivative expansion scheme outlined in the previous section.

The idea of how to extract the flow of running couplings from the flow of the inverse boson propagator coefficients for spatial cutoffs is simple and efficient: We write the diagram in matrix-form with the trace not yet being evaluated. Therein only $G(Q \pm P)$ depends on the external momentum P. We expand this expression in powers of p_0 and p, and can then read off the flow of the coefficient. Due to the "$G(Q+P) - G(Q-P)$"-structure of the flow equations, we often have cancellations which simplify the result.

Fermionic contributions

We first consider the balanced fermionic case. We expand

$$L_\psi^{S,Q+P} = L_\psi^{S,Q} + (1 + R_\psi^{\mathrm{x}})(2pqx + p^2) + \frac{1}{2} R_\psi^{\mathrm{xx}} (2pqx)^2, \tag{4.144}$$

$$\begin{aligned} \det{}_F^{Q+P} &= \det{}_F^S + 2S_\psi^2 q_0 p_0 + S_\psi^2 p_0^2 \\ &\quad + 2L_\psi^{S,Q} \Big((1 + R_\psi^{\mathrm{x}})(2pqx + p^2)^2 + \frac{1}{2} R_\psi^{\mathrm{xx}} (2pqx)^2 \Big) + (1 + R_\psi^{\mathrm{x}})^2 (2pqx)^2. \end{aligned} \tag{4.145}$$

Herein $\vec{p} \cdot \vec{q} = pqx$ and

$$R_\psi^{\mathrm{x}}(q^2) = \frac{\partial R_\psi}{\partial q^2}(q^2), \; R_\psi^{\mathrm{xx}}(q^2) = \frac{\partial R_\psi^{\mathrm{x}}}{\partial q^2}(q^2). \tag{4.146}$$

The terms with $Q-P$ are obtained according to $p_0 \to -p_0, \; x \to -x$. Note that in order to project onto higher coefficients $\sim p_0 p^2, \, p^4, \, \ldots$, a higher order expansion of the propagator would be necessary. In order to implement

$$\dot{Z}_\phi^{(F)} = -\frac{\partial}{\partial p_0} \dot{\bar{G}}^{-1,(F)}_{\phi_1 \phi_2} \Big|_{P=0}, \; \eta_\phi = -\frac{1}{A_\phi} \frac{\partial^2}{\partial p^2} \dot{\bar{G}}^{-1}_{\phi_2 \phi_2} \Big|_{P=0}, \; \dot{\bar{V}}_\phi = \frac{1}{2} \frac{\partial^2}{\partial p_0^2} \dot{\bar{G}}^{-1}_{\phi_2 \phi_2} \Big|_{P=0}, \tag{4.147}$$

we define

$$A^{(\pm)} = -\frac{\partial}{\partial p_0} G_\psi^{Q \pm P} \Big|_{P=0}, \; B^{(\pm)} = -\frac{\partial^2}{\partial p^2} G_\psi^{Q \pm P} \Big|_{P=0}, \; C^{(\pm)} = \frac{1}{2} \frac{\partial^2}{\partial p_0^2} G_\psi^{Q \pm P} \Big|_{P=0}. \tag{4.148}$$

Due to the Taylor expansions of L_ψ^S and $\det_F$ in Eqs. (4.144) and (4.145), the matrices A, B, C are rather simple. We have

$$\dot{S}_\phi^{(F)} = -\frac{1}{2}\int_Q \mathrm{tr}\Big(\gamma^{(3)}_{\phi_1 FF} A^{(+)} \gamma_{\phi_2 FF} + \gamma^{(3)}_{\phi_2 FF} A^{(-)} \gamma_{\phi_1 FF}\Big) \frac{1}{A_\psi} G_\psi^Q \dot{\bar{R}}_\psi^Q G_\psi^Q, \quad (4.149)$$

$$\eta_\phi^{(F)} = -\frac{1}{2}\int_Q \mathrm{tr}\Big(\gamma^{(3)}_{\phi_2 FF} B^{(+)} \gamma_{\phi_2 FF} + \gamma^{(3)}_{\phi_2 FF} B^{(-)} \gamma_{\phi_2 FF}\Big) \frac{1}{A_\psi} G_\psi^Q \dot{\bar{R}}_\psi^Q G_\psi^Q, \quad (4.150)$$

$$\dot{V}_\phi^{(F)} = -\frac{1}{2}\int_Q \mathrm{tr}\Big(\gamma^{(3)}_{\phi_2 FF} C^{(+)} \gamma_{\phi_2 FF} + \gamma^{(3)}_{\phi_2 FF} C^{(-)} \gamma_{\phi_2 FF}\Big) \frac{1}{A_\psi} G_\psi^Q \dot{\bar{R}}_\psi^Q G_\psi^Q. \quad (4.151)$$

The resulting expressions can typically be further simplified by using $S_\psi^2 q_0^2 = \det_F^Q - (L_\psi^{S,Q})^2 - \Delta^2$, which eliminates unnecessary Matsubara summations. We eventually arrive at

$$\dot{S}_\phi^{(F)} = -2h^2 S_\psi \int_Q \frac{\dot{\bar{R}}_\psi(q^2)}{A_\psi}\Big(\frac{1}{\det_F^2(Q)} - \frac{2h^2\rho}{\det_F^3(Q)}\Big), \quad (4.152)$$

$$\begin{aligned}\eta_\phi^{(F)} &= 4h^2 \int_Q \frac{\dot{\bar{R}}_\psi(q^2)}{A_\psi}\Big(\frac{1 + R_\psi^{\mathrm{x}} + 2q^2x^2 R_\psi^{\mathrm{xx}}}{\det_F^2(Q)} - \frac{4q^2x^2(1+R_\psi^{\mathrm{x}})^2 L_\psi^S(Q)}{\det_F^3(Q)}\Big) \\ &\overset{\text{opt}}{=} \frac{8h^2}{d}\int_Q \frac{\dot{\bar{R}}_\psi(q^2)}{A_\psi}\frac{q^2 R_\psi^{\mathrm{xx}}}{\det_F^2(Q)}, \end{aligned} \quad (4.153)$$

$$\dot{V}_\phi^{(F)} = -2h^2 S_\psi^2 \int_Q \frac{\dot{\bar{R}}_\psi(q^2)}{A_\psi}\frac{L_\psi^S(Q)}{\det_F^3(Q)}. \quad (4.154)$$

In the expression for the anomalous dimension we used that

$$\int_{\vec{p}} f(p^2) x^2 = \frac{1}{d}\int_{\vec{p}} f(p^2) \quad (4.155)$$

for $d = 3, 2, 1$. Moreover, in the third line we employed the fact that $(1 + R_\psi^{\mathrm{x}}) \equiv 0$ for the q^2-opt cutoff under the integral.

Now we turn to the imbalanced fermionic contributions to the boson propagator. There are two possibilities to regularize the fermions, either $R_{\psi 1} = R_{\psi 2}$ (symmetric scheme), or $R_{\psi 1} \neq R_{\psi 2}$ (asymmetric scheme), see Sec. 4.1.2.

We start with the symmetric scheme. The propagator matrix reads

$$G_\psi^Q = \frac{1}{\det_{12}^Q \det_{12}^{-Q}}\begin{pmatrix} A & B \\ C & D\end{pmatrix}, \quad (4.156)$$

with the matrices $A, \ldots, D$ given in Eqs. (4.107) and (4.108), and $\det_{12}^Q = L_{\psi 1}^{-Q} L_{\psi 2}^Q + \Delta^2$. We write

$$\begin{aligned} L_{\psi\sigma}^{Q+P} &= L_{\psi\sigma}^Q + \mathrm{i}S_\psi p_0 + (1 + R_\psi^{\mathrm{x}})(2pqx + p^2) + \frac{1}{2}R_\psi^{\mathrm{xx}}(2pqx)^2, \\ L_{\psi\sigma}^{-(Q+P)} &= L_{\psi\sigma}^{-Q} - \mathrm{i}S_\psi p_0 + (1 + R_\psi^{\mathrm{x}})(2pqx + p^2) + \frac{1}{2}R_\psi^{\mathrm{xx}}(2pqx)^2. \end{aligned} \quad (4.157)$$

It is the key ingredient of the symmetric scheme that $L^Q_{\psi 1}$ and $L^Q_{\psi 2}$ can be treated almost identically. We also have

$$\begin{aligned}\det{}^{Q+P}_{F12} &= L_{\psi 1}^{-(Q+P)} L^{Q+P}_{\psi 2} + \Delta^2 + \Big(\det{}^{Q}_{F12} - L^{-Q}_{\psi 1} L^{Q}_{\psi 2} - \Delta^2\Big),\\ \det{}^{-(Q+P)}_{F12} &= L^{Q+P}_{\psi 1} L_{\psi 2}^{-(Q+P)} + \Delta^2 + \Big(\det{}^{-Q}_{F12} - L^{Q}_{\psi 1} L^{-Q}_{\psi 2} - \Delta^2\Big).\end{aligned} \tag{4.158}$$

The remaining terms are obtained according to $p_0 \to -p_0,\ x \to -x$. After the trace has been performed we apply the simplifications

$$\begin{aligned}&L^{-Q}_{\psi 1} L^{Q}_{\psi 2} \to \det{}^{Q}_{F12} - \Delta^2,\ L^{Q}_{\psi 1} L^{-Q}_{\psi 2} \to \det{}^{-Q}_{F12} - \Delta^2,\\ &L^{Q}_{\psi 1} + L^{-Q}_{\psi 2} \to 2L^S_\psi(Q),\ L^{-Q}_{\psi 1} + L^{Q}_{\psi 2} \to 2L^S_\psi(Q).\end{aligned} \tag{4.159}$$

Note that $L^S_\psi(Q) = q^2 - \mu + R_\psi(q^2)$ in the symmetric scheme. Furthermore, for the anomalous dimensions we apply

$$\begin{aligned}S^2_\psi q_0^2 - 2\mathrm{i} S_\psi q_0 &\to \det{}^{Q}_{F12} - (L^S_\psi)^2 + \delta\mu^2 - \Delta^2,\\ S^2_\psi q_0^2 + 2\mathrm{i} S_\psi q_0 &\to \det{}^{-Q}_{F12} - (L^S_\psi)^2 + \delta\mu^2 - \Delta^2.\end{aligned} \tag{4.160}$$

We eventually arrive at

$$\dot S^{(F)}_\phi = -2h^2 S_\psi \int_Q \frac{\dot{\tilde R}_\psi(q^2)}{A_\psi}\Big(\frac{1}{(\det{}^{Q}_{F12})^2} - \frac{2h^2\rho}{(\det{}^{Q}_{F12})^3}\Big), \tag{4.161}$$

$$\begin{aligned}\eta^{(F)}_\phi &= 4h^2 \int_Q \frac{\dot{\tilde R}_\psi(q^2)}{A_\psi}\Big(\frac{1 + R^{\mathrm{x}}_\psi + 2q^2x^2 R^{\mathrm{xx}}_\psi}{(\det{}^{Q}_{12})^2} - \frac{4q^2x^2(1+R^{\mathrm{xx}}_\psi)^2 L^S_\psi(Q)}{(\det{}^{Q}_{12})^3}\Big)\\ &\overset{\text{opt}}{=} \frac{8h^2}{d}\int_Q \frac{\dot{\tilde R}_\psi(q^2)}{A_\psi}\frac{q^2 R^{\mathrm{xx}}_\psi}{(\det{}^{Q}_{12})^2},\end{aligned} \tag{4.162}$$

$$\dot V^{(F)}_\phi = -2h^2 S^2_\psi \int_Q \frac{\dot{\tilde R}_\psi(q^2)}{A_\psi}\frac{L^S_\psi(Q)}{(\det{}^{Q}_{F12})^3}. \tag{4.163}$$

We obtain the correct spin-balanced limit with $\det{}^{Q}_{12} \to \det{}^{Q}_{F}$.

For the asymmetric regularization of the fermion contribution we have to include the appropriate regulator insertion

$$\dot{\tilde R}^Q_\psi = \begin{pmatrix} 0 & 0 & -\dot{\tilde R}_{\psi 1}(q^2) & 0\\ 0 & 0 & 0 & -\dot{\tilde R}_{\psi 2}(q^2)\\ \dot{\tilde R}_{\psi 1}(q^2) & 0 & 0 & 0\\ 0 & \dot{\tilde R}_{\psi 2}(q^2) & 0 & 0\end{pmatrix}. \tag{4.164}$$

Furthermore, we have to modify Eqs. (4.157) according to

$$L^{Q+P}_{\psi\sigma} = L^Q_{\psi\sigma} + \mathrm{i} S_\psi p_0 + (1 + R^{\mathrm{x}}_{\psi\sigma})(2pqx + p^2) + \frac{1}{2} R^{\mathrm{xx}}_{\psi\sigma}(2pqx)^2. \tag{4.165}$$

The remaining steps are the same as for the symmetric scheme. However, we cannot apply $L^Q_{\psi 1} + L^{-Q}_{\psi 2} = 2L^S_\psi(Q)$. We arrive at

$$\dot{S}^{(F)}_\phi = -2h^2 S_\psi \int_Q \frac{(\dot{\tilde{R}}_{\psi 1} + \dot{\tilde{R}}_{\psi 2})}{2A_\psi}\Big(\frac{1}{(\det{}^Q_{F12})^2} - \frac{2h^2\rho}{(\det{}^Q_{F12})^3}\Big), \tag{4.166}$$

$$\begin{aligned}\eta^{(F)}_\phi = 2h^2 \int_Q \frac{1}{A_\psi}\Bigg(&\frac{\dot{\tilde{R}}_{\psi 1}(1 + R^{\mathrm{x}}_{\psi 2} + 2q^2x^2R^{\mathrm{xx}}_{\psi 2}) + \dot{\tilde{R}}_{\psi 2}(1 + R^{\mathrm{x}}_{\psi 1} + 2q^2x^2R^{\mathrm{xx}}_{\psi 1})}{(\det{}^Q_{F12})^2} \\ &- \frac{4q^2x^2[\dot{\tilde{R}}_{\psi 1}L^{-Q}_{\psi 1}(1 + R^{\mathrm{x}}_{\psi 2})^2 + \dot{\tilde{R}}_{\psi 2}L^Q_{\psi 2}(1 + R^{\mathrm{x}}_{\psi 1})^2]}{(\det{}^Q_{F12})^3}\Bigg),\end{aligned} \tag{4.167}$$

$$\dot{V}^{(F)}_\phi = -2h^2 S^2_\psi \int_Q \frac{(\dot{\tilde{R}}_{\psi 1} + \dot{\tilde{R}}_{\psi 2})}{2A_\psi}\frac{L^S_\psi(Q)}{(\det{}^Q_{F12})^3} + 2h^2 S^2_\psi \int_Q \frac{(\dot{\tilde{R}}_{\psi 1} - \dot{\tilde{R}}_{\psi 2})}{2A_\psi}\frac{\mathrm{i}S_\psi q_0 + \delta\mu}{(\det{}^Q_{F12})^3}. \tag{4.168}$$

For $R_{\psi 1} = R_{\psi 2}$ we recover the symmetric scheme.

Bosonic contributions

We now compute the contribution to the flow of A_ϕ and S_ϕ within a derivative expansion with inverse boson propagator

$$\bar{P}^Q_\phi = A_\phi\Big(\mathrm{i}S_\phi q_0 + \frac{1}{2}q^2\Big). \tag{4.169}$$

The case with additional V_ϕ-term will be discussed below. We expand $\widehat{G}^{Q\pm P}_\phi$ in powers of p_0 and p^2 by writing

$$\begin{aligned}L^{Q+P}_\phi &= L^Q_\phi + \mathrm{i}S_\phi p_0 + \Big(\frac{1}{2} + R^{\mathrm{x}}_\phi\Big)(2pqx + p^2) + \frac{1}{2}R^{\mathrm{xx}}_\phi\Big(2pqx\Big)^2, \\ \det{}^{Q+P}_B &= L^{-(Q+P)}_\phi L^{Q+P}_\phi - (\rho U'')^2 + \Big(\det{}^Q_B - L^{-Q}_\phi L^Q_\phi + (\rho U'')^2\Big).\end{aligned} \tag{4.170}$$

We then arrive at

$$\begin{aligned}\dot{S}^{(B)}_\phi = -4S_\phi\rho U'' \int_Q \frac{\dot{\tilde{R}}_\phi(q^2)}{A_\phi}\Bigg(&\frac{U'' + \rho U^{(3)}}{\det{}^2_B(Q)} \\ &+ \frac{2\rho U''[\rho U''(U'' + \rho U^{(3)}) - (2U'' + \rho U^{(3)})L^S_\phi(Q)]}{\det{}^3_B(Q)}\Bigg),\end{aligned} \tag{4.171}$$

$$\eta^{(B)}_\phi = 4\rho(U'')^2 \int_Q \frac{\dot{\tilde{R}}_\phi(q^2)}{A_\phi}\Bigg(\frac{1 + 2R^{\mathrm{x}}_\phi + 4q^2x^2R^{\mathrm{xx}}_\phi}{\det{}^2_B(Q)} - \frac{2q^2x^2(1 + 2R^{\mathrm{x}}_\phi)^2L^S_\phi(Q)}{\det{}^3_B(Q)}\Bigg). \tag{4.172}$$

In order to include the quadratic frequency term,

$$\bar{P}^Q_\phi = A_\phi\Big(V_\phi q_0^2 + \mathrm{i}S_\phi q_0 + \frac{1}{2}q^2\Big), \tag{4.173}$$

we write

$$L_\phi^Q = V_\phi q_0^2 + \mathrm{i}S_\phi q_0 + \underbrace{\frac{1}{2}q^2 + R_\phi(q^2) + U' + \rho U''}_{f_\phi} = V_\phi q_0^2 + \mathrm{i}S_\phi q_0 + f_\phi(q). \quad (4.174)$$

The determinant becomes

$$\det{}_B^Q = L_\phi^{-Q} L_\phi^Q - (\rho U'')^2 = V_\phi^2 q_0^4 + (S_\phi^2 + 2V_\phi f_\phi) q_0^2 + f_\phi^2 - (\rho U'')^2. \quad (4.175)$$

We expand

$$\begin{aligned} L_\phi^{Q+P} &= L_\phi^Q + V_\phi(2q_0p_0 + p_0^2) + \mathrm{i}S_\phi p_0 + \Big(\frac{1}{2} + R_\phi^{\mathrm{x}}\Big)(2pqx + p^2) + \frac{1}{2}R_\phi^{\mathrm{xx}}\Big(2pqx\Big)^2, \\ \det{}_B^{Q+P} &= L_\phi^{-(Q+P)} L_\phi^{Q+P} - (\rho U'')^2 + \Big(\det{}_B^Q - L_\phi^{-Q} L_\phi^Q + (\rho U'')^2\Big). \end{aligned} \quad (4.176)$$

This results in

$$\begin{aligned} \dot{S}_\phi^{(B)} &= -4S_\phi \rho U'' \int_Q \frac{\dot{\tilde{R}}_\phi(q^2)}{A_\phi} \Bigg(\frac{U'' + \rho U^{(3)}}{\det{}_B^2(Q)} \\ &\quad + \frac{2\rho U''[\rho U''(U'' + \rho U^{(3)}) - (2U'' + \rho U^{(3)}) L_\phi^S(Q)]}{\det{}_B^3(Q)} \Bigg), \end{aligned} \quad (4.177)$$

$$\eta_\phi^{(B)} = 4\rho(U'')^2 \int_Q \frac{\dot{\tilde{R}}_\phi(q^2)}{A_\phi} \Bigg(\frac{1 + 2R_\phi^{\mathrm{x}} + 4q^2x^2R_\phi^{\mathrm{xx}}}{\det{}_B^2(Q)} - \frac{2q^2x^2(1 + 2R_\phi^{\mathrm{x}})^2 L_\phi^S(Q)}{\det{}_B^3(Q)} \Bigg), \quad (4.178)$$

$$\begin{aligned} \dot{V}_\phi^{(B)} &= 4\rho(U'')^2 \int_Q \frac{\dot{\tilde{R}}_\phi}{A_\phi} \Bigg(\frac{3V_\phi}{\det{}_B^2(Q)} - \frac{(S_\phi^2 + 4V_\phi f_\phi) V_\phi q_0^2}{\det{}_B^3(Q)} \\ &\quad + \frac{4V_\phi \rho^2 (U'')^2 - S_\phi^2 f_\phi - 4V_\phi f_\phi^2}{\det{}_B^3(Q)} \Bigg). \end{aligned} \quad (4.179)$$

The flow equations for S_ϕ and η_ϕ formally agree with the results obtained without V_ϕ-term in Eqs. (4.171) and (4.172), respectively. However, in the present context, the right hand side depends on V_ϕ. As a consequence, we immediately see that we obtain the beta functions from above for $V_\phi \to 0$. In order to compare these equations with the ones derived by Floerchinger and Wetterich [2008] we adapt the notation $f_\phi = k^2 + 2\lambda\rho_0$, $U'' = \lambda$, and set $U^{(3)} = 0$, $1 + 2R_\phi = 0$. The determinant is given by $\det_B = V^2 q_0^4 + (S^2 + 2Vk^2 + 2V\lambda\rho_0) q_0^2 + k^4 + 2k^2\lambda\rho_0$. We then find that the equations for S_ϕ, η_ϕ, and V_ϕ indeed agree with Eqs. (D1) in Floerchinger and Wetterich [2008]. This also serves as an independent check of the beta functions in the latter reference.

4.3.2 Loop integration

For displaying the Matsubara summations we set

$$k = 1 \tag{4.180}$$

to simplify the notation. The overall prefactor of threshold functions can be determined from canonical power counting, and is often not needed when implementing the flow equations in terms of dimensionless running couplings.

Fermionic Matsubara sums

For fermionic Matsubara frequencies we have

$$\mathcal{F}_1(z) = T\sum_{n,F}\frac{1}{\omega_n^2+z^2} = \frac{1}{z}\Big(\frac{1}{2}-\tilde{N}_F(z)\Big), \tag{4.181}$$

$$\mathcal{F}_2(z) = T\sum_{n,F}\frac{1}{(\omega_n^2+z^2)^2} = \frac{1}{2z^3}\Big(\frac{1}{2}-\tilde{N}_F(z)+z\tilde{N}_F'(z)\Big), \tag{4.182}$$

$$\mathcal{F}_3(z) = T\sum_{n,F}\frac{1}{(\omega_n^2+z^2)^3} = \frac{3}{8z^5}\Big(\frac{1}{2}-\tilde{N}_F(z)+z\tilde{N}_F'(z)-\frac{z^2}{3}\tilde{N}_F''(z)\Big) \tag{4.183}$$

with

$$\tilde{N}_F(z) = \begin{cases} 0 & T=0, \\ (e^{z/T}+1)^{-1} & T>0 \end{cases}. \tag{4.184}$$

To simplify the nonthermal beta functions we set $\tilde{N}_F = 0$ at zero temperature. Still, the limit $T \to 0$ with $N_F(z) \to \theta(-z)$ gives the same result. This can also be verified explicitly in the numerics.

The fermionic Matsubara summations in the spin-imbalanced case are most easily parametrized by

$$f_\sigma = L_\sigma^S(Q) = q^2 - \mu_\sigma + R_\sigma(q^2). \tag{4.185}$$

For instance, the flow of the effective potential is given by

$$\dot{U}^{(F)}(\rho) = -\int_Q \frac{L_1^{-Q}\dot{R}_2 + L_2^Q\dot{R}_1}{\det_{F12}^Q} = -\int_Q \frac{\mathrm{i}q_0(\dot{R}_1-\dot{R}_2)+\dot{R}_1 f_2+\dot{R}_2 f_1}{q_0^2+\mathrm{i}q_0(f_1-f_2)+f_1f_2+h^2\rho}. \tag{4.186}$$

This is a Matsubara summation of the type

$$T\sum_{n,F}\frac{1}{\omega_n^2+\mathrm{i}\omega_n x+y} = T\sum_{n,F}h(\mathrm{i}\omega_n) \tag{4.187}$$

with $x = f_1 - f_2$, $y = f_1f_2 + h^2\rho$, and

$$h(z) = \frac{1}{-z^2+zx+y} = \frac{-1}{(z-z_1)(z-z_2)}. \tag{4.188}$$

We parametrize this according to

$$\begin{aligned} z_1 &= \sqrt{\frac{(f_1+f_2)^2}{4}+h^2\rho}+\frac{f_1-f_2}{2}, \\ z_2 &= -\sqrt{\frac{(f_1+f_2)^2}{4}+h^2\rho}+\frac{f_1-f_2}{2}. \\ z_1-z_2 &= 2\sqrt{\frac{(f_1+f_2)^2}{4}+h^2\rho}. \end{aligned} \tag{4.189}$$

We have

$$T\sum_{n,F}\frac{(\mathrm{i}q_0)^s}{\mathrm{det}^Q_{F12}} \overset{(*)}{=} \frac{1}{z_1-z_2}\left(\frac{z_1^s+z_2^s}{2}-z_1^s\tilde{N}_F(z_1)-z_2^s\tilde{N}_F(-z_2)\right). \tag{4.190}$$

The (*) indicates that for $s>1$ the formula only serves for generating convergent expressions with higher powers of det_{F12} in the denominator. Moreover, for odd s the sum is understood as the principal value, and yields zero for the balanced limit. Higher orders in the determinant are found from the recursion relations

$$T\sum_{n,F}\frac{(\mathrm{i}q_0)^s}{(\mathrm{det}^Q_{F,12})^2} = -\frac{\partial^2}{\partial z_1\partial z_2}T\sum_{n,F}\frac{(\mathrm{i}q_0)^s}{\mathrm{det}^Q_{F,12}}, \tag{4.191}$$

$$T\sum_{n,F}\frac{(\mathrm{i}q_0)^s}{(\mathrm{det}^Q_{F,12})^3} = \frac{-1}{4}\frac{\partial^2}{\partial z_1\partial z_2}T\sum_{n,F}\frac{(\mathrm{i}q_0)^s}{(\mathrm{det}^Q_{F,12})^2}. \tag{4.192}$$

We obtain

$$\begin{aligned} T\sum_{n,F}\frac{1}{(\mathrm{det}^Q_{F,12})^2} &= \frac{2}{(z_1-z_2)^3}\Big(1-\tilde{N}_F(z_1)-\tilde{N}_F(-z_2)\Big) \\ &\quad+\frac{1}{(z_1-z_2)^2}\Big(\tilde{N}'_F(z_1)+\tilde{N}'_F(-z_2)\Big), \end{aligned} \tag{4.193}$$

and

$$\begin{aligned} T\sum_{n,F}\frac{\mathrm{i}q_0}{(\mathrm{det}^Q_{F,12})^2} &= \frac{2}{(z_1-z_2)^3}\Big(\frac{z_1+z_2}{2}-z_1\tilde{N}_F(z_1)-z_2\tilde{N}_F(-z_2)\Big) \\ &\quad+\frac{1}{(z_1-z_2)^2}\Big(\tilde{N}_F(z_1)-\tilde{N}_F(-z_2)+z_1\tilde{N}'_F(z_1)+z_2\tilde{N}'_F(-z_2)\Big). \end{aligned} \tag{4.194}$$

The expressions involving $\mathrm{det}^3_{F12}(Q)$ in the denominator can be easily derived with a computer algebra system.

Bosonic Matsubara sums

For bosons in the B_0-truncation, we have

$$\mathcal{B}_1(z) = T\sum_{n,B}\frac{1}{\omega_n^2+z^2} = \frac{1}{z}\Big(\frac{1}{2}+\tilde{N}_B(z)\Big), \tag{4.195}$$

$$\mathcal{B}_2(z) = T\sum_{n,B}\frac{1}{(\omega_n^2+z^2)^2} = \frac{1}{2z^3}\Big(\frac{1}{2}+\tilde{N}_B(z)-z\tilde{N}_B'(z)\Big), \tag{4.196}$$

$$\mathcal{B}_3(z) = T\sum_{n,B}\frac{1}{(\omega_n^2+z^2)^3} = \frac{3}{8z^5}\Big(\frac{1}{2}+\tilde{N}_B(z)-z\tilde{N}_B'(z)+\frac{z^2}{3}\tilde{N}_B''(z)\Big), \tag{4.197}$$

with

$$\tilde{N}_B(z) = \begin{cases} 0 & T=0, \\ (e^{z/\tilde{T}}-1)^{-1} & T>0 \end{cases}. \tag{4.198}$$

In the B-truncation we need sums of the type

$$T\sum_{n,B}\frac{1}{\det{}_B^Q} = T\sum_{n,B}\frac{1}{S_\phi^2\omega_n^2+(V_\phi\omega_n^2+a)(V_\phi\omega_n^2+b)} \tag{4.199}$$

with $a=1+\omega_1$ and $b=1+\omega_1+2\omega_2$. We define

$$\begin{aligned}
z_1 &= \left(\frac{S_\phi^2+V_\phi(a+b)}{2V_\phi^2}+\sqrt{\frac{S_\phi^4+2S_\phi^2V_\phi(a+b)+V_\phi^2(a-b)^2}{4V_\phi^4}}\right)^{1/2} \xrightarrow{V_\phi\to 0} \frac{S_\phi}{V_\phi}, \\
z_2 &= -z_1 \to -\frac{S_\phi}{V_\phi}, \\
z_3 &= \left(\frac{S_\phi^2+V_\phi(a+b)}{2V_\phi^2}-\sqrt{\frac{S_\phi^4+2S_\phi^2V_\phi(a+b)+V_\phi^2(a-b)^2}{4V_\phi^4}}\right)^{1/2} \xrightarrow{V_\phi\to 0} \frac{\sqrt{ab}}{S_\phi}, \\
z_4 &= -z_3 \to -\frac{\sqrt{ab}}{S_\phi},
\end{aligned} \tag{4.200}$$

which are the poles of $h(z)=h(\mathrm{i}\omega_n)$ which we sums over. Note that $V_\phi z_1 \to S_\phi$ remains finite for $V_\phi \to 0$. Furthermore we introduce

$$\det{}_V = V_\phi^2(z_1^2-z_3^2) = \sqrt{S_\phi^4+2S_\phi^2V_\phi(a+b)+V_\phi^2(a-b)^2} \to S_\phi^2. \tag{4.201}$$

In order to present the results we write

$$\ell_V^{(n,m)} \equiv \ell_V^{(n,m)}(T,\omega_1,\omega_2,S_\phi,V_\phi) = T\sum_{n',B}\frac{(\omega_{n'}^2)^n}{\det_B(Q)^m}. \tag{4.202}$$

We then have

$$\ell_V^{(0,1)} = \frac{-1}{\det_V}\Big(\mathcal{B}_1(z_1) - \mathcal{B}_1(z_3)\Big), \tag{4.203}$$

$$\ell_V^{(0,2)} = \frac{2V_\phi^2}{\det_V^3}\Big(\mathcal{B}_1(z_1) - \mathcal{B}_1(z_3)\Big) + \frac{1}{\det_V^2}\Big(\mathcal{B}_2(z_1) + \mathcal{B}_2(z_3)\Big), \tag{4.204}$$

$$\begin{aligned}\ell_V^{(0,3)} = {} & \frac{-6V_\phi^4}{\det_V^5}\Big(\mathcal{B}_1(z_1) - \mathcal{B}_1(z_3)\Big) - \frac{3V_\phi^2}{\det_V^4}\Big(\mathcal{B}_2(z_1) + \mathcal{B}_2(z_3)\Big) \\ & - \frac{1}{\det_V^3}\Big(\mathcal{B}_3(z_1) - \mathcal{B}_3(z_3)\Big).\end{aligned} \tag{4.205}$$

For the expressions with ω_n^2 or ω_n^4 in the numerator we have

$$\ell_V^{(1,1)} = \frac{1}{\det_V}\Big(z_1^2\mathcal{B}_1(z_1) - z_3^2\mathcal{B}_1(z_3)\Big), \tag{4.206}$$

$$\begin{aligned}\ell_V^{(1,2)} = {} & \frac{-2V_\phi^2}{\det_V^3}\Big(z_1^2\mathcal{B}_1(z_1) - z_3^2\mathcal{B}_1(z_3)\Big) + \frac{1}{\det_V^2}\Big(\mathcal{B}_1(z_1) \\ & + \mathcal{B}_1(z_3) - z_1^2\mathcal{B}_2(z_1) - z_3^2\mathcal{B}_2(z_3)\Big),\end{aligned} \tag{4.207}$$

$$\begin{aligned}\ell_V^{(1,3)} = {} & \frac{6V_\phi^4}{\det_V^5}\Big(z_1^2\mathcal{B}_1(z_1) - z_3^2\mathcal{B}_1(z_3)\Big) - \frac{3V_\phi^2}{\det_V^4}\Big(\mathcal{B}_1(z_1) + \mathcal{B}_1(z_3) - z_1^2\mathcal{B}_2(z_1) \\ & - z_3^2\mathcal{B}_2(z_3)\Big) - \frac{1}{\det_V^3}\Big(\mathcal{B}_2(z_1) - \mathcal{B}_2(z_3) - z_1^2\mathcal{B}_3(z_1) + z_3^2\mathcal{B}_3(z_3)\Big),\end{aligned} \tag{4.208}$$

and

$$\ell_V^{(2,1)} \overset{*}{=} \frac{-1}{\det_V}\Big(z_1^4\mathcal{B}_1(z_1) - z_3^4\mathcal{B}_1(z_3)\Big), \tag{4.209}$$

$$\begin{aligned}\ell_V^{(2,2)} = {} & \frac{2V_\phi^2}{\det_V^3}\Big(z_1^4\mathcal{B}_1(z_1) - z_3^4\mathcal{B}_1(z_3)\Big) \\ & - \frac{1}{\det_V^2}\Big(2z_1^2\mathcal{B}_1(z_1) + 2z_3^2\mathcal{B}_1(z_3) - z_1^4\mathcal{B}_2(z_1) - z_3^4\mathcal{B}_2(z_3)\Big),\end{aligned} \tag{4.210}$$

$$\begin{aligned}\ell_V^{(2,3)} = {} & \frac{-6V_\phi^4}{\det_V^5}\Big(z_1^4\mathcal{B}_1(z_1) - z_3^4\mathcal{B}_1(z_3)\Big) \\ & + \frac{3V_\phi^2}{\det_V^4}\Big(2z_1^2\mathcal{B}_1(z_1) + 2z_3^2\mathcal{B}_1(z_3) - z_1^4\mathcal{B}_2(z_1) - z_3^4\mathcal{B}_2(z_3)\Big) \\ & - \frac{1}{\det_V^3}\Big(\mathcal{B}_1(z_1) - \mathcal{B}_1(z_3) - 2z_1^2\mathcal{B}_2(z_1) + 2z_3^2\mathcal{B}_2(z_3) + z_1^4\mathcal{B}_3(z_1) - z_3^4\mathcal{B}_3(z_3)\Big).\end{aligned} \tag{4.211}$$

The asterisk $(*)$ indicates that the sum is not convergent and only serves to generate higher moments.

Fermionic momentum integrals

The q^2-opt fermion cutoff is given by

$$\begin{aligned}\bar{R}_\psi(q^2) &= A_\psi k^2 r_\psi(z),\\ \frac{\dot{\bar{R}}_\psi(q^2)}{A_\psi} &= -\eta_\psi R_\psi + \dot{R}_\psi,\ \dot{R}_\psi(q^2) = 2k^2\mathrm{sgn}(z)\theta(1-|z|),\end{aligned} \tag{4.212}$$

with $z = (q^2-\mu)/k^2$ and

$$\begin{aligned}r_\psi(z) &= (\mathrm{sgn}(z)-z)\theta(1-|z|),\\ r'_\psi(z) &= -\theta(1-|z|),\\ r''_\psi(z) &= \mathrm{sgn}(z)\delta(1-|z|).\end{aligned} \tag{4.213}$$

We have $R_\psi^{\mathrm{xx}} = (1/k^2)r''_\psi(z)$. For simplicity we neglect the renormalization of the fermion propagator in the following, i.e. $m_\psi^2 = -\mu$, and $A_\psi = S_\psi = 1$. From the computations presented here the generalization should be straightforward. The computation employs that due to the overall $\dot{\bar{R}}_\psi$ we effectively have

$$L_\psi^S(Q) = q^2 - \mu + R_\psi(q^2) = k^2(z + r_\psi(z)) \overset{\mathrm{eff}}{\equiv} k^2\mathrm{sgn}(z). \tag{4.214}$$

For $n \in \mathbb{N}_0$ we then find

$$\int_{\vec{q}} \dot{R}_\psi(q^2)(L_\psi^S)^{2n} = \frac{8v_d k^{d+2+4n}}{d}\ell_2(\tilde{\mu}), \tag{4.215}$$

$$\int_{\vec{q}} \dot{R}_\psi(q^2)(L_\psi^S)^{2n+1} = \frac{8v_d k^{d+2+2(2n+1)}}{d}\ell_1(\tilde{\mu}), \tag{4.216}$$

$$\int_{\vec{q}} \dot{R}_\psi(q^2)q^2x^2r''_\psi(z)(L_\psi^S)^{2n} = \frac{2v_d k^{d+4+4n}}{d}\ell_3(\tilde{\mu}), \tag{4.217}$$

$$\int_{\vec{q}} \dot{R}_\psi(q^2)q^2x^2r''_\psi(z)(L_\psi^S)^{2n+1} = \frac{2v_d k^{d+4+2(2n+1)}}{d}\ell_1(\tilde{\mu}), \tag{4.218}$$

where $\tilde{\mu} = \mu/k^2$, and we introduce the threshold functions

$$\ell_1(x) \equiv \ell(x) = \theta(x+1)(x+1)^{d/2} - \theta(x-1)(x-1)^{d/2}, \tag{4.219}$$

$$\ell_2(x) \equiv \ell_S(x) = \theta(x+1)(x+1)^{d/2} - \theta(x)2x^{d/2} + \theta(x-1)(x-1)^{d/2}, \tag{4.220}$$

$$\ell_3(x) \equiv \ell_\eta(x) = \theta(x+1)(x+1)^{d/2} + \theta(x-1)(x-1)^{d/2}. \tag{4.221}$$

We define

$$v_d = \frac{1}{2^{d+1}\pi^{d/2}\Gamma(d/2)},\ v_1 = \frac{1}{4\pi},\ v_2 = \frac{1}{8\pi},\ v_3 = \frac{1}{8\pi^2}. \tag{4.222}$$

Proofs. We now perform the explicit calculation. We have

$$\begin{aligned}
&\int_{\vec{q}} \dot{R}_\psi(q^2)(L_\psi^S)^{2n} = 4v_d k^{d+2+4n} \int_{-\tilde{\mu}}^{\infty} \mathrm{d}z (z+\tilde{\mu})^{d/2-1} \mathrm{sgn}(z)\theta(1-|z|) \\
&= 4v_d k^{d+2+4n} \Big\{ \theta(-\tilde{\mu}) \int_{-\tilde{\mu}}^{\infty} \mathrm{d}z (z+\tilde{\mu})^{d/2-1} \theta(1-z) \\
&- \theta(\tilde{\mu}) \int_{-\tilde{\mu}}^{0} \mathrm{d}z (z+\tilde{\mu})^{d/2-1} \theta(1+z) + \theta(\tilde{\mu}) \int_{0}^{\infty} \mathrm{d}z (z+\tilde{\mu})^{d/2-1} \theta(1-z) \Big\} \\
&= 4v_d k^{d+2+4n} \Big\{ \theta(-\tilde{\mu})\theta(\tilde{\mu}+1) \frac{2}{d} (\tilde{\mu}+1)^{d/2} - \theta(\tilde{\mu})\theta(\tilde{\mu}-1) \frac{2}{d} \Big[\tilde{\mu}^{d/2} - (\tilde{\mu}-1)^{d/2} \Big] \\
&- \theta(\tilde{\mu})\theta(1-\tilde{\mu}) \frac{2}{d} \tilde{\mu}^{d/2} + \theta(\tilde{\mu}) \frac{2}{d} \Big[(\tilde{\mu}+1)^{d/2} - \tilde{\mu}^{d/2} \Big] \Big\}
\end{aligned} \tag{4.223}$$

Now we employ some standard tricks which are common to all the following calculations. First we drop the $\theta(\tilde{\mu})$ in the second term since $\tilde{\mu} > 1$ always implies $\tilde{\mu} > 0$:

$$\theta(\tilde{\mu})\theta(\tilde{\mu}-1) \equiv \theta(\tilde{\mu}-1). \tag{4.224}$$

Moreover, in the (first part of the) fourth term we introduce the term $\theta(\tilde{\mu}+1)$ by hand, because $\tilde{\mu} > -1$ is surely satisfied for $\tilde{\mu} > 0$:

$$\theta(\tilde{\mu}) \equiv \theta(\tilde{\mu})\theta(\tilde{\mu}+1). \tag{4.225}$$

Then we can combine the first term with the first part of the fourth term since

$$\theta(-\tilde{\mu}) + \theta(\tilde{\mu}) \equiv 1. \tag{4.226}$$

The first two parts containing $\tilde{\mu}^{d/2}$ can be combined due to $\theta(1-\tilde{\mu})+\theta(\tilde{\mu}-1) \equiv 1$. We eventually arrive at

$$\begin{aligned}
&\int_{\vec{q}} \dot{R}_\psi(q^2)(L_\psi^S)^{2n} = \frac{8v_d k^{d+2+4n}}{d} \Big\{ \Big[\theta(-\tilde{\mu}) + \theta(\tilde{\mu}) \Big] \theta(\tilde{\mu}+1)(\tilde{\mu}+1)^{d/2} \\
&+ \theta(\tilde{\mu}-1)(\tilde{\mu}-1)^{d/2} - \Big[\theta(\tilde{\mu}-1) + \theta(1-\tilde{\mu}) \Big] \theta(\tilde{\mu}) \tilde{\mu}^{d/2} - \theta(\tilde{\mu}) \tilde{\mu}^{d/2} \Big\}.
\end{aligned} \tag{4.227}$$

This agrees with Eq. (4.215). In a similar fashion we can compute the integral involving an odd power of L_ψ^S. Since there is an additional $\mathrm{sgn}(z)$–term, the $\tilde{\mu}^{d/2}$–terms cancel out.

For the integrals involving $r_\psi''(z)$ we need a smeared out step function. For instance, we can employ

$$\theta_\varepsilon(y) = \frac{1}{e^{-y/\varepsilon}+1}, \ \delta_\varepsilon(y) = \theta_\varepsilon'(y). \tag{4.228}$$

We can then apply the formula

$$\delta_\varepsilon(y)f(y,\theta_\varepsilon(y)) \stackrel{\varepsilon\to 0}{\longrightarrow} \delta(y)\int_0^1 \mathrm{d}u f(0,u), \tag{4.229}$$

which is valid for continuous f, for $f(y,u)=u$, i.e.

$$\delta_\varepsilon(1\pm z)\theta_\varepsilon(1\pm z)(z+\tilde{\mu})^{d/2} \to \frac{1}{2}\delta(1\pm z)(\tilde{\mu}\mp 1)^{d/2}. \tag{4.230}$$

Moreover, we replace $x^2 \to x_d^2 = 1/d$, see Eq. (4.155). We then find

$$\begin{aligned}
&\frac{d}{v_d k^{d+4+4n}}\int_{\vec{q}} \dot{R}_\psi(q^2)q^2x^2r_\psi''(z)(L_\psi^S)^{2n} = 4\int_{-\tilde{\mu}}^\infty \mathrm{d}z(z+\tilde{\mu})^{d/2}\theta(1-|z|)\delta(1-|z|)\\
&= 4\Big\{\theta(-\tilde{\mu})\int_{-\tilde{\mu}}^\infty \mathrm{d}z(z+\tilde{\mu})^{d/2}\theta(1-z)\delta(1-z)\\
&+\theta(\tilde{\mu})\int_{-\tilde{\mu}}^0 \mathrm{d}z(z+\tilde{\mu})^{d/2}\theta(1+z)\delta(1+z)\\
&+\theta(\tilde{\mu})\int_0^\infty \mathrm{d}z(z+\tilde{\mu})^{d/2}\theta(1-z)\delta(1-z)\Big\}\\
&= 2\Big\{\theta(-\tilde{\mu})\theta(\tilde{\mu}+1)(\tilde{\mu}+1)^{d/2}+\theta(\tilde{\mu})\theta(\tilde{\mu}-1)(\tilde{\mu}-1)^{d/2}+\theta(\tilde{\mu})(\tilde{\mu}+1)^{d/2}\Big\}.
\end{aligned} \tag{4.231}$$

We apply again the tricks from above to arrive at Eq. (4.217). For the integral involving an odd power of L_ψ^S we get a minus sign in front of the term which produces $\theta(\tilde{\mu}-1)(\tilde{\mu}-1)^{d/2}$. For this reason we arrive at $\ell_1(\tilde{\mu})$ instead of $\ell_3(\tilde{\mu})$.

Bosonic momentum integrals

The q^2-opt boson regulator reads

$$\begin{aligned}
\dot{\tilde{R}}_\phi(q^2) &= A_\phi k^2 r_\phi(y),\\
\frac{\dot{\tilde{R}}_\phi(q^2)}{A_\phi} &= -\eta_\phi R_\phi + \dot{R}_\phi = k^2\Big(-\eta_\phi(1-y)+2\Big)\theta(1-y),
\end{aligned} \tag{4.232}$$

with $y = q^2/2k^2$ and

$$\begin{aligned}
r_\phi(y) &= (1-y)\theta(1-y),\\
r_\phi'(y) &= -\theta(1-y),\\
r_\phi''(y) &= \delta(1-y).
\end{aligned} \tag{4.233}$$

Note that $R_\phi^{\mathrm{xx}}(q^2) = (1/4k^2)r_\phi''(y)$. We find

$$\int_{\vec{q}} \frac{\dot{\tilde{R}}_\phi(q^2)}{A_\phi} = \frac{8v_d 2^{d/2}k^{d+2}}{d}\Big(1-\frac{\eta_\phi}{d+2}\Big), \tag{4.234}$$

$$\int_{\vec{q}} \frac{\dot{\tilde{R}}_\phi(q^2)}{A_\phi} q^2x^2R_\phi^{\mathrm{xx}}(q^2) = \frac{v_d 2^{d/2}k^{d+2}}{d}. \tag{4.235}$$

The proof of the formulas is a simple application of

$$\int_0^\infty \mathrm{d}y y^{d/2-1}\theta(1-y) = \frac{2}{d},\ \int_0^\infty \mathrm{d}y y^{d/2}\theta(1-y)\delta(1-y) = \frac{1}{2}. \tag{4.236}$$

For the second integral we again need to smear out the step function, see the discussion of the fermionic case.

4.3.3 Flow equations

We now explicitly display the beta functions for the q^2-opt regulator in the F, FB_0, and FB-truncations. For this purpose we introduce threshold functions $\ell_F^{(n,m)}$ and $\ell_B^{(n,m)}$ which allow for particularly short expressions.

Threshold functions

For the fermionic diagrams we define

$$\int_Q \dot{R}_\psi \frac{(L_\psi^S)^n}{(\det{}_F^Q)^m} = \frac{8v_d k^{d+4+2n-4m}}{d}\ell_F^{(n,m)}(\tilde{\mu},\tilde{T},\omega_3), \tag{4.237}$$

$$\int_Q \dot{R}_\psi q^2 R_\psi^{\mathrm{xx}} \frac{(L_\psi^S)^n}{(\det{}_F^Q)^m} = 2v_d k^{d+4+2n-4m}\ell_{F,\mathrm{xx}}^{(n,m)}(\tilde{\mu},\tilde{T},\omega_3), \tag{4.238}$$

where

$$\ell_F^{(n,m)}(\tilde{\mu},\tilde{T},\omega_3) = \begin{cases} \ell_1(\tilde{\mu})\mathcal{F}_m(\sqrt{1+\omega_3}), & n \text{ odd}, \\ \ell_2(\tilde{\mu})\mathcal{F}_m(\sqrt{1+\omega_3}), & n \text{ even} \end{cases}, \tag{4.239}$$

$$\ell_{F,\mathrm{xx}}^{(n,m)}(\tilde{\mu},\tilde{T},\omega_3) = \begin{cases} \ell_1(\tilde{\mu})\mathcal{F}_m(\sqrt{1+\omega_3}), & n \text{ odd}, \\ \ell_3(\tilde{\mu})\mathcal{F}_m(\sqrt{1+\omega_3}), & n \text{ even} \end{cases}, \tag{4.240}$$

and

$$\tilde{\mu} = \frac{\mu}{k^2},\ \tilde{T} = \frac{T}{k^2},\ \omega_1 = \frac{U'}{k^2},\ \omega_2 = \frac{\rho U''}{k^2}, \omega_3 = \frac{h^2\rho}{k^4}. \tag{4.241}$$

We recall that the functions $\ell_1(x), \ell_2(x), \ell_3(x)$ are given by

$$\ell_1(x) \equiv \ell(x) = \theta(x+1)(x+1)^{d/2} - \theta(x-1)(x-1)^{d/2}, \tag{4.242}$$

$$\ell_2(x) \equiv \ell_S(x) = \theta(x+1)(x+1)^{d/2} - \theta(x)2x^{d/2} + \theta(x-1)(x-1)^{d/2}, \tag{4.243}$$

$$\ell_3(x) \equiv \ell_\eta(x) = \theta(x+1)(x+1)^{d/2} + \theta(x-1)(x-1)^{d/2}. \tag{4.244}$$

For the bosonic contributions we define

$$\int_Q \frac{\dot{\tilde{R}}_\phi}{A_\phi} \frac{(L_\phi^S)^n}{(\det{}_B^Q)^m} = \frac{8v_d 2^{d/2} k^{d+4+2n-4m}}{d}\ell_B^{(n,m)}(\tilde{T},\omega_1,\omega_2,\eta_\phi,S_\phi), \tag{4.245}$$

$$\int_Q \frac{\dot{\tilde{R}}_\phi}{A_\phi} \frac{q^2 R_\phi^{\mathrm{xx}}}{(\det{}_B^Q)^m} = \frac{1}{2}v_d 2^{d/2} k^{d+4-4m}\ell_{B,\mathrm{xx}}^{(0,m)}(\tilde{T},\omega_1,\omega_2,S_\phi). \tag{4.246}$$

We employed that $L_\phi^S = k^2(1+\omega_1+\omega_2)$ under the integral. The bosonic threshold functions read

$$\ell_B^{(n,m)} = \frac{1}{S_\phi^{2m}}\Big(1-\frac{\eta_\phi}{d+2}\Big)\Big(1+\omega_1+\omega_2\Big)^n \mathcal{B}_m\Big(\frac{\sqrt{(1+\omega_1)(1+\omega_1+2\omega_2)}}{S_\phi}\Big), \tag{4.247}$$

$$\ell_{B,\mathrm{xx}}^{(0,m)} = 2\ell_B^{(0,m)}\Big|_{\eta_\phi=0} = \frac{2}{S_\phi^{2m}}\mathcal{B}_m\Big(\frac{\sqrt{(1+\omega_1)(1+\omega_1+2\omega_2)}}{S_\phi}\Big). \tag{4.248}$$

The definitions

$$\int_Q \frac{\dot{\tilde{R}}_\phi}{A_\phi}\frac{(L_\phi^S)^n}{\mathrm{det}_B^m(Q)} = \frac{8v_d 2^{d/2}k^{d+2+2n-4m}}{d}\ell_B^{(n,m)}(\tilde{T},\omega_1,\omega_2,\eta_\phi,S_\phi,\tilde{V}_\phi), \tag{4.249}$$

$$\int_Q \frac{\dot{\tilde{R}}_\phi}{A_\phi}\frac{q^2 R_\phi^{\mathrm{xx}}}{\mathrm{det}_B^m(Q)} = \frac{1}{2}v_d 2^{d/2}k^{d+4-4m}\ell_{B,\mathrm{xx}}^{(0,m)}(\tilde{T},\omega_1,\omega_2,S_\phi,\tilde{V}_\phi) \tag{4.250}$$

can also be applied to the truncation with V_ϕ-term. We then have $L_\phi^S = V_\phi q_0^2 + k^2(1+\omega_1+\omega_2)$ under the integral and arrive at

$$\begin{aligned}
\ell_B^{(0,n)} &= \Big(1-\frac{\eta_\phi}{d+2}\Big)\ell_V^{(0,n)}\\
\ell_B^{(1,n)} &= \Big(1-\frac{\eta_\phi}{d+2}\Big)\Big(\tilde{V}_\phi\ell_V^{(1,n)} + (1+\omega_1+\omega_2)\ell_V^{(0,n)}\Big),\\
\ell_B^{(2,n)} &= \Big(1-\frac{\eta_\phi}{d+2}\Big)\Big(\tilde{V}_\phi^2\ell_V^{(2,n)} + 2\tilde{V}_\phi(1+\omega_1+\omega_2)\ell_V^{(1,n)} + (1+\omega_1+\omega_2)^2\ell_V^{(0,n)}\Big).
\end{aligned} \tag{4.251}$$

The corresponding Matsubara sums, $\ell_V^{(n,m)}$, are given in Eqs. (4.203)-(4.211). Note that we may also use

$$(L_\phi^S)^2 = \mathrm{det}_B(Q) - S_\phi^2 q_0^2 + (\rho_0\lambda_\phi)^2 \tag{4.252}$$

to write

$$\ell_B^{(2,n)} = \Big(1-\frac{\eta_\phi}{d+2}\Big)\Big(\ell_V^{(0,n-1)} - S_\phi^2\ell_V^{(1,n)} + \omega_2^2\ell_V^{(0,n)}\Big).$$

In the same fashion we apply

$$(L_\phi^S)^3 = [V_\phi q_0^2 + (1+\omega_1+\omega_2)](\mathrm{det}_B - S_\phi^2 q_0^2 + (\lambda_\phi\rho_0)^2) \tag{4.253}$$

to obtain

$$\begin{aligned}
\ell_B^{(3,n)} = \Big(1-\frac{\eta_\phi}{d+2}\Big)\Bigg[&\tilde{V}_\phi\ell_V^{(1,n-1)} + (1+\omega_1+\omega_2)\ell_V^{(0,n-1)} - S_\phi^2\tilde{V}_\phi\ell_V^{(4,n)}\\
&+\Big(-S_\phi^2(1+\omega_1+\omega_2)+\omega_2^2\tilde{V}_\phi\Big)\ell_V^{(1,n)} + \omega_2^2(1+\omega_1+\omega_2)\ell_V^{(0,n)}\Bigg].
\end{aligned} \tag{4.254}$$

The generalization of $\ell_{B,\mathrm{xx}}^{(0,m)}$ to the case of $V_\phi \neq 0$ is straightforward since

$$\ell_{B,\mathrm{xx}}^{(0,m)} = 2\ell_B^{(0,m)}\Big|_{\eta_\phi=0} = 2\ell_V^{(0,m)}. \tag{4.255}$$

Flow equations

With these definitions we eventually arrive at

$$\dot{U}^{(F)}(\rho) = -\frac{16v_d k^{d+2}}{d}\ell_F^{(1,1)}(\tilde{\mu},\tilde{T},\omega_3), \tag{4.256}$$

$$\dot{U}^{(B)}(\rho) = \frac{8v_d 2^{d/2} k^{d+2}}{d}\ell_B^{(1,1)}(\tilde{T},\omega_1,\omega_2,\eta_\phi,S_\phi,\tilde{V}_\phi) \tag{4.257}$$

for the flow of the effective potential. We refer to Sec. 4.2 for the definition of the F- and B-notation. For the boson propagator we find

$$\dot{S}_\phi^{(F)} = -\frac{16v_d h^2 k^{d-4}}{d}\Big(\ell_F^{(0,2)}(\tilde{\mu},\tilde{T},\omega_3) - 2\omega_3\ell_F^{(0,3)}(\tilde{\mu},\tilde{T},\omega_3)\Big), \tag{4.258}$$

$$\eta_\phi^{(F)} = \frac{16v_d h^2 k^{d-4}}{d}\ell_{F,\mathrm{xx}}^{(0,2)}(\tilde{\mu},\tilde{T},\omega_3), \tag{4.259}$$

$$\dot{V}_\phi^{(F)} = -\frac{16v_d h^2 k^{d-6}}{d}\ell_F^{(1,3)}(\tilde{\mu},\tilde{T},\omega_3) \tag{4.260}$$

for the fermionic contributions in the spin-balanced case, and

$$\begin{aligned}\dot{S}_\phi^{(B)} = &-\frac{32v_d 2^{d/2} k^{d-4} S_\phi \rho U''}{d}\Bigg[(U''+\rho U^{(3)})\ell_B^{(0,2)} \\ &+ 2(\rho U'')^2(U''+\rho U^{(3)})k^{-4}\ell_B^{(0,3)} - 2\rho U''(2U''+\rho U^{(3)})k^{-2}\ell_B^{(1,3)}\Bigg],\end{aligned} \tag{4.261}$$

$$\eta_\phi^{(B)} = \frac{8v_d 2^{d/2} k^{d-4}\rho(U'')^2}{d}\ell_{B,\mathrm{xx}}^{(0,2)}, \tag{4.262}$$

$$\begin{aligned}\dot{V}_\phi^{(B)} = &\frac{32v_d 2^{d/2} k^{d-6}\rho(U'')^2}{d}\Bigg[3\tilde{V}_\phi\ell_B^{(0,2)} \\ &- \Big(S_\phi^2 + 4\tilde{V}_\phi(1+\omega_1+\omega_2)\Big)\tilde{V}_\phi\Big(1-\frac{\eta_\phi}{d+2}\Big)\ell_V^{(1,3)} \\ &+ \Big(4\tilde{V}_\phi\omega_2^2 - S_\phi^2(1+\omega_1+\omega_2) - 4\tilde{V}_\phi(1+\omega_1+\omega_2)^2\Big)\ell_B^{(0,3)}\Bigg].\end{aligned} \tag{4.263}$$

for the bosonic contributions. We can apply

$$\tilde{V}_\phi\Big(1-\frac{\eta_\phi}{d+2}\Big)\ell_V^{(1,3)} = \ell_B^{(1,3)} - (1+\omega_1+\omega_2)\ell_B^{(0,3)} \tag{4.264}$$

to write the flow equation for V_ϕ as

$$\begin{aligned}\dot{V}_\phi^{(B)} = &\frac{32v_d 2^{d/2} k^{d-6}\rho(U'')^2}{d}\Bigg[3\tilde{V}_\phi\ell_B^{(0,2)} + 4\tilde{V}_\phi\omega_2^2\ell_B^{(0,3)} \\ &- \Big(S_\phi^2 + 4\tilde{V}_\phi(1+\omega_1+\omega_2)\Big)\ell_B^{(1,3)}\Bigg].\end{aligned} \tag{4.265}$$

In the spin-imbalanced case only the fermionic contributions change. We restrict here to the symmetric scheme ($R_{\psi 1} = R_{\psi 2}$), since the flow equations for the asymmetric scheme are easily deduced from Eqs. (4.166)-(4.168). For the effective potential we find

$$\dot{U}^{(F)}(\rho) = -\frac{8v_d k^{d+2}}{d\sqrt{1+\omega_3}}\ell_1(\tilde{\mu})\Big(1 - \tilde{N}_F(\sqrt{1+\omega_3} - \delta\tilde{\mu}) - \tilde{N}_F(\sqrt{1+\omega_3} + \delta\tilde{\mu})\Big) \tag{4.266}$$

with $\delta\tilde{\mu} = \delta\mu/k^2$. The anomalous dimension is given by

$$\eta_\phi^{(F)} = \frac{4v_d\tilde{h}^2}{d(1+\omega_3)^{3/2}}\ell_3(\tilde{\mu})\Bigg[\Big(1 - \tilde{N}_F(\sqrt{1+\omega_3} - \delta\tilde{\mu}) - \tilde{N}_F(\sqrt{1+\omega_3} + \delta\tilde{\mu})\Big) + \sqrt{1+\omega_3}\Big(\tilde{N}'_F(\sqrt{1+\omega_3} - \delta\tilde{\mu}) + \tilde{N}'_F(\sqrt{1+\omega_3} + \delta\tilde{\mu})\Big)\Bigg]. \tag{4.267}$$

For the frequency coefficients we have

$$\dot{S}_\phi^{(F)} = -2h^2\left[T\sum_n \frac{1}{(\det_{12})^2} - T\sum_n \frac{2h^2\rho}{(\det_{12})^3}\right]\frac{8v_d k^{d+2}}{d}\ell_2(\tilde{\mu}), \tag{4.268}$$

$$\dot{V}_\phi^{(F)} = -2h^2\left[T\sum_n \frac{1}{(\det_{12})^3}\right]\frac{8v_d k^{d+4}}{d}\ell_1(\tilde{\mu}), \tag{4.269}$$

with

$$T\sum_n \frac{1}{(\det_{12})^2} = \frac{2}{(z_1 - z_2)^3}\Big(1 - \tilde{N}_F(z_1) - \tilde{N}_F(-z_2)\Big) + \frac{1}{(z_1 - z_2)^2}\Big(\tilde{N}'_F(z_1) + \tilde{N}'_F(-z_2)\Big), \tag{4.270}$$

$$T\sum_n \frac{1}{(\det_{12})^3} = \frac{-1}{4}\frac{\partial^2}{\partial z_1 \partial z_2} T\sum_n \frac{1}{(\det_{12})^2}, \tag{4.271}$$

see Eqs. (4.192) and (4.193).

5 Three-dimensional BCS-BEC Crossover

5.1 Tan contact

The single particle momentum distribution $n_{\vec{q}}$ of a noninteracting Fermi gas in equilibrium is described by the Fermi–Dirac distribution, which decays exponentially for momenta sufficiently larger than the chemical potential. In contrast, for ultracold fermions in the BCS-BEC crossover one finds an algebraic decay (Haussmann [1993, 1994], Viverit et al. [2004]) according to

$$n_{\psi,\vec{q}\sigma} = \frac{C}{q^4} \text{ for large } q. \tag{5.1}$$

Here $n_{\psi,\vec{q}\sigma}$ is the occupation number of fermions of species σ and the precise meaning of "large q" will be specified later. It was realized by Tan [2008a,c,b] that the factor of proportionality C, called contact, makes its appearance in several exact relations describing the quantum many-body system. For instance, it allows to compute the change of the energy density of the system due to a change of the scattering length according to the adiabatic sweep theorem

$$\frac{1}{V}\frac{\mathrm{d}E}{\mathrm{d}(-1/a)} = \frac{C}{4\pi M}. \tag{5.2}$$

Moreover, the energy density of the homogeneous system is given by

$$\frac{E}{V} = \frac{C}{4\pi M a} + \sum_{\sigma=1,2}\int \frac{\mathrm{d}^3 q}{(2\pi)^3}\frac{q^2}{2M}\Big(n_{\psi,\vec{q}\sigma} - \frac{C}{q^4}\Big). \tag{5.3}$$

Interestingly, there also is a connection between the contact and the shear viscosity of the system (Punk and Zwerger [2007], Taylor and Randeria [2010]). The Tan relations (Braaten and Platter [2008], Braaten et al. [2008], Zhang and Leggett [2009], Braaten [2012], Schneider and Randeria [2010], Son and Thompson [2010], Hu et al. [2010]) have found verifications in experiments on the BCS-BEC crossover of ultracold fermionic atoms (Partridge et al. [2005], Thomas et al. [2005], Werner et al. [2009], Stewart et al. [2010], Kuhnle et al. [2010, 2011]). The measurement of the contact for a homogeneous system has been performed by Sagi et al. [2012]. The Tan relations have been generalized to the 2D (Valiente et al. [2011], Werner and Castin [2012]) and 1D case (Barth and Zwerger [2011]).

Using DSE and the FRG we derive the universal factorization property of the fermion self-energy

$$\Sigma_\psi(Q) = \frac{4C}{P_{\psi,\mathrm{cl}}(-Q)} - \delta\mu \quad \text{for large } q, \tag{5.4}$$

where $P_{\psi,\mathrm{cl}}(Q) = \mathrm{i}q_0 + q^2 - \mu$ is the classical (microscopic) fermion propagator. In Eq. (5.4), q has to be larger than any of the physical scales k_{ph} set by inverse scattering length a^{-1}, chemical potential μ, and temperature T. The first contribution in Eq. (5.4), which we refer to as Tan term, results in the large momentum decay of the momentum distribution according to $n_{\psi,\vec{q}\sigma} = C/q^4$, see Eq. (5.35) below. The second term constitutes a high momentum shift of the effective fermion chemical potential[1]. Within DSE it is not trivial to show that Σ_ψ, C and $\delta\mu$ are ultraviolet finite quantities that do not involve any counterterms. This requires a suitable split of the relevant momentum integrals, see Eq. (5.24) below.

The importance of the double fraction structure of the fermion propagator in order to quantitatively describe the BCS-BEC crossover has first been pointed out by Haussmann [1993, 1994]. Universal high momentum factorization of dynamic quantities has also been observed with the FRG in the context of finite temperature Yang–Mills theory (Fister and Pawlowski [2011]) and with the Similarity Renormalization Group applied to N-body systems at zero temperature, including deuteron, ultracold fermions and the electron gas (Anderson et al. [2010], Bogner and Roscher [2012]). The large momentum behavior of the self-energy is related to properties of energetic atoms propagating in a strongly interacting gas, see Nishida [2012] for a operator product expansion study.

Although the contact C appears in the high momentum propagator of the theory, it is a many-body quantity dominated by interaction and many-body scales. This is also reflected in its close relation to thermodynamic quantities. Thermodynamic considerations based on the Tan relations restrict the most general form of the contact as a function of temperature (Yu et al. [2009], Hu et al. [2011]). In order to compute the function $C(\mu, T, a)$ it is therefore mandatory to work within a setting which can resolve the physics on all scales of the theory. This is realized by an FRG framework, where fluctuations on distinct scales are integrated out successively, and which goes beyond the mean field approximation.

In this section we develop an FRG scheme to compute the physics related to the contact. In particular, we derive a flow equation for the flowing contact C_k, which interpolates between $C_{k=\Lambda} = 0$ in the ultraviolet and the physical contact $C_{k=0} = C$ in the infrared. The method readily applies to nonzero values of the crossover parameter $(k_{\mathrm{F}}a)^{-1}$ and any spatial dimension d. It allows for improving quantitative precision by using more elaborate truncations. We comment on this point below. We only consider the spin-balanced case here.

[1] Note that $\delta\mu$ should not be confused with the spin-imbalance discussed in Sec. 5.3.

We normalize the momentum distribution such that the integral $2\int_{\vec{q}} n_{\psi,\vec{q}\sigma} = n$ yields the density of atoms n, and thus the contact C is an intensive quantity. Defining $2\int_{\vec{q}} \bar{n}_{\psi,\vec{q}\sigma} = N$ instead, with the particle number N, results in an extensive contact $\bar{C} = CV$, where V is the volume of the system. We have $\bar{C}/Nk_\mathrm{F} = 3\pi^2 C/k_\mathrm{F}^4$.

An interesting question is related to the range of applicability of the asymptotic formula (5.4) for the fermion propagator, i.e. the momentum scale q_c such that the universal scaling form is valid for $q \geq q_\mathrm{c}$. This has direct consequences for the density of the system. Indeed, as was already noted by Tan [2008c], the contribution from large momentum atoms to the total atom density for $T = 0$ can be approximated by

$$\delta n^{(C)} = 2\int_{q\geq q_\mathrm{c}} \frac{\mathrm{d}^3 q}{(2\pi)^3}\frac{C}{q^4} = \frac{C}{\pi^2 q_\mathrm{c}}. \tag{5.5}$$

The apparent divergence of this expression for $q_\mathrm{c} \to 0$ is cured by a nonzero gap or temperature, such that $\delta n^{(C)}$ remains finite. Thus, there is no a priori lower bound for q_c.

It can be understood easily that q_c is smallest for the UFG. Indeed, the universal form of the self-energy in Eq. (5.4) is valid for q being larger than the physical scales k_ph. Typically, the inverse scattering length a^{-1} is much larger than the momentum scales set by chemical potential and temperature. In particular, this is valid in the perturbative regimes on the BEC and BCS sides, where $|a| \to 0$. However, for the UFG we have $a^{-1} = 0$ and the first physical scale is set by either $\mu^{1/2}$ or $T^{1/2}$. For this reason there is a huge *enhancement of the universal regime* where Eq. (5.4) is valid in the unitary limit. This is seen in Sec. 5.1.3. From Eq. (5.5) we then conclude that the contribution of high energetic particles on the thermodynamic functions is large at resonance.

Our findings suggest that a rather simple approximation to the full inverse fermion propagator given by

$$P_\psi(Q) = \mathrm{i}Z_\psi q_0 + A_\psi q^2 - \mu - \delta\mu + \frac{4C(\mathrm{i}q_0 + q^2 - \mu + R_k(Q))}{q_0^2 + (q^2 - \mu + R_k(Q))^2 + \kappa} \tag{5.6}$$

with k-dependent couplings Z_ψ, A_ψ, $\delta\mu$, C, and κ, and infrared cutoff $R_k(Q)$, combined with a suitable generalization of the inverse boson propagator, will lead to a substantial improvement of the quantitative precision in the FRG treatment of strongly interacting fermionic systems. We observe that in the superfluid regime the inverse fermion propagator has an additional anomalous contribution $\sim \Delta_0$. This regularizes the momentum integrals such that the explicit regulator $\sim \kappa$ may not be needed. The occupation number corresponding to this ansatz reads

$$n_{\psi,\vec{q}\sigma} = -\Big(T\sum_n \frac{P_\psi(Q)}{P_\psi(Q)P_\psi(-Q) + \Delta_0^2} - \frac{1}{2}\Big) \tag{5.7}$$

with k-dependent density $n_k = 2\int_{\vec{q}} n_{\psi,\vec{q}\sigma}$. The flowing density, and therefore the total density $n = n_{k=0}$, can thus be inferred from the flowing couplings Z_ψ, A_ψ, $\delta\mu$, C and κ.

5.1.1 Perturbative contact from the equation of state

We derive the contact from the equation of state in the perturbative BEC- and BCS-regimes by means of the adiabatic sweep theorem in Eq. (5.2). We first consider the BEC-limit of the crossover, i.e. the region

$$(k_\mathrm{F} a)^{-1} \gg 1. \tag{5.8}$$

Moreover, we restrict the considerations to the case of zero temperature. We closely follow Tan [2008c]. The energy density of the system (in the canonical variables) is given by the Lee–Huang–Yang (Lee et al. [1957], Lee and Yang [1958]) expression

$$\frac{E}{V} = n_\mathrm{d}\varepsilon_\mathrm{B} + \frac{g_\mathrm{d}}{2} n_\mathrm{d}^2 \Big(1 + \frac{128}{15\sqrt{\pi}}\sqrt{n_\mathrm{d} a_\mathrm{d}^3}\Big), \tag{5.9}$$

where n_d is the number of dimer atoms, which is related to the density according to $n_\mathrm{d} = n/2$ on the far BEC side, and ε_B is the binding energy of a dimer. From Eq. (5.8) we find the gas parameter $n_\mathrm{d} a_\mathrm{d}^3$ to be small. The coupling constant for the dimers is given by

$$g_\mathrm{d} = \frac{4\pi a_\mathrm{d}}{M_\mathrm{d}} = 4\pi c_\mathrm{d} a, \tag{5.10}$$

where we used that $M_\mathrm{d} = 2M = 1$ and $a_\mathrm{d} = c_\mathrm{d} a$. The dimensionless constant c_d relates the scattering length of dimers to the fermionic scattering length. The exact value of c_d is known to be 0.6 (Petrov et al. [2004]). However, within the truncation of the flow equation presented below we have $c_\mathrm{d} = 0.72$ from a solution of the vacuum problem (Diehl et al. [2010a]). The energy density in terms of n and a is found to be

$$\frac{E}{V} = n\frac{\varepsilon_\mathrm{B}}{2} + \frac{\pi c_\mathrm{d} a n^2}{2}\Big(1 + \frac{128}{15\sqrt{2\pi}}\sqrt{n c_\mathrm{d}^3 a^3}\Big). \tag{5.11}$$

We compute the chemical potential according to $\mu(n) = \mathrm{d}(E/V)/\mathrm{d}n$ and subtract half the binding energy to obtain the (positive) many-body chemical potential

$$\mu_\mathrm{mb}(n) = \mu - \frac{\varepsilon_\mathrm{B}}{2} = \pi c_\mathrm{d} a n\Big(1 + \frac{32}{3\sqrt{2\pi}}\sqrt{n c_\mathrm{d}^3 a^3}\Big). \tag{5.12}$$

Inverting this relation to the same order of approximation we find

$$n(\mu_\mathrm{mb}) = \frac{\mu_\mathrm{mb}}{\pi c_\mathrm{d} a}\Big(1 - \frac{32 c_\mathrm{d}}{3\pi\sqrt{2}}\sqrt{\mu_\mathrm{mb}} a\Big). \tag{5.13}$$

This is the equation of state in the grand canonical variables at $T = 0$ to leading order in the gas parameter $\sqrt{\mu_{\rm mb}}a$.

By virtue of the adiabatic sweep theorem, Eq. (5.2), we can derive an expression for the contact in the BEC regime. For this purpose we employ $\varepsilon_{\rm B} = -1/Ma^2 = -2/a^2$. From Eq. (5.11) we then find

$$C_{\rm BEC} = \frac{4\pi n}{a} + c_{\rm d}\pi^2 a^2 n^2 \Big(1 + \frac{64}{3\sqrt{2\pi}}\sqrt{n c_{\rm d}^3 a^3}\Big) \tag{5.14}$$

at zero temperature. By dividing by $k_{\rm F}^4$ we obtain

$$\frac{C_{\rm BEC}}{k_{\rm F}^4} = \frac{4}{3\pi}(k_{\rm F}a)^{-1} + \frac{c_{\rm d}}{9\pi^2}(k_{\rm F}a)^2\Big(1 + \frac{64 c_{\rm d}^{3/2}}{3\pi\sqrt{6\pi}}(k_{\rm F}a)^{3/2}\Big). \tag{5.15}$$

Inserting the equation of state (5.13) we arrive at

$$\frac{C_{\rm BEC}}{\mu_{\rm mb}^2} = \frac{4}{c_{\rm d}}(\sqrt{\mu_{\rm mb}}a)^{-2}\Big(1 - \frac{32 c_{\rm d}}{3\pi\sqrt{2}}\sqrt{\mu_{\rm mb}}a\Big). \tag{5.16}$$

We now consider the asymptotic behavior on the BCS side. The equation of state at zero temperature from Fermi liquid theory is given by

$$\frac{E}{V} = \frac{3}{5}k_{\rm F}^2 n\Big(1 + \frac{10}{9\pi}k_{\rm F}a\Big), \tag{5.17}$$

see Sec. 6.1.3. We deduce for the chemical potential that

$$\mu(k_{\rm F}) = \frac{\rm d}{{\rm d}n}\frac{E}{V} = k_{\rm F}^2\Big(1 + \frac{4}{3\pi}k_{\rm F}a\Big). \tag{5.18}$$

The contact is found from

$$C = 2\pi\frac{{\rm d}(E/V)}{{\rm d}(-1/a)} = 4\pi^2 n^2 a^2. \tag{5.19}$$

Thus we have

$$\frac{C_{\rm BCS}}{k_{\rm F}^4} = \frac{4}{9\pi^2}(k_{\rm F}a)^2. \tag{5.20}$$

Inserting the equation of state $k_{\rm F}(\mu) = \sqrt{\mu}$ we then arrive at

$$\frac{C_{\rm BCS}}{\mu^2} = \frac{4}{9\pi^2}(\sqrt{\mu}a)^2. \tag{5.21}$$

5.1.2 Contact from Dyson–Schwinger equations

High momentum factorization of the fermion self-energy

The physics of the contact is based on a separation of scales. This scale dependence is most efficiently resolved within a Renormalization Group analysis. Nevertheless it is instructive to first consider a self-consistent gap equation or DSE equation for the fermion propagator. From this exact equation, the factorization property of the self-energy at large external momenta is deduced easily. Moreover, we use this formalism to show how the perturbative results $C_{\mathrm{BEC}} = 4\pi n/a$ and $C_{\mathrm{BCS}} = 4\pi^2 a^2 n^2$ arise naturally on the BEC and BCS sides of the crossover after a proper ultraviolet renormalization scheme has been applied.

From the two-channel model we infer the inverse classical fermion and boson propagators, respectively, to be given by

$$\begin{aligned} P_{\psi,\mathrm{cl}}(q_0, q^2) &= \mathrm{i}q_0 + q^2 - \mu, \\ P_{\varphi,\mathrm{cl}}(q_0, q^2) &= \nu + \mathrm{i}\varepsilon q_0. \end{aligned} \tag{5.22}$$

We introduce an infinitesimal contribution $\mathrm{i}\varepsilon q_0$ with $\varepsilon \to 0^+$ in the inverse boson propagator to regularize momentum integrals involving P_φ. With this single modification we will make manifest that only one single coupling, the detuning ν, requires an ultraviolet renormalization in the BCS-BEC crossover, see Eqs. (5.40) and (5.41). Alternatively, one can add a counterterm $\propto f_\Lambda \psi_\sigma^* \psi_\sigma$ in the fermionic part of the microscopic action and then adjust f_Λ appropriately.

Due to quantum and thermal fluctuations, the classical propagators $P_{\psi,\mathrm{cl}}(Q)$ and $P_{\varphi,\mathrm{cl}}(Q)$ get dressed to yield the macroscopic propagators $P_\psi(Q)$ and $P_\varphi(Q)$. This correction is encoded in the self-energies $\Sigma_{\psi/\varphi}(Q) = P_{\psi/\varphi}(Q) - P_{\psi/\varphi,\mathrm{cl}}(Q)$. The DSE for the full inverse fermion propagator reads

$$P_\psi(Q) = P_{\psi,\mathrm{cl}}(Q) + \int_P \frac{h^2}{P_\psi(P-Q)P_\varphi(P)} \tag{5.23}$$

according to the graph shown in Fig. 5.1. The corresponding momentum integral involves the fully dressed propagators. It is in this sense that the equation is self-consistent and cannot be solved in a straightforward manner. In Eq. (5.23) we approximate the full Feshbach coupling by the microscopic one, which is momentum independent. This approximation is justified due to the weak effect of fluctuations on the Feshbach coupling.

The BCS-BEC crossover across a broad Feshbach resonance can be parametrized by the physical scales temperature, chemical potential and scattering length. We denote the highest physical momentum scale by k_{ph}. In the perturbative regimes, this corresponds to the inverse scattering length, whereas this is not valid close to resonance where $a^{-1} = 0$. Only momenta $p^2 < k_{\mathrm{ph}}^2$ in the loop-integral in Eq. (5.23) can resolve the details of the choice of parameters. For this reason we split

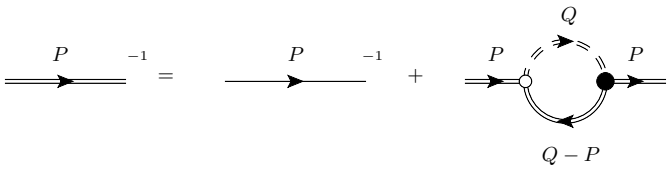

Figure 5.1: DSE for the inverse fermion propagator. A single line corresponds to a classical propagator and a double line denotes a full propagator. Fermions and bosons are represented by solid and dashed lines, respectively. In the loop integral we have one fully dressed Feshbach coupling and a microscopic one. The latter is momentum independent. Figure taken from Boettcher et al. [2013].

up the integration according to

$$\Sigma_\psi(Q) = h^2 T \sum_n \int_{p^2<k_{\rm tr}^2} \frac{1}{P_\psi(P-Q)P_\varphi(P)} + h^2 T \sum_n \int_{p^2>k_{\rm tr}^2} \frac{1}{P_\psi(P-Q)P_\varphi(P)}, \tag{5.24}$$

where the transition momentum $k_{\rm tr}$ is sufficiently larger than $k_{\rm ph}$, such that for $p^2 > k_{\rm tr}^2$ the p^2-dependence of $P_\varphi(P)$ can be neglected. We can then replace

$$P_\varphi(P) \to P_\varphi(p_0, p^2 = k_{\rm tr}^2) =: P_{\varphi,{\rm tr}}(p_0) \tag{5.25}$$

in the second integral. By adding and subtracting a convenient piece we can now write $\Sigma_\psi(Q)$ in terms of two contributions, $\Sigma_\psi = \Sigma_\psi^{(1)} + \Sigma_\psi^{(2)}$, with

$$\begin{aligned}
\Sigma_\psi^{(1)}(Q) &= h^2 T \sum_n \int_{p^2<k_{\rm tr}^2} \frac{1}{P_\psi(P-Q)} \left(\frac{1}{P_\varphi(P)} - \frac{1}{P_{\varphi,{\rm tr}}(p_0)} \right), \\
\Sigma_\psi^{(2)}(Q) &= h^2 \int_P \frac{1}{P_\psi(P-Q)P_{\varphi,{\rm tr}}(p_0)}.
\end{aligned} \tag{5.26}$$

Both pieces are manifestly ultraviolet finite and do not depend on $k_{\rm tr}$ for sufficiently large $k_{\rm tr}^2 \gg k_{\rm ph}^2$.

We emphasize that the splitting of the self-energy in Eq. (5.24) enables us to show that the superficially divergent loop-integral in Eq. (5.23) is indeed finite for large q^2. This nontrivial statement results from a scale argument only and thus does not imply any restrictions on coupling strength, density, or temperature. Moreover, the particular choice of the artificially introduced momentum $k_{\rm tr}$ does not play a role for the final result.

We are interested in the behavior of $\Sigma_\psi(Q)$ for large momenta $q^2 \gg k_{\rm tr}^2$. The scale hierarchy in this case is given by

$$k_{\rm ph}^2 \ll k_{\rm tr}^2 \ll q^2 \ll \Lambda^2. \tag{5.27}$$

In $\Sigma_\psi^{(1)}(Q)$ we can then replace $P_\psi(P-Q)$ by $P_{\psi,\mathrm{cl}}(-Q)$, because the integral is restricted to momenta which are small in comparison to Q and we can neglected self-energy corrections to leading order at high momenta. This results in the factorization

$$\Sigma_\psi^{(1)}(Q) = \frac{4C}{P_{\psi,\mathrm{cl}}(-Q)} \text{ for large } q^2. \tag{5.28}$$

We define the contact according to

$$C = \frac{h^2}{4} T \sum_n \int_{p^2<k_{\mathrm{tr}}^2} \left(\frac{1}{P_\varphi(P)} - \frac{1}{P_{\varphi,\mathrm{tr}}(p_0)} \right), \tag{5.29}$$

since the numerator in Eq. (5.28) is seen below to result in the prefactor C of the $1/q^4$-tail of the momentum distribution. Again, formulas (5.28) and (5.29) only rely on the splitting of the loop-integral at k_{tr}, which gives us a precise notion of "large q^2", namely $q^2 \gg k_{\mathrm{tr}}^2$. The factorization is thus a generic feature of theories which can be described by similar Feshbach- or Yukawa-type gap equations.

We can define an effective boson occupation number as

$$n_{\varphi,\vec{p}} = T \sum_n \left(\frac{1}{P_\varphi(P)} - \frac{1}{P_{\varphi,\mathrm{tr}}(p_0)} \right) \tag{5.30}$$

with total boson number density $n_\varphi = \int_{\vec{p}} n_{\varphi,\vec{p}}$. This yields

$$C = \frac{h^2}{4} n_\varphi \tag{5.31}$$

and hence shows the close relation between the contact and the number of atoms bound in bosonic pairs. Note that the definition of n_φ has to be renormalization group invariant and thus involves a wave function renormalization constant, which we set to unity here for simplicity. The second term in $\Sigma_\psi(Q)$ results in a Hartree-like shift of the effective chemical potential

$$\Sigma_\psi^{(2)}(Q) = -\delta\mu \text{ for large } q^2. \tag{5.32}$$

The correction to the momentum distribution of particles at high momenta which results from the self-energy in Eqs. (5.28) and (5.32) is found from the generally valid formula

$$n_{\psi,\vec{q}\sigma} = -\left(T \sum_n \frac{1}{P_\psi(Q)} - \frac{1}{2} \right). \tag{5.33}$$

Treating the self-energy perturbatively for large external momentum q^2, we find

$$n_{\psi,\vec{q}\sigma} = -\left(T \sum_n \frac{1}{P_{\psi,\mathrm{cl}}(Q) - \delta\mu} - \frac{1}{2} \right) + T \sum_n \frac{4C}{P_{\psi,\mathrm{cl}}^2(Q) P_{\psi,\mathrm{cl}}(-Q)}. \tag{5.34}$$

The first two terms yield $N_F(q^2-\mu-\delta\mu)$ with Fermi function $N_F(z) = (e^{z/T}+1)^{-1}$. This contribution vanishes for large q^2. Evaluating the Matsubara summation we find for the second contribution

$$n_{\psi,\vec{q}\sigma} = T\sum_n \frac{4C}{P^2_{\psi,\mathrm{cl}}(Q)P_{\psi,\mathrm{cl}}(-Q)} = 4C\Big(\frac{1-N_F(q^2-\mu)}{4(q^2-\mu)^2} + \frac{N_F'(q^2-\mu)}{2(q^2-\mu)}\Big)$$
$$\stackrel{q^2\gg\mu,T}{\longrightarrow} \frac{C}{q^4} \text{ for large } q^2. \tag{5.35}$$

This justifies the identification of C in the numerator of the asymptotic self-energy (5.28) with the contact as defined from $C = \lim_{p\to\infty} p^4 n_{p\sigma}$. Higher order contributions to the fermion self-energy do not enter the $1/q^4$-tail of the momentum distribution.

The formulas derived in this section become particularly simple in the perturbative BEC and BCS regimes, because the integrals in Eq. (5.26) can be performed analytically. We present the calculation below, but give here already the results. The shift $\delta\mu$ of the effective chemical potential vanishes on the BEC side of the crossover. On the BCS side, it is given by

$$\delta\mu = -\lambda_\psi n_{\psi,\sigma}, \tag{5.36}$$

with four-fermion coupling $\lambda_\psi = 8\pi a$. Since all atoms are bound to dimers in the BEC limit, the boson density in Eq. (5.31) equals half the particle density and we arrive at

$$C_{\mathrm{BEC}} = \frac{4\pi n}{a}. \tag{5.37}$$

The relation $h^2 = 32\pi/a$ results from the wave function renormalization of the boson propagator, see Eq. (5.42). In the BCS limit, the first nonvanishing contribution to the contact arises at second order in perturbation theory in the coupling a. Inserting the DSE for the boson propagator (5.40) into Eq. (5.31), we obtain a double integral over two fermion propagators, each resulting in a fermion density $n_{\psi,\sigma}$. We find

$$C_{\mathrm{BCS}} = 4\pi^2 a^2 n^2. \tag{5.38}$$

These perturbative results derived from DSE agree with the expressions found from the zero temperature equation of state.

Contact in the perturbative regime

To exemplify our statements on C and $\delta\mu$ from the DSE, we consider here the perturbative BEC and BCS regimes, where the integrals in Eqs. (5.28) and (5.32) can be performed analytically. For weak interactions, the largest physical scale is given by $k_{\mathrm{ph}} = a^{-1}$. To study the contact in the whole crossover we employ

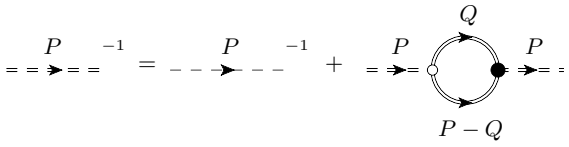

Figure 5.2: DSE for the inverse boson propagator. The notation is chosen as in Fig. 5.1. Figure taken from Boettcher et al. [2013].

the Functional Renormalization Group in Sec. 5.1.3. One of the merits of this method is that all expressions are automatically renormalized.

On the BEC and BCS sides of the crossover, the fermion propagator only gets weakly dressed because either the fermion or the boson propagator is gapped. This leads to a suppression of the loop-integral originating from the diagram shown in Fig. 5.1. Hence we can always treat the fermion self-energy perturbatively in these regimes. We identify the Hartree shift of the chemical potential as

$$\begin{aligned} -\delta\mu &= h^2 \int_{\vec{p}}^{\Lambda} T\sum_n \frac{1}{(\mathrm{i}(p_0-q_0)+p^2-\mu)(\nu+\mathrm{i}\varepsilon p_0)} \\ &= h^2 \int_{\vec{p}} \frac{-N_F(p^2-\mu)-N_B(\nu/\varepsilon)}{\varepsilon(\mathrm{i}q_0-p^2+\mu)+\nu} = -\frac{h^2}{\nu} n_{\psi,\sigma} \end{aligned} \tag{5.39}$$

on the BCS side. The Bose function is denoted by $N_B(z) = (e^{z/T}-1)^{-1}$. In the last expression we take the limit $\varepsilon \to 0^+$. The q_0-dependence of $\delta\mu$ defined in Eq. (5.32) is seen to vanish.

For computing the contact we first consider the BEC limit, where $\mu \simeq -1/a^2$ is large and negative. The shift of the chemical potential vanishes due to the suppression of the Fermi function $N_F(p^2-\mu)$ in the integral in Eq. (5.39). The inverse boson propagator is derived from the DSE (Diehl and Wetterich [2007]) for the bosonic self-energy

$$\Sigma_\varphi(Q) = P_\varphi(Q) - P_{\varphi,\mathrm{cl}}(Q) = \delta\nu_\Lambda - h^2 \int_P \frac{1}{P_\psi(Q-P)P_\psi(P)}, \tag{5.40}$$

shown diagrammatically in Fig. 5.2. The counterterm is given by

$$\delta\nu_\Lambda = \frac{h^2\Lambda}{4\pi^2}. \tag{5.41}$$

In the perturbative regime we can replace the full fermion propagators in the loop-integral by the classical ones. The Matsubara summation and angular integration can then be evaluated analytically. We do not need the full expression but only note that

$$P_{\varphi,\mathrm{BEC}}(Q) = \nu + \frac{h^2}{8\pi}\sqrt{\frac{\mathrm{i}q_0}{2}+\frac{q^2}{4}-\mu} \simeq Z_\varphi\Big(\mathrm{i}q_0+\frac{q^2}{2}\Big) \tag{5.42}$$

for $|q_0|, q^2 \ll a^{-2}$ in the BEC regime. (We used $-h^2/\nu = 8\pi a$ and $\mu = -1/a^2$) The boson propagator resembles particles with classical dispersion relation $\omega_q = q^2/2M_\varphi$ and mass $M_\varphi = 2M = 1$. The wave function renormalization constant is $Z_\varphi = h^2 a/32\pi$.

Inserting the boson propagator from Eq. (5.42) into Eq. (5.29) we arrive at

$$\begin{aligned} C_{\mathrm{BEC}} &= \frac{8\pi}{a} \int_{p^2<k_{\mathrm{tr}}^2} T\sum_n \Big(\frac{1}{\mathrm{i}p_0 + p^2/2} - \frac{1}{\mathrm{i}p_0 + k_{\mathrm{tr}}^2} \Big) \\ &= \frac{8\pi}{a} \int_{p^2<k_{\mathrm{tr}}^2} \Big(N_B(p^2/2) - N_B(k_{\mathrm{tr}}^2) \Big) = \frac{8\pi n_{\varphi,\mathrm{cl}}}{a}, \end{aligned} \tag{5.43}$$

where we used $k_{\mathrm{ph}} \gg T^{1/2}$ and $n_{\varphi,\mathrm{cl}}$ defines the number density of boson with classical dispersion relation from Eq. (5.30). Due to the equation of state $n_{\varphi,\mathrm{cl}} = n/2$ on the BEC side of the crossover we conclude

$$C_{\mathrm{BEC}} = \frac{4\pi n}{a} \tag{5.44}$$

as expected.

In the BCS regime the bosons are resonant excitations and $n_{\varphi,\mathrm{cl}} = 0$. The corresponding formula for the contact is most easily derived from inserting the DSE (5.40) into formula (5.29). Therein, the boson self-energy $\Sigma_\varphi \propto h^2$ can be treated perturbatively, since it is small in comparison to the boson gap ν due to the small scattering length $a = -h^2/8\pi\nu$. We then find

$$\begin{aligned} C_{\mathrm{BCS}} &= -\frac{h^2}{4} T\sum_n \int_{p^2<k_{\mathrm{tr}}^2} \frac{\Sigma_\varphi(P) - \Sigma_\varphi(p_0, k_{\mathrm{tr}}^2)}{(\nu + \mathrm{i}\varepsilon p_0)^2} \\ &= \frac{h^4}{4\nu} T\sum_n \int_{p^2<k_{\mathrm{tr}}^2} \int_K \frac{1}{P_{\psi,\mathrm{cl}}(K)(\nu + \mathrm{i}\varepsilon p_0)} \\ &\times \left(\frac{1}{P_{\psi,\mathrm{cl}}(P-K)} - \frac{1}{P_{\psi,\mathrm{cl}}(p_0 - k_0, (k_{\mathrm{tr}} - k)^2)} \right) \\ &= -\frac{h^4}{4\nu} \int_K \int_{p^2<k_{\mathrm{tr}}^2} \frac{N_F((\vec{p}-\vec{k})^2 - \mu)}{P_{\psi,\mathrm{cl}}(K)(\nu + \mathrm{i}\varepsilon k_0)} \\ &= -\frac{h^4}{4\nu} n_{\psi,\sigma} \int_K \frac{1}{P_{\psi,\mathrm{cl}}(K)(\nu + \mathrm{i}\varepsilon k_0)} \\ &= -\frac{h^4}{4\nu} n_{\psi,\sigma} \int_{\vec{k}} \frac{N_F(k^2-\mu) - N_F(\nu/\varepsilon)}{\varepsilon(k^2-\mu) - \nu} = \frac{h^4}{4\nu^2} n_{\psi,\sigma}^2. \end{aligned} \tag{5.45}$$

We again applied the limit $\varepsilon \to 0^+$. With the BCS equation of state $n_{\psi,\sigma} = n/2$ we arrive at

$$C_{\mathrm{BCS}} = 4\pi^2 a^2 n^2. \tag{5.46}$$

This agrees with Eq. (5.19).

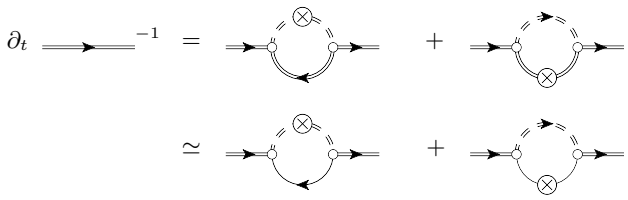

Figure 5.3: Flow equation for the fermion self-energy. The notation is chosen as in Fig. 5.1. The crossed circle indicates an insertion of $\dot{R}_k$ in the loop integral. Figure taken from Boettcher et al. [2013].

5.1.3 Contact from Functional Renormalization

Fermion self-energy and contact term in the symmetric regime

For conceptual clarity we first isolate the contact term and the shift of the chemical potential from the flow equation of the self-energy $\Sigma_\psi(Q) = P_\psi(Q) - P_{\psi,\Lambda}(Q)$ in the symmetric or disordered regime, where the field expectation value of the boson field is zero. The procedure will be extended below to the ordered regime of the flow with a nonvanishing expectation value ϕ_0. In general the self-energy is a 4×4–matrix. For equal population of the two hyperfine states $\sigma = 1, 2$, the most general form of the self-energy can be parametrized by two complex functions $\Sigma_\psi(P)$ and $\Sigma_{\psi,\mathrm{an}}(P)$, where the second one is called the anomalous contribution. We neglect the anomalous self-energy in the following.

The fermions are treated perturbatively but in a *momentum resolved fashion*. Perturbatively here means that we neglect the feedback of the self-energy on the other running couplings. Of course, they can be implemented iteratively, thus enhancing the quantitative precision of the results. We have an additional flow equation for the fermion self-energy shown in Fig. 5.3. In the second line of the figure we replaced the full fermion propagator by the microscopic one, in accordance with our perturbative treatment. Note that all quantities on the right hand side of the flow equation in Fig. 5.3 are known to us and the fermionic self-energy can be readily integrated.

The flow of the inverse fermion propagator, which is identical to the flow of the self-energy, is given in the symmetric regime by

$$\partial_k \Sigma_{\psi,k}(P) = -\bar{h}^2 \int_Q \left\{ \frac{\partial_k \bar{R}_{\phi,k}(Q)}{(\bar{P}_{\phi,k}(Q) + \bar{R}_{\phi,k}(Q))^2} \frac{1}{P_{\psi,k}(Q-P) + R_{\psi,k}(Q-P)} + \frac{\partial_k R_{\psi,k}(Q)}{(P_{\psi,k}(Q) + R_{\psi,k}(Q))^2} \frac{1}{\bar{P}_{\phi,k}(Q+P) + \bar{R}_{\phi,k}(Q+P)} \right\}. \tag{5.47}$$

We emphasize that the external momentum P is a free parameter and for each P we have an individual flow equation. The Feshbach or Yukawa coupling $\bar{h}$ does not depend on momentum in our truncation. We also neglect a possible scale

dependence of $\bar{h}$. The expressions $P_{\psi,k}(Q) = P_{\psi,\Lambda}(Q) + \Sigma_{\psi,k}(Q)$ and $\bar{P}_{\phi,k}(Q)$ are the full inverse propagators at scale k. We have

$$P_{\psi,\Lambda}(Q) = \mathrm{i}q_0 + q^2 - \mu. \tag{5.48}$$

Since the boson propagator is gapped for $k \gg k_{\mathrm{ph}}$, where k_{ph} is a physical scale given by either the inverse scattering length, temperature or chemical potential, we effectively only have a nonvanishing contribution to Eq. (5.47) for $k \lesssim k_{\mathrm{ph}}$. Choosing a large external momentum $p^2 \gg k_{\mathrm{ph}}^2 \geq k^2$, we can use the property $\lim_{q^2/k^2\to\infty} R_k(Q) = 0$ of the regulator functions $R_k(Q)$ to approximate

$$P_k(Q \pm P) + R_k(Q \pm P) \simeq P_k(\pm P). \tag{5.49}$$

Thus, for large external momentum p^2, the flow of the self-energy simplifies according to

$$\begin{aligned}\partial_k \Sigma_{\psi,k}(P) \simeq &- \frac{\bar{h}^2}{P_{\psi,k}(-P)} \int_Q \frac{\partial_k \bar{R}_{\phi,k}(Q)}{(\bar{P}_{\phi,k}(Q) + \bar{R}_{\phi,k}(Q))^2} \\ &- \frac{\bar{h}^2}{\bar{P}_{\phi,k}(P)} \int_Q \frac{\partial_k R_{\psi,k}(Q)}{(P_{\psi,k}(Q) + R_{\psi,k}(Q))^2}.\end{aligned} \tag{5.50}$$

We now show that this results in an asymptotic self-energy $\Sigma_\psi = \Sigma_{\psi,k=0}$ of the form

$$\Sigma_\psi(P) \simeq \frac{4C}{P_{\psi,\Lambda}(-P)} - \delta\mu. \tag{5.51}$$

The first term in Eq. (5.50) yields the contact term. Indeed, for large external momenta P, renormalization effects on the fermion propagator are small and we can approximate $P_{\psi,k}(-P) \simeq P_{\psi,\Lambda}(-P)$. We then find the P-dependent term being multiplied by an integral which receives contributions from the physical scales k_{ph}. Since $P_{\psi,\Lambda}(-P)$ is k-independent, we can integrate the first term in Eq. (5.50) and identify the contact as being given by

$$\begin{aligned}4C &= -\int_\Lambda^0 \mathrm{d}k \bar{h}^2 \int_Q \frac{\partial_k \bar{R}_{\phi,k}(Q)}{(\bar{P}_{\phi,k}(Q) + \bar{R}_{\phi,k}(Q))^2} \\ &= \int_\Lambda^0 \mathrm{d}k \tilde{\partial}_k \int_Q \frac{\bar{h}^2}{\bar{P}_{\phi,k}(Q) + \bar{R}_{\phi,k}(Q)}.\end{aligned} \tag{5.52}$$

In the second line, we introduced the formal derivative $\tilde{\partial}_k$, which only acts on the k-dependence of the regulator R_k. The advantage of this rewriting is to make the simple one-loop structure of the equations manifest. Eq. (5.52) allows us to define a scale dependent contact C_k according to the flow equation

$$\partial_k C_k = \frac{\bar{h}^2}{4} \tilde{\partial}_k \int_Q \frac{1}{\bar{P}_{\phi,k}(Q) + \bar{R}_{\phi,k}(Q)} \tag{5.53}$$

with $C_\Lambda = 0$ and $C_{k=0} = C$. This flow equation and its generalization to the ordered regime are the basis for our numerical evaluation of C in Sec. 5.1.5.

The second term in Eq. (5.50) contains the boson propagator evaluated for large momentum. Since the microscopic boson propagator is constant and the momentum dependence only builds up due to the renormalization group flow, this contribution to the fermion self-energy is independent of P and constitutes a shift of the effective chemical potential. The asymptotic value is then equal to the one evaluated for a large momentum k_{tr}. We conclude

$$\delta\mu = -\int_\Lambda^0 \mathrm{d}k \frac{\bar{h}^2}{\bar{m}_\phi^2} \tilde{\partial}_k \int_Q \frac{1}{P_{\psi,k}(Q) + R_{\psi,k}(Q)}. \tag{5.54}$$

With the effective four-fermion vertex $-\bar{h}^2/\bar{m}_\phi^2 = \lambda_\psi$ we find $\delta\mu = -\lambda_\psi n_{\psi\sigma}$.

Contact term in the ordered regime

For low enough temperatures, a nonvanishing expectation value $\rho_{0,k}$ of the boson field $\rho = \phi^*\phi$ appears during the renormalization group flow. If $\rho_{0,k=0} = \rho_0 > 0$, we say that the system is in its superfluid phase and some of the bosons have condensed. Note that, due to interactions, the condensate fraction does not coincide with the superfluid fraction. Above the critical temperature there is a region where a nonvanishing value of $\rho_{0,k}$ appears for $k > 0$ during the flow, but does not persist for $k \to 0$. We then arrive in the symmetric (normal) phase of the system. We may call this intermediate region the precondensation regime. It is characterized by local but not global superfluid order.

Conceptually the above derivation of the flow of the self-energy and the asymptotic scaling with contact term $\sim 4C/P_{\psi,\Lambda}(-P)$ remains valid also in the presence of a possibly nonvanishing boson field expectation value. We write

$$\Sigma(P) = \begin{pmatrix} \Sigma_{\psi,\mathrm{an}}(P)\varepsilon & -\Sigma_\psi(-P) \\ \Sigma_\psi(P) & -(\Sigma_{\psi,\mathrm{an}}(P))^*\varepsilon \end{pmatrix}, \tag{5.55}$$

with

$$\begin{aligned} \Sigma_{\psi,k}(P) &= P_{\psi,k}(P,\rho_{0,k}) - P_{\psi,\Lambda}(P,\rho_{0,k}) \\ &= P_{\psi,k}(P,\rho_{0,k}) - \Big(\mathrm{i}p_0 + p^2 - \mu\Big). \end{aligned} \tag{5.56}$$

The complex functions $\Sigma_\psi(P)$ and $\Sigma_{\psi,\mathrm{an}}(P)$ are called (normal) self-energy and anomalous self-energy, respectively. The parametrization in Eq. (5.55) is the most general form of the self-energy in the spin-balanced case of equal chemical potentials for the hyperfine components.

Evaluating the self-energy for each k on the expectation value $\rho_{0,k}$ of the bosonic field properly takes into account the fluctuations on different scales. As a result,

the flow equation of the $\psi_1^*\psi_1$-component of Σ_k (i.e. the normal contribution) is given by

$$\partial_t \Sigma_{\psi,k}(P) = (\eta_\phi \rho_{0,k} + \partial_t \rho_{0,k}) \frac{\partial \Sigma_{k,\psi}}{\partial \rho}(P, \rho_{0,k}) + \underbrace{\Big(\partial_t|_{\bar\rho} \Sigma_{\psi,k}\Big)(P, \rho_{0,k})}_{\text{diagram}}. \tag{5.57}$$

The derivative is performed for fixed $\bar\rho$. On the right hand side, the self-energy appears as a function of the background field, whereas the left hand side only depends on k and P. We indicated that the last term in Eq. (5.57) is the actual diagrammatic contribution to the beta function.

Within our truncation we have for this term

$$\begin{aligned}\Big(\partial_t|_{\bar\rho} \Sigma_{\psi,k}\Big)(P, \rho_0) = \; & h^2 \int_Q \frac{\dot{\bar R}_\phi}{A_\phi} \frac{\Big(S_\phi^2 q_{0,B}^2 - 2(\mathrm{i} S_\phi q_{0,B} + \lambda\rho_0)(\lambda\rho_0 + p_\phi(\vec q)) - p_\phi^2(\vec q)\Big)}{\det{}_B^2(Q)} \\ & \times \frac{\Big(\mathrm{i}(p_0 + q_{0,B}) + p_\psi(\vec q + \vec p)\Big)}{\det_F(Q+P)} \\ & - h^2 \int_Q \dot R_\psi \frac{\Big(\mathrm{i} S_\phi (p_0 + q_{0,F}) - \lambda\rho_0 - p_\phi(\vec q + \vec p)\Big)}{\det_B(Q+P)} \\ & \times \frac{\Big(q_{0,F}^2 + 2\mathrm{i} q_{0,F} p_\psi(\vec q) + h^2\rho_0 - p_\psi^2(\vec q)\Big)}{\det_F^2(Q)},\end{aligned} \tag{5.58}$$

with $q_{0,B} = 2\pi n T$ and $q_{0,F} = 2\pi(n+1/2)T$ being bosonic or fermionic Matsubara frequencies, respectively, and $p_0 = 2\pi(m+1/2)T$. We introduced

$$\det{}_B(Q) = S_\phi^2 q_{0,B}^2 + p_\phi(\vec q)(p_\phi(\vec q) + 2\lambda\rho_0), \tag{5.59}$$

$$\det{}_F(Q) = q_{0,F}^2 + p_\psi^2(\vec q) + h^2\rho_0 \tag{5.60}$$

and used $p_\psi = q^2 - \mu + R_\psi(q^2)$, $p_\phi = q^2/2 + m_\phi^2 + R_\phi(q^2)$. The Matsubara summations can be performed analytically and we arrive at an explicit expression for the third term in the flow equation (5.57).

The flow equation for $\Sigma_{\psi,k}(P)$ is valid for arbitrary values of P. For large P, the equation simplifies considerably and, eventually, allows to derive the renormalization group flow of the contact C_k. We restrict the following discussion to the first integral in Eq. (5.58), which is responsible for the high momentum behavior. We have

$$\frac{\mathrm{i}(p_0 + q_0) + p_\psi(Q+P)}{\det_F(Q+P)} \simeq \frac{1}{-\mathrm{i}p_0 + p^2 - \mu} \tag{5.61}$$

for large p^2 and find

$$\Big(\partial_t|_{\bar\rho} \Sigma_{\psi,k}\Big)(P, \bar\rho) \simeq \frac{(\partial_t|_{\bar\rho} \bar c_k)(\bar\rho)}{P_{\psi,\Lambda}(-P)} \tag{5.62}$$

with

$$(\partial_t|_{\bar\rho}\bar c_k)(\bar\rho) = h^2\int_Q \frac{\dot{\bar R}_\phi(\vec q^{\,2})}{A_\phi}\frac{S_\phi^2 q_{0,B}^2 - 2(\mathrm{i}S_\phi q_{0,B}+\lambda\rho_0)(\lambda\rho_0+p_\phi(\vec q)) - p_\phi^2(\vec q)}{\det{}_B^2(Q)}$$
$$= h^2\int_{\vec q}\frac{\dot{\bar R}_\phi}{A_\phi}T\sum_n\Big(\frac{1}{\det_B(Q)} - \frac{2S_\phi^2\omega_{\phi,k}^2+2\lambda^2\rho_0^2}{\det_B^2(Q)}\Big). \tag{5.63}$$

For the definition of $\omega_{\phi,k}$ see Eq. (5.74).

We define the flowing contact according to

$$C_k = \frac{1}{4}c_k(\rho_{0,k}), \tag{5.64}$$

where $c_k(\rho) := \bar c_k(\bar\rho)$ is expressed in terms of the normalized field $\rho = \bar\rho A_\phi$. Since

$$c(k,\rho) = \bar c(k,\bar\rho(\rho,k)) \tag{5.65}$$

we have

$$\frac{\partial c}{\partial k} = \frac{\partial \bar c}{\partial k} + \frac{\partial \bar c}{\partial\bar\rho}\cdot\left(\frac{\partial\bar\rho}{\partial k}\right)_\rho = \frac{\partial\bar c}{\partial k} + \frac{1}{k}\eta_\phi\bar\rho\frac{\partial\bar c}{\partial\bar\rho}, \tag{5.66}$$

$$\frac{\partial c}{\partial\rho} = \frac{1}{A_\phi}\frac{\partial\bar c}{\partial\bar\rho}. \tag{5.67}$$

From these two relations we deduce the flow equation for $c_k(\rho)$ in the presence of the k–dependent background field $\rho = A_\phi\bar\rho$ to be given by

$$(\partial_t|_\rho c_k)(\bar\rho) = (\partial_t|_{\bar\rho}\bar c_k)(\bar\rho=\bar\rho(\rho)) + \eta_\phi\rho\frac{\partial c_k}{\partial\rho}(\rho). \tag{5.68}$$

Thus we arrive at

$$\partial_t C_k = \frac{1}{4}\Big((\partial_t|_{\bar\rho}\bar c_k)(\rho_{0,k}) + (\eta_\phi\rho+\partial_t\rho_{0,k})\frac{\partial c_k}{\partial\rho}(\rho_{0,k})\Big). \tag{5.69}$$

We show that $\partial c/\partial\rho = h^2 + \mathcal{O}(\Sigma_\psi)$. For this purpose we consider the limit of classical fermion propagators $P_\psi(Q) = P_{\psi,\Lambda}(Q) = \mathrm{i}q_0 + q^2 - \mu$. For the momentum distribution per species we have

$$n_{\psi,\vec q\sigma} = -\Big(T\sum_n\frac{P_{\psi,\Lambda}(-Q)}{P_{\psi,\Lambda}(Q)P_{\psi,\Lambda}(-Q)+h^2\rho} - \frac{1}{P_{\psi,\Lambda}(Q)}\Big)$$
$$= T\sum_n\frac{h^2\rho}{P_{\psi,\Lambda}(Q)\Big[P_{\psi,\Lambda}(Q)P_{\psi,\Lambda}(-Q)+h^2\rho\Big]}$$
$$\simeq \frac{h^2\rho}{2\sqrt{q^4+h^2\rho}\Big(\sqrt{q^4+h^2\rho}+q^2\Big)} \simeq \frac{h^2\rho}{4q^4} \tag{5.70}$$

for large q. Whereas the Fermi–Dirac distribution decays exponentially for large q, a q^4-tail arises from the presence of a bosonic background field with contact parameter $C = h^2\rho/4$. This completes the proof of

$$\frac{\partial c}{\partial \rho}(\rho_{0,k}) = h^2 + \mathcal{O}(\Sigma_\psi). \tag{5.71}$$

The flow equation for the contact becomes

$$\partial_t C_k = \frac{h^2}{4}(\eta_\phi \rho_{0,k} + \partial_t \rho_{0,k}) + \frac{h^2}{4}\int_{\vec{q}} \frac{\dot{\tilde{R}}_\phi}{A_\phi} T \sum_n \Big(\frac{1}{\det_B(Q)} - \frac{2S_\phi^2 \omega_{\phi,k}^2 + 2\lambda^2\rho_0^2}{\det_B^2(Q)} \Big). \tag{5.72}$$

The result of the Matsubara summation and the $\vec{q}$–integration is given by

$$\begin{aligned}\partial_t C_k = \frac{h^2}{4}(\eta_\phi \rho_{0,k} + \partial_t \rho_{0,k}) + \frac{2^{d/2+1} v_d}{d}\frac{h^2}{S_\phi^2} k^{d+2}\Big(1 - \frac{\eta_\phi}{d+2}\Big)\Big[N_B'(\omega_{\phi,k}) \\ - \frac{\lambda^2\rho_0^2}{S_\phi^2 \omega_{\phi,k}^3}\Big(\frac{1}{2} + N_B(\omega_{\phi,k}) - \omega_{\phi,k} N_B'(\omega_{\phi,k})\Big)\Big],\end{aligned} \tag{5.73}$$

with

$$\omega_{\phi,k} = \frac{\sqrt{(k^2 + m_{\phi,k}^2)(k^2 + m_{\phi,k}^2 + 2\lambda_k \rho_{0,k})}}{S_\phi}. \tag{5.74}$$

The Bose function is defined as $N_B(z) = (e^{z/T} - 1)^{-1}$ and $N_B' = \mathrm{d}N_B/\mathrm{d}z$. Typical renormalization group flows of C_k for the UFG are shown in Fig. 5.4.

At zero temperature we obtain a nonvanishing value for the contact C. The corresponding value is found from Eq. (5.73) by setting the Bose functions to zero. We have

$$\partial_t C_k|_{T=0} = \frac{h^2}{4}(\eta_\phi \rho_{0,k} + \partial_t \rho_{0,k}) - \frac{2^{d/2} v_d}{d}\frac{h^2 \lambda^2 \rho_0^2}{S_\phi^4 \omega_{\phi,k}^3} k^{d+2}\Big(1 - \frac{\eta_\phi}{d+2}\Big). \tag{5.75}$$

In the limit where the density is dominated by the superfluid density of condensed bosons, the first term in Eq. (5.73) dominates. For small anomalous dimension η_A and neglecting the running of h^2 this yields the simple relation

$$C \approx \frac{h^2}{4}\rho_0, \tag{5.76}$$

which coincides with Eq. (5.31) for $n_\varphi \approx \rho_0$.

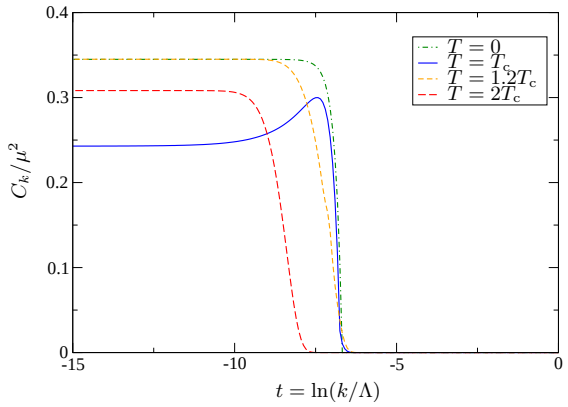

Figure 5.4: RG-scale dependence of the flowing contact C_k at unitarity $a^{-1} = 0$. We have $k = \Lambda e^t$ such that $t = 0$ corresponds to the ultraviolet and $t \to -\infty$ to the infrared. We observe that the contact is unaffected by fluctuations of ultraviolet modes and it starts to build up on the many-body scales of the system, which are set here by the chemical potential and temperature corresponding to $t_\mu = \ln(\mu^{1/2}/\Lambda) = -6.9$ and $t_T \simeq t_\mu$. Obviously, all curves saturate at a certain value of t and we can read off the physical value at $k = 0$. Figure taken from Boettcher et al. [2013].

5.1.4 Relation between Tan contact and boson density

To clarify the relation between $\partial_t C_k$ and $\partial_t n_{\phi,k}$, we consider the scale-dependent density n_k defined by

$$n_k = -\frac{\partial U_k}{\partial \mu}(\rho_{0,k}). \tag{5.77}$$

The μ-derivative is performed for fixed R_ψ. For $k = 0$ we arrive at the physical density

$$n = \frac{\partial P(\mu, T)}{\partial \mu} = -\frac{\partial U(\mu, T, \rho_0)}{\partial \mu} \tag{5.78}$$

with pressure $P(\mu, T)$. The corresponding flow equation is given by

$$\partial_t n_k = -\alpha_\phi(\eta_\phi \rho_{0,k} + \partial_t \rho_{0,k}) - \left(\partial_\mu \partial_t|_{\tilde{\rho}} U_k\right)(\rho_{0,k}). \tag{5.79}$$

with

$$\alpha_\phi = \frac{\partial^2 U}{\partial \mu \partial \rho}(\rho_{0,k}). \tag{5.80}$$

The flow of the effective potential receives contributions from bosonic and fermionic fluctuations. Defining

$$\partial_t n^{(U)}_{\phi,k} = -\Big(\partial_\mu \partial_t|_{\bar\rho} U^{(B)}_k\Big)(\rho_{0,k}), \tag{5.81}$$

$$\partial_t n^{(U)}_{\psi,k} = -\Big(\partial_\mu \partial_t|_{\bar\rho} U^{(F)}_k\Big)(\rho_{0,k}) \tag{5.82}$$

as the bosonic or fermionic contribution, respectively, we can employ

$$\Big(\partial_t|_{\bar\rho} U^{(B)}_k\Big)(\rho) = \int_Q \frac{\dot{\bar R}_\phi}{A_\phi} \frac{k^2 + U'_k(\rho) + \rho U''_k(\rho)}{[k^2 + U'(\rho) + 2\rho U''_k(\rho)][k^2 + U'(\rho)] + S^2_\phi q^2_0} \tag{5.83}$$

to find

$$\partial_t n^{(U)}_{\phi,k} = -\alpha_\phi \int_Q \frac{\dot{\bar R}_\phi}{A_\phi}\Big(\frac{1}{\det{}_B(Q)} - \frac{2S^2_\phi \omega^2_{\phi,k} + 2\lambda^2\rho^2_0}{\det{}^2_B(Q)}\Big). \tag{5.84}$$

This is precisely the third term in the flow equation (5.63) for C_k. We can summarize these findings in the generally valid relation

$$\partial_t C_k = -\frac{h^2}{4\alpha_\phi}\Big(-\alpha_\phi(\eta_\phi \rho_{0,k} + \partial_t \rho_{0,k}) + \partial_t n^{(U)}_{\phi,k}\Big) = -\frac{h^2}{4\alpha_\phi}\Big(\partial_t n_k - \partial_t n^{(U)}_{\psi,k}\Big), \tag{5.85}$$

where $n^{(U)}_{\phi/\psi,k}$ are contributions which arise from effects of bosonic/fermionic fluctuations on the effective potential and hence the density. In contrast, the term $-\alpha_\phi(\eta_\phi\rho_{0,k} + \partial_t\rho_{0,k})$ accounts for the nontrivial scaling of the renormalized propagator and the contribution from condensed bosons.

In the BEC limit, Eq. (5.85) simplifies considerably. Indeed, following the flow of C_k from $k = \Lambda$ to $k = 0$ we see that in the early stages of the flow, where k is much larger than the many body-scales set by μ and T, the flow of C_k is zero, because $\rho_{0,k} = 0$ and there are no bosonic fluctuations on high energy scales. Hence

$$\partial_k C_k = 0 \quad \text{for } k \gg \mu^{1/2}, T^{1/2}. \tag{5.86}$$

However, the flow of the prefactor $h^2/\alpha_\phi = \bar h^2/\bar\alpha_\phi$ is governed by the scale set by the scattering length a^{-1}. On the far BEC side, this quantity is large and these renormalization effects set in far above the many-body scales. At such high scales the vacuum relation $\bar\alpha_{\phi,k} = -2Z_{\phi,k}$, with wave function renormalization $Z_{\phi,k}$ of the bosons, is valid. The relation stems from the appearance of the combination $Z_{\phi,k}(\partial_\tau - 2\mu)$ in the propagator due to semi-local U(1)–invariance and the symmetry preserving nature of the flow equation. One can show that the vacuum flow of $Z_{\phi,k}$ is solved by $Z_{\phi,k=0} = \bar h^2 a/32\pi$ on the BEC side (Diehl et al. [2007a]), i.e.

$$-\frac{\bar h^2}{4\bar\alpha_\phi} \to \frac{4\pi}{a} \text{ for } k \gg \mu^{1/2}, T^{1/2}. \tag{5.87}$$

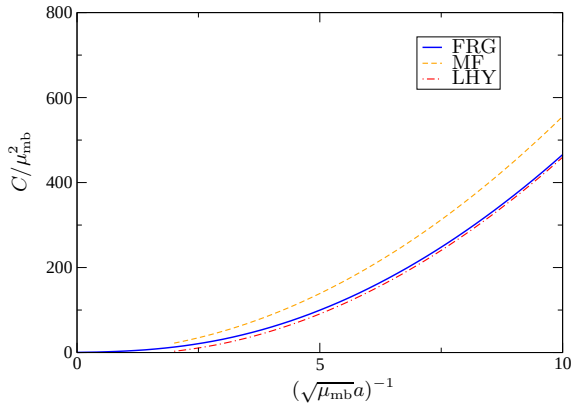

Figure 5.5: Zero temperature contact on the BEC side of the crossover. The many-body chemical potential is defined as $\mu_{\rm mb} = \mu - \varepsilon_{\rm B}/2$ and thus is a positive quantity. (See for instance Eq. (5.12) in the context of a weakly interacting Bose gas.) The FRG treatment captures the Lee–Huang–Yang (LHY) correction, see. Eq. (5.16). Mean field theory (MF) is shown by the dashed curve. Figure taken from Boettcher et al. [2013].

This prefactor effectively enters the renormalization group equation of C_k which takes place on the many-body scales and thus we can write

$$\partial_k C_k = \frac{4\pi}{a} \partial_k n_{\phi,k}. \tag{5.88}$$

Due to the fact that there are no fermion fluctuations contributing to the density on the BEC side, we have $n_{\phi,k} = n_k$ and thus arrive at the well-known relation $C_{\rm BEC} = 4\pi n/a$. The mean field result $C_{\rm BEC} = 4\pi n/a$ receives corrections from bosonic fluctuations, which are incorporated in the renormalization group flow.

5.1.5 Results of the FRG analysis

Within the above truncation scheme we can compute the contact as a function of the crossover parameters μ, T, and a. Moreover, the high momentum factorization of the self-energy can be shown explicitly by solving the flow equation for $\Sigma_\psi(P)$ for different values of P. In order to translate the results expressed in terms of the chemical potential for the density, the equation of state $P(\mu, T)$ has to be applied. Since the density (and, iteratively, the contact itself) receives substantial contributions from the contact term in the fermion self-energy, fully self-consistent results can only be obtained from a self-consistent treatment of the Tan term in the flow equations. Here we restrict to an analysis of the qualitative behavior of the contact and do not aim at quantitative precision.

The result of the integration of the renormalization group equations at zero temperature on the BEC side is given in Fig. 5.5. We find excellent agreement

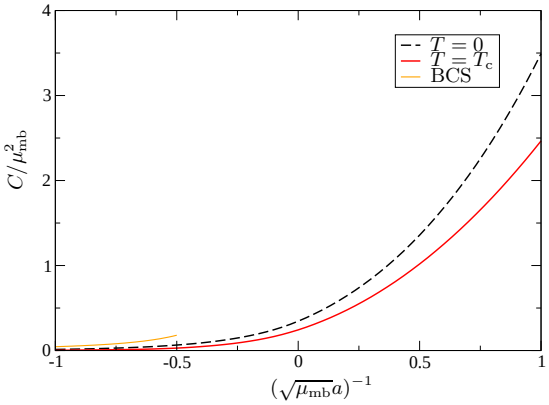

Figure 5.6: The contact close to resonance as a function of the scattering length for both $T = 0$ and $T = T_c(a, \mu)$. The labels of the axes are analogous to Fig. 5.5. At unitarity we obtain $C(T = 0)/\mu^2 = 0.34$ and $C(T = T_c)/\mu^2 = 0.24$. Far on the BCS side our present truncation becomes inappropriate as is discussed in the main text. For better visibility we show the asymptotic BCS/Fermi liquid value up to $(\sqrt{\mu}a)^{-1} = -0.5$, which is already beyond the applicability of BCS theory. Figure taken from Boettcher et al. [2013].

with the prediction from LHY theory, whereas the mean field curve deviates substantially. From Eq. (5.85) it is apparent that the LHY correction, which is reproduced in the equation of state on the BEC side as well, is also visible in the contact, because both share a common flow equation. The nontrivial renormalization of the prefactor in Eq. (5.85) ensures the result to be beyond mean field.

As we approach unitarity from the BEC side, we leave the perturbative regime, and the contact is no longer described by the LHY expression. The FRG result within the truncation of this work is shown in Fig. 5.6. For $a^{-1} = 0$ we find $C/\mu^2 = 0.34$ and $C/k_F^4 = 0.11$ at zero temperature. The Bertsch parameter within this approximation is $\xi = 0.55$. We observe the contact to be a monotonous function of the crossover parameter $(\sqrt{\mu_{mb}}a)^{-1}$, or, equivalently, $(k_F a)^{-1}$.

For negative scattering lengths we find our zero temperature results to be far below the BCS/Fermi liquid prediction. The reason for the failure of the present truncation is that the momentum dependence of the boson propagator is not well-approximated by a derivative expansion on the BCS side, although momentum independent observables like the equation of state are described correctly. This becomes transparent in the derivation of the relation $C_{BCS} = 4\pi^2 n^2 a^2$ from the DSE (5.46), where we explicitly use the momentum dependence of the bosonic self-energy $\Sigma_\varphi(Q)$.

In Fig. 5.6 we also show the value of the critical contact $C(T_c, a)$ in the crossover. We find the corresponding value always to be below the zero tem-

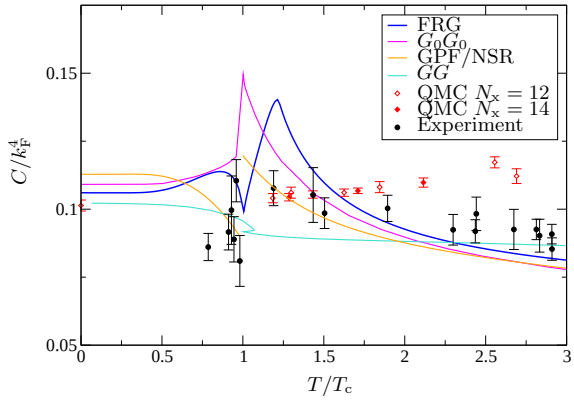

Figure 5.7: The contact of the UFG normalized by k_F^4 with Fermi momentum $k_F = (3\pi^2 n)^{1/3}$. We compare predictions from Functional Renormalization Group (FRG, this work, $T_c/T_F = 0.276$), non-self-consistent T-matrix theory (G_0G_0: Palestini et al. [2010], $T_c/T_F = 0.242$), Gaussian pair fluctuations and Nozières–Schmitt-Rink theory (GPF/NSR: Hu et al. [2011], $T_c/T_F = 0.235$), self-consistent T-matrix theory (GG: Enss et al. [2011], $T_c/T_F = 0.15$) and Quantum Monte Carlo calculations (QMC: Drut et al. [2011], $T_c/T_F = 0.15$) for lattice sizes $N_x = 12, 14$. In this list, the brackets indicate the label in the plot, the corresponding reference and the chosen value for the critical temperature. For the experimental data of Sagi et al. [2012] we employed $T_c/T_F = 0.16$, which suffices here to obtain a qualitative comparison of the data. Figure taken from Boettcher et al. [2013].

perature value. The full temperature dependence of the contact of the unitary Fermi gas is shown in Figs. 5.7 and 5.8. We observe a sharp dip at the critical temperature, hence $C(0) > C(T_c)$ in Fig. 5.6. Since the contact is related to a first derivative of the energy (or pressure) according to the adiabatic sweep theorem, it has to be continuous at T_c as a result of the second order nature of the phase transition. We confirm this behavior in our results with a critical contact parameter $C(T = T_c)/k_F^4 = 0.11$. The contact C/k_F^4 shows a maximum above T_c.

Fig. 5.7 also compares our result for C/k_F^4 to other theoretical approaches and to a recent experimental measurement of the homogeneous contact. Due to the disagreement of predictions for T_c/T_F from different theoretical methods, we have rescaled the abscissa by the corresponding critical temperatures. This allows to compare the qualitative features of the temperature dependence like monotony or location of peaks and minima. In order to relate the contact C in Fig. 5.7 to an extensive contact $\bar{C} = CV$ with volume V we use $\bar{C}/Nk_F = 3\pi^2 C/k_F^4$, see our discussion of the normalization in the introduction. The Fermi momentum of the FRG data in Fig. 5.7 is not corrected due to the high momentum contribution to the particle number density. Hence, k_F will in general be larger than plotted

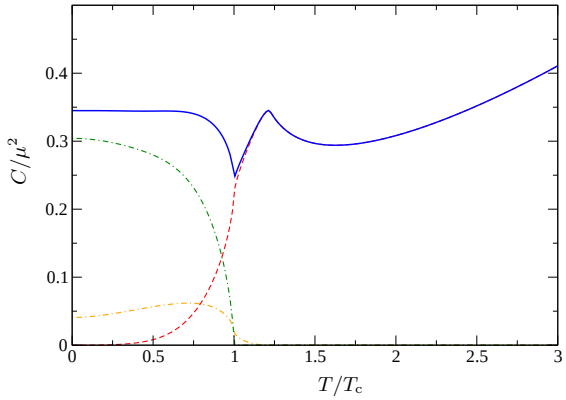

Figure 5.8: The blue solid line shows the temperature dependence of the contact normalized by the chemical potential for the UFG. We observe a decrease of C/μ^2 as we approach the critical temperature from below, resulting in a sharp dip at T_c. The function is monotonic for $T/T_c \gtrsim 1.75$. The green, red, and orange curves correspond to different contributions to the contact and are explained in Eqs. (5.89)–(5.91). Figure taken from Boettcher et al. [2013].

here.

We find largely different predictions for the temperature dependence of the contact in the critical region. This indicates a sensitivity of this observable with respect to approximations in theoretical calculations, which makes further investigation even more interesting. Note that for higher temperatures, the second and third order virial expansions by Hu et al. [2011] allow for a solid comparison of the temperature dependence of the contact. However, we focus here on the region around T_c, which is well-captured by our truncation of the effective action.

From Eq. (5.73) we observe that the contact receives contributions from different terms in the flow equation. These are important in distinct regimes of the system. To visualize this, we split up the flow of C_k into three parts according to $\partial_t C_k = \partial_t C_k^{(1)} + \partial_t C_k^{(2)} + \partial_t C_k^{(3)}$ with

$$\partial_t C_k^{(1)} = \frac{h^2}{4}(\eta_\phi \rho_{0,k} + \partial_t \rho_{0,k}), \tag{5.89}$$

$$\partial_t C_k^{(2)} = \frac{2^{d/2+1} v_d}{d} \frac{h^2}{S_\phi^2} k^{d+2} \Big(1 - \frac{\eta_\phi}{d+2}\Big) N_B'(\omega_{\phi,k}), \tag{5.90}$$

$$\begin{aligned} \partial_t C_k^{(3)} = {} & \frac{2^{d/2+1} v_d}{d} \frac{h^2}{S_\phi^2} k^{d+2} \Big(1 - \frac{\eta_\phi}{d+2}\Big) \\ & \times \Big(-\frac{\lambda^2 \rho_0^2}{S_\phi^2 \omega_{\phi,k}^3}\Big)\Big(\frac{1}{2} + N_B(\omega_{\phi,k}) - \omega_{\phi,k} N_B'(\omega_{\phi,k})\Big). \end{aligned} \tag{5.91}$$

The only term which persists in the stages of the flow where $\rho_{0,k} = 0$, is $C_k^{(2)}$.

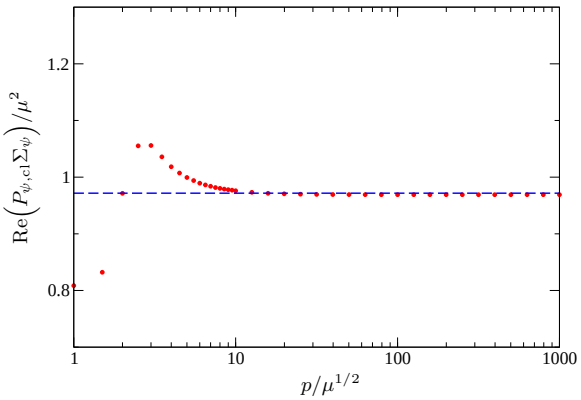

Figure 5.9: The asymptotic approach of the contact for the UFG at the critical temperature. We plot the real part of $P_{\psi,\mathrm{cl}}(-P)\Sigma_\psi(P)$ with $P_{\psi,\mathrm{cl}}(-P) = -\mathrm{i}p_0 + \vec{p}^2 - \mu$ and $p_0 = \pi T$ (red dots). In accordance with formula (5.4), the factorization at large momenta leads to the approach of the constant value $4C$ (blue dashed line). For very low momenta our perturbative treatment of the fermion propagator becomes quantitatively less accurate, but still the deviations do not exceed 20% even for $p \to 0$. We restrict the self-energy here to the diagram in Fig. 5.3 where the external momentum P appears in the fermion line and which is responsible for the contact term. Figure taken from Boettcher et al. [2013].

Therefore, it is the leading contribution above T_c (red dashed line in Fig. 5.8). Both $C_k^{(1)}$ and $C_k^{(3)}$ start to build up in the precondensation phase. However, $C_k^{(3)}$ is never really large (orange dashed-dotted line in Fig. 5.8). For small T, the contribution from $C_k^{(1)}$ dominates (green dashed-dotted line in Fig. 5.8). Above T_c this contribution is negligible. In the zero temperature limit, the term $C_k^{(1)}$ becomes most important. This can be understood easily from Eq. (5.79), where we identify this term as the contribution from condensed bosons to the density.

We already addressed the question whether the scaling formula (5.4) can be applied for a large part of the momenta or only yields an asymptotic, but practically irrelevant contribution. For this purpose we solve the flow equation for the self-energy $\Sigma_{\psi,k}(P)$ on a grid of P-values according to Eq. (5.58). Therein we restrict to the first integral, which corresponds to the diagram in Fig. 5.3 where the external momentum appears in the fermion line. Only this diagram contributes to the contact. The universal regime of validity is expected to be large for the UFG. In Figs. 5.9 and 5.10 we underline this statement at $T = T_\mathrm{c}$ and $a^{-1} = 0$.

Since the self-energy $\Sigma_\psi(P)$ is a complex valued function of $P = (p_0, \vec{p})$, we gain information about the high momentum behavior from plotting both the real and imaginary part at the lowest possible fermionic Matsubara frequency $p_0 = \pi T$ as a function of $|\vec{p}|$. To see the asymptotic approach of the form $P_{\psi,\mathrm{cl}}(-P)\Sigma_\psi \simeq 4C$ we

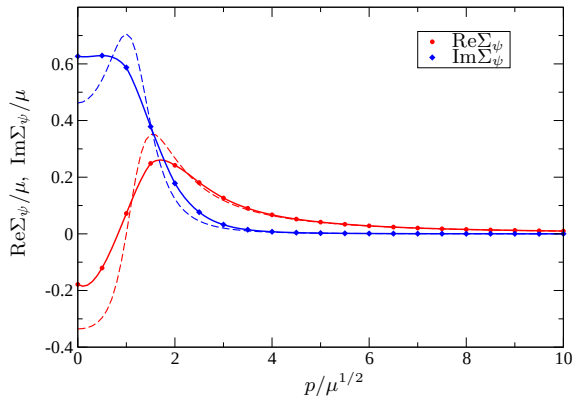

Figure 5.10: The fermion self-energy $\Sigma_{\psi,k=0}(P)$ at $a^{-1} = 0$ and $T = T_c$ computed from the first diagram in Fig. 5.3. We evaluate the function for $p_0 = \pi T$ and find the large momentum behavior to be a reasonable approximation for both the real and imaginary parts even at low momenta. The asymptotic form (5.4) is shown by a dashed line. The self-energy vanishes for large momenta since we effectively added the constant $\delta\mu$ for $p \to \infty$ by neglecting the second diagram in Fig. 5.3. Figure taken from Boettcher et al. [2013].

plot the real part of this particular combination in Fig. 5.9. The imaginary part of this product vanishes for $p \to \infty$, showing that the contact indeed is real-valued.

We plot $\mathrm{Re}\Sigma_\psi(P)$ and $\mathrm{Im}\Sigma_\psi(P)$ in Fig. 5.10 for the same set of parameters as before. We find that the scaling form is a good description for all momenta at the critical temperature. Although this does not come unexpected for a scale invariant, critical system, this behavior could be a relict of our perturbative treatment of the propagator for small momenta, where this is not necessarily a valid assumption. Further improvement of the truncation and iterative solution of the flow equation will shed light on the reliability of this finding, but is beyond the scope of the present work.

5.2 Unitary Fermi Gas

In this section we compute the critical temperature and the superfluid gap of the spin-balanced UFG. The focus is on quantitative precision and the comparison of different truncation and regularization schemes.

5.2.1 Mean field analysis

The simplest truncation capturing the superfluid phase transition for all values of the scattering length consists in mean field theory. The latter is built on a saddle-point approximation to the effective action. We first review the mean

field predictions for the zero temperature gap Δ/μ and the critical temperature T_c/μ. Then we discuss how the mean field approximation is recovered in an FRG framework by taking into account fermionic diagrams (F), but neglecting bosonic fluctuations.

From a saddle-point expansion of the effective action we obtain the effective potential in mean field approximation

$$U(\Delta^2,\mu,T) = -\frac{\Delta^2}{\lambda_{\psi,\Lambda}} - \int_Q^\Lambda \log\Big(q_0^2 + (q^2-\mu)^2 + \Delta^2\Big). \tag{5.92}$$

The UV-divergent integral is regularized by means of a sharp momentum cutoff enforcing $q^2 \leq \Lambda^2$. We impose the vacuum renormalization condition

$$-\frac{1}{\lambda_\psi} \stackrel{!}{=} \frac{\partial U}{\partial \Delta^2}(0,0,0) = -\frac{1}{\lambda_{\psi,\Lambda}} - \frac{1}{2}\int^\Lambda \frac{\mathrm{d}^3 q}{(2\pi)^3}\frac{1}{q^2}, \tag{5.93}$$

where $\lambda_\psi = 4\pi\hbar^2 a/M = 8\pi a$ is related to the fermion scattering length, see Sec. 5.3.1 for a discussion of the vacuum renormalization procedure. The renormalized gap equation at zero temperature reads

$$\begin{aligned} 0 = \frac{\partial U}{\partial \Delta^2}(\Delta_0^2,\mu,0) &= -\frac{1}{\lambda_\psi} - \int_Q^\Lambda \frac{1}{q_0^2 + (q^2-\mu)^2 + \Delta_0^2} + \frac{1}{2}\int^\Lambda \frac{\mathrm{d}^3 q}{(2\pi)^3}\frac{1}{q^2} \\ &= -\frac{1}{\lambda_\psi} - \frac{1}{4\pi^2}\int_0^\infty \mathrm{d}q\Big(\frac{q^2}{\sqrt{(q^2-\mu)^2+\Delta_0^2}} - 1\Big). \end{aligned} \tag{5.94}$$

The integral is UV finite and we can send $\Lambda \to \infty$.

For $\mu > 0$, we can rewrite the gap equation (5.94) in the dimensionless form

$$\frac{\pi}{2\mu^{1/2}a} = f\Big(\frac{\Delta_0}{\mu}\Big) \tag{5.95}$$

with

$$f(y) = -\int_0^\infty \mathrm{d}x\Big(\frac{x^2}{\sqrt{(x^2-1)^2+y^2}} - 1\Big). \tag{5.96}$$

The BCS-formula for an exponentially small gap is obtained from $f(y) \to \log(e^2 y/8)$ for $y \to 0$. We then find

$$\frac{\Delta_{\mathrm{BCS}}}{\mu} = \frac{8}{e^2}\exp\Big(\frac{\pi}{2\mu^{1/2}a}\Big). \tag{5.97}$$

However, this asymptotic formula cannot be applied to the unitary Fermi gas with $a^{-1} = 0$. In this case, the BCS-formula results in $\Delta_0/\mu = 1.083$, whereas the correct solution to the gap equation (5.95) is given by

$$\Delta_0/\mu = 1.162 \text{ for } a^{-1} = 0. \tag{5.98}$$

The gap vanishes at the critical temperature and thus we have

$$0 = \frac{\partial U}{\partial \Delta^2}(0,\mu,T_\mathrm{c}) = -\frac{1}{\lambda_\psi} - \frac{1}{2\pi^2}\int_0^\infty \mathrm{d}q \left[\frac{q^2}{|q^2-\mu|}\Big(\frac{1}{2} - \frac{1}{e^{|q^2-\mu|/T_\mathrm{c}}+1}\Big) - \frac{1}{2}\Big)\right]. \tag{5.99}$$

This can be cast into the form

$$\frac{\pi}{2\mu^{1/2}a} = g\Big(\frac{T_\mathrm{c}}{\mu}\Big), \tag{5.100}$$

where

$$g(y) = -\int_0^\infty \mathrm{d}x \left[\frac{x^2}{|x^2-1|}\Big(1 - \frac{2}{e^{|x^2-1|/y}+1}\Big) - 1\right]. \tag{5.101}$$

For small critical temperatures we can apply $g(y) \to \log(\pi e^2 y/8e^\gamma)$ for $y \to 0$ to obtain the BCS-formula

$$\frac{T_\mathrm{c,BCS}}{\mu} = \frac{8e^\gamma}{\pi e^2}\exp\Big(\frac{\pi}{2\mu^{1/2}a}\Big). \tag{5.102}$$

An extrapolation of this asymptotic formula to the unitary point yields $T_\mathrm{c}/\mu = 0.6138$. In contrast, the solution to Eq. (5.100) is given by

$$T_\mathrm{c}/\mu = 0.6646 \text{ for } a^{-1} = 0. \tag{5.103}$$

The mean field prediction for the ratio Δ/T_c for the Unitary Fermi gas is thus given by $\Delta/T_\mathrm{c} = 1.75$.

We now turn to the FRG analysis. In the mean field limit, there is no feedback of bosonic fluctuations onto the flow of running couplings. Therefore, neither the inverse boson propagator $P_\phi(Q)$, nor the boson regulator $R_\phi(Q)$ appear in the loop integrals. Hence, the mean field limit is a good testbed for benchmarking the implementation of the fermionic diagrams. The set of running couplings consists of the boson anomalous dimension $\eta_\phi = -k\partial_k \log A_\phi$ and the effective potential $U_k(\rho)$. The inverse fermion propagator remains in its initial shape given by $P_\psi(Q) = \mathrm{i}q_0 + q^2 - \mu$.

Considering only fermion diagrams, the n-th derivative of the flow equation for the effective average potential is given by

$$\partial_k \bar{U}_k^{(n)}(\bar{\rho}) = -n!(-\bar{h}^2)^n \int_Q \frac{L_\psi^Q \partial_k R_\psi^{-Q} + L_\psi^{-Q}\partial_k R_\psi^Q}{(L_\psi^Q L_\psi^{-Q} + h^2\rho)^{n+1}}, \tag{5.104}$$

with $L_\psi^Q = P_\psi(Q) + R_\psi(Q)$. The flow of $\bar{u}_n = \bar{U}^{(n)}(\bar{\rho}_0)$ receives an additional contribution proportional to $\partial_k\bar{\rho}_0$. The flow of the n-th expansion coefficient of the effective potential is thus given by

$$\partial_k \bar{u}_n = \partial_k \bar{U}_k^{(n)}(\bar{\rho}_0) + \bar{u}_{n+1}\partial_k\bar{\rho}_0 \tag{5.105}$$

for $n \geq 2$. We emphasize that only due to the second term there is a feedback of the higher couplings $u_3, u_4, \ldots$ onto the remaining couplings. This observation has also been made by Strack et al. [2008]. The flow equations for $\bar{\rho}_0$ and A_ϕ are given in Sec. 4.2.2.

In an FRG treatment, no precondensation appears on the mean field level for the spin-balanced system. Therefore, the symmetric phase is accessible from the symmetric regime of the flow, where $\rho_{0,k} = 0$. In particular, the flow equation for the effective potential is given by the F-diagram with microscopic fermion propagator $\mathrm{i}q_0 + q^2 - \mu$. We then find in the symmetric regime

$$\dot{\bar{U}}'_k(0) = \bar{h}^2 \int_Q \frac{L_\psi^Q \dot{R}_\psi^{-Q} + L_\psi^{-Q} \dot{R}_\psi^Q}{(L_\psi^Q L_\psi^{-Q})^2} = -\partial_t \bar{h}_\Lambda^2 \int_Q \frac{1}{L_\psi^Q L_\psi^{-Q}}, \tag{5.106}$$

since $\bar{h}_k^2 = \bar{h}_\Lambda^2$ and the only k-dependence of $L_\psi^Q = \mathrm{i}q_0 + q^2 - \mu + R_\psi^Q$ arises from the regulator. Eq. (5.106) can readily be integrated to yield

$$\frac{1}{\bar{h}_\Lambda^2}\Big[\bar{U}'(0,\mu,T) - \bar{U}'_\Lambda(0)\Big] = -\int_Q \left(\frac{1}{q_0^2 + (q^2-\mu)^2} - \frac{1}{|\mathrm{i}q_0 + q^2 - \mu + R_{\psi,\Lambda}(Q)|^2} \right). \tag{5.107}$$

We used that $R_{\psi,k=0}(Q) = 0$. The regularization of the UV divergent integral is performed by means of the regulator $R_{\psi,\Lambda}(Q)$, which vanishes for $q_0, q^2 \geq \Lambda^2$ and thus gives finite support to the integration. We have

$$\bar{U}'_\Lambda(0) = \bar{m}^2_{\phi,\Lambda} = -\frac{\bar{h}_\Lambda^2}{\lambda_{\psi,\Lambda}}. \tag{5.108}$$

Accordingly, we reproduce the gap equation (5.99) for $T = T_\mathrm{c}$ and $\bar{U}'(0,\mu,T_\mathrm{c}) = 0$. Therefore, the critical temperature found from the flow equation in the mean field limit trivially coincides with the standard mean field result.

In order to reproduce the gap equation (5.94) we have to include higher orders terms u_n ($n \geq 3$) in the effective potential. The mean field zero temperature gap $\Delta/\mu = 1.162$ provides a benchmark for testing the regulator and truncation dependence of the fermionic contributions to the flow. We find that the quantitative difference between a ϕ^4- and a ϕ^8-truncation is at the 10 percent level. By further extending to a ϕ^{2N}-expansion, the results converge quickly to the expected value. We summarize our findings in Table 5.1.

Due to the absence of a precondensation regime in the mean field treatment, the critical temperature T_c/μ at the mean field level is not affected by terms proportional to $\partial_k \bar{\rho}_0$. Indeed, whenever $\rho_{0,k} > 0$ for some k, we also have $\rho_{0,k=0} > 0$. Accordingly, the correct value is already found in a ϕ^2-truncation, because the condition $m_\phi^2 = 0$ can be satisfied independently of λ_ϕ at the mean field level. Higher orders in a ϕ^{2N}-expansion of the effective potential influence the critical temperature once bosonic diagrams are included in the RG flow.

	Δ/μ		T_c/μ	
Truncation	q^2-opt	Q-exp	q^2-opt	Q-exp
F, ϕ^4	1.045	1.056	0.665	0.664
F, ϕ^8	1.133	1.141	0.665	0.664
F, ϕ^{12}	1.154	1.157	0.665	0.664
F, ϕ^{16}	1.160	1.160	0.665	0.664
F, ϕ^{20}	1.162	1.161	0.665	0.664
F, ϕ^{24}	1.162	1.161	0.665	0.664
Mean field	1.162		0.6646	

Table 5.1: Critical temperature and superfluid gap obtained from the inclusion of fermionic diagrams (F). When including higher order terms in the effective potential, we recover the mean field result for both types of regulators considered in this work. In particular, a ϕ^8-truncation already yields a good approximation to the exact result. The value of T_c/μ is unaffected by this change in truncation, as is discussed in the main text.

5.2.2 Bosonic fluctuations

The boson dynamics emerge in the crossover due to the F-diagram containing two fermion lines. Once built up, the boson propagator has an important impact on the flow of running couplings due to diagrams containing two bosonic lines (B). These bosonic fluctuations are particularly important for an accurate description of the superfluid phase transition. We find here that the effect of B-diagrams is most prominent on the value of the critical temperature, whereas mixed diagrams change the latter only moderately.

The truncation FB_0 has been studied in previous works by means of the optimized momentum q^2-opt regulator (Diehl et al. [2007b], Floerchinger et al. [2008], Diehl et al. [2010a]). Here we aim at comparing these results to the application of a Q-exp regulator. Moreover, we include the $V_\phi q_0^2$-term, which has been left out so far. We further increase the truncation of the effective potential in order to estimate the effect of higher order bosonic scattering processes on physical observables. As previous studies mainly employed the q^2-opt regulator with relative cutoff scale $c_\phi = 1$, we choose this value here. Below we will discuss the relative cutoff scale dependence for the Q-exp regulator in more detail. The results of our investigation are summarized in Table 5.2.

By including bosonic fluctuations we observe the critical temperature to drop dramatically as compared to its mean field value. This behavior is expected as bosons generically tend to wash out the ordering and thus to decrease the critical temperature. In this context, it is interesting to study the influence of the emergent "relativistic" term $V_\phi q_0^2$ in the boson propagator. Whereas the effect of including this running coupling is strong for the purely momentum q^2-opt

	Δ/μ		T_c/μ	
Truncation	q^2-opt	Q-exp	q^2-opt	Q-exp
FB_0, ϕ^4	1.09	1.244(5)	0.441	0.399(2)
FB_0, ϕ^8	1.13	1.227	0.424	0.380
FB_0, ϕ^{10}	1.16	-	0.427	0.394
FB, ϕ^4	1.05	1.228(10)	0.405	0.389(2)
FB, ϕ^8	1.23	1.240	-	0.380
FB, ϕ^{10}	-	-	-	0.386

Table 5.2: Influence of the regularization scheme and higher orders in the effective potential when including bosonic diagrams (B), where B_0 and B correspond to a boson propagator without and with the term $V_\phi q_0^2$, respectively. We observe that the scheme with a frequency and momentum cutoff is less sensitive to the inclusion of this term. The values for this table have been obtained for $c_\phi = 1$. The errors in brackets estimate the numerical error.

regulator, its effect is only moderate for a regulator which cuts off both frequencies and momenta. This is an indication for the efficiency of the latter cutoff, which incorporates the frequency behavior of the boson propagator already within a simple truncation. In contrast, the q^2-opt cutoff needs a higher resolution of the nontrivial q_0-dependence in order to obtain reliable results.

The superfluid gap comes out substantially larger for a Q-exp regulator. This is also true when including higher terms in the effective potential, see also Fig. 5.12.

The effects of higher orders in a series expansion of the effective potential are less conclusive as in the mean field case. We find a trend to decrease the critical temperature by applying an order ϕ^8-truncation, but this effect is almost cancelled at order ϕ^{10}. The critical temperature in the FB-truncation is particularly stable with variations of a few percent.

When going to higher orders in the effective potential one eventually expects the results to converge to a fixed value. Within our investigation, however, we found that the series expansion of $U(\rho)$ in powers of $\rho - \rho_0$ breaks down during the flow, indicating the nonanalytic shape of the effective potential. The latter is well-known to be reproduced with the FRG, see e.g. Berges et al. [2002], Litim et al. [2006]. Thus we cannot report on values beyond ϕ^8 for the superfluid gap, and ϕ^{10} for the critical temperature. This shortcoming may be resolved by an expansion about a field value $\rho > \rho_0$, or by incorporating the full function $U(\rho)$ on a grid of ρ-values.

5.2.3 Renormalization of the fermion propagator

We now proceed by discussing the highest truncations employed in this section. By including mixed diagrams (M) containing both a boson and a fermion line, we can resolve renormalization effects on the fermion propagator and the Feshbach coupling h^2.

When applying a truncation with $V_\phi = 0$ and a purely momentum cutoff (such as the q^2-opt regulator), the fermion propagator does not get renormalized in vacuum. This property is due to the analytic structure of the regularized propagators, which have both poles lying in the same half-plane for the M-diagrams. Accordingly, the contour of the frequency integration can be closed in the other half-plane, thereby yielding a vanishing beta function.

This simple behavior is spoiled by the application of the Q-exp regulator or the inclusion of the $V_\phi q_0^2$-term. This is not problematic for the FB-truncations, as an appropriate renormalization in vacuum removes the corresponding unphysical flow. However, as we allow for a running of the fermion mass term m_ψ^2, the interpretation of the chemical potential $\bar{\mu}$, which enters the initial conditions through

$$m_{\psi\Lambda}^2 = C\Lambda^2 - \bar{\mu}, \tag{5.109}$$

is complicated. $C = \tilde{m}_{\psi\star}^2$ is a bare renormalization constant fixed in vacuum. The value of C only depends on the truncation and the regularization scheme.

In general, for the truncations FBM_0 and FBM, we do not have $\bar{\mu} = \mu$, whereas this is true for all other truncations discussed so far. To see this, we vary $\bar{\mu}$, and check whether $\Delta(\bar{\mu})/\bar{\mu}$ or $T_\mathrm{c}(\bar{\mu})/\bar{\mu}$ are independent of $\bar{\mu}$. We then find a logarithmic $(\bar{\mu}/\Lambda^2)$-dependence of both observables when including M-diagrams. However, we checked that the ratio Δ/T_c is indeed independent of $\bar{\mu}$. This shows that the uncertainty in the ratios Δ/μ and T_c/μ dominantly results from the inequality $\bar{\mu} \neq \mu$.

As is discussed in Sec. 4.1.4, for the FBM_0- and FBM-truncations the initial conditions only allow to interpret $\bar{\mu} = \mu$ for a special choice of c_ϕ within our setting, which is $c_0 = 0.2454 \simeq 1/4$. For $c_\phi = c_0$, the observables $\Delta/\bar{\mu}$ and $T_\mathrm{c}/\bar{\mu}$ are independent of $\bar{\mu}$. Therefore, the values of T_c/μ and Δ/μ can only be read off for this particular choice. Results for $c_\phi = c_0$ are summarized in Table 5.3.

We emphasize that the renormalization group flow in the truncations with M-diagrams is well-defined for every choice of c_ϕ. However, it requires to determine the function $\mu(\bar{\mu}, c_\phi)$, which is $\mu = \bar{\mu}$ for $c_\phi = c_0$. For other values of c_ϕ, an appropriate infrared renormalization condition has to relate the initial value $\bar{\mu}$ to the physical chemical potential. The determination of this condition is postponed to future work. Here we restrict ourselves to the simpler task of discussing the physical point $c_\phi = c_0$. An error estimate in the FBM-truncations, however, can still be obtained by means of the subtraction prescription discussed in Sec. 5.2.5.

The ratio Δ/T_c can be computed consistently for every truncation. We display our results in Fig. 5.11 and Table 5.4. Whereas the c_ϕ-dependence is rather

	Δ/μ				
Truncation	F	FB_0	FB	FBM_0	FBM
ϕ^4	1.04	0.97	0.99	0.94	0.82
ϕ^8	1.13	1.11	1.13	1.04	0.89
	T_c/μ				
Truncation	F	FB_0	FB	FBM_0	FBM
ϕ^4	0.664	0.381	0.381	0.385	0.383

Table 5.3: Critical temperature and superfluid gap for all truncations applied in this work. By improving the truncation of the effective potential to order ϕ^8, the gap is increased by approximately 10 percent. This is independent of the given truncation scheme. The values for this table have been obtained for a Q-exp regulator and with $c_\phi = c_0$, which also allows to compare to truncations which include mixed diagrams (M) with both fermionic and bosonic lines.

	Δ/T_c			
Truncation	FB_0	FB	FBM_0	FBM
$c_\phi = 1$	3.1	3.2	2.5	2.4
$c_\phi = c_0$	2.9	2.9	2.7	2.3

Table 5.4: Relative cutoff scale c_ϕ-dependence of the ratio Δ/T_c for a Q-exp regularization scheme. The values of the gap are obtained for a ϕ^8-truncation, whereas for the critical temperature we have chosen a ϕ^4-truncation of the effective potential. We observe a substantial lowering when including mixed diagrams (M).

strong in a ϕ^4-truncation, we find the ϕ^8-truncation to flatten the curve for all truncations. Moreover, there is a systematic increase of Δ/T_c when going to order ϕ^8. We find that all four curves in a ϕ^8-truncation show a maximum in the interval $I_c = [0.2, 1]$. It is a generic finding of our analysis that observables tend to have minima or maxima within this interval. Accordingly, we can use the variation within I_c for an error estimate. This procedure is applied below.

The fermion anomalous dimension $\eta_{\psi k}$ receives strong corrections at the symmetry breaking scale $k^2 \simeq \mu$, where it becomes of order 0.2. For $k \to 0$, it eventually vanishes. The renormalization effects on the Feshbach coupling h^2 are found to be small.

5.2.4 Error estimates

Now we can estimate the errors of Δ/μ and T_c/μ within each individual truncation. We estimate the errors from the variation with c_ϕ shown in Figs. 5.11, 5.12, and 5.13. From the figures presented in this section it is apparent that

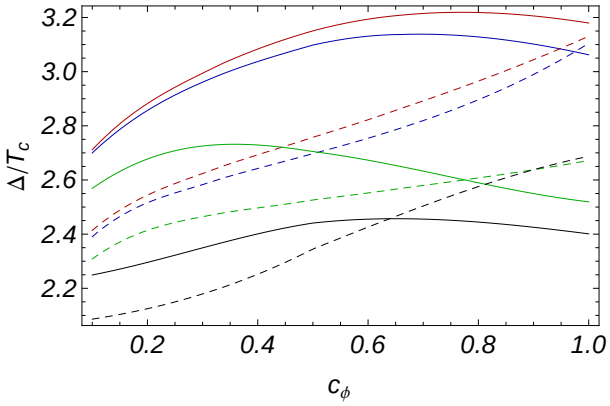

Figure 5.11: Dependence of the ratio Δ/T_c on the choice of the relative cutoff scale c_ϕ. We employ the Q-exp regulator. Here and in Figs. 5.12 and 5.13, we choose the following labelling of the curves: Solid lines correspond to a ϕ^8-truncation for computing the gap, whereas dashed lines give the results for the gap in a ϕ^4-truncation. The critical temperature is always computed in a ϕ^4-truncation. The colors correspond to the truncations (from top to bottom) FB (red), FB_0 (blue), FBM_0 (green), and FBM (black). Upon including higher orders in the effective potential, the gap increases by 10 percent in all truncation schemes. Figure taken from Boettcher et al. [2014c].

observables show pronounced features like minima or maxima inside the interval $c_\phi \in I_c = [0.2, 1]$. It is therefore reasonable to concentrate on this interval to estimate the error.

Our final results of the error analysis are summarized in Table 5.5, where we apply the following notation:

- Mean field: F-truncation to order ϕ^{24}
- Truncation 1: FB_0-truncation to order ϕ^8 (ϕ^4) for Δ/μ (T_c/μ)
- Truncation 2: FB-truncation to order ϕ^8 (ϕ^4) for Δ/μ (T_c/μ)
- Truncation 3: FBM_0-truncation to order ϕ^8 (ϕ^4) for Δ/μ (T_c/μ)
- Truncation 4: FBM-truncation to order ϕ^8 (ϕ^4) for Δ/μ (T_c/μ)

The running couplings associated to the truncations are listed at the end of Sec. 4.1.1.

For the FB_0- and FB-truncations, the c_ϕ-dependence of the superfluid gap is small within the ϕ^8-truncation. Moreover, the improvement $\phi^4 \to \phi^8$ in the effective potential seems to equilibrate the values, since the value at $c_\phi = 1$ remains almost unchanged, whereas the values for smaller c_ϕ are increased. We choose the

Observable	T_c/μ	Δ/μ	Δ/T_c
Mean field	0.664	1.16	1.75
Truncation 1	0.38(2)	1.17(6)	2.9(2)
Truncation 2	0.376(14)	1.18(6)	3.0(2)
Truncation 3	0.385(20)	1.04(5)	2.6(1)
Truncation 4	0.38(2)	0.89(5)	2.4(1)
Best estimate	0.38(2)	1.04(15)	2.7(3)

Table 5.5: Critical temperature and superfluid gap of the Unitary Fermi Gas obtained by successivley extending the truncation of the effective average action. The truncations with a smaller number are contained in the ones with a larger number. The particular choices of running couplings for each truncation are explained at the beginning of Sec. 5.2.4. The error in brackets gives the systematic error within the given truncation. The errors of T_c/μ and Δ/μ in truncations 3 and 4 result from an uncertainty in the chemical potential μ.

central value in the interval I_c and find $\Delta/\mu = 1.17(6)$ and $\Delta/\mu = 1.18(6)$ for the FB_0- and FB-truncations, respectively. The error is given by the distance from the minimum and maximum inside the interval I_c. In the same fashion we find $T_c/\mu = 0.38(2)$ and $T_c/\mu = 0.376(14)$ for FB_0 and FB, respectively. Applying this procedure to the ratio Δ/T_c in Fig. 5.11, we find $\Delta/T_c = 2.9(2)$ and 3.0(2), respectively. The relative error of all observables is thus consistently given by 5 percent.

Estimating the error within the FBM_0- and FBM-truncations is complicated by the fact that $\bar{\mu} \neq \mu$ for $c_\phi \neq c_0$. We therefore choose the physical point c_0 to obtain our central values for Δ/μ and T_c/μ. These values are given in Table 5.5. A good estimate of the relative error can be obtained from Δ/T_c, which is independent of $\bar{\mu}$. To estimate the error we apply the procedure described in Sec. 5.2.5 below.

We find $\Delta/T_c = 2.6(1)$ for the FBM_0-truncation, which corresponds to a 4 percent error. Averaging Δ/μ which is obtained by means of the η_μ-subtraction procedure of Eq. (5.111) over the interval I_c yields 1.04(3). This coincides with the central value. Given the fact that Δ/T_c is indeed very flat as a function of c_ϕ, we conclude that $\Delta/\mu = 1.04(5)$ is a reasonable error estimate.

The dotted curve in Fig. 5.13 gives the error estimate of T_c/μ when subtracting the anomalous running of the chemical potential in the FBM_0-truncation. The rather strong dependence on c_ϕ (when compared to the c_ϕ-dependence of Δ/T_c and Δ/μ) can be explained by the fact that the subtraction procedure in Eq. (5.111) strongly influences the flow at $k^2 \simeq \mu$. As this is precisely the scale where precondensation occurs and decides over the value of T_c, the critical temperature is strongly affected by Eq. (5.111). Hence, the error estimate also contains unphysical contributions and should not be extrapolated too far into the region where η_μ

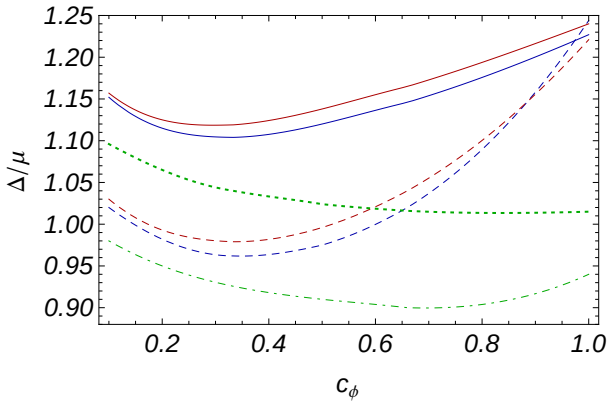

Figure 5.12: Relative cutoff scale dependence of the superfluid gap Δ/μ. Colors are as in Fig. 5.11, and solid (dashed) lines correspond to a ϕ^8-(ϕ^4-) truncation. The FB_0- and FB-truncations become much more stable when including higher terms in the effective potential. For an error estimate we show the FBM_0-truncation where we subtracted the anomalous running of the chemical potential according to Eq. (5.111). This corresponds to the dotted (dotdashed) curve for a ϕ^8-(ϕ^4-) truncation. We emphasize that the latter two curves are applied here only for estimating the error. Figure taken from Boettcher et al. [2014c].

is large. A reasonable error estimate is thus again found to be $T_\mathrm{c}/\mu = 0.385(20)$. This is also in harmony with the relative variation of Δ/T_c in dependence of c_ϕ.

Finally, for the FBM-truncation we find within the interval I_c that $\Delta/T_\mathrm{c} = 2.4(1)$. The insensitivity of this result with respect to c_ϕ is similar to the FBM_0-truncation. Since both truncations are similar to each other, we assume a 5 percent error within the FBM-truncation just like for the FBM_0-case. The central values are taken at $c_\phi = c_0$. We then arrive at $\Delta/\mu = 0.89(5)$ and $T_\mathrm{c}/\mu = 0.38(2)$.

Our best estimates for Δ/T_c and Δ/μ are obtained as the central value within the 4 truncations, with the error being given by the distance to the maximum (minimum). This yields $\Delta/\mu = 1.04(15)$ and $\Delta/T_\mathrm{c} = 2.7(3)$. For the critical temperature we obtain 0.381(6) with this procedure of averaging. However, this underestimates the error of the individual truncations, so we choose $T_\mathrm{c}/\mu = 0.38(2)$ which is valid in all four truncations.

In Tables VI and VII we display reference values on T_c/μ and Δ/μ from other theoretical approaches, and from experiment. The stability of our result $T_\mathrm{c}/\mu = 0.38(2)$ within all truncations considered in this work indicates the efficiency of the Q-exp regulator. In particular, we found a strong decrease of the critical temperature in comparison to previous FRG calculations with the q^2-regulator, which places our calculation in the range $T_\mathrm{c}/\mu = 0.3 - 0.4$ of the reference values. A missing key feature in our approach is the particle-hole channel. However,

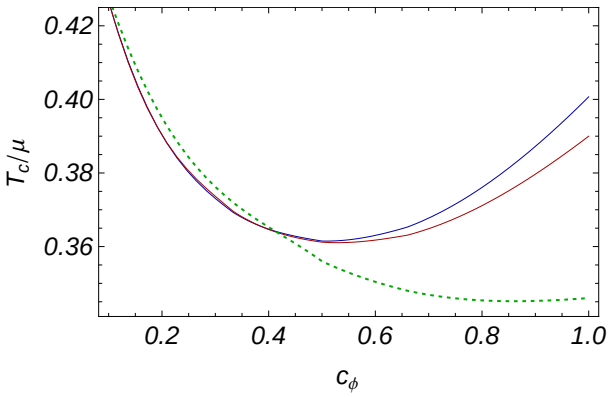

Figure 5.13: Relative cutoff scale dependence of the critical temperature T_c/μ for the FB_0- (upper curve) and FB-truncation (middle curve). The critical temperatures shown here have been obtained in a ϕ^4-truncation. The dotted curve gives the error estimate for the FBM_0-truncation according to the subtraction of the anomalous running of the chemical potential in Eq. (5.111). Figure taken from Boettcher et al. [2014c].

from previous studies by Floerchinger et al. [2008], we expect its effect to be small at unitarity due to the less pronounced Fermi surface. For the superfluid gap we obtain $\Delta/\mu = 1.04(15)$, which is smaller than all of the reference values. In particular, by improving the truncation due to the inclusion of the running fermion propagator, we do not find a convergence of results, in contrast to the critical temperature. Thus, the limit $T = 0$ requires additional running couplings, which are less important at criticality. We expect the inclusion of the full effective potential $U(\rho)$ to significantly improve our results at zero temperature.

5.2.5 Estimated effective chemical potential

In the presence of mixed diagrams, the nontrivial running of the fermion propagator in the symmetric regime spoils the interpretation of $\bar{\mu}$ as the chemical potential. Due to the presence of the relevant initial perturbation $\Delta m^2_{\psi\Lambda} = m^2_{\psi\Lambda} - C\Lambda^2 = -\bar{\mu}$, all beta functions of the remaining running couplings scale linear in $\Delta\tilde{m}^2_{\psi k} = \Delta m^2_{\psi k}/k^2$ for large k. However, the latter acquires an (unphysical) anomalous running due to the presence of the regulator function. We have

$$\partial_t \tilde{m}^2_\psi(\bar{\mu}, c_\phi) = 0 - \Big(2 + \eta_\mu(c_\phi)\Big)\Big(-\frac{\bar{\mu}}{k^2}\Big) + \dots \tag{5.110}$$

for large k. The leading term vanishes due to the fixing of the initial conditions at the vacuum fixed point, where $\partial_t \tilde{m}^2_\psi(\bar{\mu} = 0) = 0$. The anomalous dimension η_μ of the term linear in $-\bar{\mu}/k^2$ leads to a nontrivial running of the supposed "chemical

	T_c/ε_F	μ_c/ε_F	T_c/μ
BBurovski et al. [2006] (DDMC)	0.152(7)	0.493(14)	0.308
Haussmann et al. [2007] (LW)	0.160	0.394	0.406
Bulgac et al. [2008] (QMC)	0.15(1)	0.43(1)	0.35
Nascimbène et al. [2010] (Exp)	0.157(15)	0.49(2)	0.32(3)
Horikoshi et al. [2010] (Exp)	0.17(1)	0.43(1)	0.40
Goulko and Wingate [2010] (DDMC)	0.171(5)	0.429(9)	0.399
Floerchinger et al. [2010] (FRG)	0.248	0.55	0.45
Ku et al. [2012] (Exp)	0.167(13)	0.42*	0.40
This work	-	-	0.38(2)

Table 5.6: Reference values for the critical temperature T_c/μ from different theoretical and experimental works. The abbreviations correspond to Diagrammatic determinant Monte Carlo (DDMC), Quantum Monte Carlo (QMC), Self-consistent T-matrix approach or Luttinger-Ward formalism (LW), and experiment (Exp). (*We estimated the critical chemical potential of the MIT data (Ku et al. [2012]) by the maximal chemical potential $\mu_{max}/\varepsilon_F = 0.42(1)$ at $T/\varepsilon_F = 0.171(10)$.)

Method	Δ/ε_F	μ/ε_F	Δ/μ
Carlson et al. [2003] (QMC)	0.55(5)	0.44(1)	1.3
Carlson and Reddy [2005] (QMC)	0.50(5)	0.42(1)	1.2
Haussmann et al. [2007] (LW)	0.46	0.36	1.3
Carlson and Reddy [2008]	0.45(5)	-	-
Bulgac et al. [2008] (QMC)	-	0.37(5)	-
Schirotzek et al. [2008](Exp)	0.44(3)	-	-
Bartosch et al. [2009] (FRG)	0.61	0.32	1.9
Floerchinger et al. [2010](FRG)	0.46	0.51	0.90
Carlson et al. [2011] (QMC)	-	0.372(5)	-
Ku et al. [2012] (Exp)	-	0.376(4)	-
Zürn et al. [2013] (Exp)	-	0.370(5)(8)	-
This work	-	-	1.04(15)

Table 5.7: Reference values for the superfluid gap Δ/μ at $T = 0$. The abbreviations are as in Table 5.6. The values by Carlson and Reddy [2008] have been extracted from measured density distributions from partially spin-polarized trapped atoms. The overall trend of the Monte Carlo and experimental data indicates a preferred value $\Delta/\mu \simeq 1.2 - 1.3$. The Bertsch parameter μ/ε_F from Zürn et al. [2013] is based on the one measured by Ku et al. [2012] with an improved determination of the location of the ^{6}Li Feshbach resonance.

potential" with k. Consequently, $\bar{\mu} \neq \mu$. For $c_\phi = c_0$ we have $\eta_\mu(c_0) = 0$, such that the problem does not arise in this case. The value of η_μ can be extracted from the flow equation of the fermion mass term at $t = 0$. It is given by $\eta_\mu(1) = 0.21892$ for $c_\phi = 1$, decreasing for smaller values of c_ϕ. The value of η_μ also depends on the truncation and receives small corrections in a ϕ^8-truncation.

To estimate the influence of the anomalous running induced by η_μ, we can subtract the corresponding contribution to the flow equation by hand. This is not a self-consistent procedure and serves here only for an error estimate. For this purpose, we replace the flow equation for the running fermion mass term according to

$$\partial_t \tilde{m}_\psi^2(\bar{\mu}, c_\phi) \to \partial_t \tilde{m}_\psi^2(\bar{\mu}, c_\phi) - \eta_\mu(c_\phi) f\Big(\frac{\bar{\mu}}{k^2}\Big), \tag{5.111}$$

where $f(x)$ is chosen such that $f(x) = x$ for $x \ll 1$ and $f(x) = 0$ for $x \gg 1$. This choice of $f(x)$ removes the anomalous running for large k, whereas we leave the flow equation unchanged for small k as soon as higher powers of $\bar{\mu}/k^2$ become relevant. The leading contribution is then given by these higher terms, which are well-behaved. We employ $f(x) = x/(e^{(x-1)/0.1} + 1)$ for the following analysis, but the precise form of $f(x)$ is not important. In fact, also $f(x) = x$ gives almost the same values for Δ/μ and T_c/μ within the purpose of this error estimate.

The subtraction in Eq. (5.111) could also be elaborated to a systematic renormalization of the field with anomalous dimension $\eta_\psi = \mathcal{O}(\bar{\mu}/k^2)$. Since the value of η_μ can be inferred from the flow at $t = 0$ (or the flow of $\partial m_\psi^2/\partial\mu$ in vacuum), it is fixed a priori by the truncation and regularization scheme.

With the η_μ-subtraction (5.111), we find that the observables T_c/μ and Δ/μ are indeed independent of $\bar{\mu}$ for all c_ϕ. Moreover, the qualitative running of couplings compared to their vacuum values, $g_k - g_\mathrm{vac} = \mathcal{O}(\tilde{\mu})$, is similar to the well-understood case of $c_\phi = c_0$.

It is instructive to study the behavior of

$$\Delta m_{\psi k}^2 = m_{\psi k}^2 - m_{\psi,\mathrm{vac}}^2 = \mathcal{O}(\mu/k^2) \tag{5.112}$$

within the subtracted scheme just described. (Or, equivalently, for the physical point $c_\phi = c_0$ without the subtraction.) Herein, $m_{\psi,\mathrm{vac}}^2 = \tilde{m}_{\psi\star}^2 k^2$ only shows a canonical running fixed in vacuum. For large k we have $\Delta m_{\psi,k}^2 \simeq -\mu$. As k is lowered towards the many-body scales given by μ and T, the absolute value of $|\Delta m_{\psi,k}^2| = \mu_\mathrm{eff}$ *increases*, thereby yielding an effectively enhanced chemical potential appearing in the denominator of the fermionic propagator. We find the enhancement μ_eff/μ to be of order 50 %. We show the behavior of Δm_ψ^2 in Fig. 5.14.

Closing the Q-loop over $G_\psi(Q) = (\mathrm{i}q_0 + q^2 - \mu_\mathrm{eff})^{-1}$ yields a larger value $\sim \mu_\mathrm{eff}^{3/2}$ when compared to the loop over the microscopic propagator $(\mathrm{i}q_0 + q^2 - \mu)^{-1}$. As a result, the density of the system (which is related to this loop-integral) is enhanced. This increase of the density due to many-body effects is well-known for

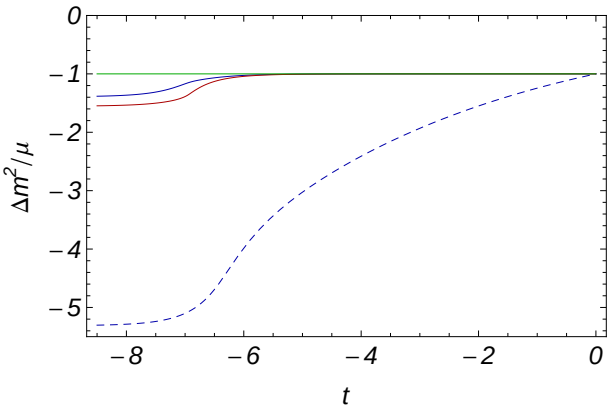

Figure 5.14: Running of $\Delta m_\psi^2 = m_\psi^2 - m_{\psi,\mathrm{vac}}^2$ in units of the initial chemical potential μ. The constant line (green) at the top corresponds to a truncation without running of m_ψ^2, and hence $\Delta m_\psi^2 = -\mu$ for all k. The remaining curves from top to bottom correspond to $c_\phi = 1$ in the η_μ-subtracted scheme of Eq. (5.111) (blue, solid), $c_\phi = c_0$ (red), and $c_\phi = 1$ without the η_μ-subtraction (blue, dashed). Clearly, the anomalous running for large k screens the physical effects in the latter case. For $c_\phi = c_0$ we see that renormalization effects on Δm_ψ^2 only show up at the many-body scales $k^2 \simeq \mu$, and result in an effective chemical potential $\mu_{\mathrm{eff}}/\mu \simeq 1.5$. Figure taken from Boettcher et al. [2014c].

the UFG and can be attributed to the Tan effect, see Sec. 5.1. Hence we found evidence that the running of m_ψ^2 within our truncation correctly incorporates this effect on the density.

5.3 Spin-imbalance

A particularly interesting question for understanding fermion pairing concerns the stability of superfluidity in the presence of mismatching Fermi surfaces. Such an asymmetry between the pairing partners is realized in electronic materials in an external magnetic field (Clogston [1962], Chandrasekhar [1962], Sarma [1963], Fulde and Ferrell [1964], Larkin and Ovchinnikov [1964]), or is expected to be found in neutron stars (Lombardo and Schulze [2001], Dean and Hjorth-Jensen [2003], Alford et al. [2008], Page et al. [2013], Gezerlis et al. [2014], Krüger et al. [2014]).

With ultracold atoms this situation can easily be simulated by introducing a population imbalance between different hyperfine states. In a microscopic model this manifests itself in a difference in chemical potentials. Hereafter, μ_1 and μ_2 denote the chemical potentials of atoms in hyperfine state $|1\rangle$ and $|2\rangle$, respectively.

We

assume the $|1\rangle$-atoms to be the majority species, i.e. $\mu_1 \geq \mu_2$. In the following we study the spin-imbalanced system with mean field theory and with the FRG.

While the ground state of the spin-balanced UFG ($\mu_1 = \mu_2 > 0$) is widely believed to be a homogeneous superfluid, the phase structure in the imbalanced situation is less clear. Given $\mu_1 > 0$ the density of minority atoms vanishes for $\mu_2 \lesssim -0.6\mu_1$ (Lobo et al. [2006], Chevy [2006], Bulgac and Forbes [2007], Prokof'ev and Svistunov [2008], Pilati and Giorgini [2008], Schmidt and Enss [2011]). This is the so-called polaron energy. As a consequence superfluidity has to break down at a finite critical value of the spin-imbalance. For a BCS superfluid this already happens for an exponentially small mismatch of Fermi surfaces (Clogston [1962], Chandrasekhar [1962]). However, since the UFG has less pronounced Fermi surfaces, it might still be favourable to compensate the mismatch due to the gain from pairing energy. We find below that within our approximation superfluidity at zero temperature persists down to $\mu_2 \simeq 0.09\mu_1$, where it vanishes in a first order phase transition.

Allowing for a finite scattering length, our FRG analysis not only allows to study the phase structure of the spin-imbalanced UFG, but rather the whole BCS-BEC crossover. We are here particularly interested in the quantum phase structure, i.e. the zero temperature case. On the so far largely unexplored BEC-side of the crossover we find a quantum critical point (QCP) where the breakdown of superfluidity changes from first to second order. The location of the QCP deviates from the mean field prediction.

Besides the breakdown of superfluidity, the existence of exotic phases has been conjectured for the spin-imbalanced BCS-BEC crossover. In the mean field approximation (Sheehy and Radzihovsky [2006], Gubbels et al. [2006], Parish et al. [2007]), the homogeneous Sarma phase (Sarma [1963]) is unstable at zero temperature on the BCS-side of the crossover. This scenario is found below to persist upon inclusion of bosonic fluctuations. We find that the Sarma phase only appears on the BEC-side of the crossover, its onset being shifted from the mean field prediction. The Sarma phase, or special cases of it, is also referred to as interior gap superfluid, breached pair phase, or magnetized superfluid in the literature (Liu and Wilczek [2003], Wu and Yip [2003], Bedaque et al. [2003], Liu et al. [2004], Carlson and Reddy [2005], Gubbels et al. [2006], Sheehy and Radzihovsky [2006], Parish et al. [2007], Nikolić and Sachdev [2007], Parish et al. [2007], Gubbels and Stoof [2008], Radzihovsky and Sheehy [2010], Gubbels and Stoof [2013]). It consists of a homogeneous superfluid with gapless fermionic excitations.

Furthermore, inhomogeneous phases such as the ones studied by Fulde and Ferrell [1964] and Larkin and Ovchinnikov [1964] represent competing orders to the homogeneous superfluid. They have to be taken into account for a complete study of the phase structure. Here we restrict the investigation to the stability of homogeneous superfluid order. A competing effect from inhomogeneous order is expected to show precursors in the renormalization group flow. One of those

is the vanishing of $A_{\phi,k}$ at some nonzero momentum scale $k > 0$, see e.g. Krahl et al. [2009]. At this point, the truncation employed here becomes insufficient. Since we do not detect signs of such a behaviour anywhere near the superfluid phase, it seems reasonable to restrict ourselves to a homogeneous order parameter $\Delta_0 \neq \Delta_0(\vec{x})$. A more detailed discussion of the appearance of inhomogeneous order in the presence of spin- and mass-imbalance from an FRG perspective is provided by Braun and Roscher [2014].

The FRG makes it possible to include the effect of bosonic fluctuations onto the many-body state. Besides a large quantitative improvement, this analysis is also mandatory for a solid understanding of the qualitative features of the phase diagram. For instance, the feedback of fluctuations may change the order of the phase transition compared to the mean field prediction. In addition, a commonly encountered situation is the suppression of long-range order due to long wavelength fluctuations. Moreover, the FRG is not plagued by the sign problem, which hampers lattice simulations of spin-imbalanced fermions.

The grid code for the evolution of the effective potential employed in Secs. 5.3.2 and 5.3.3 has been developed by Dietrich Roscher and Tina Katharina Herbst, which is highly appreciated here by the author.

5.3.1 Mean field analysis

We first study the mean field theory of the spin-imbalanced BCS-BEC crossover. This allows for an introduction of most relevant concepts, and also constitutes the starting point for an analysis including bosonic fluctuations. In an FRG setup, mean field theory is recovered by keeping only the fermionic particle-particle diagram on the right hand side of the flow equation.

Our analysis is built on the microscopic Lagrangian

$$\mathcal{L} = \sum_{\sigma=1,2} \psi_\sigma^* \Big(\partial_\tau - \nabla^2 - \mu_\sigma\Big)\psi_\sigma - h\Big(\phi^*\psi_1\psi_2 + \text{h.c.}\Big) + \phi^*\Big(\partial_\tau - \frac{\nabla^2}{2}\Big)\phi + \nu_\Lambda \phi^*\phi\,. \tag{5.113}$$

The two species of fermions couple to chemical potentials μ_σ, which can be different in general. We write

$$\mu_1 = \mu + \delta\mu,\ \ \mu_2 = \mu - \delta\mu\,, \tag{5.114}$$

with spin-imbalance $\delta\mu = \tilde{h} = (\mu_1 - \mu_2)/2 \geq 0$. The quantity $\tilde{h}$ is also referred to as Zeeman field.

Mean field theory is based on the one-loop formula or saddle-point approximation to the effective action, see Eq. (3.26). For a detailed derivation of the effective potential for a BCS superfluid in mean field approximation by means of a Hubbard–Stratonovich transformation we refer to Boettcher et al. [2012]. Mean field theory can be applied to the whole BCS-BEC crossover when allowing for a

negative chemical potential. In the case of the spin-imbalanced system we obtain

$$U(\Delta^2,\mu,\delta\mu,T) = -\frac{\Delta^2}{\lambda_{\psi\Lambda}} - \frac{1}{2}\int_Q^\Lambda \log\left[\left(q_0^2+(E_q+\delta\mu)^2\right)\left(q_0^2+(E_q-\delta\mu)^2\right)\right], \tag{5.115}$$

where

$$E_q \pm \delta\mu = \sqrt{\varepsilon_q^2+\Delta^2} \pm \delta\mu. \tag{5.116}$$

Here $\varepsilon_q = q^2-\mu$ is the dispersion relation of fermionic quasiparticles. The integral

$$\int_Q^\Lambda = T\sum_n \int_{\vec{q},q^2\leq\Lambda^2} \tag{5.117}$$

is defined with an upper boundary Λ. The chemical potential is given by

$$\mu = \begin{cases} \mu_{\mathrm{mb}} & (a^{-1}\leq 0), \\ \mu_{\mathrm{mb}} - a^{-2} & (a^{-1}>0) \end{cases} \tag{5.118}$$

with bound state energy $\varepsilon_{\mathrm{B}} = -2a^{-2}\theta(a)$. For the numerical implementation it is convenient to set $\mu_{\mathrm{mb}} = 1$. In the following we restrict to the zero temperature case for simplicity, but the generalization to nonzero temperatures is straightforward.

We have mainly two goals: (i) Determine the minimum $\Delta_0(\mu,\delta\mu)$ of the effective potential, thereby obtain the mean field phase diagram. (ii) Compute the density of the system by means of $n = \mathrm{d}P/\mathrm{d}\mu$, where $P(\mu,\delta\mu) = -U(\Delta_0)$ is the pressure of the system. For the first task we have to account for the possibility of first order phase transitions for $\delta\mu > 0$. Their appearance is well-known in the BCS limit (Clogston [1962], Chandrasekhar [1962]), and this behavior will be found to extend even into the BEC regime.

We study the breakdown of superfluidity by computing the condensation energy density defined by

$$\varepsilon_{\mathrm{con}}(\mu,\delta\mu) = U(\Delta_0^2,\mu,\delta\mu) - U(0,\mu,\delta\mu), \tag{5.119}$$

where $\Delta_0 = \Delta_0(\mu,\delta\mu)$ is the minimum of the effective potential. In the superfluid phase we have $\Delta_0^2 > 0$ and $\varepsilon_{\mathrm{con}} < 0$, whereas we have $\Delta_0^2 = 0$ and $\varepsilon_{\mathrm{con}} = 0$ in the normal phase. Coming from the superfluid phase we locate the transition at $\varepsilon_{\mathrm{con}} \nearrow 0$. At the critical point the condensation energy vanishes, and the gap Δ_0^2 either vanishes continuously (second order phase transition) or discontinuously (first order transition).

The minimum of the effective potential should be found from an unbiased global analysis of the function $U(\Delta^2)$. From mean field studies of the BCS-BEC crossover (Sheehy and Radzihovsky [2006], Parish et al. [2007]) we already know that Δ_0 in the superfluid phase can also be found from solving the gap equation $U'(\Delta_0^2) = 0$.

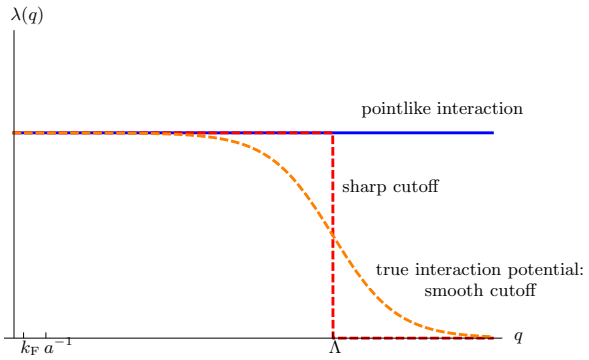

Figure 5.15: The effective Hamiltonian for ultracold atoms assumes a pointlike interaction. This is valid on the length scales we encounter in experiments $(k_F^{-1}, a, \lambda_T, \ell_{osc})$. However, when calculating the effective action in perturbation theory, we are confronted with divergences when integrating over all momenta. These singularities arise because of momenta $q^2 \gtrsim \Lambda^2$. At these scales, the microscopic details of the interatomic potential can be resolved and we cannot rely on a pointlike approximation. We cure the problem by observing that the true coupling $\lambda(q)$ is derived from a more realistic potential and falls off smoothly in the UV. This cannot be described in the pointlike approximation, but is taken into account by introducing a sharp cutoff at Λ. Figure taken from Boettcher et al. [2012]

Due to the simplicity of the approach, we concentrate on this method here. From Eq. (5.115) we find

$$\begin{aligned} 0 \stackrel{!}{=} U'(\Delta_0^2) &= -\frac{1}{\lambda_{\psi\Lambda}} - \frac{1}{2}\int_Q \frac{1}{E_q}\left(\frac{E_q+\delta\mu}{q_0^2+(E_q+\delta\mu)^2} + \frac{E_q-\delta\mu}{q_0^2+(E_q-\delta\mu)^2}\right) \\ &= -\frac{1}{\lambda_{\psi\Lambda}} - \frac{1}{2}\int_{\vec{q}}^{\Lambda} \frac{\theta(E_q-\delta\mu)}{E_q}. \end{aligned} \tag{5.120}$$

The integrand approaches unity for large q, and thus the integral diverges $\sim \Lambda$. This is related to an inappropriate treatment of the short distance details of the atomic interactions, see Fig. 5.15 and the discussion in Boettcher et al. [2012]. We cure the divergence by a proper vacuum renormalization according to

$$-\frac{1}{\lambda_{\psi\Lambda}} = -\frac{1}{8\pi a} + \frac{1}{2}\int_{\vec{q}} \frac{1}{q^2}, \ (a^{-1} \leq 0), \tag{5.121}$$

$$-\frac{1}{\lambda_{\psi\Lambda}} = \frac{1}{2}\int_{\vec{q}} \frac{1}{q^2+a^{-2}}, \ (a^{-1} > 0). \tag{5.122}$$

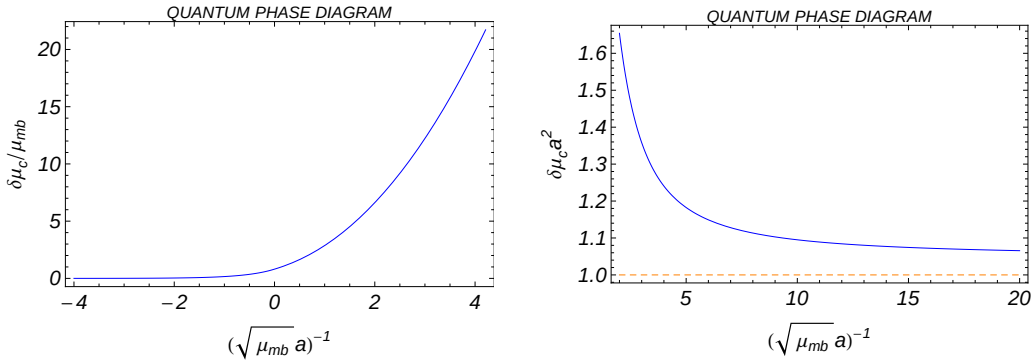

Figure 5.16: *Left:* Mean field quantum phase diagram in grand canonical coordinates, with $\mu_{\mathrm{mb}} = \mu - \varepsilon_{\mathrm{B}}/2$. Everything below the curve is superfluid, whereas the region above the curve is in the normal phase. *Right:* The same phase diagram, but with $\delta\mu_{\mathrm{c}}$ scaled to $|\varepsilon_{\mathrm{B}}|/2 = a^{-2}$. We see that the critical imbalance is on the order of the bound state energy, and thus very large.

The renormalized gap equation then reads

$$0 = -\frac{1}{8\pi a} + \frac{1}{2}\int_{\vec{q}} \Big(\frac{1}{q^2} - \frac{\theta(E_q - \delta\mu)}{E_q} \Big), \ (a^{-1} \leq 0), \tag{5.123}$$

$$0 = \frac{1}{2}\int_{\vec{q}} \Big(\frac{1}{q^2 + a^2} - \frac{\theta(E_q - \delta\mu)}{E_q} \Big), \ (a^{-1} > 0). \tag{5.124}$$

The condensation energy is given by

$$\begin{aligned} \varepsilon_{\mathrm{con}} &= U(\Delta_0^2) - U(0) \\ &= -\frac{\Delta_0^2}{\lambda_{\psi\Lambda}} - \frac{1}{2}\int_Q^\Lambda \log\Big[\Big(q_0^2 + (E_q + \delta\mu)^2 \Big) \Big(q_0^2 + (E_q - \delta\mu)^2 \Big) \Big] \\ &\quad + \frac{1}{2}\int_Q^\Lambda \log\Big[\Big(q_0^2 + (|\varepsilon_q| + \delta\mu)^2 \Big) \Big(q_0^2 + (|\varepsilon_q| - \delta\mu)^2 \Big) \Big]. \end{aligned} \tag{5.125}$$

To evaluate the frequency integrals we employ

$$\int_{-W}^{W} \frac{\mathrm{d}q_0}{2\pi} \log(q_0^2 + a^2) = -\frac{2W}{\pi} + \frac{W}{\pi}\log(W^2 + a^2) + |a| - \frac{2a}{\pi}\arctan\Big(\frac{a}{W}\Big). \tag{5.126}$$

For $W \gg |a|$ only the term $|a|$ will be important for the rest. We then find

$$\varepsilon_{\mathrm{con}} = -\frac{\Delta_0^2}{\lambda_{\psi\Lambda}} - \frac{1}{2}\int_{\vec{q}}^\Lambda \Big(|E_q + \delta\mu| + |E_q - \delta\mu| - \Big||\varepsilon_q| + \delta\mu\Big| - \Big||\varepsilon_q| - \delta\mu\Big| \Big). \tag{5.127}$$

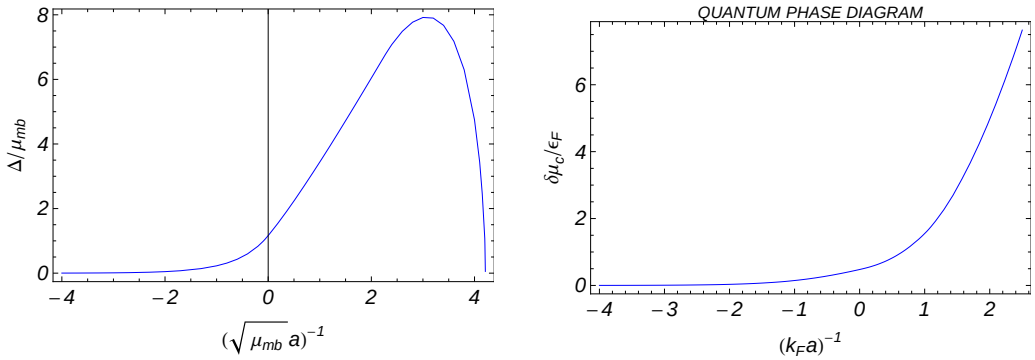

Figure 5.17: *Left:* Critical gap Δ_c at the phase transition border for $T = 0$. For $(\sqrt{\mu_{mb}}a)^{-1} = 4.193$ the transition turns second order. At the quantum critical point we find $\delta\mu_c/\mu_{mb} = 21.56$, $(k_F a)^{-1} = 2.367$ and $\delta\mu_c/\varepsilon_F = 6.871$. *Right:* Mean field quantum phase diagram in terms of the Fermi momentum. The critical line $\delta\mu_c/\varepsilon_F$ shown here gives the lower boundary, and it is separated via a forbidden region from the normal phase.

For the proper renormalization of $\lambda_{\psi\Lambda}$ we can either use the gap Eq. (5.120) or the vacuum renormalization conditions in Eqs. (5.121) and (5.122). The corresponding quantum phase diagram in grand canonical coordinates is shown in Fig. 5.16. The critical gap $\Delta_c(a)$ at the superfluid phase transition is shown in Fig. 5.17 (left). We observe that $\Delta_c = 0$ for $a^{-1} = 4.193$, where the transition becomes of second order. The corresponding quantum critical point is discussed below.

The density of particles, $n = n_1 + n_2$, is found from

$$n(\mu, \delta\mu) = -\frac{\partial U}{\partial \mu}(\Delta_0) = -\int_{\vec{q}}^{\Lambda} \frac{\varepsilon_q \theta(E_q - \delta\mu)}{E_q}. \tag{5.128}$$

We again need to cure an unphysical divergence, see Boettcher et al. [2012], and arrive at

$$n(\mu, \delta\mu) = 2\int_{\vec{q}} \frac{1}{2}\Big(1 - \frac{\varepsilon_q \theta(E_q - \delta\mu)}{E_q}\Big). \tag{5.129}$$

From the density (equation of state) we can compute the quantum phase diagram in canonical variables, Fig. 5.17 (right). The population imbalance, $\delta n = n_1 - n_2$, is given by

$$\delta n(\mu, \delta\mu) = -\frac{\partial U}{\partial \delta\mu}(\Delta_0^2) = \int_{\vec{q}} \theta(\delta\mu - E_q). \tag{5.130}$$

We see that $\delta n > 0$ at zero temperature if and only if $\delta\mu > \min_q E_q$. We call this the *Sarma criterion*. In Sec. 5.3.3 we discuss the Sarma phase in more detail.

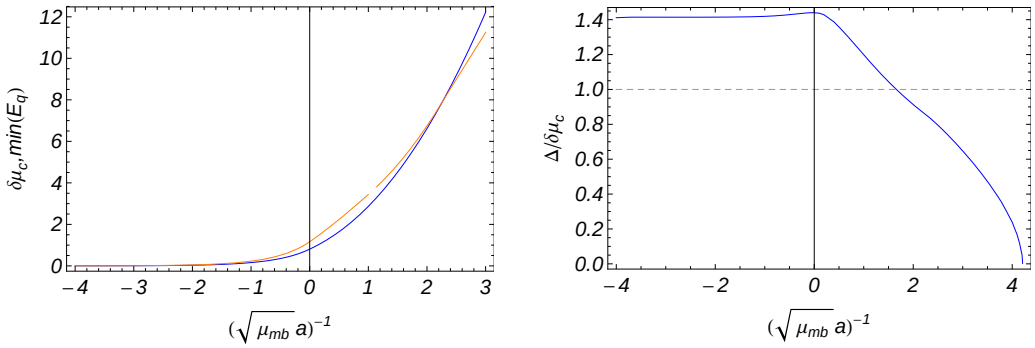

Figure 5.18: *Left:* The Sarma phase is found from the intersection point $\delta\mu_c = \min_q E_q = \sqrt{\mu^2 + \Delta_0^2}$ on the BEC side (blue and orange curves, respectively). We locate the onset point at $(\sqrt{\mu_{mb}}a)^{-1} = 2.27$. This corresponds to $(k_F a)^{-1} = 1.01$ and $\delta\mu_c/\varepsilon_F = 1.57$. *Right:* Ratio of the gap over the critical imbalance. We find $\Delta/\delta\mu_c = \sqrt{2} = 1.41$ on the BCS side, as is expected from BCS theory.

Note that, due to the possibility of a negative fermion chemical potential on the BEC side of the crossover, we have

$$\min_q E_q = \begin{cases} \Delta_0 & (a \leq 0) \\ \sqrt{\mu^2 + \Delta_0^2} & (a > 0). \end{cases} \tag{5.131}$$

Note also that $\sqrt{\mu^2 + \Delta_0^2} \simeq |\mu| \simeq |\varepsilon_B|/2$ far on the BEC side. The Sarma criterion is plotted in Fig. 5.18.

The quantum critical point (QCP) on the BEC side, where the first and second order phase boundaries meet, can be found from the solution of

$$0 = U'(\Delta^2 = 0, a, \delta\mu) = U''(\Delta^2 = 0, a, \delta\mu). \tag{5.132}$$

Herein a prime denotes a derivative with respect to Δ^2. In order to solve these equations it is useful to introduce a small nonzero temperature $T > 0$ and to solve the equations

$$0 = U'(0) = -\frac{1}{\lambda_{\psi\Lambda}} - \int_{\vec{q}} \frac{1}{E_q}\Big[1 - N_F(E_q + \delta\mu) - N_F(E_q - \delta\mu)\Big], \tag{5.133}$$

$$0 = U''(0) = \int_{\vec{q}} \frac{1}{2E_q^2}\Bigg[\frac{1}{E_q}\Big(1 - N_F(E_q + \delta\mu) - N_F(E_q - \delta\mu)\Big) + \Big(N_F'(E_q + \delta\mu) + N_F'(E_q - \delta\mu)\Big)\Bigg], \tag{5.134}$$

with $N_F(z) = (e^{z/T} + 1)^{-1}$ and $E_q = \sqrt{(q^2 - \mu)^2 + \Delta^2} \to |q^2 - \mu|$. The second contribution to $U''(0)$ is particularly important. For the numerics we found it

convenient to set $\mu_{\rm mb} = 1$ and use $T = 0.005$. However, $T \leq 0.1$ seems to be sufficient. The vanishing of the critical gap can be seen in both Figs. 5.17 (left) and 5.18 (right). The QCP has coordinates $(\sqrt{\mu_{\rm mb}}a)_{\rm c}^{-1} = 4.193$, $\delta\mu_{\rm c}/\mu_{\rm mb} = 21.56$, $(k_{\rm F}a)_{\rm c}^{-1} = 2.367$ and $\delta\mu_{\rm c}/\varepsilon_{\rm F} = 6.871$.

5.3.2 Phase structure

We now discuss the phase structure of the system as obtained with the FRG in the FB_0-truncation with $S_\phi = 1$ and grid-evolved effective potential. In particular, we show results computed with the symmetric choice of fermionic regulators,

$$R_{\psi\sigma}(q^2) \equiv R_\psi(q^2) = \Big[\mathrm{sgn}(q^2-\mu)k^2 - (q^2-\mu)\Big]\theta\Big(k^2 - |q^2-\mu|\Big), \tag{5.135}$$

where $\mu = (\mu_1+\mu_2)/2$. As we demonstrate in Fig. 5.20, these results agree very well with the ones obtained using the asymmetric scheme given by

$$R_{\psi\sigma}(q^2) = \Big[\mathrm{sgn}(q^2-\mu_\sigma)k^2 - (q^2-\mu_\sigma)\Big]\theta\Big(k^2 - |q^2-\mu_\sigma|\Big), \tag{5.136}$$

but are numerically more stable due to the analytical expressions for the beta functions. We do not consider the possibility for inhomogeneous superfluid states in our analysis, see Braun and Roscher [2014] for a discussion with the FRG.

Phase diagram

The phase diagram of the spin-imbalanced UFG beyond mean field theory is shown in Fig. 5.19. The overall phase structure is qualitatively similar to the mean field result, see Fig. 5.25 for a direct comparison. However, the critical temperature is reduced drastically when fluctuations are included. In the balanced limit we find a second order phase transition with $T_c/\mu = 0.40$. This is in good agreement with recent measurements (Ku et al. [2012]) and consistent with the calculations based on a Taylor expansion of the effective potential presented in Secs. 5.2.2 and 6.1.2.

As the spin-imbalance is increased, the transition changes from second to first order in a tricritical point located at $(\delta\mu_{\rm CP}/\mu, T_{\rm CP}/\mu) = (0.76, 0.20)$. Below this point we find a first order transition line, which appears to extend down to $T \approx 0$ (red, solid line). From an extrapolation of the transition line computed for $T \geq 0.01$, we deduce a first order phase transition for $\delta\mu_{\rm c}/\mu = 0.83$ at vanishing temperature. This is in reasonable agreement with the recent experimental finding of a first order transition at $\delta\mu_{\rm c}/\mu = 0.89$ (Navon et al. [2013]).

The critical imbalance at zero temperature lies above the mean field value $(\delta\mu_c^{\rm MFA}/\mu = 0.807)$. This is an interesting observation since usually bosonic fluctuations tend to destroy ordering. In this case, however, the latter influence the running of the Feshbach coupling h^2 via $\eta_\phi^{(B)}$, which is then fed back into $\dot{U}^{(F)}$. In this way, for large enough $\delta\mu$ and low enough T, the nontrivial minimum of U_k is stabilized rather than washed out. This illustrates how the competition

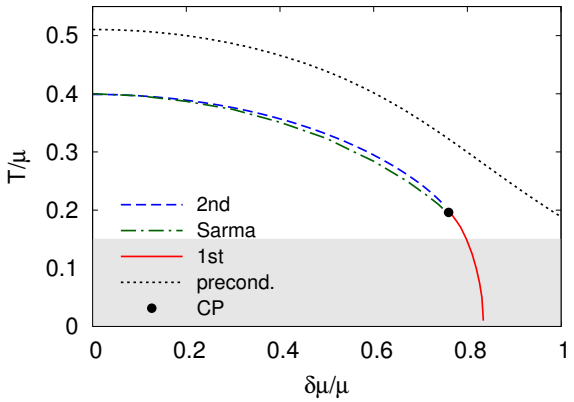

Figure 5.19: Phase diagram of the spin-imbalanced UFG beyond mean field theory. The phase boundaries are obtained from the FRG evolution of the effective potential including the feedback of bosonic fluctuations. The critical temperature of the balanced system is found to be $T_c/\mu = 0.40$. For small $\delta\mu/\mu$ we find a second order phase transition with a reduced critical temperature. For low temperatures, spin-imbalance results in a breakdown of superfluidity by means of a first order phase transition. We extract $\delta\mu_c/\mu = 0.83$ for the critical imbalance at zero temperature. The second order line terminates in a tricritical point (CP). We indicate the Sarma crossover by the green, dash-dotted line. The region between the precondensation line (black, dotted) and the phase boundary gives an estimate for the pseudogap region as is explained in the main text.

of fermionic and bosonic contributions results in nontrivial effects on the phase structure of the system.

Note that it is numerically impossible to calculate observables at exactly $k = 0$. However, the flow usually freezes out at a finite scale below the relevant many-body scales present in the theory. In order to reliably extract the phase structure we may hence stop the integration of the flow equation at any sufficiently small k such that $\Delta_{0,k} \simeq \Delta_{0,k=0}$ is frozen out. Especially in the first order region at low temperatures $T/\mu \lesssim 0.15$, the complexity of the flow equation makes it harder to reach the deep infrared. Due to accumulating numerical errors, the flow needs to be stopped at relatively high $k < 1$. This entails that a sufficient convergence of $\Delta_{0,k}$ inside the superfluid phase might not be achieved yet. However, we will argue in Sec. 5.3.2 below that the position of the first order phase transition is not affected by this and can still be determined accurately. A conservative estimate of the domain where the IR scale is modified is indicated by the gray band in Fig. 5.19.

We find the result for the phase boundary to differ by less than 5% for the

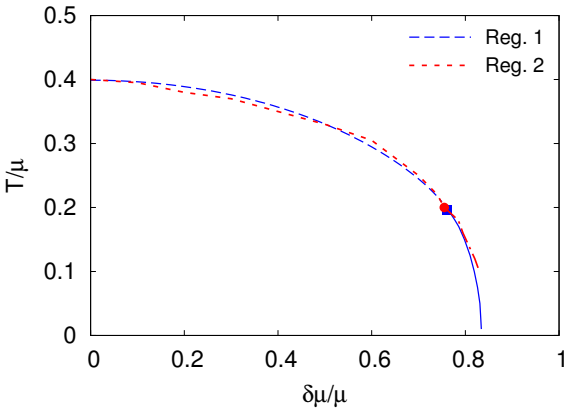

Figure 5.20: Regularization scheme dependence of the phase boundary. We display the phase diagram obtained by applying the fermion regulator $R_{\psi\sigma}$ from Eqs. (5.135) ("Reg. 1") and (5.136) ("Reg. 2"). Figure taken from Boettcher et al. [2014a].

two choices of fermion regulators in Eqs. (5.135) and (5.136), respectively. We compare both phase diagrams in Fig. 5.20. A more detailed discussion is provided in Boettcher et al. [2014a]. The insensitivity of the critical line to the regularization scheme indicates the stability of our predictions within the given truncation scheme for the effective average action. We also note here that the second order line for the transition is quantitatively only insufficiently resolved by a Taylor expansion of the effective potential $U_k(\rho)$ to order ϕ^4. The discrepancy increases for larger spin-imbalance, see Fig. 5.21.

Scale evolution and precondensation

In Fig. 5.22 we show the scale evolution of the minimum of the effective average potential as a function of the RG-scale k for fixed $T/\mu = 0.17$ and two different spin-imbalances, $\delta\mu_{\rm SF} = 0.78\mu$ and $\delta\mu_{\rm NF} = 0.79\mu$. For large k the running of couplings is attracted to an ultraviolet fixed point. This scaling regime is left when k becomes of the order of the many-body scales. For low enough temperatures local symmetry breaking occurs at $k^2 \simeq \mu$, associated to a nonzero minimum of the effective potential, $\Delta_{0,k} > 0$. Competing bosonic and fermionic fluctuations then determine whether the non-vanishing gap remains (red, solid line) or vanishes (green, dotted line) in the infrared (IR) for $k \to 0$.

The two values of $\delta\mu$ shown in Fig. 5.22 are chosen such that they lie on opposite sides of the first order phase boundary. In both cases a non-vanishing gap, $\Delta_{0,k} > 0$, is generated during the flow at $t_{\rm sb}$. Only for $\delta\mu = \delta\mu_{\rm SF}$ it persists for $t \to -\infty$, leading to superfluidity (SF) and symmetry breaking in the IR. For $\delta\mu = \delta\mu_{\rm NF}$ instead, $\Delta_{0,k}$ jumps back to zero at the finite scale $t_{\rm sr} = -7.69$ below which the symmetry remains restored such that one finds a normal fluid (NF). In both cases,

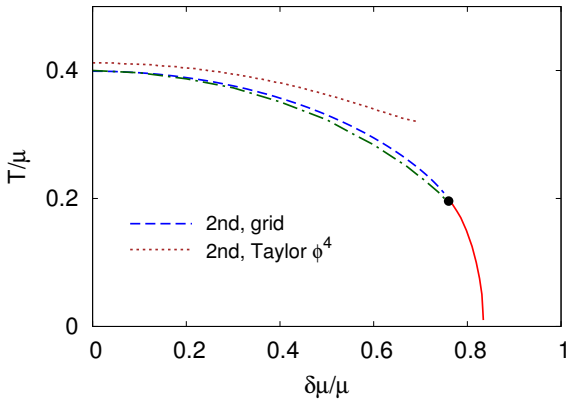

Figure 5.21: By Taylor expanding the effective average action $U_k(\rho)$ to order ϕ^4 (red dotted line) in the flow equation, the location of the second order line deviates quantitatively from the grid solution (blue dashed line) as we increase $\delta\mu/\mu$. Figure taken from Boettcher et al. [2014a].

the effective potential at intermediate k exhibits two minima (inset C), but for $\delta\mu_{\mathrm{NF}}$ the non-trivial one is raised above $U_k(\rho = 0)$ and disappears (inset D) during the flow.

The appearance of a nonzero $\Delta_{0,k}$ in a limited range $t_{\mathrm{sr}} < t < t_{\mathrm{sb}}$ is called *precondensation*, see e.g. Boettcher et al. [2012]. It can be interpreted as the formation of pairs and local phase coherence, although long-range order is destroyed due to fluctuations. The associated coherence length can be estimated by k_{sr}^{-1}. In Fig. 5.19 the precondensation region is enclosed by the black, dotted line and the phase boundary. The phenomenon of precondensation is closely related to pseudogap physics. This close relation between both effects can be understood by the observation that we can estimate the momentum dependence of the fermion spectrum by setting $k \simeq q$ in the fermion propagator. We then obtain the fermion dispersion relation $E_q \simeq [(q^2 - \mu)^2 + \Delta_{0,q}^2]^{1/2}$. For $\Delta_{0,\sqrt{\mu}} > 0$ this spectrum displays a gap at the Fermi surface ($q^2 \simeq \mu$), although the system is not superfluid due to $\rho_{0,k=0} = 0$.

For vanishing or small spin-imbalance, $\Delta_{0,k}$ approaches zero continuously in the precondensation region, see e.g. Fig. 28 in Boettcher et al. [2012]. For configurations with large $\delta\mu/\mu$ and low T/μ as in Fig. 5.22, a jump of $\Delta_{0,k}$ can be observed instead. This behaviour is only possible in the vicinity of a first order phase transition. It is generated by a second, non-trivial local minimum of the effective potential which is raised above $U_k(\rho = 0)$ during the flow (cf. insets C and D). An interesting consequence is that this type of precondensation is not necessarily induced by order parameter fluctuations alone. Even in mean field theory, where the latter are absent, we find a pseudogap regime for large $\delta\mu/\mu$, see Fig. 1 in Boettcher et al. [2014a].

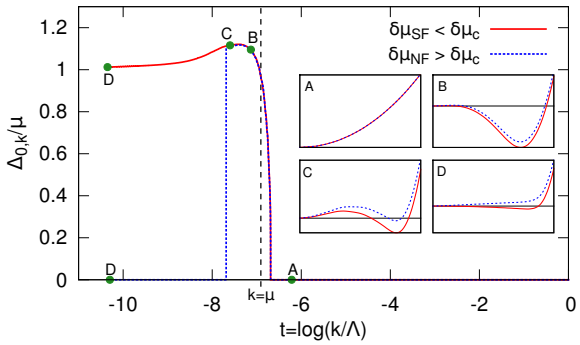

Figure 5.22: Scale evolution of the minimum $\Delta_{0,k}$ of the effective average potential close to a first order phase transition at $\delta\mu_c$. The insets show the shape of the effective potential $U_k(\Delta)$ at several points along the scale evolution. The solid (red) lines correspond to a point in the broken phase ($\delta\mu_{\mathrm{SF}} = 0.78\mu$), where the global minimum of the effective potential is non-zero in the infrared. The dotted (blue) line represents a point with $\delta\mu_{\mathrm{NF}} = 0.79\mu$, where the global minimum in the infrared is located at $\Delta_{0,k=0} = 0$. For all plots, $T/\mu = 0.17$. Figure taken from Boettcher et al. [2014a].

Furthermore, the peculiar k-dependence of the gap at the first order transition region can be exploited numerically. A smooth decrease to zero of $\Delta_{0,k}$, as occurring close to a second order phase transition, may take arbitrarily long in RG-time. Therefore, an IR scale of about $t \approx -11$ should be considered as an upper limit for the reliable extraction of results for finite $\Delta_{0,k=0}$. However, for $T/\mu \leq 0.15$ (shaded area in Fig. 5.19), $t \approx -9$ is often the utmost that can be reached, due to the increasing stiffness of the flow equations. Thus, the estimate for the *value* of $\Delta_{0,k=0} > 0$ in the superfluid phase is less reliable for such low temperatures. In contrast, the *position* of the first order phase transition is determined by the occurrence of a sudden breakdown of the condensate. Indeed, we find that this jump to $\Delta_{0,k} = 0$ always occurs at some $t > -8$ for $T/\mu \leq 0.15$. Since these scales are not affected by the IR problems mentioned above, we conclude that our results for the position of the phase transition can be trusted even in the shaded area.

As a final remark, we mention that the scale evolution of $U_k(\rho)$ as shown in Fig. 5.22 allows to check the quality and consistency of the truncation. For example, it can be seen in inset D that the FRG-evolved effective potential is convex for $k \to 0$ within our truncation, cf. Litim et al. [2006]. This exact property is reproduced by FRG flows (Berges et al. [2002], Ringwald and Wetterich [1990]). It can, however, be spoiled by an insufficient truncation. The mean field approximation, for instance, is included in the FRG equation as a truncation that neglects all bosonic contributions, cf. our discussion above. However, the mean field effective

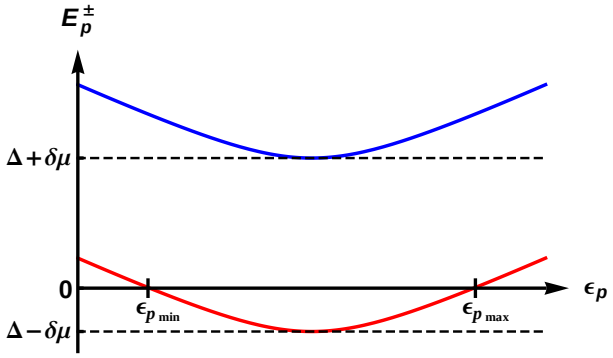

Figure 5.23: The two lowest branches of the dispersion relation, Eq. (5.137), relevant for the Sarma transition. Increasing the imbalance $\delta\mu$, the lowest branch extends below zero, yielding gapless excitations around the Fermi surfaces at p_{min} and p_{max}. Note that for $\min_p \varepsilon_p > 0$ the minimal momentum p_{min} can become negative, and the Sarma phase appears with only one Fermi surface in this case. Figure taken from Boettcher et al. [2014b].

potential is non-convex in the IR.

5.3.3 Sarma phase

The Sarma phase is a homogeneous superfluid phase with gapless fermionic quasiparticle excitations. To understand its origin we consider a gas of two-component fermions with chemical potential imbalance $\delta\mu = (\mu_1 - \mu_2)/2 \geq 0$. After including renormalization effects on the propagator of fermionic quasiparticles, we can infer their dispersion relation from the quadratic part of the spin-imbalanced effective Lagrangian. It typically splits into two lowest branches given by

$$E_p^{(\pm)} = \sqrt{\varepsilon_p^2 + \Delta^2} \pm \delta\mu, \tag{5.137}$$

where ε_p is the microscopic dispersion relation of particles, and Δ is the pairing gap. For ultracold atoms we have $\varepsilon_p = p^2 - \mu$, but ε_p might also describe relativistic particles.

The Sarma phase is characterised by a non-vanishing gap Δ and the parameters in Eq. (5.137) are tuned such that the lower branch becomes negative in a momentum interval $p_{\mathrm{min}} < p < p_{\mathrm{max}}$, see Fig. 5.23. Accordingly, this interval becomes occupied even at zero temperature, and we find gapless excitations around the built-up Fermi surfaces at p_{min} and p_{max}. For the remaining momenta, fermionic excitations are gapped. For nonzero temperature the Fermi surfaces are smeared out and a sharp distinction between the unpolarized superfluid and the Sarma phase is not possible. Hence, we speak of a Sarma crossover in this case.

The criterion for a zero crossing of the lower branch in Eq. (5.137), and thus for the onset of the Sarma phase, is equivalent to

$$\delta\mu > \min_p \sqrt{\varepsilon_p^2 + \Delta^2}\,. \tag{5.138}$$

We emphasize again that this equation is understood in terms of renormalized single-particle quantities. Assuming for simplicity that $\min_p \varepsilon_p = 0$, we then arrive at the condition $\delta\mu > \Delta$. Then there are three possible scenarios for a spin-imbalanced system with $\Delta > 0$, which decide over the fate of the Sarma phase. By increasing $\delta\mu$ we make pairing less favourable and superfluidity generically breaks down at a critical imbalance $\delta\mu_\mathrm{c}$. If this happens continuously, i.e. by means of a second order phase transition, the Sarma criterion is necessarily fulfilled somewhere, since $\Delta \to 0$ (scenario I). This is depicted in Fig. 5.24. At a first order phase transition, on the other hand, the gap jumps from a critical value $\Delta_\mathrm{c} > 0$ to zero. For $\delta\mu_\mathrm{c} > \Delta_\mathrm{c}$ a Sarma phase exists (scenario II), whereas the required condition cannot be fulfilled for $\delta\mu_\mathrm{c} < \Delta_\mathrm{c}$ (scenario III). We see that the existence of a Sarma phase at a second order transition line is a universal feature, whereas it becomes non-universal in the vicinity of a first order transition line.

We recall that the binding energy $\varepsilon_\mathrm{B} < 0$ is nonzero on the BEC side and the fermion chemical potential eventually becomes negative for large positive scattering length. In contrast, we set $\varepsilon_\mathrm{B} = 0$ on the BCS side. The quantity $\mu_\mathrm{mb} = \mu - \varepsilon_\mathrm{B}/2 > 0$ is manifestly positive for non-vanishing density, and we choose units such that $\mu_\mathrm{mb} = 1$ when discussing the whole crossover. A negative chemical potential shifts the minimum in the Sarma criterion (5.138). Taking this possibility into account, the criterion generalizes to

$$\delta\mu > \min_p \sqrt{\varepsilon_p^2 + \Delta_0^2} = \begin{cases} \Delta_0\,, & (\mu \geq 0) \\ \sqrt{\mu^2 + \Delta_0^2}\,, & (\mu < 0) \end{cases}, \tag{5.139}$$

see also the mean field theory discussion above.

In experiments with ultracold atoms the Sarma phase can be inferred from a non-monotonous or non-continuous momentum distribution after time-of-flight expansion (Gubbels and Stoof [2013]). At nonzero temperature, the sharp features in the momentum distribution are smeared out. The Sarma phase also shows up in shell-structured in-situ density images, where the polarized superfluid manifests itself in a population imbalance between the spin species (Gubbels et al. [2006]): If the transition to the normal gas is of first order, an intermediate population imbalanced region in the cloud, which smoothly connects to the balanced superfluid, indicates the Sarma phase. If the transition is of second order, the superfluidity of the population imbalanced region can be probed by the excitation of vortices. The presence of Fermi surfaces is also expected to induce metallic features in the superfluid, which are observable in its transport properties. This makes the system an unconventional superfluid. The transport properties of neutron stars are known to strongly influence the life time of the star. A possible Sarma phase is thus of relevance for interpreting the stellar evolution.

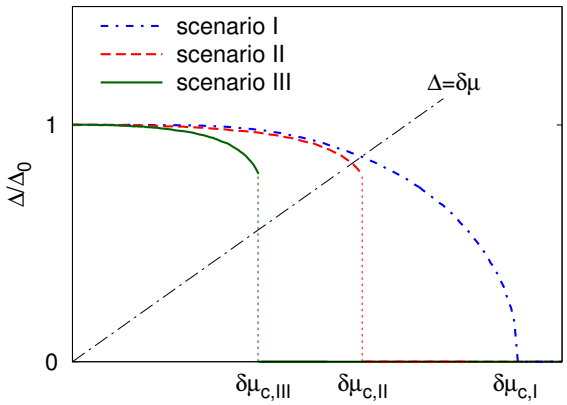

Figure 5.24: The three possible scenarios for the Sarma condition $\Delta = \delta\mu$; see discussion below (5.138) for details. In the case of a second-order superfluid phase transition the criterion is always fulfilled for some $\delta\mu$ (Scenario I), whereas the size of the critical gap at a first-order transition decides whether it is fulfilled (Scenario II) or not (Scenario III). Figure taken from Boettcher et al. [2014b].

To highlight the impact of bosonic fluctuations, we compare results in the mean field approximation to those obtained with the FRG. In many cases mean field theory predicts a first order breakdown of superfluidity due to spin-imbalance at $T = 0$. Including fluctuations, this first order transition can turn into a continuous one. This interesting effect has indeed been found in FRG studies of two-dimensional Hertz-Millis type actions (Jakubczyk et al. [2009]), and a non-relativistic spin-imbalanced Fermi gas on the BCS-side of the crossover in two spatial dimensions (Strack and Jakubczyk [2014]). In the present analysis we do not find such a smoothing of the transition. It can, however, be seen in a relativistic system of quarks and mesons with isospin density, see Boettcher et al. [2014b].

For the investigation of the Sarma phase, we set $A_\phi = Z_\phi$ and $V_\phi = 0$ in the boson propagator. Moreover, we neglect the renormalization of the fermion propagator. At first sight this might invalidate the analysis as the Sarma criterion is formulated in terms of renormalized fermion quantities of the fermion excitation spectrum. However, here we argue why we believe that a truncation with $P_{\psi,k}(Q) = \mathrm{i}q_0 + q^2 - \mu$ for all k is sufficient.

From studies of the polaron (Lobo et al. [2006], Gubbels and Stoof [2008]) and the balanced UFG (Boettcher et al. [2014c]) it is known that fluctuations effects tend to *increase* the individual chemical potential, μ_σ, by a contribution approximately proportional to the chemical potential of the other species, $\mu_{\bar{\sigma}}$. In both cases, fluctuations induce renormalization effects on the order of 60%,

$$\mu_{\sigma,\mathrm{eff}} \simeq \mu_\sigma + 0.6\,\mu_{\bar{\sigma}}. \tag{5.140}$$

Assuming this relation to be generally valid, we can estimate the effective imbalance to be given by

$$\delta\mu_{\text{eff}} = (\mu_{1,\text{eff}} - \mu_{2,\text{eff}})/2 \simeq 0.4\,\delta\mu, \tag{5.141}$$

i.e. the effective imbalance is smaller than the unrenormalized one. The Sarma criterion $\Delta_c < \delta\mu_{\text{eff}}$, which has to be true for the renormalized parameters, is even less likely fulfilled. In particular, for most cases discussed below we find that the Sarma criterion is violated already for the unrenormalized chemical potential imbalance. According to our argument here, this implies that it is also violated for the renormalized one.

Unitary Fermi Gas

We start our discussion with the imbalanced UFG, where the superfluid is strongly correlated.

The mean field phase structure is recovered by neglecting bosonic fluctuations in the FRG flow equation. This is demonstrated in Fig. 5.25 (upper lines labelled "MFA"). The Sarma phase appears in the vicinity of the second order transition line. Note that the dotted green line, corresponding to the condition $\Delta = \delta\mu$, only serves as an orientation, since the transition is a crossover at nonzero temperature. The onset of the Sarma phase terminates close to the critical point, where it hits the first order transition. The jump in the gap prevents the Sarma condition from being fulfilled for lower temperatures. This corresponds to Scenario III discussed above. We conclude that, at the mean field level, there is no stable Sarma phase at $T = 0$.

Next we include the feedback of bosonic fluctuations. The resulting phase diagram is also shown in Fig. 5.25 (lower lines labelled "FRG"). At vanishing imbalance we again find a second order phase transition. The inclusion of bosonic fluctuations makes the transition sharper, resulting in a *shrinking* Sarma phase. Furthermore, this phase appears at relatively high temperatures only. In this regime the presence of gapless fermionic excitations is smeared out and may be difficult to detect in experiment.

Due to its complexity, it is hard to evolve the FRG flow for very small k in the low temperature region. A conservative estimate for the latter is indicated by the grey band in Fig. 5.25. The determination of the phase boundary, however, is still reliable in this region. A more detailed discussion of this point is provided in Sec. 5.3.2 above. The end of the Sarma phase, however, lies well above this band. Hence we can draw our conclusions independent of this limitation.

BCS-BEC crossover

We extend our study to finite scattering lengths in order to identify a region that might support a stable Sarma phase at $T = 0$. We note that the phase structure

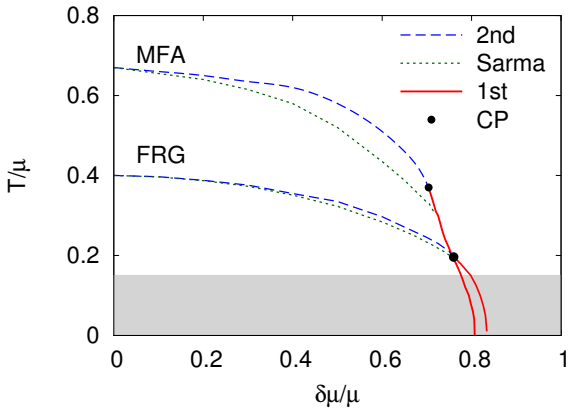

Figure 5.25: Phase structure of the spin-imbalanced UFG. The upper lines correspond to the mean field approximation (MFA), the lower ones to the FRG result. We observe a substantial decrease in the critical temperature due to bosonic fluctuations. The tricritical point is indicated by a black dot. The Sarma condition $\Delta = \delta\mu$ is fulfilled along the dotted green line close to the second order phase boundary. Interestingly, in both cases we do not find a Sarma phase at zero temperature. Figure taken from Boettcher et al. [2014b].

of the imbalanced BCS-BEC crossover beyond mean field had been unexplored to a large extent so far.

In the following we focus on the phase structure of the imbalanced BCS-BEC crossover at zero temperature, i.e. the quantum phase diagram. The mean field result has been calculated by Sheehy and Radzihovsky [2006], Parish et al. [2007]. The superfluid-to-normal transition is of first order on the BCS side ($a^{-1} \leq 0$). This behavior persists on the BEC side ($a^{-1} > 0$) up to a quantum critical point (QCP) where the transition turns to second order. Within the mean field approximation, the QCP is located at

$$(\sqrt{\mu_{\mathrm{mb}}}a)^{-1}_{\mathrm{MF}} = 4.19, \;\; \delta\mu_{\mathrm{MF}} = 21.6\mu_{\mathrm{mb}} = 0.61|\varepsilon_{\mathrm{B}}|. \tag{5.142}$$

The quantum phase diagram including the feedback of bosonic fluctuations from the FRG is shown in Fig. 5.26. Its structure is quantitatively very similar to the mean field result. Hence we only show the FRG result and superimpose the locations of the QCP and the onset of the Sarma transition from the MFA. On the BCS side and in the vicinity of the resonance the transition is of first order. On the BEC side there is a quantum critical point where a second order line emerges. Its coordinates read

$$(\sqrt{\mu_{\mathrm{mb}}}a)^{-1}_{\mathrm{FRG}} = 7.1, \;\; \delta\mu_{\mathrm{FRG}} = 56.2\mu_{\mathrm{mb}} = 0.56|\varepsilon_{\mathrm{B}}| \tag{5.143}$$

within our approximation. We see that fluctuations rather induce a first order

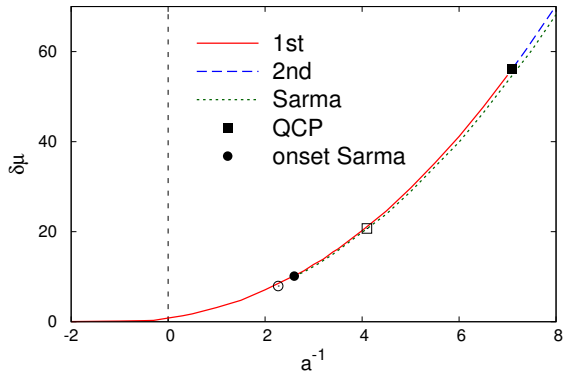

Figure 5.26: Quantum phase diagram of the spin-imbalanced BCS-BEC crossover from the FRG. Units are such that $\mu_{\mathrm{mb}} = 1$. The first order superfluid phase transition appearing on the BCS side persists on the BEC side up to the quantum critical point (QCP). The QCP is marked by a filled (open) square for the result from the FRG (mean field) analysis. The onset of the Sarma phase along the first order line according to Scenario II is indicated by the filled (open) circle for the FRG (mean field) result. The boundary of the Sarma phase on the BEC side is given by the dotted green line. Figure taken from Boettcher et al. [2014b].

phase transition than a second order one. This is in contrast to the relativistic system mentioned above.

The onset of the Sarma phase on the BEC side is located to the left of the QCP, and thus happens according to Scenario II in the terminology introduced above. The boundary of the Sarma phase according to (5.139) is indicated by the dotted green line in Fig. 5.26. It terminates in the first order line at $(\sqrt{\mu_{\mathrm{mb}}}a)^{-1}_{\mathrm{MF}} = 2.27$ in MFA, which is shifted towards $(\sqrt{\mu_{\mathrm{mb}}}a)^{-1} = 2.6$ when including bosonic fluctuations. To the right of the QCP, we always find a stable Sarma phase below the second order line according to Scenario I. Since the Sarma phase only appears on the BEC side, the corresponding magnetized superfluid constitutes a homogeneous state consisting of a BEC of diatomic molecules and majority atoms.

Hence we find that there is no parameter set that supports a bosonic-fluctuation induced Sarma phase at $T = 0$ in the 3D BCS-BEC crossover. The onset of the Sarma phase occurs closer to resonance in MFA compared to the FRG-analysis. Moreover, distinct from the relativistic case discussed in Boettcher et al. [2014b], a Sarma phase arises only on the *BEC-side* of the crossover, whereas the corresponding relativistic system rather corresponds to a BCS-like system.

An interesting question concerns the critical exponents at the QCP on the BEC side. The FRG is capable of computing critical exponents to a high accuracy

beyond mean field theory, see e.g. Litim [2002]. A more detailed analysis of the quantum critical properties of the QCP will be presented elsewhere.

5.3.4 Experimental signatures

Our findings on the phase structure of the spin-imbalanced UFG have immediate consequences on the qualitative behavior of in-situ density profiles, $n(\vec{r})$, obtained for this system in experiment. Here, we briefly recapitulate the phenomenology of second- and first order phase transitions in an external potential, and also discuss the impact of the precondensation region on the interpretation of experimental results. The generalization of the following arguments for nonzero a^{-1} are straightforward. We define the density and population imbalance by

$$n(\mu, T, \delta\mu) = n_1 + n_2 = \left(\frac{\partial P}{\partial \mu}\right)_{\delta\mu, T}, \tag{5.144}$$

$$\delta n(\mu, T, \delta\mu) = n_1 - n_2 = \left(\frac{\partial P}{\partial \delta\mu}\right)_{\mu, T}, \tag{5.145}$$

respectively. Herein P is the pressure, and n_σ is the density of atoms in hyperfine state $|\sigma\rangle$.

For an ultracold quantum gas confined to an external trapping potential $V(\vec{r})$, the thermodynamic equilibrium state depends on the particular shape of the trap. In many cases, however, we can apply the local density approximation (LDA), which assigns a local chemical potential $\mu(\vec{r}) = \mu_0 - V(\vec{r})$ to each point in the trap. Here μ_0 is the central chemical potential. In this way, thermodynamic observables computed for the homogeneous system are translated into those of the trapped system, see the discussion in Sec. 2.1. Note that T and $\delta\mu$ are constant throughout the trap within LDA. The LDA can be applied if the length scale associated to the trap, ℓ_0, is much larger than all other scales of the many-body system. For instance, in a harmonic trap, $V(\vec{r}) = M\omega_0^2 r^2/2$, the former scale is given by the oscillator length $\ell_0 = \sqrt{\hbar/M\omega_0}$.

If the central chemical potential is sufficiently larger than T, the inner region of the trapped system is in the superfluid phase. Above a certain critical radius, r_c, superfluidity vanishes and is replaced by a quantum gas in the normal phase, which eventually becomes classical and decays exponentially in the outer wings of the cloud. The critical radius is related to the critical chemical potential, $\mu_\mathrm{c}(T, \delta\mu)$, according to $\mu_\mathrm{c} = \mu_0 - V(\vec{r}_\mathrm{c})$. At a first order phase transition the density at μ_c exhibits a jump. Accordingly, the superfluid core and the normal region are separated by of a jump in density at r_c. We visualize this in Fig. 5.27. In contrast, the transition is continuous for a second order phase transition. In this way, the order of the phase transition, and e.g. our prediction for the temperature of the tricritical point of the UFG, $T_\mathrm{CP}/\mu_0 = 0.20$, can be verified from in-situ images at different temperatures.

In experiments with cold atoms, the imbalance between spin-partners is introduced by differing atom numbers $N_1 \geq N_2$ for atoms in state $|1\rangle$ and $|2\rangle$, respec-

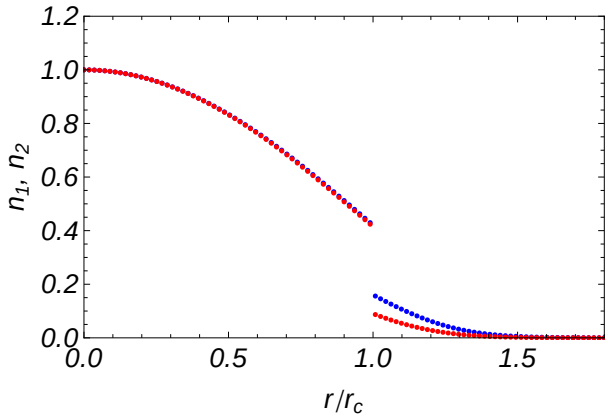

Figure 5.27: Schematic in-situ density profile $n_\sigma(r)$ for a population-imbalanced ensemble of the UFG with $N_1 > N_2$ at low temperature. The blue and red points correspond to atoms in hyperfine state $|1\rangle$ and $|2\rangle$, respectively. For $T < T_{\mathrm{CP}}$ the superfluid transition is of first order, such that the superfluid inner region is separated from the polarized normal gas by a jump in density at the critical radius r_c. Figure taken from Boettcher et al. [2014a].

tively. The influence of a non-zero polarization $p = (N_1 - N_2)/(N_1 + N_2)$ is very distinct for trapped systems in comparison to homogeneous ones (Braun et al. [2014]). In a *homogeneous system*, we have $N_\sigma = n_\sigma V$ with volume V, and the critical spin-imbalance, $\delta\mu_\mathrm{c}$, translates to a critical polarization $p_\mathrm{c} = \delta N_\mathrm{c}/\delta N = \delta n_\mathrm{c}/n$, with n and δn from Eqs. (5.144) and (5.145) in the normal phase. At zero temperature, the superfluid phase is found for $p = 0$, whereas the system is in a normal polarized phase for $p > p_\mathrm{c}$. When preparing N_1 and N_2 such that $0 < p < p_\mathrm{c}$, the equilibrium state of the system will not be homogeneous, but rather a mixed phase consisting of a superfluid with bubbles of normal phase majority atoms. For a *trapped system* instead, the particle numbers N_σ are obtained from an integral over the whole cloud, $N_\sigma = \int_{\vec{r}} n_\sigma(\vec{r})$. As a consequence, phase separation takes place in real space by means of a superfluid inner region and a normal outer region. Both are separated by the mentioned jump in the density.

With a state-resolved detection of individual densities, $n_1(\vec{r})$ and $n_2(\vec{r})$, it is possible to measure the local in-situ polarization $p(\vec{r})$ of the trapped gas. According to our finding that there is no Sarma phase at zero temperature, a nonzero polarization inside the superfluid core of the cloud can only be detected at $T > 0$. As we find the Sarma phase only to appear at very high temperatures and close to the phase boundary, a substantial local polarization $p(\vec{r})$ of the superfluid should only be detectable for $r \lesssim r_\mathrm{c}$.

The length scale ℓ_0 divides the trapped system into cells of spatial extend ℓ_0^3 where the local chemical potential does not vary substantially. Thus within each

cell the system is approximately homogeneous and only fluctuations with wavelengths $\leq \ell_0$ are present. In this way, ℓ_0 approximately corresponds to the final k_f where we stop integrating the flow of $U_k(\rho)$ according to $k_\mathrm{f}^{-1} = \ell_0$. The homogeneous system corresponds to $\ell_0 = \infty$, i.e. $k_\mathrm{f} = 0$. By stopping at a nonzero $k_\mathrm{f} > 0$, which is still sufficiently smaller than the many-body scales, we can simulate the effect of a large trapping potential and the corresponding infrared cutoff which suppresses long wavelength fluctuations. However, despite being intuitively reasonable, the association $k_\mathrm{f} = \ell_0^{-1}$ does not always provide the correct picture (Braun et al. [2005], Braun et al. [2011], Braun et al. [2012]).

In our analysis of the UFG we find a substantial precondensation region in the phase diagram, Fig. 5.19, where a minimum $\rho_{0,k} > 0$ appears during the flow, but is eventually washed out such that $\rho_{0,k=0} = 0$. The restoration of symmetry is due to long wavelength fluctuations on length scales $k^{-1} \to \infty$. However, if long wavelength fluctuations are cut off by a trap with scale ℓ_0, a superfluid order parameter $\rho_0 \approx \rho_{0,k=k_\mathrm{f}}$ can be observed experimentally even in the precondensation phase.

As discussed in Sec. 5.3.2, the first order transition is barely influenced by the final scale k_f as long as the latter is below the many-body scales. Therefore, the first order transition and its location can also be deduced in a finite trapping geometry. On the other hand, for smaller spin-imbalance, where the transition is of second order, this effect can be substantial. As a consequence, the second order phase boundary of the homogeneous system is likely to be overestimated by applying LDA to a trapped gas. It would be very interesting to study this effect by means of varying the trapping frequency.

6 Two-dimensional BCS-BEC Crossover

6.1 Fermion pairing in three and two dimensions

We systematically approach the balanced 2D BCS-BEC crossover with the FRG by applying the beta functions whose range of applicability is well-understood for the 3D system to the lower-dimensional setting. In this way we obtain a qualitative picture of the phase structure of the system and find many similarities between the 3D and 2D setup. However, it turns out to be characteristic that variations of the truncation scheme which have almost no effect on the quantitative features of the 3D system, substantially influence the 2D results.

6.1.1 Scattering properties

The scattering or vacuum physics in 2D is different to the 3D analogue in the sense that a sufficiently strong attraction between two particles (which is present in our model) always results in a bound state with binding energy ε_B. This allows to define a 2D scattering length a according to

$$\varepsilon_\mathrm{B} = -\frac{\hbar^2}{Ma^2} = -\frac{2}{a^2}, \tag{6.1}$$

where $M = 1/2$ is the atomic mass, which we assume to be equal for both scattering partners. This is in contrast to the 3D case where a bound state in the spectrum only appears for $a > 0$. The 2D vacuum physics thus seem to be close to the BEC-side in 3D. However, the binding energy on the BCS-side of the 2D system is exponentially small such that the overall phenomenology of the crossover is similar to the 3D case. Nevertheless, the presence of a bound state for all a allows to drive the 2D crossover parameter $\log(k_\mathrm{F}a)$ by *either* changing a or $k_\mathrm{F} = (2\pi n)^{1/2}$. In the latter case we say that the crossover is density-driven.

In the following we first discuss the scattering physics in 3D and 2D from elementary quantum mechanics, and then discuss the modification which are necessary to initialize the RG-flow in 2D. For a comparison of scattering in 3D, 2D, and 1D we refer to the presentation of Morgan et al. [2002]. We model interactions between atoms by a pointlike δ-potential. This requires renormalization of the coupling constant, see the discussion below Fig. 5.15, but also supports a bound state for all values of the coupling constant in 2D. Since ultracold atoms are faithfully described by such a δ-potential, see Sec. 2.1, we conclude that the sufficiently strong attraction required for the two-body bound state is guaranteed for ultracold atoms.

Bound state and scattering length

We start with computing the bound state energy of two particles interacting via a δ-potential. For the bound state wave function in the center-of-mass frame with relative coordinate $\vec{r}$ between the atoms we have

$$\Big(-\frac{\nabla^2}{M}+\lambda_\Lambda\delta^{(d)}(\vec{r})\Big)\psi(\vec{r})=\varepsilon_\mathrm{B}\psi(\vec{r}). \tag{6.2}$$

Herein $\varepsilon_\mathrm{B}<0$ is the binding energy, which is to be determined. We apply $\int_{\vec{r}} e^{\mathrm{i}\vec{q}\cdot\vec{r}}$ to both sides to obtain

$$\frac{q^2}{M}\tilde{\psi}(\vec{q})+\lambda_\Lambda\underbrace{\int_{\vec{r}} e^{\mathrm{i}\vec{q}\cdot\vec{r}}\psi(\vec{r})\delta^{(d)}(\vec{r})}_{\psi(\vec{r}=0)}=\varepsilon_\mathrm{B}\tilde{\psi}(\vec{q}), \tag{6.3}$$

where $\tilde{\psi}(\vec{q})$ is the Fourier transform of $\psi(\vec{r})$. Hence

$$\tilde{\psi}(\vec{q})=-\frac{\lambda_\Lambda}{q^2/M-\varepsilon_\mathrm{B}}\psi(\vec{r}=0). \tag{6.4}$$

Integrating both sides over $\vec{q}$ yields

$$\psi(\vec{r}=0)=\int_{\vec{q}}\tilde{\psi}(\vec{q})=-\psi(\vec{r}=0)\int_{\vec{q}}\frac{\lambda_\Lambda}{q^2/M-\varepsilon_\mathrm{B}}. \tag{6.5}$$

The integral requires UV regularization and we choose a sharp momentum cutoff here. We arrive at

$$-\frac{1}{\lambda_\Lambda}=\int_{\vec{q}}^{\Lambda}\frac{1}{q^2/M-\varepsilon_\mathrm{b}}\overset{M=1/2}{=}\frac{1}{2}\int_{\vec{q}}^{\Lambda}\frac{1}{q^2-\frac{\varepsilon_\mathrm{b}}{2}}. \tag{6.6}$$

We conclude that a solution of Eq. (6.2) with $\varepsilon_\mathrm{B}<0$ necessarily requires $\lambda_\Lambda<0$. To further constrain the microscopic couplings which allow for a bound state we first consider $d=2$, where Eq. (6.6) becomes

$$-\frac{1}{\lambda_\Lambda}=\frac{1}{8\pi}\log\Big(1+\frac{\Lambda^2}{|\varepsilon_\mathrm{B}|/2}\Big)\simeq-\frac{1}{8\pi}\log\Big(\frac{|\varepsilon_\mathrm{B}|/2}{\Lambda^2}\Big), \tag{6.7}$$

where we applied $\log(1+\epsilon^{-1})\simeq-\log(\epsilon)+\epsilon$ for small ϵ in the second equality and assumed the UV cutoff Λ to be large enough such that we can neglect higher order terms. Apparently, no further constraint on λ_Λ is set by this equation and we always find a bound state with energy

$$\varepsilon_\mathrm{B}=-2\Lambda^2e^{8\pi/\lambda_\Lambda}. \tag{6.8}$$

We observe that a small binding energy requires $|\lambda_\Lambda|$ to be rather small, which is ensured on the BCS-side of the crossover. Introducing the 2D scattering length a via $\varepsilon_\mathrm{B}=-2/a^2$ we find

$$a=\Lambda^{-1}e^{-8\pi/\lambda_\Lambda} \tag{6.9}$$

for a sharp momentum cutoff Λ. Note that a in 2D is large on the BCS-side, see also Table. 6.2.

In 3D Eq. (6.6) reads

$$-\frac{1}{\lambda_\Lambda} = \frac{1}{4\pi^2}\left[\Lambda - \sqrt{\frac{|\varepsilon_\mathrm{B}|}{2}}\arctan\Big(\frac{\Lambda}{(|\varepsilon_\mathrm{B}|/2)^{1/2}}\Big)\right] \simeq \frac{1}{4\pi^2}\Big(\Lambda - \frac{\pi}{2}\sqrt{\frac{|\varepsilon_\mathrm{B}|}{2}}\Big) \tag{6.10}$$

for $\varepsilon_\mathrm{B} < 0$, where we employed $\arctan(\epsilon^{-1}) \simeq \mathrm{sgn}(\epsilon)\frac{\pi}{2} - \epsilon$ for small ϵ and again assumed Λ to be large. Eq. (6.10) is solved by $\varepsilon_\mathrm{B} = -2/a^2$ with positive scattering length a defined according to

$$\frac{1}{8\pi a} = \frac{1}{\lambda_\Lambda} + \frac{1}{4\pi^2}\Lambda > 0. \tag{6.11}$$

Contrary to the 2D case, we only find a bound state in 3D for

$$\lambda_\Lambda < -4\pi^2\Lambda^{-1}. \tag{6.12}$$

For a different regularization scheme, the prefactor on the right hand side of this equation will change, but the qualitative statement remains valid.

To connect the previous consideration to the FRG approach within the two-channel model we rederive the results from a different perspective. It is an exact property that the fermion propagator is not renormalized for $\mu \leq 0$ and $T = 0$. The corresponding effective potential reads

$$U(\Delta^2, \mu) = -\frac{\Delta^2}{\lambda_{\psi\Lambda}} - \int_Q^\Lambda \log\Big(q_0^2 + (q^2 - \mu)^2 + \Delta^2\Big), \tag{6.13}$$

and for the density per species in the presence of a boson background field $\Delta^2 = h^2\rho$ we find

$$n_\sigma(\Delta^2, \mu) = \int_{\vec{q}} \frac{1}{2}\Big(1 - \frac{q^2 - \mu}{\sqrt{(q^2 - \mu)^2 + \Delta^2}}\Big). \tag{6.14}$$

To define the physical vacuum we require both the boson field expectation value, Δ_0, and the density, $n_\sigma = n_\sigma(\Delta_0, \mu)$, to vanish. Given $\Delta_0 = 0$ the latter condition is indeed fulfilled for $T = 0$ and $\mu \leq 0$. For the vacuum to be stable towards condensation of bosons we need to have $m_\phi^2 := (\partial U/\partial\rho)(0, \mu) \geq 0$. We have

$$0 \overset{!}{\leq} \frac{m_\phi^2}{h^2} = -\frac{1}{\lambda_{\psi\Lambda}} - \int_Q^\Lambda \frac{1}{q_0^2 + (q^2 - \mu)^2} = -\frac{1}{\lambda_{\psi\Lambda}} - \frac{1}{2}\int_{\vec{q}}^\Lambda \frac{1}{q^2 + |\mu|}. \tag{6.15}$$

We used $|q^2 - \mu| = q^2 + |\mu|$ for $\mu \leq 0$.

We first look for solutions of Eq. (6.15) with $\mu = 0$. They correspond to the atomic side of the resonance. For $\mu = 0$ we have

$$0 \overset{!}{\leq} \frac{m_\phi^2}{h^2} = -\frac{1}{\lambda_{\psi\Lambda}} - 2v_d\int_0^\Lambda \mathrm{d}q q^{d-3}. \tag{6.16}$$

A finite result for the boson mass is only found for $d > 2$. For lower dimensions the integration range cannot extend to $q = 0$. The physical cure of this infrared divergence is, in fact, simply the appearance of the bound state. From Eq. (6.16) we find

$$0 \leq \frac{m_\phi^2}{h^2} = -\frac{1}{\lambda_{\psi\Lambda}} - \frac{1}{4\pi^2}\Lambda =: -\frac{1}{8\pi a} \tag{6.17}$$

for $d = 3$ and $a \leq 0$. Note that this definition of the 3D scattering length coincides with the one given for $a > 0$ in Eq. (6.11). We also note here that

$$\mu = 0,\ m_\phi^2 = 0 \tag{6.18}$$

in vacuum corresponds to the resonance point with $a^{-1} = 0$. At this point, both bosons and fermions (the latter with mass term $m_\psi^2 = -\mu$) become gapless.

To proceed we now consider solutions of Eq. (6.15) for a stable vacuum with $\mu < 0$. As mentioned in the previous paragraph, this corresponds to a nonzero mass term $-\mu$ in the excitation spectrum for fermions, and thus bosons are the elementary excitations with vanishing mass term. Therefore, this situation describes the bosonic side of the resonance. We have

$$0 \stackrel{!}{=} \frac{m_\phi^2}{h^2} = -\frac{1}{\lambda_{\psi\Lambda}} - \frac{1}{2}\int_{\vec{q}}^{\Lambda} \frac{1}{q^2 + |\mu|}. \tag{6.19}$$

However, this coincides with Eq. (6.6), where we associate

$$\mu = \frac{\varepsilon_\mathrm{B}}{2} < 0,\ \text{for } a > 0, \tag{6.20}$$

in vacuum. Eq. (6.20) is valid in both 3D and 2D.

Dimer propagator in vacuum

For later reference we compute here also the inverse dimer propagator, P_ϕ, in vacuum. Its kinetic coefficients, which are regularization-scheme independent, can be used as a benchmark for truncation schemes in the FRG analysis. For $\mu \leq 0$ and external momentum $P = (p_0, \vec{p})$ we have

$$\begin{aligned}
P_\phi(P) &= -\frac{h^2}{\lambda_{\psi\Lambda}} - h^2 \int_Q^\Lambda \frac{1}{P_\psi(Q+P)P_\psi(-Q)} \\
&= -\frac{h^2}{\lambda_{\psi\Lambda}} - h^2 \int_Q^\Lambda \frac{1}{[\mathrm{i}(q_0+p_0) + (\vec{q}+\vec{p})^2 - \mu][-\mathrm{i}q_0 + q^2 - \mu]} \\
&= -\frac{h^2}{\lambda_{\psi\Lambda}} - h^2 \int_{\vec{q}}^\Lambda \frac{1}{\mathrm{i}p_0 + (\vec{q}+\vec{p})^2 + q^2 - 2\mu} \\
&= -\frac{h^2}{\lambda_{\psi\Lambda}} - h^2 \int_{\vec{q}}^\Lambda \frac{1}{\mathrm{i}p_0 + \left(\vec{q}+\frac{\vec{p}}{2}\right)^2 + \left(\vec{q}-\frac{\vec{p}}{2}\right)^2 - 2\mu} \\
&= -\frac{h^2}{\lambda_{\psi\Lambda}} - 2v_d h^2 \int_0^\Lambda \mathrm{d}q q^{d-1} \frac{1}{q^2 + \frac{\mathrm{i}p_0}{2} + \frac{p^2}{4} - \mu},
\end{aligned} \tag{6.21}$$

where $-h^2/\lambda_{\psi\Lambda} = m^2_{\phi\Lambda}$ is the unrenormalized boson mass term. For $P = 0$ we recover Eqs. (6.16) and (6.19) with $P_\phi(0) = m^2_\phi$. In 3D the integration yields

$$\begin{aligned} P_\phi(P) &= -\frac{h^2}{\lambda_{\psi\Lambda}} - \frac{h^2}{4\pi^2}\Lambda + \frac{h^2}{8\pi}\sqrt{\frac{\mathrm{i}p_0}{2} + \frac{p^2}{4} - \mu} \\ &= \frac{h^2}{8\pi}\left(-\frac{1}{a} + \sqrt{\frac{\mathrm{i}p_0}{2} + \frac{p^2}{4} - \mu}\right), \end{aligned} \tag{6.22}$$

where we have dropped higher order terms $\sim |p_0|/\Lambda^2, p^2/\Lambda^2$. On the bosonic side of the resonance this expression can be expanded further in powers of P due to the negative chemical potential given by $\mu = -a^{-2} < 0$. Note that $m^2_\phi = 0$ in this case. We write

$$P_\phi(P) = A_\phi\Big(S_\phi \mathrm{i}p_0 + \frac{p^2}{2} + V_\phi p_0^2 - V_2 \mathrm{i}p_0 p^2 - V_3\frac{p^4}{4} + \dots\Big) \tag{6.23}$$

and find

$$A_\phi = \frac{h^2 a}{32\pi},\ S_\phi = 1,\ V_\phi = V_2 = V_3 = \frac{a^2}{8}. \tag{6.24}$$

Similarly, in 2D we obtain

$$\begin{aligned} P_\phi(P) &= -\frac{h^2}{\lambda_{\psi\Lambda}} - \frac{h^2}{8\pi}\log\left(\frac{\frac{\mathrm{i}p_0}{2} + \frac{p^2}{4} - \mu}{\Lambda^2}\right) \\ &= -\frac{h^2}{8\pi}\log\left(1 + \frac{\mathrm{i}p_0 a^2}{2} + \frac{p^2 a^2}{4}\right), \end{aligned} \tag{6.25}$$

and, for the kinetic coefficients,

$$A_\phi = \frac{h^2 a^2}{16\pi},\ S_\phi = 1,\ V_\phi = V_2 = V_3 = \frac{a^2}{4}. \tag{6.26}$$

Note that, of course, we always have $P_\phi(0) = m^2_\phi = 0$ and $\mu = -a^{-2}$ for the 2D vacuum case.

FRG analysis

The analysis presented above suggests a very simple and clear picture of the vacuum renormalization with the FRG which is only based on static properties at vanishing frequency and momentum. We assume that the fermion propagator is not renormalized in vacuum. We further assume the vacuum setup, i.e. $T = \Delta = 0$ and $\mu \leq 0$, in the following.

If there is a microscopic bound state, i.e. for $a > 0$ in 3D, and for all a in 2D, we set

$$\mu = \frac{\varepsilon_\mathrm{B}}{2} = -a^{-2},\ (a > 0), \tag{6.27}$$

and tune $h_\Lambda^2/m_{\phi\Lambda}^2 = \bar{h}_\Lambda^2/\bar{m}_{\phi\Lambda}^2$ such that

$$m_{\phi,k=0}^2 = 0, \ (a > 0). \tag{6.28}$$

In this way the scattering length is defined via $\varepsilon_\mathrm{B} = -2a^{-2}$. For $a \leq 0$ in the 3D case we set $\mu = 0$ and tune $h_\Lambda^2/m_{\phi\Lambda}^2$ such that

$$\frac{m_\phi^2}{h^2}\Big|_{k=0} = -\frac{1}{\lambda_{\psi,k=0}} = -\frac{1}{8\pi a}. \tag{6.29}$$

Note that we often apply truncations where $\bar{h}_{k=0}^2 = \bar{h}_\Lambda^2$.

This scheme can be applied very generally. For the F- (mean field) and FB_0-truncations with q^2-opt regulators, however, the equations simplify considerably such that many scattering properties can be derived analytically. We then have $\dot{\bar{h}} = 0$, such that $\bar{h}_k^2 = \bar{h}_\Lambda^2$ for all k. The flow of the renormalized dimensionless Feshbach coupling is given by

$$\partial_t \tilde{h}^2 = (d - 4 + \eta_\phi)\tilde{h}^2. \tag{6.30}$$

The flow is attracted to a partial UV fixed point with

$$\eta_\phi = \eta_{\phi,\star} = 4 - d = \begin{cases} 1 & (d = 3) \\ 2 & (d = 2) \end{cases}. \tag{6.31}$$

Note that the fixed point anomalous dimension reflects the scaling of the vacuum dimer propagator, Eqs. (6.22) and (6.25), according to $P_\phi \sim A_\phi q^2 \sim q^{2-\eta_\phi}$, see also Sec. 4.1.3. In the early stage of the flow we have $\tilde{\mu} = \mu/k^2 \simeq 0$. We can then read off the anomalous dimension from Eq. (4.259) to be given by

$$\eta_\phi^{(F)} = \frac{16 v_d \tilde{h}^2}{d} \ell_{F,\mathrm{xx}}^{(0,2)}(0,0,0) = \frac{4 v_d \tilde{h}^2}{d}. \tag{6.32}$$

The initial value for the Feshbach coupling is not important as long as it is large enough, because it will be attracted to the UV fixed point. For concreteness we directly start at the fixed point and thus set $\bar{h}_\Lambda^2 = \tilde{h}_\star^2 \Lambda^{4-d}$ with

$$\tilde{h}_\star^2 = \frac{(4-d)d}{4 v_d}. \tag{6.33}$$

For the UV cutoff we may choose $\Lambda = 1000$, which has to be compared to $\mu_\mathrm{mb} = \mu - \varepsilon_\mathrm{B}/2 = 1$ in the many-body problem. Given a scattering length a we further need to fine-tune the boson mass term $\bar{m}_{\phi\Lambda}^2$. As outlined above we set

$$\mu = -a^{-2}\theta(a). \tag{6.34}$$

For the flow of the boson mass term we have

$$\dot{\bar{m}}_\phi^2 = \frac{16 v_d \bar{h}_\Lambda^2 k^{d-2}}{d} \ell_F^{(1,2)}(\tilde{\mu}, 0, 0) = \frac{4 v_d \bar{h}_\Lambda^2 k^{d-2}}{d} \theta(\tilde{\mu} + 1)(\tilde{\mu} + 1)^{d/2}. \tag{6.35}$$

Note that for $\mu < 0$ the flow of the coupling is stopped at $\tilde{\mu} = -1$, i.e. $k = a^{-1}$. This provides for a physical infrared cutoff. In the 3D atomic limit, i.e. for $a \leq 0$ and $\mu = 0$, we find $\dot{\bar{m}}^2_\phi = 4v_d \bar{h}^2 k^{d-2}/d$, and thus fix the initial mass from

$$-\frac{1}{8\pi a} = \frac{\bar{m}^2_{\phi,k=0}}{\bar{h}^2_\Lambda} = \frac{\bar{m}^2_{\phi\Lambda}}{\bar{h}^2_\Lambda} + \int_\Lambda^0 \frac{\mathrm{d}k}{k} \frac{4v_d k}{d}. \tag{6.36}$$

We then arrive at

$$\bar{m}^2_{\phi\Lambda} = \frac{\bar{h}^2_\Lambda}{6\pi^2}\Lambda - \frac{\bar{h}^2_\Lambda}{8\pi a}. \tag{6.37}$$

For $a > 0$ we employ

$$0 = \bar{m}^2_{\phi,k=0} = \bar{m}^2_{\phi\Lambda} + \frac{4v_d \bar{h}^2_\Lambda}{d} \int_\Lambda^{a^{-1}} \frac{\mathrm{d}k}{k} k^{d-2} \Big(1 - \frac{1}{k^2 a^2}\Big)^{d/2} \tag{6.38}$$

to find

$$\begin{aligned} \bar{m}^2_{\phi\Lambda} &= \frac{\bar{h}^2_\Lambda}{6\pi^2}\left[\sqrt{\Lambda^2+\mu}\Big(1 - \frac{\mu}{2\Lambda^2}\Big) - \frac{3}{2}\sqrt{-\mu}\arctan\Big(\frac{\sqrt{\Lambda^2+\mu}}{-\mu}\Big)\right] \\ &= \frac{\bar{h}^2_\Lambda}{6\pi^2 a}\left(\sqrt{\Lambda^2 a^2 - 1}\Big(1 + \frac{1}{2\Lambda^2 a^2}\Big) - \frac{3}{2}\arctan\Big(\sqrt{\Lambda^2 a^2 - 1}\Big)\right) \end{aligned} \tag{6.39}$$

in 3D, and

$$\bar{m}^2_{\phi\Lambda} = \frac{\bar{h}^2_\Lambda}{4\pi}\left(\log\Big(\frac{\Lambda}{\sqrt{-\mu}}\Big) - \frac{\mu}{2\Lambda^2} - \frac{1}{2}\right) = \frac{\bar{h}^2_\Lambda}{4\pi}\Big(\log(\Lambda a) + \frac{1}{2\Lambda^2 a^2} - \frac{1}{2}\Big) \tag{6.40}$$

in 2D. Note that for $\Lambda^2 a^2 \gg 1$ we find

$$-\frac{1}{\lambda_{\psi\Lambda}} = \frac{\bar{m}^2_{\phi\Lambda}}{\bar{h}^2_\Lambda} = c_3\Lambda - \frac{1}{8\pi a}, \ (d=3), \tag{6.41}$$

$$-\frac{1}{\lambda_{\psi\Lambda}} = \frac{\bar{m}^2_{\phi\Lambda}}{\bar{h}^2_\Lambda} = c_2 \log(\Lambda a), \ (d=2), \tag{6.42}$$

with $c_3 = 1/6\pi^2$ for the q^2-opt regulator and $c_3 = 1/4\pi^2$ for the sharp cutoff, see Eqs. (6.11) and (6.17), and $c_2 = 1/4\pi$ for both regularization schemes, see Eq. (6.7).

Due to the particular shape of the exact dimer propagator in vacuum, which only depends on the invariant

$$\frac{\mathrm{i}p_0}{2} + \frac{p^2}{4} - \mu \tag{6.43}$$

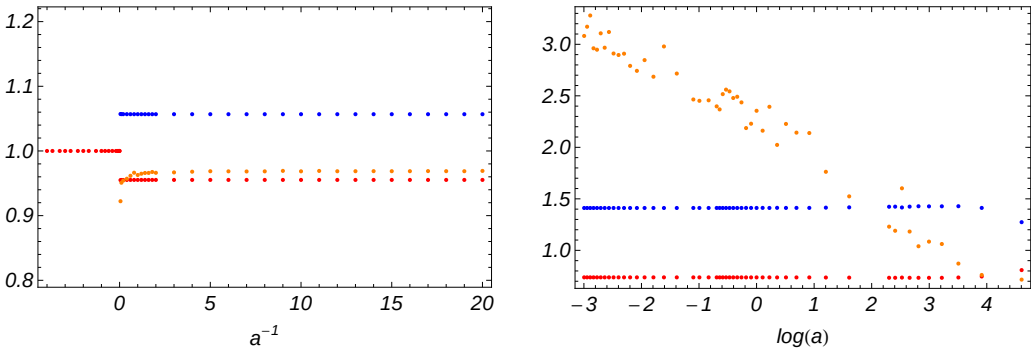

Figure 6.1: Vacuum scaling of h^2, S_ϕ, and V_ϕ within the FB-truncation with q^2-opt regulator in 3D (left) and 2D (right). We plot $h^2/(32\pi/a)$ ($h^2/(16\pi/a^2)$)) in blue, S_ϕ in red, and $V_\phi/(a^2/8)$ ($V_\phi/(a^2/4)$) in orange for the 3D (2D) case. Hence, with the appropriate scaling of the dimer propagator in vacuum according to Eqs. (6.24) and (6.26), all curves should saturate at unity for $a > 0$. We find the deviations to be rather small in the 3D-case, whereas the 2D-vacuum is only poorly resolved with this setup. Units are such that $\Lambda = 1000$ and $k = \Lambda e^{-12} = 0.006$. To obtain the proper scaling close to resonance in 3D, we need to further lower k such that $k < a^{-1}$.

with $\mu \leq 0$, the boson mass term $\bar{m}_\phi^2$ receives no contribution from the bosonic tadpole diagram, since the closed loop vanishes as all poles in the frequency integration lie in the same half-plane. Therefore, only F-diagrams should contribute to the vacuum running of m_ϕ^2. However, a contribution $\dot{m}_\phi^{2(B)} \neq 0$ can arise due to either the particular choice of regulator $R_\phi(Q)$ or the truncation applied for $P_\phi(Q)$ inside the loop. For instance, the Q-exp regulator leads to a nonzero contribution $\dot{m}_\phi^{2(B)}$ in vacuum, as well the FB-truncations with V_ϕ-term.

The renormalization scheme described in Eqs. (6.27)-(6.29) can also be applied to a situation with nonzero $\dot{m}_\phi^{2(B)}$. However, it is less clear whether this still gives a faithful description of the scattering properties. The reason for this is that $a > 0$ typically requires a small vacuum precondensate, i.e. a nonzero $\rho_{0,k}$ appears during the flow, but $\rho_0 = 0$ at $k = 0$. As a consistency check we investigate here the kinetic coefficients A_ϕ, S_ϕ, and V_ϕ. For the F- and FB$_0$-truncation with q^2-opt regulator, the relations (6.24) and (6.26) in 3D and 2D, respectively, are exactly fulfilled for $a > 0$ within the numerical precision. In contrast, we find deviations for a FB-truncation with q^2-opt regulator, where the V_ϕ-term in the boson propagator leads to $\dot{m}_\phi^{2(B)} \neq 0$. We display the results in Fig. 6.1. We observe that the deviations are on the 5%-level in 3D, whereas they become substantial in 2D. In Table. 6.1 we summarize the scattering properties, and also display results for the Q-exp regulator with $c_\phi = 1$.

In the bosonic limit the system can be modelled by an effective description in

	2D		3D		
Observable	FB_0, q^2-opt	FB, q^2-opt	FB_0, q^2-opt	FB, q^2-opt	FB, Q-exp
h^2/h^2_{exact}	1	1.4	1	1.06	1.17
$S_\phi/S_{\phi,\mathrm{exact}}$	1	0.7	1	0.96	0.88
$V_\phi/V_{\phi,\mathrm{exact}}$	1	-	1	0.97	-
a_{dd}/a	-	-	0.72	0.54	0.36

Table 6.1: Scattering properties for different truncation and regularization schemes. The values of h^2_{exact}, $S_{\phi,\mathrm{exact}}$, and $V_{\phi,\mathrm{exact}}$ correspond to those given in Eqs. (6.24) and (6.26), see also Fig. 6.1. The Q-exp regulator is evaluated for $c_\phi = 1$. The exact value for the dimer-dimer scattering length in 3D is given by $a_{\mathrm{dd}} = 0.6a$ (Petrov et al. [2004]). For the missing entries of V_ϕ in the table we do not find constant scaling.

terms of bosons. In 3D an important observable consists in the effective dimer-dimer scattering length a_{dd}. The exact value for the ratio a_{dd}/a is known to be 0.6 (Petrov et al. [2004]). Within our approach the ratio can be deduced from the boson-boson coupling λ_ϕ in vacuum. We use

$$\lambda_{\phi,k=0}\Big|_{\mathrm{VAC}} = \frac{4\pi\hbar^2}{M_\phi} a_{\mathrm{dd}} = 4\pi a_{\mathrm{dd}} \tag{6.44}$$

to find

$$\frac{a_{\mathrm{dd}}}{a} = \frac{\lambda_{\phi,k=0}}{4\pi a}\Big|_{\mathrm{VAC}}. \tag{6.45}$$

In the FB_0-truncation with q^2-opt regulator we find 0.72 for the ratio. We show below that the many-body sector on the BEC-side is strongly affected by this value, since both the Lee–Huang–Yang (LHY) correction to the equation of state and the interaction-induced shift of the critical temperature can be obtained from the purely bosonic theories with an appropriate insertion of a_{dd} into the bosonic formulas.

6.1.2 Phase structure

We now compare the phase structure of the BCS-BEC crossover in both 3D and 2D. For this purpose we apply the FB_0-truncation with q^2-opt regulator and a Taylor expansion of the effective potential to order ϕ^4. This scheme has the advantage that the scattering properties in vacuum are accurately resolved, see Table 6.1. Moreover, it allows to investigate the stability of results by comparing the outcome with $\dot{S}_\phi = 0$ or $\dot{S}_\phi \neq 0$, respectively. We show that this modification has only minor influence in 3D, whereas it leads to significant changes in 2D. The FB_0-truncation has several shortcomings such as the neglect of particle-hole fluctuations, the insufficient resolution of the infrared Goldstone regime, and the

inability to capture the Fermi liquid correction to the equation of state on the BCS-side. Still it yields a solid qualitative picture in 3D.

To determine the phase structure we find the highest temperature such that $\rho_{0,k=0} > 0$. In practice the flow cannot be evolved down to $k = 0$ (or $t = -\infty$). In addition, physical systems always have a finite volume which sets an infrared cutoff on long wavelength fluctuations. Therefore, we stop the flow at a nonzero "final" k_f (or t_f) and determine physical observables at this scale. In 3D, the running of couplings often saturates for sufficiently small t, resulting in $g_{k=0} \approx g_{k_\mathrm{f}}$ for many couplings g_k.

We search for the critical temperature by means of an algorithm which finds $T \approx T_\mathrm{c}(k_\mathrm{f})$ such that

$$0 < \Delta_{k_\mathrm{f}}(T_\mathrm{c}, \mu, a) < \frac{1}{100}\Delta_{k_\mathrm{f}}(0, \mu, a), \tag{6.46}$$

where $\Delta_k(T, \mu, a) = h^2\rho_0$ is the gap in the fermion spectrum. The limitation to 1% of the zero temperature gap is a very efficient way to compute the critical temperature for the whole crossover, as it appropriately accounts for very small gaps on the BCS-side, whereas a rather large gap is allowed on the BEC-side. We checked that a further limitation to 0.1% yields identical results in both 3D and 2D within the numerical precision. However, the outcome of Eq. (6.46) is strongly influenced by the choice of t_f in 2D: Whereas changes in t_f of order unity result in a change of the higher digits of T_c/μ in 3D, they change $T_\mathrm{c}/\mu_\mathrm{mb}$ in 2D by approximately 10%. We visualize this behavior in Fig. 6.2. Therein, and in the remainder of this section, we choose $\Lambda = 1000$ and

$$\mu_\mathrm{mb} = \mu - \varepsilon_\mathrm{B}/2 = 1. \tag{6.47}$$

The final cutoff scale is varied according to $t_\mathrm{f} = -12, -15, -18$, corresponding to $k_\mathrm{f}/\sqrt{\mu_\mathrm{mb}} = 0.006, 0.0003, 0.00002$, respectively.

The limiting BCS-formulas

$$T_\mathrm{c,BCS}/T_\mathrm{F} = \frac{8e^\gamma}{\pi e^2} e^{\pi/2k_\mathrm{F}a}, \ (d = 3), \tag{6.48}$$

$$T_\mathrm{c,BCS}/T_\mathrm{F} = \frac{2e^\gamma}{\pi} e^{-\log(k_\mathrm{F}a)}, \ (d = 2), \tag{6.49}$$

with $\varepsilon_\mathrm{F} = \mu$ are found independently of t_f in both dimensions. We cannot resolve the Gorkov-correction as we do not account for particle-hole fluctuations within our truncation. The 2D curve possesses a sharp kink at $\log(\sqrt{\mu_\mathrm{mb}}a) \approx 0$, where $T_\mathrm{c}/\mu_\mathrm{mb} = 0.364, 0.327, 0.304$ for $t_\mathrm{f} = -12, -15, -18$, respectively. In contrast we have $T_\mathrm{c}/\mu = 0.44124$ (0.44120) for $t_\mathrm{f} = -12$ (-15) in 3D.

It is interesting to study the effect of enforcing $S_\phi = 1$ during the flow. In Fig 6.3 we show the result for the phase boundary with and without running of S_ϕ for $t_\mathrm{f} = -15$. In 3D there is hardly any difference in the phase boundary. The effect of S_ϕ is strongest in the crossover region, where $S_\phi = 1$ reduces the

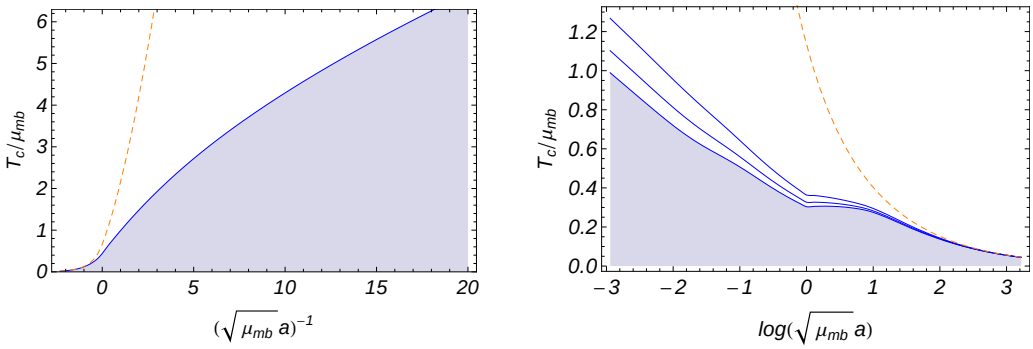

Figure 6.2: Critical temperature T_c/μ in 3D (left) and 2D (right) for the FB_0-truncation with q^2-opt regulator and ϕ^4-potential. This scheme is also used for the remaining phase diagram plots. The blue region constitutes the superfluid phase. In 2D we show the phase boundary for final cutoff scales $t_f = -12, -15, -18$ from top to bottom, see the discussion below Eq. (6.47) in the main text. The positive many-body chemical potential is given by $\mu_{mb} = \mu - \varepsilon_B/2$. In 3D the BCS-BEC crossover is from left to right, whereas the direction is reversed in the 2D case. We also plot the BCS-result (orange, dashed) in both dimensions.

critical temperature to $T_c/\mu = 0.41$. In contrast, we obtain $T_c/\mu_{mb} = 0.192$ in 2D, which has to be compared to $T_c/\mu_{mb} = 0.327$ mentioned above. Again the critical temperature in 2D strongly depends on t_f, with a relative variation comparable to the one of the result obtained with running of S_ϕ. The sharp kink at $\log(\sqrt{\mu_{mb}}a) \approx 0$ disappears when we set $S_\phi = 1$, suggesting that this feature is probably a truncation-artefact. However, the qualitative shape of a curve which is flatter on the atomic side and which becomes steeper in the bosonic limit, remains valid independent of S_ϕ.

In order to relate the phase diagram in grand canonical coordinates (μ_{mb}, T, a) to the one in canonical ones, i.e. (k_F, T, a), we need to determine the equation of state $n(\mu_{mb}, T, a)$. This is a difficult task. Here we employ the simple approach to the density already used in Sec. 5.1.4. In 3D we know that the phase structure obtained in this manner is quantitatively accurate in the perturbative limits, but only qualitatively correct in the crossover region. Keeping this in mind we apply the same beta functions also to the 2D case. The phase diagram obtained in this manner serves as a guide for the experimental phase diagram determined in Sec. 6.2.4.

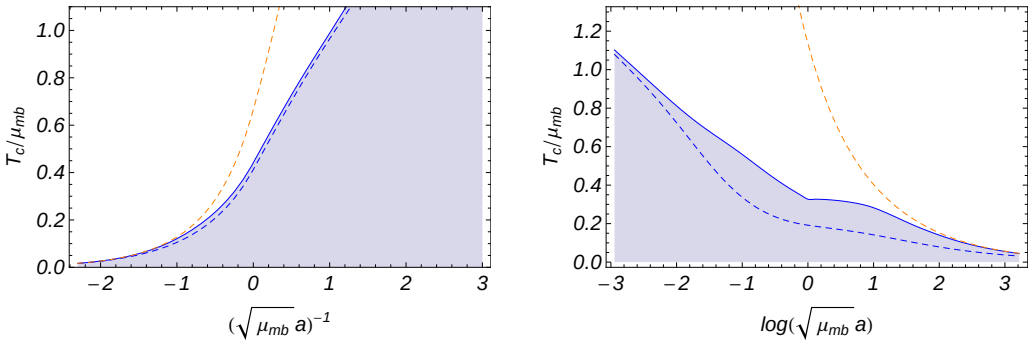

Figure 6.3: Phase structure for the truncation as in Fig. 6.2, however with S_ϕ treated as a running coupling (solid, blue) and with constant $S_{\phi,k} = 1$ for all k (dashed, blue). We only find minor modifications in 3D, where the effect is strongest in the crossover regime. The critical temperature of the UFG is reduced from $T_c/\mu = 0.44$ to $T_c/\mu = 0.41$. In 2D a constant choice of $S_\phi = 1$ results in a dramatically reduced critical temperature. Moreover, the phase boundary becomes smoother. The BCS-limit (dashed, orange) is not affected by the running of S_ϕ in 3D. In contrast, the 2D curve is significantly below the BCS-curve.

The flow equation for the density is approximated here by $\dot{n} = \dot{n}^{(F)} + \dot{n}^{(B)}$ with

$$\dot{n}^{(F)} = \frac{-16 v_d}{d} k^d \left(\ell_F^{(0,1)} - 2\ell_F^{(2,2)}\right), \tag{6.50}$$

$$\dot{n}^{(B)} = -\frac{8 v_d 2^{d/2} k^d \alpha_\phi}{d} \left(\ell_B^{(0,1)} - 2\ell_B^{(2,2)}\right). \tag{6.51}$$

For the definition of the threshold functions ℓ_F and ℓ_B we refer to Sec. 4.3.3. The initial condition reads $n_\Lambda = \theta(\mu)\mu^{3/2}/3\pi^2$ and $n_\Lambda = \theta(\mu)\mu/2\pi$ in 3D and 2D, respectively. The flow of $\alpha_\phi = (\partial_\mu \partial_\rho U)(\rho_0)$ is truncated according to $\dot{\alpha}_\phi = \eta_\phi \alpha_\phi + \dot{\alpha}_\phi^{(F)} + \dot{\alpha}_\phi^{(B)}$ with

$$\dot{\alpha}_\phi = \frac{-16 v_d \tilde{h}^2}{d} \left(\ell_F^{(0,2)} - 4\ell_F^{(2,3)}\right), \tag{6.52}$$

$$\dot{\alpha}_\phi = \frac{8 v_d 2^{d/2}}{d} \left[-4\tilde{\lambda}_\phi \left(3\ell_B^{(1,2)} - 4\ell_B^{(3,3)}\right) + 2\tilde{\rho}_0 \tilde{\lambda}_\phi^2 \left(\ell_B^{(0,2)} - 4\ell_B^{(2,3)}\right)\right], \tag{6.53}$$

and initial condition $\alpha_{\phi\Lambda} = -2$. In the broken regime of the flow, the flowing density receives an additional contribution $-\bar{\alpha}_\phi \dot{\tilde{\rho}}_0$. For a detailed discussion of this treatment of the density we refer to Diehl et al. [2010a], where the same approximation was employed.

The resulting phase diagrams in canonical coordinates for the 3D and 2D case are shown in Fig. 6.4. Again we find a significant t_f-dependence of the phase boundary in 2D. The critical temperature for $\log(k_F a) = 0$ is given by

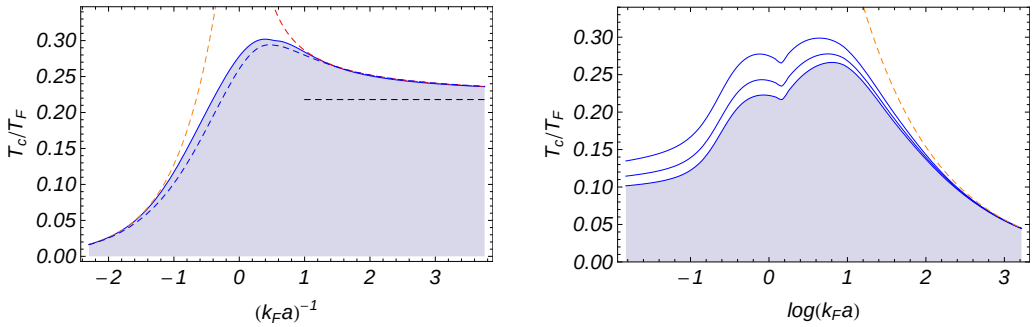

Figure 6.4: Phase diagram in canonical coordinates obtained with the equation of state from Eqs. (6.50-6.53). In 3D this resolves the BEC-limit in a very accurate manner, where it resolves the interaction-induced shift (dashed, red) compared to the ideal-BEC critical temperature (dashed, black), see Eqs. (6.54) and (6.55). The crossover regime is, however, only qualitatively correct. We find a maximum of the phase boundary at $(k_F a)^{-1} \approx 0.5$. Applying the same truncation to the 2D system we find a phase diagram possessing two local maxima and a dip, the latter being at $\log(k_F a) \approx 0$. We find again a strong dependence on $t_f = -12, -15, -18$, shown here from top to bottom. We also show the result obtained for $S_\phi = 1$ in 3D (dashed, blue).

$T_c/T_F = 0.275, 0.242, 0.222$ for $t_f = -12, -15, -18$, respectively. In 3D we find $T_c/T_F = 0.278$ independent of the infrared scale. The sharp feature of the 2D grand canonical phase diagram results in a sharp dip of the corresponding phase diagram in the plane spanned by T_c/T_F and $\log(k_F a)$. This feature is independent of the infrared cutoff scale.

Analogous to the previous analysis we set $S_\phi = 1$ to study the stability of the phase structure. In 3D we only find a small correction, see Fig. 6.4. At unitarity the critical temperature is reduced to $T_c/T_F = 0.261$. The impact on the 2D phase structure is again substantial. However, the reduction of T_c/T_F is mainly due to the reduced value of T_c/μ_{mb}, as the influence of $S_\phi = 1$ on the equation of state is small (approximately 5%). Moreover, the equation of state is found to be t_f-independent. We show the corresponding 2D phase diagrams with $S_\phi = 1$ in Fig. 6.5. Due to numerical limitations we restrict the analysis with $S_\phi = 1$ to $\log(k_F a) \leq 2.8$, where the BCS-limit is not yet reached. This behavior, however, can be traced back to the value of T_c/μ_{mb}, see Fig. 6.3, since $\mu_{mb} = \varepsilon_F$ is well satisfied both with and without the running of S_ϕ.

On the BEC-side in 3D the critical temperature is shifted due to the repulsive interactions of the bosons. Indeed, compared to the condensation temperature of an ideal Bose gas

$$T_{c,id}/T_F = 0.218, \tag{6.54}$$

rescaled here to appropriate units for the BCS-BEC crossover, we parametrize the

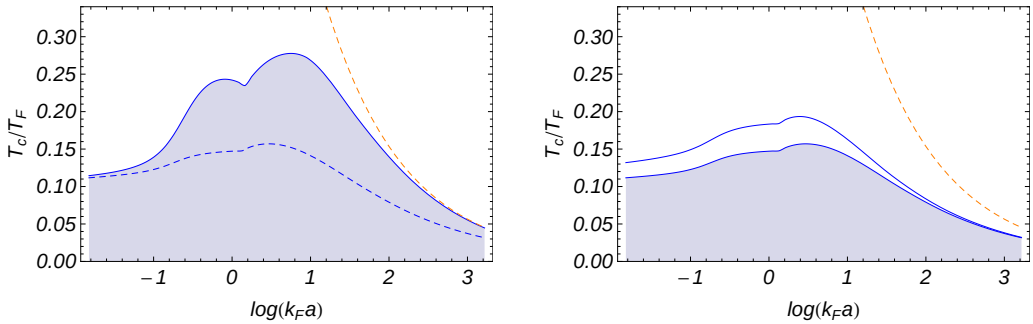

Figure 6.5: *Left:* 2D Phase diagram for $\dot{S}_\phi \neq 0$ (solid, blue) and $\dot{S}_\phi = 0$ (dashed, blue). The critical temperature is strongly reduced for $S_\phi = 1$. In the example shown here we have chosen $t_\mathrm{f} = -15$ and find $T_\mathrm{c}/T_\mathrm{F} = 0.242$ (0.147) for the truncation with (without) running of S_ϕ. *Right:* 2D critical temperature in a truncation with $S_\phi = 1$ for $t_\mathrm{f} = -12$ and -15, displayed by the upper and lower curve, respectively. The superfluid region appears for much lower temperatures. However, the qualitative shape of the phase boundary with two local minima and a dip at $\log(k_\mathrm{F} a) \approx 0$ persists.

deviation according to

$$\frac{T_\mathrm{c} - T_\mathrm{c,id}}{T_\mathrm{c,id}} = \frac{\kappa}{(6\pi^2)^{1/3}} \frac{a_\mathrm{dd}}{a} (k_\mathrm{F} a). \tag{6.55}$$

The parameter κ can be determined independently of the fermionic system from a purely bosonic theory. For a discussion we refer to Boettcher et al. [2012]. Within our truncation we have $a_\mathrm{dd}/a = 0.72$, see Table 6.1, and $\kappa = 1.7$. The ideal gas and interaction-corrected curves are shown in Fig. 6.4 (left) by the dashed black and red curve, respectively. Together with the exponentially increasing BCS- or Gorkov-results on the BCS-side it is reasonable to assume that the critical temperature curve possess a maximum. This point can be associated with the transition from the fermionic to the bosonic theory, and, indeed, is found in 3D to be close to the zero-crossing of the chemical potential, i.e. at $\mu_\mathrm{mb} a^2 = 1$.

The theory of 2D bosons (Prokof'ev et al. [2001], Prokof'ev and Svistunov [2002], Petrov et al. [2003]) predicts a BKT-temperature

$$\frac{T_\mathrm{BKT}}{T_\mathrm{F}} = \frac{1}{2} \left(\log\Big[\frac{C}{4\pi} \log\Big(\frac{4\pi}{k_\mathrm{F}^2 a_\mathrm{2D}^2} \Big) \Big] \right)^{-1}, \quad C = 380(3), \tag{6.56}$$

see also the discussion in Sec. 6.2.4. Again, together with the exponential increase on the atomic side, we expect the curve to have a maximum in the plane spanned by $T_\mathrm{c}/T_\mathrm{F}$ and $\log(k_\mathrm{F} a)$. Within our truncation we verify this statement. The zero-crossing of the chemical potential $\mu = \mu_\mathrm{mb} - a^{-2}$ in 2D occurs for $\log(k_\mathrm{F} a) > 0$.

Indeed, since there is always a bound state in 2D, we find $1 = \sqrt{\mu_{\rm mb}}a < k_{\rm F}a$, and thus $\log(k_{\rm F}a) > \log(1) = 0$. The fact that $\mu_{\rm mb}/\varepsilon_{\rm F}$ is smaller than unity is verified in Fig. 6.6. For the truncations with running S_ϕ we find the maximum to be located at $\log(k_{\rm F}a) \approx 1$, whereas for constant $S_\phi = 1$ it appears for $\log(k_{\rm F}a) \approx 0.5$.

We close the discussion on the phase structure of the balanced 2D BCS-BEC crossover by remarking that for sufficiently low k fermions always decouple from the flow due to $\tilde{\mu} = \mu/k^2 \to -\infty$ and $\tilde{\Delta} = \Delta/k^2 \to \infty$. Accordingly, the flow equations for the full system are reduced to the flow equations for nonrelativistic bosons in 2D in the deep infrared. Moreover, at the critical temperature, the beta functions coincide with those of the classical statistical O(2)-model in $d = 2$ dimensions. It is well-known (Gräter and Wetterich [1995], Gersdorff and Wetterich [2001]) that the BKT-physics of the latter can be resolved with the FRG, even for purely fermionic systems (Krahl and Wetterich [2007]). We found that the FB-truncation is sufficient to obtain a temperature dependent anomalous dimension $\eta(T)$ with all the right properties, i.e. $\eta(0) = 0$, linear increase for small T, and a jump from $\eta_{\rm max} \approx 0.25$ to zero at $T = T_{\rm c}$. However, due to the $t_{\rm f}$-dependence of $T_{\rm c}$ the FB-truncation cannot capture the BKT-transition which is valid for an infinitely large system. In a recent analysis by Jakubczyk et al. [2014] the BKT-transition in a ϕ^4-model was computed to high precision with field dependent coefficients in a derivative expansion.

6.1.3 Equation of state

We turn to an extended discussion of the equation of state (EOS) in the 3D and 2D BCS-BEC crossover, respectively. It is the key observable in order to compare with experiments for two reasons: First, the EOS can be measured directly from in-situ density images. Second, more indirect, we need the EOS to translate a phase diagram computed in grand canonical variables to the one measured in canonical ones.

We again limit the investigation to an FB_0-truncation with q^2-opt regulator and ϕ^4-expansion of the effective potential. To check for stability we again employ truncations with and without the running of S_ϕ. The flow of the density is determined according to Eqs. (6.50-6.53) here. We discuss the shortcomings of this approach below.

In Fig. 6.6 we show the result for the EOS at $T = 0$ and $T = T_{\rm c}$ throughout the crossover in terms of

$$\xi(n, T, a) = \frac{\mu_{\rm mb}(n, T, a)}{\varepsilon_{\rm F}} = \frac{\mu(n, T, a) - \theta(\varepsilon_{\rm B})\varepsilon_{\rm B}/2}{\varepsilon_{\rm F}}, \tag{6.57}$$

where $\varepsilon_{\rm F} = (3\pi^2 n)^{2/3}$ and $\varepsilon_{\rm F} = 2\pi n$ in 3D and 2D, respectively. In 3D, for $T = a^{-1} = 0$, the quantity defined in Eq. (6.57) equals the Bertsch parameter. For comparison we also show the zero temperature EOS from mean field theory and the Fermi-liquid theory (FLT) predictions in Fig. 6.6. We note that the EOS does not depend sensitively on the infrared scale $t_{\rm f}$, even in 2D, and we show

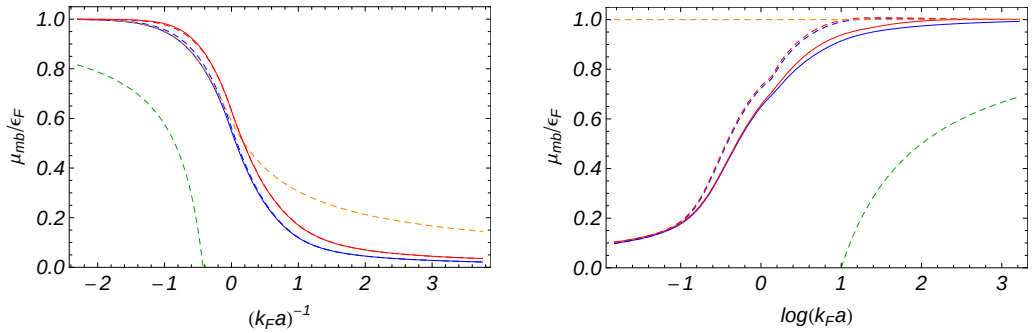

Figure 6.6: EOS in terms of $\xi = \mu_{\rm mb}/\varepsilon_{\rm F}$ with $\mu_{\rm mb} = \mu - \theta(\varepsilon_{\rm B})\varepsilon_{\rm B}/2$ in 3D (left) and 2D (right), respectively. We show several curves for comparison purposes: The zero temperature EOS from the FRG-truncation discussed in the text is shown in solid (dashed) blue for the truncation with (without) running of S_ϕ. In the same way, the critical EOS at $T = T_{\rm c}$ is shown in solid (dashed) red for the truncation with (without) running of S_ϕ. The zero temperature mean field result is shown by the dashed orange curve. The FLT-prediction on the atomic side is plotted by the dashed green curve.

the 2D result for $t_{\rm f} = -15$. We find a mild dependence on S_ϕ in 2D, whereas, remarkably, the EOS in 3D is almost independent on the running of S_ϕ. This indicates that the important contributions to the running of n come from scales k where $S_{\phi,k} \simeq 1$. In contrast, the critical temperature is sensitive to the deep infrared, where $S_{\phi,k} < 1$. In 2D the S_ϕ-dependence of the EOS is probably related to the logarithmic running of the fermion gap Δ_k in the Goldstone regime for truncations without V_ϕ.

On the BCS-side of the crossover we find $\xi = 1$ for $T = 0$. It is a major drawback of our truncation that it systematically underestimates the density in the atomic regime, i.e. for $\mu > 0$. The EOS corresponds to the mean field theory prediction in this regime. (Note that the zero temperature EOS in 2D from mean field theory is given by $\xi(a) = 1$ for all a.) The leading correction on the BCS-side to the EOS comes from the Hartree shift of the chemical potential, i.e. the fermion self-energy correction. We summarize here only the phenomenological approach to arrive at the FLT-formulas for the EOS (Engelbrecht and Randeria [1990, 1992]). For this purpose we use the ideal Fermi gas EOS and shift the chemical potential according to

$$\mu \to \tilde{\mu} = \begin{cases} \mu - 4\pi n a & (d = 3) \\ \mu + 2\pi n / \log(k_{\rm F} a) & (d = 2) \end{cases} . \tag{6.58}$$

Note that $a < 0$ in 3D such that the Hartree shift always increases the effective chemical potential, thereby increasing the density $n(\mu)$ for fixed μ. Physically this can be understood by the attraction of atoms which energetically allows to put

more particles into the Fermi sphere. We then arrive at

$$\mu_{\rm FLT}(n,a) = \varepsilon_{\rm F}\Big(1+\frac{4}{3\pi}k_{\rm F}a\Big),\ (d=3), \tag{6.59}$$

$$\mu_{\rm FLT}(n,a) = \varepsilon_{\rm F}\Big(1-\frac{1}{\log(k_{\rm F}a)}\Big),\ (d=2), \tag{6.60}$$

in 3D and 2D, respectively. The corresponding ξ-parameters on the BCS-sides of the crossover are also shown in Fig. 6.6. Note that the FLT-correction in 2D is large even for moderate $\log(k_{\rm F}a) \geq 1$ such that the applicability of perturbation theory is already questionable.

There are two ways to interpret the Hartree shift given by

$$n(\mu,a) = \frac{\tilde{\mu}}{2\pi} = \frac{1}{2\pi}\Big(\mu + \frac{2\pi n_0}{\log(k_{\rm F0}a)}\Big). \tag{6.61}$$

The first one is that n_0 and $k_{\rm F0}$ refer to the noninteracting gas formulas. This is called non-self-consistent Hartree–Fock (or Fermi liquid theory). In contrast, one may insert the full density n and $k_{\rm F} = (2\pi n)^{1/2}$ on the right hand side of Eq. (6.61), thereby regarding the equation as a self-consistent equation, which can then be solved numerically. This is called self-consistent Hartree–Fock approach. We have

$$n = \frac{\tilde{\mu}}{2\pi} = \frac{1}{2\pi}\Big(\mu + \frac{2\pi n_0}{\log(k_{\rm F0}a)}\Big)\ \text{(non-self-consistent)}, \tag{6.62}$$

$$n = \frac{\tilde{\mu}}{2\pi} = \frac{1}{2\pi}\Big(\mu + \frac{2\pi n}{\log(k_{\rm F}a)}\Big)\ \text{(self-consistent)}. \tag{6.63}$$

We use the non-self-consistent equation in Fig. 6.6 and regard it as the leading perturbative correction. For a FLT correction of $(n-n_0)/n_0 \approx 17\%$, the difference is at most a 2-3% effect at small temperatures, and it decreases for larger temperatures. We display this behavior in Fig. 6.7. For almost all cases where $\mu > 0$, we can replace $k_{\rm F0} \to \sqrt{\mu}$ in the logarithm. However, this breaks down for very small or negative chemical potentials, which is relevant for the outer regions of a trapped system.

We summarize the Fermi liquid corrections. For the noninteracting gas we have

$$n_0(\mu) = \frac{\mu}{2\pi},\ (T=0), \tag{6.64}$$

$$n_0(\mu,T) = \frac{2}{\lambda_T^2}\log\Big(1+e^{\mu/T}\Big) = \frac{T}{2\pi}\log\Big(1+e^{\mu/T}\Big),\ (T>0), \tag{6.65}$$

with $k_{\rm F0} = (2\pi n_0)^{1/2}$. These expressions have to be inserted into the interacting gas formulas, which read

$$n(\mu,a) = \frac{1}{2\pi}\Big(\mu + \frac{2\pi n_0}{\log(k_{\rm F0}a)}\Big),\ (T=0), \tag{6.66}$$

$$n(\mu,T,a) = \frac{T}{2\pi}\log\left(1+\exp\Big[\frac{1}{T}\Big(\mu+\frac{2\pi n_0}{\log(k_{\rm F0}a)}\Big)\Big]\right),\ (T>0). \tag{6.67}$$

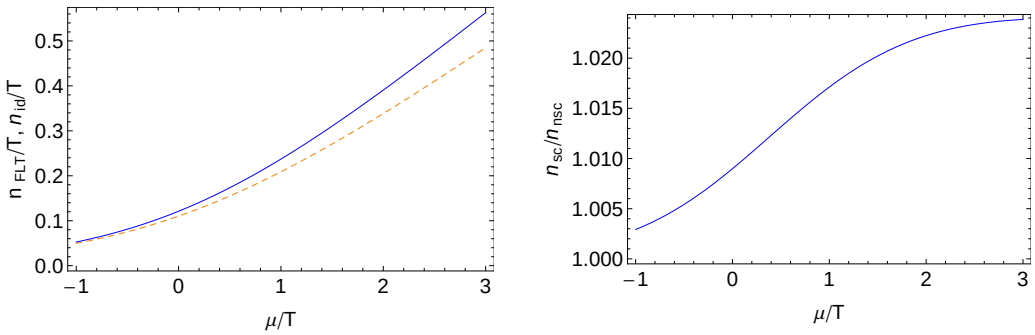

Figure 6.7: *Left:* Interacting gas Fermi liquid formula for a ^{6}Li-gas at 1400G (blue), which corresponds to an interaction correction $\approx 17\%$, compared to a noninteracting ideal gas formula (orange, dashed). *Right:* Self-consistent formula divided by the non-self-consistent (Fermi liquid) formula.

The bosonic side of the resonance, where $\mu < 0$ and fermions are gapped, is resolved to high accuracy in 3D. In this regime we obtained the Lee–Huang–Yang (LHY) (Lee et al. [1957], Lee and Yang [1958]) correction for a dimer gas with scattering length $a_{\mathrm{dd}} = 0.72a$, see Table 6.1. The corresponding perturbative formulas at zero temperature are given in Sec. 5.1.1. We have

$$n_{\mathrm{LHY}}(\mu_{\mathrm{mb}}, a) = \frac{\mu_{\mathrm{mb}}}{\pi a_{\mathrm{dd}}}\left(1 - \frac{32}{3\pi\sqrt{2}}\sqrt{\mu_{\mathrm{mb}}}a_{\mathrm{dd}}\right), \tag{6.68}$$

where the leading term is the mean field prediction. We compare the zero temperature EOS in 3D from FRG with the results from mean field and LHY-theory in Fig. 6.8.

6.2 Observation of pair condensation in two dimensions

In this section we describe the experimental realization of the 2D BCS-BEC crossover in the Jochim Group at the PI Heidelberg. The setup allows for measuring many-body observables such as phase diagram, equation of state, momentum distribution, and phase correlations. The author's contribution to the experiment consists of conceptual considerations on the measurements and support with the data analysis. Both aspects are outlined here. First results on the phase structure of the system are available in Ries et al. [2014].

6.2.1 Experimental setup

The experiment utilizes ^{6}Li-atoms to simulate the 2D BCS-BEC crossover. The spin degree of freedom is given by the hyperfine state $|\sigma\rangle$ of the atoms: The single valence electron of a lithium atom has vanishing orbital angular momentum. This

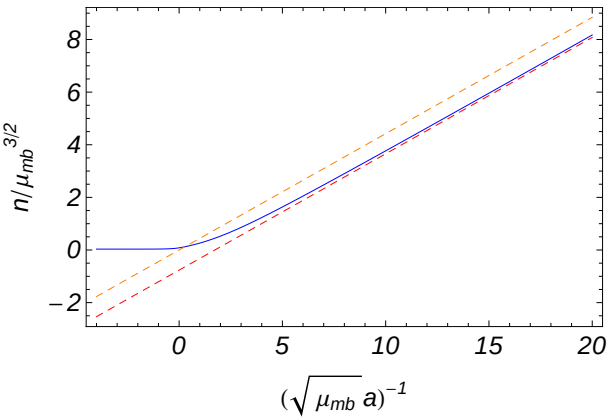

Figure 6.8: Zero temperature EOS in 3D from the FRG (solid blue) compared to mean field (dashed orange) and LHY-theory (dashed red), see Eq. (6.68). For comparison we insert the dimer scattering length $a_{\mathrm{dd}} = 0.72a$ to be consistent with our vacuum solution. We find perfect agreement with LHY-theory, and significant deviations from the mean field prediction. This indicates the correct resolution of effects beyond mean field theory on the bosonic side of the crossover, where the chemical potential is negative.

corresponds to the quantum numbers $L = 0$, $S = 1/2$, and $J = 1/2$ in the usual notation. Accordingly, there is no fine structure of the energy levels. However, due to the nuclear spin ($I = 1$), we have a hyperfine splitting with $F = 3/2, 1/2$. This is visualized in Fig. 6.9.

The hyperfine state of an atom is thus characterized by the quantum numbers F and $m_F = -F, \ldots, +F$. However, this description is only useful in the Zeeman regime for small magnetic fields $B \sim 30$G. As we will employ a magnetic Feshbach resonance at $B = 832.2$G (Zürn et al. [2013]), we are rather in the high-field Paschen–Back regime, where m_I instead of m_F is a good quantum number. We denote $|1\rangle$- and $|2\rangle$-atoms by those in hyperfine state $|1\rangle = |F = \frac{1}{2}, m_I = 1\rangle$ and $|2\rangle = |F = \frac{1}{2}, m_I = 0\rangle$, respectively.

After a sequence of cooling steps the gas consisting of 50000-60000 particles per spin state is transferred to a highly anisotropic hybrid trap consisting of a standing-wave optical dipole trap (SWT) and a superimposed magnetic trap. The SWT confines the system to a pancake-shaped geometry and thereby simulates 2D physics in the xy-plane. It is created from two elliptical focussed Gaussian beams which intersect at a small angle (14°), see Figs. 6.10 and 6.11. For a detailed review of optical traps we refer to Grimm et al. [2000].

The effective trapping potential in the xy-plane is given by

$$V_{\mathrm{opt}}(x, y) = \frac{M_{\mathrm{Li}}}{2}\left(\omega_x^2 x^2 + \omega_y^2 y^2\right) + c_{4x}x^4 + c_{4y}y^4. \tag{6.69}$$

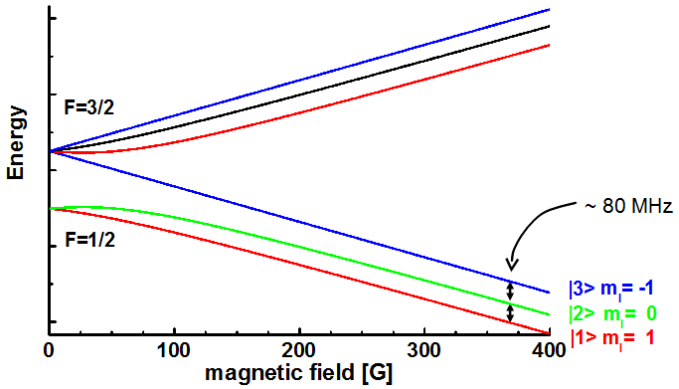

Figure 6.9: Hyperfine structure of ^{6}Li. The BCS-BEC crossover is simulated with the magnetic Feshbach resonance at $B_0 = 832.2$G between $|1\rangle$- and $|2\rangle$-atoms. The atoms populate the lowest two sublevels in the high-field Paschen–Back regime. Since the energy difference $\Delta E \sim 80$MHz is much larger than any other energy scale in the experiment, there is no conversion between the atom species (e.g. due to thermal fluctuations). The population of the state $|\sigma\rangle$ is thus constant. However, it may be changed by applying a radio-frequency pulse tuned to the transition frequency.

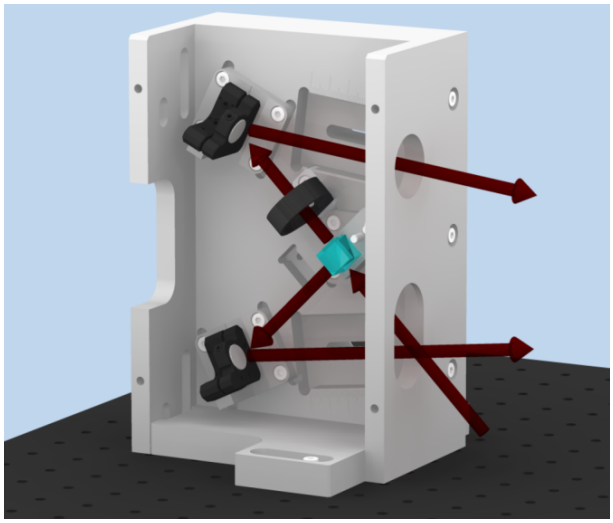

Figure 6.10: The standing-wave optical dipole trap is created by crossing two elliptical focussed 1064 nm Gaussian beams which intersect with an angle of 14°. This results in a large aspect ratio $\frac{\omega_z}{\omega_r} \approx 300$ of transverse versus radial trapping. However, in order to simulate 2D physics, the system also needs to be kinematically in the 2D limit, which requires the typical energies of particles of be much smaller than $\hbar\omega_z$.

Higher order terms are not important for the fillings (i.e. particle numbers) of the experiment. We have $\omega_{x/y}^2 = \omega_{x/y,\mathrm{opt}}^2 + \omega_{\mathrm{mag}}^2$ with

$$\begin{aligned}
\omega_{x,\mathrm{opt}} &= 2\pi \times 14.10(2)\ \mathrm{Hz}, \\
\omega_{y,\mathrm{opt}} &= 2\pi \times 14.02(3)\ \mathrm{Hz}, \\
\omega_{\mathrm{mag}} &= 2\pi \times 0.39\sqrt{B[\mathrm{G}]}\ \mathrm{Hz}, \\
c_{4x} &= -1.04 \times 10^{-16}\ \frac{\mathrm{kg}}{\mathrm{m^2 s^2}}, \\
c_{4y} &= -1.34 \times 10^{-16}\ \frac{\mathrm{kg}}{\mathrm{m^2 s^2}}.
\end{aligned} \tag{6.70}$$

The lithium mass is given by

$$M_{\mathrm{Li}} = 9.98834 \times 10^{-27}\ \mathrm{kg}. \tag{6.71}$$

The errors for the magnetic frequency and the quartic terms are $\approx 10\%$ and $\approx 25\%$, respectively. Note that the magnetic trapping frequency depends on the magnetic field B, which is tuned across the Feshbach resonance. The optical trap is tuned such that the frequencies in x- and y-direction are almost identical, whereas this is generally true for the magnetic frequencies. As a result, the harmonic part of the hybrid trap is almost radially symmetric. The transverse trapping frequency and oscillator length, respectively, are given by

$$\omega_z = 2\pi \times 5.53(3)\ \mathrm{kHz},\ \ell_z = \sqrt{\hbar/M\omega_z} = 0.551\mu\mathrm{m}. \tag{6.72}$$

Hence, to give an example, at 795G we obtain an aspect ratio of $\omega_x : \omega_y : \omega_z = 1 : 0.997 : 309$. The experimental setup is summarized in Fig. 6.11.

After the gas has been evaporatively cooled and transferred to the SWT, it can be heated in two ways. For the lowest three temperatures the gas is held for a variable hold time of 300ms to 1s in the trap, where it is heated by technical noise. To achieve higher temperatures, the trap depth is modulated with varying amplitude. Eventually a proper thermometry is required to translated these temperature variables to a physical temperature T in nK, see Sec. 6.2.3.

Imaging the cloud with a beam along the z-direction as shown in Fig. 6.11 yields the (column) optical density $\mathrm{OD}(x, y)$. The optical density has to be corrected for saturation effects and the reduced detectability of atoms bound in dimers, see Ries et al. [2014]. We assume that this is already done. We then still face the problem that the optical density has to be normalized such that it gives the particle number density n in $\mu\mathrm{m}^{-2}$. It is empirically motivated to assume

$$n(x, y) = c \cdot \mathrm{OD}(x, y), \tag{6.73}$$

where c is approximately constant throughout the crossover, i.e. independent of temperature, density, or magnetic field. Thus the constant c has to be fixed once. This can be achieved by a series of images with different intensities of the trapped

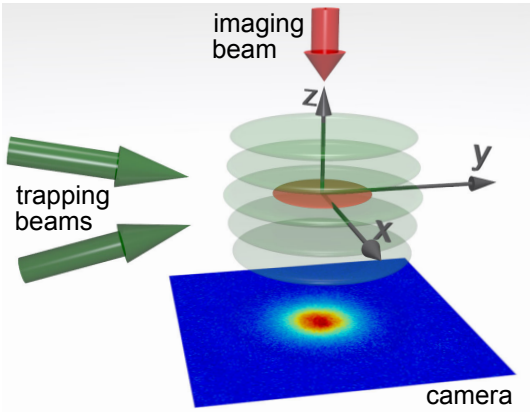

Figure 6.11: Experimental setup. The SWT generates a stack of trap layers. Approximately 89% of the particles are trapped in the central layer. The ultracold quantum gas (red disk) is trapped in the xy-plane by the hybrid trap. Imaging proceeds along the z-direction (red arrow). A typical optical density profile is shown at the bottom of the figure. The almost radial symmetry of the image is in line with the nearly equal trapping frequencies ω_x and ω_y in Eqs. (6.70). Figure taken from Ries et al. [2014].

gas, or of the empty trap. We refer to Ries et al. [2014] for details, especially Sec. VI. of the supporting online material therein.

To tune interactions between $|1\rangle$- and $|2\rangle$-atoms, the magnetic Feshbach resonance at 832.2G is employed in the range $692\text{G} \leq B \leq 1400\text{G}$. The 3D scattering length as a function of the magnetic field has been determined to high precision by Zürn et al. [2013]. We display characteristic values of $a_{3\text{D}}(B)$ in Table. 6.2.

For a truly 2D system, a sufficiently strong attractive interaction between the atoms always results in a two-body bound state with binding energy ε_{B}. The energy scale associated to the bound state allows to define the 2D scattering length $a_{2\text{D}}$ according to $\varepsilon_{\text{B}} = -\hbar^2/Ma_{2\text{D}}^2$, see the discussion in Sec. 6.1.1. The interaction parameter $a_{2\text{D}}$ can also, with the same result, be defined from the 2D scattering amplitude or T-matrix of two colliding atoms.

In our experiment we simulate an effectively 2D setting by means of a tight confinement along the z-direction. The system is then characterized by an additional length scale, $\ell_z = \sqrt{\hbar/M\omega_z}$, which is the oscillator length along the axial direction. Together with the 3D scattering length this allows to determine the effective 2D scattering length we are simulating: $a_{2\text{D}} = a_{2\text{D}}(\ell_z, a_{3\text{D}})$.

There are mainly two ways of finding the effective 2D scattering length of the trapped system. The first one, which we choose, is based on reading off $a_{2\text{D}}$ from the T-matrix of the confined quasi-2D system. The second one employs the confinement induced bound state energy $\tilde{\varepsilon}_{\text{B}}$ to define a scattering length according

B[G]	$a_{3D}[a_0]$	$a_{2D}[a_0]$	$\tilde{a}_{2D}[a_0]$	$\Omega = \lvert\tilde{\varepsilon}_B\rvert/\hbar\omega_z$	$a_{2D}/\tilde{a}_{2D}$
692	1463	2.585	1456	51	0.00178
782	6718	2780	6130	2.9	0.453
832	2 324 337	19 300	20 970	0.25	0.920
892	-8554	89 300	89 720	0.013	0.995
1042	-3656	690 000	690 100	0.00023	1.000

Table 6.2: 3D and 2D scattering lengths, a_{3D} and a_{2D}, as a function of the magnetic field B across the Feshbach resonance. Values for $B \leq 782$ G ($B \geq 892$) correspond to the BEC (BCS) limit. The asymptotic formula (6.74) provides a reliable estimate for the 2D scattering length in the whole crossover region. In contrast, $\tilde{a}_{2D}$ defined from the confinement induced bound state energy $\tilde{\varepsilon}_B$ via $\tilde{\varepsilon}_B = -\hbar^2/M\tilde{a}_{2D}^2$ largely overestimates the interaction strength on the BEC side. We find $\tilde{a}_{2D} = a_{3D}$ on the BEC side such that the confinement induced bound state is equal to the 3D bound state. In order to display the phase diagram of the 2D BCS-BEC crossover from experimental data, $a_{2D}(B)$ is the optimal choice for defining the 2D scattering length.

to $\tilde{\varepsilon}_B = -\hbar^2/M\tilde{a}_{2D}^2$. The outcome does not coincide on the BEC side of the crossover, where a_{2D} and $\tilde{a}_{2D}$ differ by orders of magnitude. In this work we use the first definition of a_{2D} for all magnetic fields because it gives the correct limit of a weakly interacting 2D Bose gas far on the BEC-side of the crossover. However, a_{2D} and $\tilde{a}_{2D}$ are related to each other in a one-to-one fashion, and thus no information is lost with a particular choice.

Scattering length from T-matrix of two body scattering. This method has recently been applied by Makhalov et al. [2014] and it is discussed in detail by Levinsen and Parish [2014]. It relies on the low-energy expansion of the T-matrix of the tightly confined system. It thus directly relates the 2D scattering length a_{2D} to a scattering property between atoms. Although the atoms might be tightly bound with a large binding energy, their energy of relative motion is still small compared to $\hbar\omega_z$. As a result one finds

$$a_{2D} = \ell_z \sqrt{\frac{\pi}{A}} \exp\Big(-\sqrt{\frac{\pi}{2}}\frac{\ell_z}{a_{3D}}\Big), \tag{6.74}$$

with $A = 0.905$ (Petrov and Shlyapnikov [2001], Bloch et al. [2008]). This formula is applied here for all magnetic fields.

Scattering length from confinement induced bound state. The confinement along the z-direction induces a two-body bound state for all values of the 3D scattering length a_{3D}. The corresponding binding energy $\tilde{\varepsilon}_B$ is found from solving $\ell_z/a_{3D} =$

$f_1(|\tilde{\varepsilon}_\mathrm{B}|/\hbar\omega_z)$ (Petrov and Shlyapnikov [2001], Bloch et al. [2008]) with

$$f_1(\Omega) = \int_0^\infty \frac{\mathrm{d}u}{\sqrt{4\pi u^3}} \left(1 - \frac{e^{-\Omega u}}{\sqrt{(1-e^{-2u})/2u}}\right). \tag{6.75}$$

We denote $\tilde{\varepsilon}_\mathrm{B}$ with a tilde to distinguish it from ε_B of the truly 2D system. For small binding energies, i.e. far on the BCS side, the integral can be expanded in Ω. We then have $f_1(\Omega) \simeq \log(\pi\Omega/A)/\sqrt{2\pi}$ for $\Omega \lesssim 0.1$, and we arrive at the asymptotic expression $\tilde{a}_\mathrm{2D} = \ell_z\sqrt{\pi/A}\exp(-\sqrt{\pi/2}\ell_z/a_\mathrm{3D})$ equivalent to Eq. 6.74. We find this limit of Eq. (6.75) to be appropriate for magnetic fields $\geq$ 852G. On the other hand, far on the BEC side, we have $f_1(\Omega) \simeq \sqrt{\Omega}$ for $\Omega \gg 1$, and thus find the induced binding energy to coincide with the 3D binding energy,. Accordingly $\tilde{a}_\mathrm{2D} \simeq a_\mathrm{3D}$ in this limit. In our case this applies to 692G and 732G.

Comparison of both approaches. For a magnetic field of 692G we find $a_\mathrm{2D}/\tilde{a}_\mathrm{2D} = 0.0018$, and thus a substantial difference in both definitions. Associating $\tilde{a}_\mathrm{2D}$ with the simulated 2D scattering length of the effectively 2D system would indicate that system at 692G is still strongly interacting, with $\log(k_\mathrm{F}\tilde{a}_\mathrm{2D}) \simeq -1$, whereas we have $\log(k_\mathrm{F}a_\mathrm{2D}) \simeq -7$ instead. Moreover, it has been shown by Makhalov et al. [2014] that the T-matrix based approach gives the correct limit of weakly interacting 2D bosons far on the BEC side of the crossover. We show the results on a_2D and $\tilde{a}_\mathrm{2D}$ as a function of the magnetic field in Table. 6.2.

6.2.2 Momentum distribution from T/4-imaging

The momentum distribution of ultracold atoms can be obtained after time of flight (TOF) expansion. The commonly applied TOF method is based on switching off the trapping potential $V(\vec{r})$ at time $t = 0$, and allowing the gas to expand freely for a sufficiently long expansion time t_exp. If the expansion can be approximated to be ballistic, the position of a particle with initial velocity $\vec{v}$ is given by $\vec{x}(t_\mathrm{exp}) = \vec{x}(0) + \vec{v}\cdot t_\mathrm{exp}$ after TOF. It is important that $|\vec{x}(t_\mathrm{exp})|$ is much larger than the spatial extend of the in-situ cloud such that the initial position of the atom inside the trap is negligible in comparison to the travelled distance: $|\vec{x}(t_\mathrm{exp})| \gg |\vec{x}(0)|$. In order to ensure ballistic expansion it is convenient to ramp shortly before the TOF to a magnetic field B where the scattering length $a_\mathrm{3D}(B)$ is small. This suppresses mutual interaction between the atoms during the TOF.

An immediate disadvantage of the TOF method just described is that a long expansion time t_exp also results in a very dilute sample, which is more difficult to resolve by imaging. On the other hand, for too short t_exp, the influence of the initial position of the atom is large. In addition, slow particles need to travel for a longer time. Here we apply a simple but efficient modification of the standard TOF approach. Instead of releasing the gas into free space, we let it expand in a shallow harmonic trap with frequency ω_exp. In this way the position of the particle at a quarter of the trap period $T = 2\pi/\omega_\mathrm{exp}$ is given by its initial momentum inside the trap.

Below we derive this statement, which holds for ballistic expansion, from a field theoretical point of view. However, it can also be understood in terms of a classical particle in an external potential $V(\vec{x}) = M\omega_{\mathrm{exp}}^2\vec{x}^2/2$. For this purpose we note that due to energy conservation the energy

$$E(t) = \frac{\vec{p}^2(t)}{2M} + \frac{M}{2}\omega_{\mathrm{exp}}^2\vec{x}^2(t) \tag{6.76}$$

is constant for all times $t \geq 0$. In particular, for a particle initially at the trap center we have

$$\frac{\vec{p}^2(0)}{2M} = \frac{\vec{p}^2(t)}{2M} + \frac{M}{2}\omega_{\mathrm{exp}}^2\vec{x}^2(t) \tag{6.77}$$

for all times. Due to the time evolution $\vec{x}(t) \propto \sin(\omega_{\mathrm{exp}}t)$ and $\vec{p}(t) \propto \cos(\omega_{\mathrm{exp}}t)$ we have

$$\vec{p}(0) = M\omega_{\mathrm{exp}} \cdot \vec{x}(t_{\mathrm{exp}}) \tag{6.78}$$

for $t_{\mathrm{exp}} = \pi/(2\omega_{\mathrm{exp}}) = T/4$. This beautifully states the merit of the method: From a density image at $t_{\mathrm{exp}} = T/4$ we obtain the full (trap averaged) momentum distribution of the gas.

Evolution equation for the field operator

We now give a self-contained derivation of Eq. (6.78) from a field theoretical point of view. To do so, we consider the bosonic field operators $\hat{\psi}^\dagger(\vec{x})$ and $\hat{\psi}(\vec{x})$, which, respectively, create and annihilate an atom at point $\vec{x}$. The second quantized Hamiltonian in terms of these operators reads

$$\hat{H} = H(\hat{\psi}, \hat{\psi}^\dagger) = \int \mathrm{d}^2x \hat{\psi}^\dagger(\vec{x}) \left(-\frac{\hbar^2}{2M}\nabla^2 + \frac{M}{2}\omega^2\vec{x}^2 \right) \hat{\psi}(\vec{x}). \tag{6.79}$$

Note that $\vec{x}$ is labelling the field operator, and thus is not an operator $\hat{x}$ like in the quantum mechanical harmonic oscillator $\hat{p}^2 + \hat{x}^2$. The bosonic operators obey the canonical commutation relations

$$[\hat{\psi}(\vec{x}), \hat{\psi}^\dagger(\vec{y})] = \delta^{(2)}(\vec{x} - \vec{y}). \tag{6.80}$$

By assuming a bosonic field operator we limit the derivation to the BEC side of the resonance. The same result can, however, easily be derived for a fermionic field operator, since the evolution of a single non-interacting atom is not influenced by statistics.

Within the Heisenberg picture, we now construct time-dependent operators $\hat{\Psi}^\dagger(\vec{x}, t)$ and $\hat{\Psi}(\vec{x}, t)$ which obey the canonical equal-time commutation relations

$$[\hat{\Psi}(\vec{x}, t), \hat{\Psi}^\dagger(\vec{y}, t)] = \delta^{(2)}(\vec{x} - \vec{y}). \tag{6.81}$$

At $t = 0$ we demand

$$\hat{\Psi}(\vec{x}, t = 0) = \hat{\psi}(\vec{x}). \tag{6.82}$$

For $t > 0$ the time evolution of the operators is given by

$$\partial_t \hat{\Psi}(\vec{x}, t) = \frac{\mathrm{i}}{\hbar}[\hat{H}(t), \hat{\Psi}(\vec{x}, t)], \tag{6.83}$$

where the Hamiltonian $\hat{H}(t)$ is constructed from $\hat{H}$ according to

$$\hat{H}(t) = H(\hat{\Psi}(t), \hat{\Psi}^\dagger(t)) = \int \mathrm{d}^2x \hat{\Psi}^\dagger(\vec{x}, t)\left(-\frac{\hbar^2}{2M}\nabla^2 + \frac{M}{2}\omega^2\vec{x}^2\right)\hat{\Psi}(\vec{x}, t). \tag{6.84}$$

Inserting this into the field equation, and using the canonical equal-time commutation relation, we then find

$$\begin{aligned}
\mathrm{i}\hbar\partial_t\hat{\Psi}(\vec{x}, t) &= [\hat{\Psi}(\vec{x}, t), \hat{H}(t)] \\
&= \int \mathrm{d}^2y \Bigg(\hat{\Psi}(\vec{x}, t)\hat{\psi}^\dagger(\vec{y}, t)\Big(-\frac{\hbar^2}{2M}\nabla_y^2 + \frac{M}{2}\omega^2\vec{y}^2\Big)\hat{\Psi}(\vec{y}, t) \\
&\quad - \hat{\Psi}^\dagger(\vec{y}, t)\left[\Big(-\frac{\hbar^2}{2M}\nabla_y^2 + \frac{M}{2}\omega^2\vec{y}^2\Big)\hat{\psi}(\vec{y}, t)\right]\hat{\Psi}(\vec{x}, t)\Bigg) \\
&= \int \mathrm{d}^2y [\hat{\Psi}(\vec{x}, t), \hat{\Psi}^\dagger(\vec{y}, t)]\Big(-\frac{\hbar^2}{2M}\nabla_y^2 + \frac{M}{2}\omega^2\vec{y}^2\Big)\hat{\Psi}(\vec{y}, t) \\
&= \int \mathrm{d}^2y \delta^{(2)}(\vec{x} - \vec{y})\Big(-\frac{\hbar^2}{2M}\nabla_y^2 + \frac{M}{2}\omega^2\vec{y}^2\Big)\hat{\Psi}(\vec{y}, t) \\
&= \Big(-\frac{\hbar^2}{2M}\nabla^2 + \frac{M}{2}\omega^2\vec{x}^2\Big)\hat{\Psi}(\vec{x}, t).
\end{aligned} \tag{6.85}$$

This looks like a Schroedinger equation. However, it is the full evolution equation of the field operator (in the absence of interaction terms in the Hamiltonian, i.e. for ballistic expansion.)

Our goal is to construct the momentum distribution

$$\tilde{n}(t, \vec{p}) = \langle\tilde{\Psi}^\dagger(t, \vec{p})\tilde{\Psi}(t, \vec{p})\rangle \tag{6.86}$$

at $t = 0$ from the density image

$$n(t, \vec{x}) = \langle\hat{\Psi}^\dagger(t, \vec{x})\hat{\Psi}(t, \vec{x})\rangle \tag{6.87}$$

at $t = T/4 = \pi/2\omega$. Herein,

$$\tilde{\Psi}(t, \vec{p}) = \ell^{-2}\int \mathrm{d}^2x e^{-\mathrm{i}\vec{p}\cdot\vec{x}/\hbar}\hat{\Psi}(t, \vec{x}) \tag{6.88}$$

is the field operator in momentum space, and $\ell = \sqrt{\hbar/M\omega}$ is the oscillator length.

Hermite function expansion

To solve the evolution equation

$$\mathrm{i}\hbar\partial_t\hat{\Psi}(t,\vec{x}) = \Big(-\frac{\hbar^2}{2M}\nabla^2 + \frac{M}{2}\omega^2\vec{x}^2\Big)\hat{\Psi}(t,\vec{x}),\ \ \hat{\Psi}(0,\vec{x}) = \hat{\psi}(\vec{x}) \tag{6.89}$$

we first note that the solution can be factorized due to the assumption of ballistic expansion. We thus restrict to a 1D setting without loss of generality. With the ansatz

$$\hat{\Psi}(t,x) = \sum_n e^{-\mathrm{i}E_n t/\hbar}\hat{\psi}_n(x) \tag{6.90}$$

we find

$$E_n\hat{\psi}_n(x) = \Big(-\frac{\hbar^2}{2M}\partial_x^2 + \frac{M}{2}\omega^2x^2\Big)\hat{\psi}_n(x) \tag{6.91}$$

for each n individually. This is, of course, of the form of the Hermite differential equation

$$H_n''(x) + (2n+1-x^2)H_n(x) = 0, \tag{6.92}$$

where $H_n(x)$ are the Hermite functions. Indeed, with $\tilde{x} = x/\ell = x\sqrt{M\omega/\hbar}$ and $E_n = \hbar\omega(n+1/2)$ we find

$$\Big(\frac{\partial^2}{\partial\tilde{x}^2} + (2n+1-\tilde{x}^2)\Big)\hat{\psi}_n(x) = 0. \tag{6.93}$$

Hence

$$\hat{\Psi}(t,x) = \sum_n e^{-\mathrm{i}E_n t/\hbar}H_n(x/\ell)\hat{\psi}_n(0). \tag{6.94}$$

For an expansion time $t = T/4$ we use

$$e^{-\mathrm{i}E_n(T/4)/\hbar} = e^{-\mathrm{i}\frac{\pi}{2}(n+1/2)} = (e^{-\mathrm{i}\pi/2})^n e^{-\mathrm{i}\pi/4} = (-\mathrm{i})^n e^{-\mathrm{i}\pi/4}, \tag{6.95}$$

to arrive at

$$\hat{\Psi}(T/4,x) = \sum_n (-\mathrm{i})^n e^{-\mathrm{i}\pi/4}H_n(\tilde{x})\hat{\psi}_n(0). \tag{6.96}$$

We now employ that for the Fourier transform of the Hermite functions, $\tilde{H}_n$, we have

$$\tilde{H}_n(y) = (-\mathrm{i})^n H_n(y). \tag{6.97}$$

For the field operator in momentum space we then obtain

$$\begin{aligned}\tilde{\Psi}(t,p) &= \ell^{-1}\int \mathrm{d}x e^{-\mathrm{i}px/\hbar}\hat{\Psi}(t,x) = \ell^{-1}\sum_n e^{-\mathrm{i}E_n t/\hbar}\hat{\psi}_n(0)\int \mathrm{d}x e^{-\mathrm{i}px/\hbar}H_n(\tilde{x}) \\ &= \ell^{-1}\sum_n e^{-\mathrm{i}E_n t/\hbar}\hat{\psi}_n(0)\ell\int \mathrm{d}\tilde{x} e^{-\mathrm{i}\tilde{p}\tilde{x}}H_n(\tilde{x}) = \sum_n e^{-\mathrm{i}E_n t/\hbar}\hat{\psi}_n(0)(-\mathrm{i})^n H_n(\tilde{p}),\end{aligned} \tag{6.98}$$

where we defined $\tilde{p} = \ell p/\hbar$ in the last equality. From this we conclude that

$$\begin{aligned}\hat{\Psi}^\dagger(T/4,\vec{x})\hat{\Psi}(T/4,\vec{x}) &= \sum_{n,n'}\mathrm{i}^n(-\mathrm{i})^{n'}H_n(\tilde{x})H_{n'}(\tilde{x})\hat{\psi}_n^\dagger(0)\hat{\psi}_{n'}(0) \\ &= \tilde{\Psi}^\dagger(0,\tilde{p}=\tilde{x})\tilde{\Psi}(0,\tilde{p}=\tilde{x}).\end{aligned} \tag{6.99}$$

Of course, $\tilde{p} = \tilde{x}$ is equivalent to $p = \hbar x/\ell^2 = M\omega x$, and we eventually arrive at the desired result

$$\begin{aligned}n(T/4,x) &= \langle\hat{\Psi}^\dagger(T/4,x)\hat{\Psi}(T/4,x)\rangle \\ &= \langle\tilde{\Psi}^\dagger(t,p=M\omega x)\tilde{\Psi}(t,p=M\omega x)\rangle \\ &= \tilde{n}(0,p=M\omega x).\end{aligned} \tag{6.100}$$

6.2.3 Thermometry

Temperature determination of the trapped gas is an important and nontrivial aspect of the experimental setup. As mentioned in Sec. 6.2.1, we only have technically defined temperature variables, which qualitatively corresponds to a heated gas, but do not yield the precise temperature in nK. Here we describe how this can be achieved from the momentum distribution, and from in-situ density images. Together with the measured density n, the temperature determination allows to specify the phase diagram, i.e. the curve $T_\mathrm{c}/T_\mathrm{F}$. In contrast, a determination of the equation of state $n(\mu,T)$ also requires to determine the chemical potential - an experimentally even more delicate task.

From the momentum distribution after time of flight (see Sec. 6.2.2) we can extract the temperature from a Boltzmann fit to the large momentum part according to

$$\tilde{n}(p) \sim z_\mathrm{eff}e^{-p^2/2Mk_\mathrm{B}T}. \tag{6.101}$$

The Gaussian behavior for large momenta is clearly visible in the log-p^2-plot of the radially average momentum distribution, see Fig. 6.12. The radial average is justified by the almost radial symmetry of the trap. The effective fugacity z_eff in Eq. (6.101) does not coincide with the fugacity $z = e^{\beta\mu}$, which would multiply the tail for a homogeneous system. This is a result of the fact that we measure the trap-averaged momentum distribution after TOF.

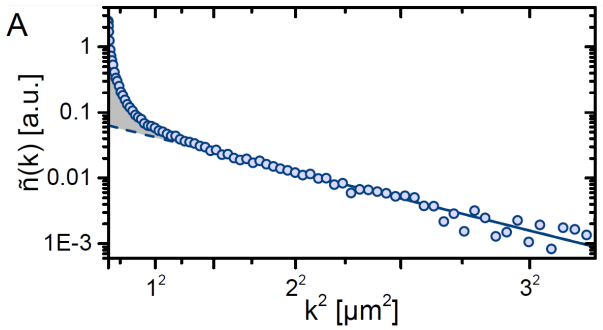

Figure 6.12: Radially averaged momentum distribution $\tilde{n}(k)$ at 782G, obtained after $T/4$-TOF for the coldest accessible temperature. The image is the average over approximately 30 realizations. We clearly see the Boltzmann tail $\tilde{n}(p) \sim \exp(-p^2/2Mk_\mathrm{B}T)$ for large momenta, where $M = 2M_\mathrm{Li}$ is the dimer mass for this particular value of the magnetic field. At low momenta we see an enhanced occupation of low-momentum states, which we associate with condensation. The determination of the critical temperature is discussed in Sec. 6.2.4. Figure taken from Ries et al. [2014].

In Eq. (6.101) the particle mass M enters the exponential function. It is the same mass M which also appears in the evolution equation for the field operator, Eq. (6.85). Therefore, it is the mass of the expanding particles, which are composite bosons on the BEC side ($M = 2M_\mathrm{Li}$), and atoms ($M = M_\mathrm{Li}$) on the BCS side of the crossover. In the intermediate region it is problematic to decide which M has to be inserted. In particular, the fitted temperature sensitively depends on this choice. However, from the limiting regimes it appears that the degeneracy T/T_F is almost constant for a fixed temperature variable over the whole crossover. We thus linearly interpolate T/T_F in the magnetic field region $783\mathrm{G} \leq B \leq 892\mathrm{G}$.

An alternative way to determine the temperature is from a Boltzmann fit to the outer region of the in-situ density profile. In contrast to the thermometry from the momentum distribution, we here apply the Boltzmann form of the equation of state (EOS) at large negative local chemical potential $\mu(\vec{r}) = \mu_0 - V(\vec{r})$. For this purpose we apply LDA to the whole cloud such that

$$n(\vec{r}) = n(\mu_0 - V(\vec{r}), T) \tag{6.102}$$

for all $\vec{r}$. In particular, using the Boltzmann EOS $n(\mu_\mathrm{cl}, T) = e^{\beta\mu_\mathrm{cl}}/\lambda_T^2$, we then find

$$n(\vec{r}) \sim e^{\beta\mu_\mathrm{cl}(\vec{r})} \tag{6.103}$$

for large $|\vec{r}|$. In this equation μ_cl refers to the chemical potential of the classical particles, i.e. the few-body degrees of freedom. Similar to the above problem of

determining the mass M of the expanding particle, we find $\mu_{\mathrm{cl}} = 2\mu$ and $\mu_{\mathrm{cl}} = \mu$ in the BEC and BCS limit, respectively.

We write

$$\mu_{\mathrm{cl}} = \alpha\mu \tag{6.104}$$

with fermion chemical potential μ and $1 \leq \alpha \leq 2$, and arrive at

$$n(\vec{r}) \sim e^{-\alpha\beta V(\vec{r})} \tag{6.105}$$

for large radii. This equation may also be read in a different way: The potential energy of tightly bound bosons in the external potential is twice as large as the one of single atoms, since they consist of two atoms. Accordingly, we have $V_\phi(\vec{r}) = 2V(\vec{r})$ for the potential seen by the dimers. The weaker response to the trapping potential can also be rephrased in an enhanced mass due to

$$M = \alpha M_{\mathrm{Li}}. \tag{6.106}$$

Interestingly, the problem of assigning the right mass to Eq. (6.101) is equivalent to finding α in Eq. (6.105). In both cases the proper few-body degrees of freedom have to be determined. A non-integer α is understood as an effective number of degrees of freedom. We have chosen the symbol α here to make contact with the running coupling

$$\alpha_\phi = \frac{\partial^2 U}{\partial\mu\partial\rho}(\rho_0) \tag{6.107}$$

introduced in the FRG context, see e.g. Diehl et al. [2010a], or Eqs. (6.52) and (6.53).

To extract the temperature from the in-situ images, we map out the function $n(V)$, which groups the density profile $n(\vec{r})$ with the corresponding value of the trapping potential $V(\vec{r})$, Eq. (6.69). The asymptotic behavior in Eq. (6.105) then corresponds to $n(V) \sim e^{-\alpha V/k_{\mathrm{B}}T}$. The function $n(V)$ is obtained from approximately $300^2 = 90000$ pixels, which we group into 500 bins for $n(V_i)$ with discrete equidistant V_i. The fit range consists in those bins where $n(V)$ decays exponentially, which typically is the part of the cloud where the density is below 10% of the central density. To account for a possible background noise we then fit the function

$$n(V) = A \cdot e^{-V/kT} + n_0 \tag{6.108}$$

to the data. The rescaling with the factor α is performed later. A typical example of the fit procedure is shown in Fig. 6.13.

For obtaining the function $n(V)$ it is important to account for the anharmonic terms in $V(\vec{r})$, which becomes relevant in the outer regions of the trap. They lead to an decrease of typically 10nk in the fitted temperature. For $782\mathrm{G} \leq B \leq 922\mathrm{G}$

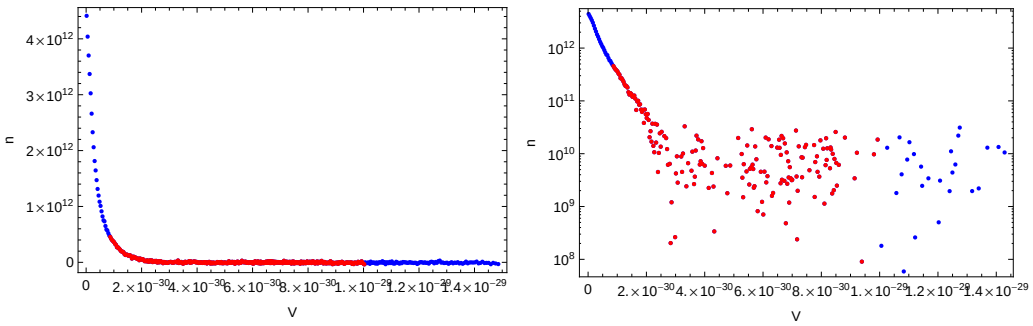

Figure 6.13: *Left:* Binned density profile $n(V)$ for a low temperature variable on the far BEC side (692G). We plot $n(\mathrm{m}^{-2})$ vs. $V(\mathrm{J})$. Note that due to grouping the data into 500 bins, the central region $p \to 0$ is only poorly captured, whereas we obtain a reliable picture of the large momentum tail. *Right:* The same configuration plotted on a logarithmic scale. We fit the model of Eq. (6.108) to the red region. With this we obtain a temperature of 74nK. For this value of the magnetic field we use $\alpha = 2$ to account for the bosonic nature of the classical particles.

we linearly interpolate α in Eq. (6.105) between 2 and 1. The result of the in-situ thermometry is shown in Fig. 6.14.

The results of the in-situ thermometry agree well with the temperatures obtained from the momentum distribution on the BEC side of the resonance. However, as we approach the atomic limit, the lowest values are reduced by a factor of two in comparison to the $T/4$-fit results. However, the error of the fit is also very large in both cases. Interestingly, without the rescaling by α, the in-situ Boltzmann method yields a temperature that is almost independent of the magnetic field for the whole crossover.

For 1042G, the correction to the free fermion EOS from Fermi liquid theory (FLT) is 22%. This motivates to fit a FLT-profile $n(\vec{r}) = n_{\mathrm{FLT}}(\mu_0 - V(\vec{r}), T, a_{2\mathrm{D}})$ with

$$n_{\mathrm{FLT}}(\mu, T, a_{2\mathrm{D}}) = \frac{2M_{\mathrm{Li}}}{\hbar^2}\frac{k_{\mathrm{B}}T}{2\pi}\log\left(1+\exp\left[\frac{1}{k_{\mathrm{B}}T}\left(\mu + \left(\frac{\hbar^2}{2M_{\mathrm{Li}}}\right)\frac{2\pi n_{\mathrm{id}}}{\log(k_{\mathrm{F,id}}a_{2\mathrm{D}})}\right)\right]\right),$$
$$n_{\mathrm{id}}(\mu, T) = \frac{2M_{\mathrm{Li}}}{\hbar^2}\frac{k_{\mathrm{B}}T}{2\pi}\log\left(1+e^{\mu/k_{\mathrm{B}}T}\right) \tag{6.109}$$

to the in-situ density profile. Using $a_{2\mathrm{D}} = 3.7\times10^{-5}\mathrm{m}$ for the 2D scattering length, the only free parameters are the central chemical potential μ_0, the prefactor $c = \mathrm{OD}/n$ (or particle number N), and the temperature T. In particular, since LDA should work reasonably well in the central region of the cloud, the values of μ_0 and N can be fitted independently of T in the inner region, with a subsequent estimate for T from the outer regions. In order to get a reasonable fit, we typically

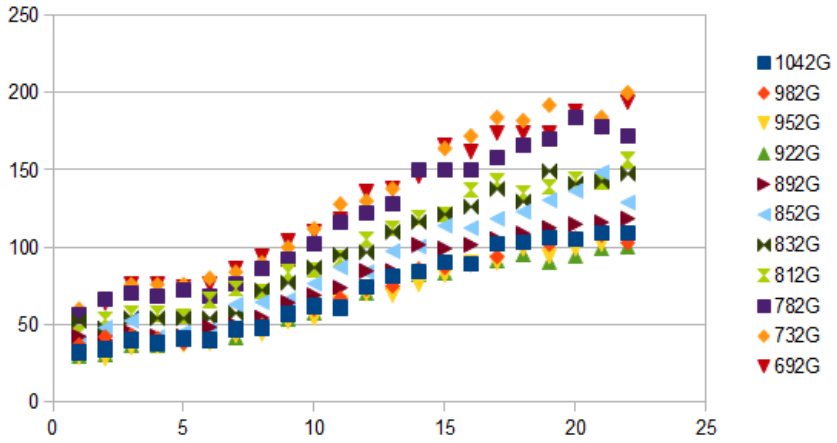

Figure 6.14: Temperature in nK obtained from an in-situ Boltzmann fit of the thermal wing of the cloud vs. temperature variable 1-22. For temperature variables 1-3 the sample is held in the trap for varying time where it is heated due to technical noise, whereas 4-22 correspond to a periodic modulation of the trap depth with increasing amplitude.

have to leave the particle number N free, i.e. cannot fix it to the experimentally determined value. Again, the quartic terms substantially influence the result of the fit for the temperature. The latter is decreased by $\approx$ 10nK due to the anharmonicity. In contrast, the chemical potential is barely affected by the latter, as it is determined mostly from the central region. The result of the FLT fit at 1042G is shown in Table 6.3.

Comparing the temperature obtained from the in-situ Boltzmann fit to those found from the Boltzmann tail of the momentum distribution after TOF, we find that the lowest temperatures in the atomic limit disagree, but are still compatible within their errors. We find good agreement on the BEC side of the resonance. The most conflicting result is that the in-situ Boltzmann method finds the lowest attainable temperatures to be on the atomic side, whereas the lowest temperatures seem to be reached in the bosonic limit from the $T/4$-imaging. However, the influence on the critical temperature, and thus on the phase structure, is only weak, as we display in Fig. 6.15.

We close the discussion of thermometry with a summary of systematic errors of both methods to determine the temperature. An immediate advantage of the method based on the momentum distribution is that the Gaussian tail is clearly visible in the logarithmic plot over a wide range. The resulting fit error due to the fitting range is approximately 7% for low and up to 13% for high temperatures. In contrast, the fit range for the in-situ Boltzmann method is often very small. The variation due to changing the fit range is usually $10-20$nK in absolute units.

For the T/4-imaging to give a reliable account of the actual momentum distri-

TempVar	N	μ_0 (nK)	T (nK)	T_F (nK)	T/T_F
1	103 000	224	27	306	0.09
3	102 000	222	34	303	0.11
5	102 000	222	36	301	0.12
7	98 000	223	42	292	0.14
9	105 000	209	51	294	0.17
11	116 000	193	57	301	0.19
13	101 000	201	67	274	0.24
15	97 000	200	74	263	0.28
17	88 000	208	76	248	0.31

Table 6.3: Results of the FLT fit to the density profile at 1042G, which is far on the BCS side. Still there is a 22% Fermi liquid correction to the free fermion gas density. Note that the energy spacing in the (tight) transverse direction is $\hbar\omega_z = 265$nK. We find good agreement of the temperatures with the ones from the Boltzmann fit at low temperatures, whereas the FLT-temperatures are lower by $\approx 20\%$ at high temperature variables.

bution, we need to ensure that (i) the expansion is ballistic, (ii) the expansion plane is orthogonal to the z-direction, i.e. not tilted, and (iii) we measure exactly at the turning point $t_{\rm exp} = T/4$ such that Eq. (6.100) is applicable. (i) Due to the highly anisotropic tapping of the cloud, the expansion after release from the trap is very rapid in z-direction. This leads to a fast dilution of the gas during TOF. In addition, before the release from the trap, the gas is ramped to 692G ("jump") with a speed of $\simeq 1.9$G/s such that the 3D scattering length is maximally small within the range of accessible values. The ramp is sufficiently slow to ensure that it does not result in heating[1], but still fast enough such that the many-body system cannot adjust to the new value of $a_{\rm 2D}$. Murthy et al. [2014] have shown that less than 10% of the particles undergo scattering during the expansion time $t_{\rm exp} = 25$ms, and that collisions are only important for the first 0.5ms after the release. (ii) A relative tilt of the expansion plane compared to the imaging plane results in a weak ellipticity of the cloud after $T/4$-imaging. This effect, however, has been found to be less then 5%. (iii) The measured $t_{\rm exp}$ is very close to the exact $T/4$, as $t = T/4$ corresponds to the turning point in the evolution in the harmonic trap, and thus results in a maximal value for the temperature. By fitting the temperature to images obtained for $t < t_{\rm exp}$ and $t > t_{\rm exp}$ it has been verified that the image at $t_{\rm exp}$ has indeed maximal temperature with an error of approximately 5%.

Fitting the wings of the in-situ profiles is mostly limited by the applicability of the LDA. As we have discussed in Sec. 2.1, the latter becomes invalid for very

[1] This has been checked by measuring the temperature with and without jump, and by ramping back and forth and then comparing the temperature at the initial magnetic field before and after the ramp.

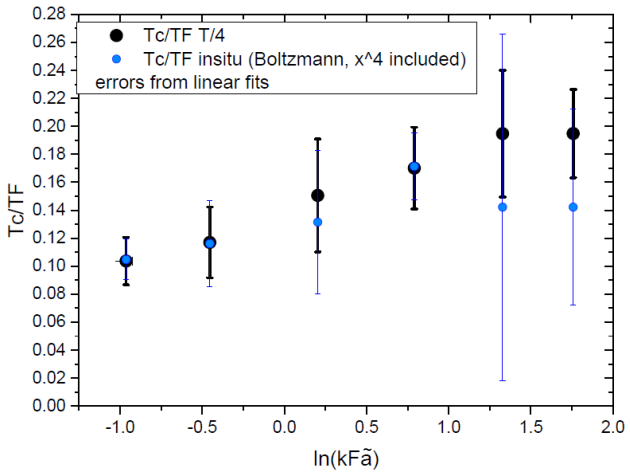

Figure 6.15: Comparison of the ratio T_c/T_F in the crossover with the temperature being determined from $T/4$-imaging after TOF and the in-situ Boltzmann fit, respectively. Both methods coincide for $\log(k_F\tilde{a}_{2D}) \leq 1$, but the central values disagree in the atomic limit. Still they are compatible within their errors. Note that we show the data normalized to $\tilde{a}_{2D}$ here, see Table. 6.2 for the translation to a_{2D}.

low densities. This is the case for the Boltzmann tail, which we find to set in for approximately 10% of the central peak density. As the latter decreases by a factor of 3 when going from the bosonic to the atomic limit, the applicability on the BCS side is most questionable. On the other hand, the global FLT fit gives quantitatively good agreement with the Boltzmann fit for low temperatures at 1042G. In contrast to the Boltzmann fit, the FLT-ansatz of Eq. (6.109) is applied to the whole cloud. As a consequence, it is very robust against changes of the fitting region. However, we also find that we have to leave the particle number N as a free fit parameter for the FLT-ansatz to be compatible with the density profile. The obtained N disagrees by $\approx 10\%$ with the measured values, and appears to be too high. Moreover, at higher temperatures, the agreement between the in-situ FLT- and Boltzmann-methods becomes worse, but both are still compatible within the errors. It is also puzzling that, for a fixed temperature variable, the in-situ method gives the same temperature almost independent of the magnetic field: $T \neq T(B)$. Only due to the rescaling with $1 \leq \alpha \leq 2$ we obtain the spread shown in Fig. 6.14.

For the temperature determination for the phase diagram we use the method based on the momentum distribution since we believe that the Gaussian part of the momentum distribution over a wide range is a very convincing signature of an equilibrated temperature, whereas the applicability of LDA to an extremely dilute, almost classical gas is questionable. The influence on the phase boundary

is rather small as we do not observe condensation far on the atomic side of the resonance. For lower magnetic fields, both methods coincide within their errors, see Fig. 6.15. For a more detailed discussion of systematic errors we refer to Ries et al. [2014].

6.2.4 Phase diagram

We now describe the experimental determination of the phase diagram of the 2D BCS-BEC crossover within the setup outlined above. In order to compare the measurements of the trapped gas to predictions for the homogeneous system we normalize the data to the peak density n_0 by employing the LDA to the trap center. We define

$$T_{\mathrm{F}} = \frac{\hbar^2}{2Mk_{\mathrm{B}}} 2\pi n_0, \tag{6.110}$$

where $n = n_1 + n_2$ is the total density of atoms. Together with a measurement which allows for the distinction of the condensed from the normal phase, we can then obtain the critical temperature ratio $T_{\mathrm{c}}/T_{\mathrm{F}}$ for each value of the magnetic field. This results in the phase diagram shown in Fig. 6.18. To determine T_{c} we associate the broken phase with largely enhanced occupation of low-momentum modes.

In Fig. 6.16 we show low-temperature in-situ density profiles and momentum distributions for magnetic fields $B = 692\mathrm{G}, 782\mathrm{G}, 832\mathrm{G}, 852\mathrm{G}, 922\mathrm{G}$ across the Feshbach resonance. This corresponds to inverse 3D scattering lengths $a_{\mathrm{3D}}^{-1} = 7.11, 1.55, 0, -0.46, -1.67$ in units of ℓ_z. The latter parametrization allows for a possibly more intuitive comparison to the 3D case with crossover parameter $(k_{\mathrm{F}} a_{\mathrm{3D}})^{-1}$. When crossing from the BEC (left in the figure) to the BCS side (right in the figure), we observe a decrease of the peak density n_0 together with a broadening of the cloud. The central density at 692G is $2.7\mu\mathrm{m}^{-2}$ per species, whereas we have $0.76\mu\mathrm{m}^{-2}$ per species at 922G. The qualitative shape of the density profiles is in accordance with the expectation of a crossover from bosonic degrees of freedom to an atomic ensemble. An analogous phenomenology is found in the 3D BCS-BEC crossover.

From the in-situ density profiles it is hard to decide whether the system is in a symmetry broken phase. In fact, although it is possible to identify a second order phase transition by means of a kink in the number density, a more direct signature is highly desirable. Here we use the enhanced occupation of low-momentum modes in the momentum distribution $\tilde{n}(p)$ as a signature of phase coherence in the system. We then call the system to be in the condensed phase. For a finite system, as is realized by the trapped gas, a nonzero condensate can appear at low momenta. To distinguish it from a mere enhanced occupation of low-momentum modes with $p > 0$ is inherently difficult in experiment due to the finite resolution of the imaging apparatus after TOF. We thus follow the common standard of associating a bimodal structure of the momentum distribution with a condensate.

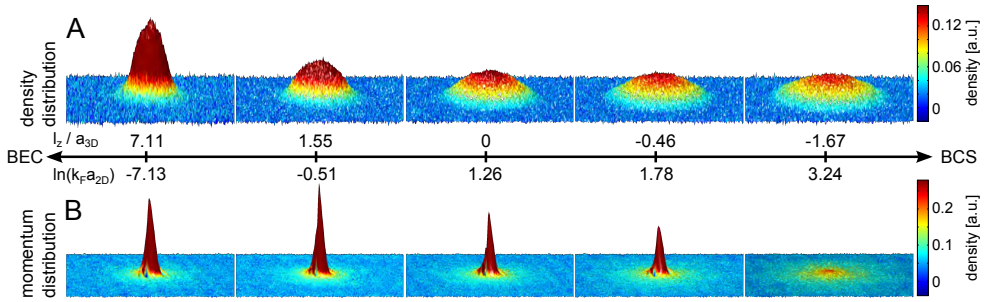

Figure 6.16: By varying the 2D scattering length across the Feshbach resonance we tune the system from the bosonic ($\log(k_\mathrm{F}a_\mathrm{2D}) \ll -1$) to the fermionic regime ($\log(k_\mathrm{F}a_\mathrm{2D}) \gg 1$). Here we show the in-situ density profile, $n(r)$, and the momentum distribution, $\tilde{n}(p)$, at the lowest accessible temperatures. The in-situ profile decreases in height and becomes broader as we approach the fermionic limit. However, a clear signature of the phase transition cannot be inferred from it. In contrast, a greatly enhanced occupation of low-momentum modes signals condensation in the momentum distribution. In order to compare to the 3D crossover we also display a_3D^{-1} in units of ℓ_z. Figure taken from Ries et al. [2014].

A better resolution of the low-momentum region is, however, possible with the techniques described by Murthy et al. [2014].

The phase transition to the condensed phase is identified with the sharp rise of the central peak momentum density, $\tilde{n}(p = 0)$, normalized by the in-situ spatial density, $n(r = 0)$. In Fig. 6.17C we show the corresponding ratio as a function of T/T_F for 782G. We clearly observe two distinct linear regimes at low and high temperatures, respectively. The critical temperature is defined from the intersection of linear fits to both regimes. For the configuration shown in Fig. 6.17 we obtain $T_\mathrm{c}/T_\mathrm{F} = 0.151(40)$, where the uncertainty is obtained from the standard error of the linear fits. The phase boundary extracted with this method for the whole crossover region is shown in Fig. 6.18 by the black dots.

Apart from the phase transition to the condensed phase the momentum distribution also allows to quantify the deviation of the trapped gas from a thermal ensemble. For this purpose we determine the gray area under the curve shown in Fig. 6.12, which we define as the non-thermal or quantum fraction, N_q/N. The latter observable depends on the trap parameters due to the fact that we only measure the trap-averaged momentum distribution. Nevertheless, it is a useful quantity to measure deviations from the thermal gas density, and in this spirit it is related to the determination of the transition point from the density mentioned above. In Fig. 6.17B we show the quantum fraction as a function of T/T_F for 782G. In contrast to $\tilde{n}(0)$, the decay of N_q/N with increasing temperature is rather smooth. The increase for $T \geq T_\mathrm{c}$ implies quantum degeneracy of the

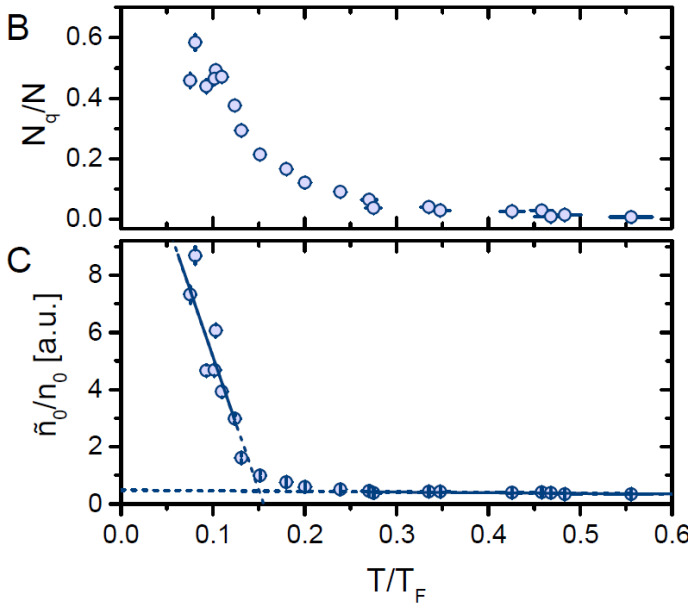

Figure 6.17: Temperature dependence of the quantum fraction N_q/N and peak momentum density $\tilde{n}(p=0)$ for 782G. The quantum fraction is obtained from the gray area in Fig. 6.12, quantifying the non-thermal fraction of particles. It gives a good account for the quantum degeneracy of the gas, but does not allow to locate the transition point. In contrast, from the ratio $\tilde{n}(p=0)/n(r=0)$ we find a clear separation between two temperature regimes. The critical temperature is obtained from the intersection point of linear fits of the data in both regimes. Note that an enhanced occupation value for $\tilde{n}(p=0)$ signals phase coherence of the system. We associate this with condensation. Figure taken from Ries et al. [2014].

gas, and heralds condensation. We obtain a picture which is consistent with the method of extracting T_c from the peak momentum distribution since the increase in N_q/N appears to become steeper at T_c. We show the quantum fraction as a color scale in the phase diagram, Fig. 6.18. The condensed region roughly corresponds to $N_q/N \gtrsim 0.3$.

We are now in the position to discuss the main result of the present analysis, the experimentally measured phase diagram of the 2D BCS-BEC crossover in Fig. 6.18. On the BEC side we find the critical temperature to agree reasonably well with an effective description in terms of strongly coupled composite bosons: Based on the a Monte Carlo analysis of two-dimensional bosons by Prokof'ev et al. [2001], Prokof'ev and Svistunov [2002], the BKT transition temperature on the

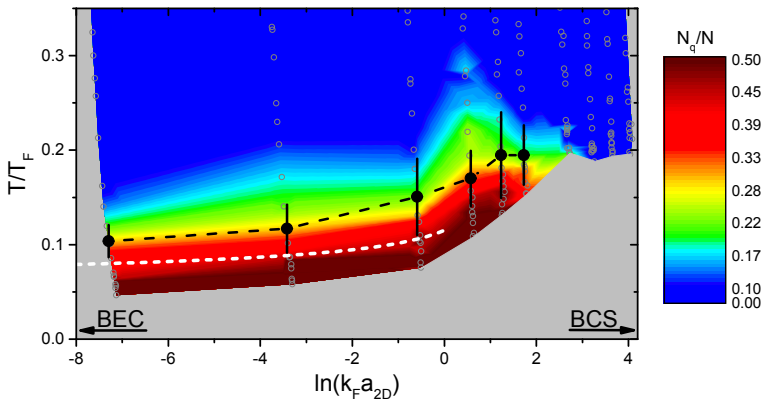

Figure 6.18: Measured phase diagram of the 2D BCS-BEC crossover. The 2D scattering length is determined according to Eq. (6.74), and the Fermi momentum is given by $k_\mathrm{F} = (2\pi n_0)^{1/2}$. The black dots corresponds to the estimated critical temperature from $\tilde{n}(p = 0)$. The color scale shows the quantum fraction N_q/N. We do not detect condensation for $\log(k_\mathrm{F} a_\mathrm{2D}) > 2$ on the BCS side, which puts an upper bound on the critical temperature in this regime. The white dashed line corresponds to the BKT-transition temperature of a gas of composite bosons from Eq. (6.111). Figure taken from Ries et al. [2014].

BEC side was shown by Petrov et al. [2003] to be

$$\frac{T_\mathrm{BKT}}{T_\mathrm{F}} = \frac{1}{2}\left(\log\left[\frac{C}{4\pi}\log\left(\frac{4\pi}{k_\mathrm{F}^2 a_\mathrm{2D}^2}\right)\right]\right)^{-1} \tag{6.111}$$

with $C = 380(3)$. Within the errors this formula provides a good description of the data up to $\log(k_\mathrm{F} a_\mathrm{2D}) = 0$. This is supported by the fact that the zero-crossing of the chemical potential, due to the microscopic two-body bound state, is located on the BCS side of the 2D crossover. (In contrast, it appears on the BEC side in the 3D system.) Apart from the good agreement of the measured critical temperature with the prediction from Eq. (6.111) within the experimental error, we find the central experimental value to be systematically larger.

The phase diagram in Fig. 6.18 shows a maximum for $\log(k_\mathrm{F} a_\mathrm{2D}) \approx 1$, where we find $T_\mathrm{c}/T_\mathrm{F} = 0.19$. We associate this point with the crossover from bosonic molecules to fermionic Cooper pairs. The location of the maximum thus approximately corresponds to the location of the zero-crossing of the chemical potential. This statement is also supported by the FRG analysis for both the 3D and 2D system, respectively.

Far on the BCS side, perturbation theory predicts an exponential decrease of

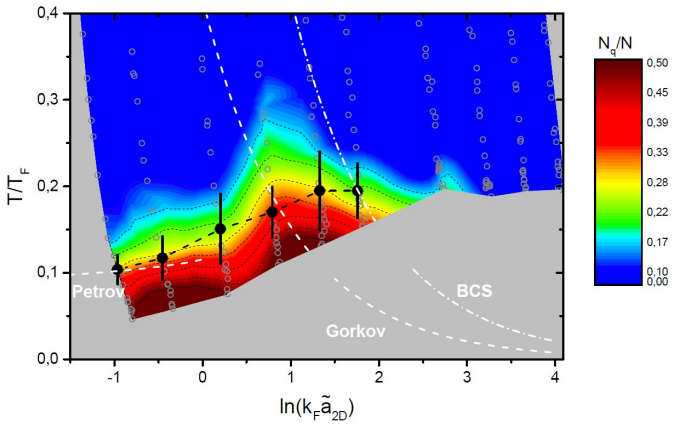

Figure 6.19: We plot the phase diagram in terms of $\log(k_{\mathrm{F}}\tilde{a}_{2\mathrm{D}})$. Here $\tilde{a}_{2\mathrm{D}}$ is the 2D interaction parameter obtained from the confinement induces binding energy ($\tilde{\varepsilon}_{\mathrm{b}}$) according to $\tilde{\varepsilon}_{\mathrm{b}} = -\hbar^2/M\tilde{a}_{2\mathrm{D}}^2$, see the discussion below Eq. (6.75). The Bose limit at 692G corresponds to $\log(k_{\mathrm{F}}\tilde{a}_{2\mathrm{D}}) \simeq -1$. If we associated $\tilde{a}_{2\mathrm{D}}$ with the 2D scattering length $a_{2\mathrm{D}}$, this would indicate that the gas is still strongly coupled at 692G. In contrast, $\log(k_{\mathrm{F}}a_{2\mathrm{D}}) \simeq -7$ for this magnetic field. On the BCS side both definitions coincide and we have $\tilde{a}_{2\mathrm{D}} = a_{2\mathrm{D}}$. We show the GMB and BCS results from Eq. (6.112) extrapolated to strong coupling in this regime. The Petrov curve corresponds to the dashed white curve in Fig. 6.18, however applied with $a_{2D} \to \tilde{a}_{2D}$ here.

$T_{\mathrm{c}}/T_{\mathrm{F}}$ (Petrov et al. [2003]) according to

$$\left.\frac{T_{\mathrm{c}}}{T_{\mathrm{F}}}\right|_{\mathrm{GMB}} = \frac{1}{e}\left.\frac{T_{\mathrm{c}}}{T_{\mathrm{F}}}\right|_{\mathrm{BCS}} = \frac{2e^{\gamma}}{\pi}\frac{1}{k_{\mathrm{F}}a_{2\mathrm{D}}}, \tag{6.112}$$

where GMB (BCS) indicates the expressions associated to Gorkov and Melik-Barkhudarov (Bardeen–Cooper–Schrieffer) in 3D. Due to the limitation on experimentally accessible values for T/T_{F} on the atomic side of the crossover, we can only provide a lower bound of $T_{\mathrm{c}}/T_{\mathrm{F}} \leq 0.19$ for $\ln(k_{\mathrm{F}}a_{2\mathrm{D}}) \geq 2$. The observed non-Gaussian fraction, however, supports a decrease towards the BCS limit. Note also that the thermometry from the in-situ profiles, which indicates a lower central value of the temperature on the far BCS side, does not invalidate the bound. The extrapolation of the GMB- and BCS-predictions into the strongly-correlated regime are shown in Fig. 6.19, although the perturbative calculations become invalid in this regime.

Our estimate for the critical temperature for $\log(k_F a_{2D}) > 0$ is systematically above corresponding theoretical predictions for a homogeneous system (Bauer

B (G)	$\log(k_\mathrm{F}a_\mathrm{2D})_\mathrm{c}$	$\log(k_\mathrm{F}\tilde{a}_\mathrm{2D})_\mathrm{c}$	$T_\mathrm{c}/T_\mathrm{F}$	$(T_\mathrm{c}/T_\mathrm{F})_\mathrm{in-situ}$
692	- 7.30 (4)	- 0.96 (4)	0.104 (17)	0.105 (15)
732	- 3.42 (2)	- 0.45 (2)	0.117 (25)	0.116 (31)
782	- 0.59 (1)	0.20 (1)	0.151 (40)	0.131 (51)
812	0.57 (1)	0.79 (2)	0.170 (29)	0.171 (24)
832	1.23 (1)	1.33 (1)	0.195 (45)	0.142 (120)
852	1.72 (1)	1.76 (1)	0.195 (32)	0.142 (70)

Table 6.4: Phase boundary of the 2D BCS-BEC crossover. The results are shown for both a_2D and $\tilde{a}_\mathrm{2D}$, see also Table 6.2 for the translation $a_\mathrm{2D} \leftrightarrow \tilde{a}_\mathrm{2D}$. The critical temperature T_c is determined from the Boltzmann fit to the high momentum tail of the momentum distribution. We also display the corresponding value for the critical temperature obtained from the in-situ fit to the density profile, see the discussion in Sec. 6.2.3. Both thermometry methods are compatible within their errors for magnetic fields which support a condensed phase in the experimentally accessible temperature region. The error given in this table corresponds to the statistical error. For a detailed discussion of uncertainties see Ries et al. [2014].

et al. [2014]). We address part of this deviation to the influence of the finite aspect ratio of our trap, which leads to residual influence of the third dimension (Fischer and Parish [2014]). Furthermore, local equilibration and thus applicability of the local density approximation at the trap center is not guaranteed. This effect becomes more pronounced for decreasing central peak density. Still, due to the reasonable agreement with theory on the BEC side, we believe that the phase diagram shown in Fig. 6.18 gives a reliable account for the phase structure of the homogeneous system. We display selected values for the phase boundary in Table 6.4.

From a Fourier transform of the momentum distribution $\tilde{n}(p)$ we obtain the correlation function $g_1(r)$. In the low temperature phase we observe a clearly visible power law decay according to $g_1(r) \sim r^{-\alpha}$ for large r. In contrast the decay is exponential in the high temperature region. This is in line with a BKT-transition of a spin-wave phase with algebraically decaying phase correlations into a disordered phase at $T = T_\mathrm{BKT}$. In particular, the correlation length ξ_cor is anomalously large below T_c. For a truly 2D system we have $\xi_\mathrm{cor} = \infty$ in the superfluid phase. Here, however, due to the finite extent of the trapped system, correlations are cut off at length scales on the order of the oscillator length ℓ_0. Indeed, we find that $g_1(r) = r^{-\alpha}\exp(-r/\xi_\mathrm{cor})$ is a good fit function for large r with $\xi_\mathrm{cor} \approx 20\mu$m being on the order of the radial oscillator length.

Single-shot density images of the cloud after short TOF display density fluctuations on length scales which are sufficiently larger than the thermal wavelength. Those fluctuations have to be due to initial (i.e. in-situ) phase fluctuations. In-

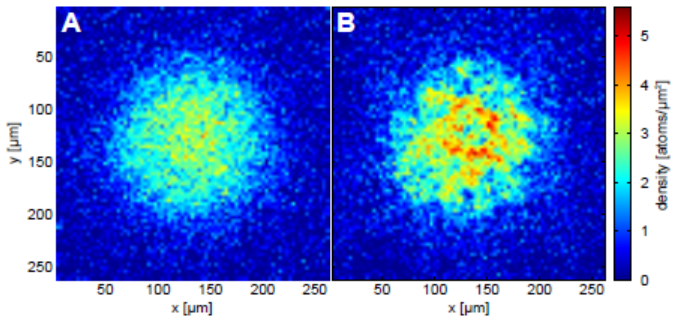

Figure 6.20: Density profile in-situ (*left*) and after short TOF (*right*) at a low-temperature on the BEC-side. We observe density fluctuations after TOF which cannot be explained by the far smaller initial density fluctuations. Accordingly, they have to result from initial phase correlations. The size of the patches after TOF is larger than the thermal wavelength. This rules out thermal correlations and the observed pattern must result from a superfluid with large correlation length. Figure taken from Ries et al. [2014].

deed, the size of initial density fluctuations can be estimated from shot-by-shot images of the trapped cloud before the release, and they are too small to explain the signature after TOF. We show an in-situ density image and a density image after short TOF in Fig. 6.20.

We conclude from (i) the good agreement of T_c with the BKT-prediction on the BEC-side, (ii) the algebraic decay of phase correlations and an 'infinite' correlation length ($< \ell_0$) below T_c, and (iii) the imprint of initial phase correlations on the density profile after short TOF that the observed transition is consistent with a BKT-transition to a superfluid phase. The observation of vortices above the critical temperature would be a further important experimental signature.

7 Conclusions and Outlook

For the theoretical analysis of the BCS-BEC crossover in ultracold Fermi gases in 3D and 2D we employed the FRG and DSE. In addition, the 2D setup has also been investigated from the experimental side. A central finding is that the phenomenology of the 2D many-body system is similar to the 3D counterpart, and that the reduction of dimension results in a smooth dimensional crossover. Indeed, the FRG equations can be employed for continuous spatial dimension $3 \geq d \geq 2$ and, although we only considered the limits of $d = 3$ and $d = 2$ here, there is no indication that the qualitative features in the many-body context change for an intermediate critical d_c. Furthermore, the experimental setup in a highly anisotropic trap with aspect ratio $\omega_z/\omega_x \approx 300$ effectively simulates a truly 2D system with the same qualitative features found from the FRG or other theoretical approaches in 2D. We conclude that when going from 3D to 2D we indeed find a smooth dimensional BCS-BEC crossover.

Both system, however, also feature some inherent differences. In the few-body (or vacuum) sector we always find a two-body bound state in 2D. Therefore, the 2D BCS-BEC crossover with crossover parameter $\log(k_\mathrm{F}a)$ can be driven solely by density. In contrast, the resonance condition $a^{-1} = 0$ is located at a vacuum quantum critical point in 3D, and the regimes with positive or negative sign of the crossover parameter $(k_\mathrm{F}a)^{-1}$ cannot be connected by an increase of particle number. In experiment, however, the 2D crossover is driven by a magnetic Feshbach resonance changing the 3D scattering length, which induces an effective 2D scattering length a, and the change of $\log(k_\mathrm{F}a)$ due to density is only weak.

Another important difference of both systems is the nature of the superfluid phase transition. Whereas we have a second order phase transition in 3D with critical exponents in the O(2)-universality class, the transition is of the BKT-type in 2D. As a consequence, the correlation length is infinite below the critical temperature T_c in the latter case and a nonzero anomalous dimension is found for temperatures $0 < T \leq T_\mathrm{c}$. Both features are recovered within the theoretical FRG-framework and they are observed in experiment. Condensation of zero momentum pairs, which is forbidden for the infinitely extended 2D system due to the Mermin–Wagner theorem, can be observed in a finite system. In fact, the condensate fraction only vanishes logarithmically with the system size and is thus always present in an experimental realization. For the interpretation of the experiments discussed in this thesis, the appearance of an enhanced occupation of low momentum modes has been associated with condensation. This allowed us to extract the phase diagram of the 2D BCS-BEC crossover from the momentum distribution.

In order to obtain a quantitatively precise description of the phase structure and the equation of state in the BCS-BEC crossover one has to resolve fluctuation effects which go beyond mean field theory. We have employed the FRG in a variety of truncation and regularization schemes to identify important contributions onto observables such as the phase diagram or the equation of state.

To leading order bosonic fluctuations have impact onto both the effective potential and the boson propagator. These contributions are particularly important to obtain the critical physics, i.e. the correct universality class in 3D, and the BKT physics in 2D. Moreover, bosonic fluctuations are important to resolve the bosonic side of the crossover beyond mean field theory, and to account for the correct zero temperature physics in $d < 3$. In this manner a qualitative picture of the dimensional BCS-BEC crossover can be obtained in the whole parameter range spanned by chemical potential, temperature, scattering length, dimension, and spin-imbalance. Moreover, important quantitative benchmarks such as the critical temperature T_c/μ of the UFG or the LHY-correction and critical temperature on the bosonic side in 3D are accurately resolved within a derivative expansion.

The equation of state, instead, is not resolved in a satisfactory fashion in this truncation scheme. Rather, as we have shown explicitly for 3D, the fermion self-energy receives important fluctuation corrections which significantly increase the density of the system. We have shown that in a purely fermionic picture the boson contribution enters the density through the Tan contact, which is the coefficient of the large momentum part $n_{p\sigma} \sim C/p^4$ of the momentum distribution of fermions in state $|\sigma\rangle$. We derived the RG evolution equation for the scale dependent Tan contact, C_k, which interpolates between $C_\Lambda = 0$ in the UV and $C_0 = C$ in the IR. Again, only on the bosonic side of the crossover the Tan contact is resolved to quantitative precision within the FB_0-truncation.

On the atomic side we observe that the missing Hartree shift of the chemical potential results in the failure to capture the Fermi liquid correction to the equation of state and the Tan contact. In the perturbative limit, the Fermi liquid correction to the equation of state can be obtained easily by integrating the flow equation for the fermion propagator in a way that the direct feedback of the fermion self-energy is neglected. The density is then defined by means of the closed fermion loop. In this way a parametrization of the fermion propagator which includes both Hartree shift and Tan contact should give a reliable account for the equation of state in the perturbative limits.

At unitarity, a running fermion mass term has been included in the FBM_0- and FBM-truncations with the Q-exp regulator. In this case we found a substantial correction of approximately 60% to the effective chemical potential for the UFG. This strong renormalization suggests that a running chemical potential shift needs to be taken into account at resonance. We believe that the combination of such a truncation together with the definition of the density from the closed fermion loop gives a very good account of the whole crossover region to $5 - 10\%$ accuracy. In

first studies we obtained very promising results from this approach to the equation of state.

We moved further towards quantitative precision in the FRG-approach to the BCS-BEC crossover by evolving the effective potential on a grid of field variables. For the spin-balanced 3D system we found a rather good stability of the critical temperature of the UFG as compared to the results obtain within a ϕ^4-expansion of the effective potential. This suggests that the corresponding second order phase transition is well-captured by a Taylor expansion. However, for small enough spin-imbalances such that the transition is still of second order, we found the result for the critical temperature of the UFG within a ϕ^4-expansion to overestimate the one obtained from the full evolution. It will be very interesting to study the behavior of the effective potential in the spin-balanced and -imbalanced 2D BCS-BEC crossover.

The grid-solution for the effective potential allows for the discussion of the impact of spin-imbalance in the BCS-BEC crossover. This additional direction in parameter space introduces qualitatively new aspects to the pairing properties of fermions. Due to the mismatch of (approximate) Fermi spheres, pairing with zero relative momentum and a homogeneous superfluid might be energetically disfavoured. In particular, it is known from BCS theory that the breakdown of superfluidity due to spin-imbalance proceeds by means of a first order phase transition at low temperatures. We have extended the mean field analysis of the spin-imbalanced 3D BCS-BEC crossover by including bosonic fluctuations in the FB_0-truncation. We find the qualitative structure of the mean field phase diagram of the imbalanced UFG to persist after inclusion of fluctuations. However, the location of the phase boundary changes significantly: In the balanced limit we reproduce the substantially lowered critical temperature, whereas the critical spin-imbalance is found to be above the mean-field prediction.

Several exotic phases have been conjectured for spin-imbalanced Fermi gases. Here we studied in detail the stability of the Sarma phase, where the system is a homogeneous, but polarized superfluid. Moreover, the formation of one or two Fermi surfaces in this phase results in gapless excitations of the fermionic excess quasiparticles. Strictly speaking, the Sarma phase is only well-defined for $T = 0$, but the criterion for its existence can be extended for the case of $T > 0$ as well. However, in order to observe the characteristic features of this phase in experiment, sufficiently low temperatures are required. We thus investigated the stability of the Sarma phase at zero temperature in the 3D BCS-BEC crossover beyond the mean-field approximation with the FRG. This analysis was also motivated by studies of a relativistic system where fluctuations induce a stable Sarma phase. We find that for 3D ultracold fermions the Sarma phase at $T = 0$ is only stable on the BEC-side of the crossover, where it appears close to the prediction from mean field theory.

Our analysis constitutes the first study of the quantum phase diagram of the spin-imbalanced 3D BCS-BEC crossover including bosonic fluctuations beyond

mean field theory. Again, the extension to the 2D case will be very interesting. Another promising direction of research consists in computing the properties of the quantum critical point on the BEC-side of the crossover. It is well-known that the FRG is capable of resolving critical phenomena in bosonic systems to high accuracy. Incorporating fluctuation effects onto the fermion self-energy and Feshbach coupling might, however, result in a new universality class beyond the bosonic classification as O(2)-model. Those corrections are gapped for the balanced system, but become important in the Sarma phase. This leads to interesting infrared physics dominated by both bosonic Goldstone modes and gapless fermionic excitations.

By applying the well-understood FB_0-truncation to the 2D BCS-BEC crossover we obtained a qualitative picture of the phase structure and the equation of state of the system. The superfluid transition is consistent with the BKT-mechanism for all values of the 2D scattering length within our truncation. We find a strong dependence of the critical temperature $T_\mathrm{c}/\mu_\mathrm{mb}$ and the zero temperature gap parameter Δ/μ_mb on the infrared scale $k_\mathrm{f} > 0$ at which we stop the flow. Furthermore, the truncations with or without a running of the linear frequency coefficient S_ϕ show significant quantitative changes. However, they also share common features: Both ways to treat the running of S_ϕ result in a logarithmic k_f-dependence of the critical line. The phase boundary plotted as $T_\mathrm{c}/T_\mathrm{F}$ vs. $\log(k_\mathrm{F}a)$ shows two local maxima and a dip at $\log(k_\mathrm{F}a) \approx 0$. Whereas a maximum is expected from extrapolation of the BCS- and BEC-limiting formulas, the additional substructure appears to be an effect of the competition between bosonic (few-body) and fermionic (many-body) features of the system. From improvements of the truncation it will be possible to decide whether these features are physical effects or mere truncation artefacts.

The system size introduces a physical cutoff onto the maximal length of long wavelength fluctuations. In the FRG approach to the BCS-BEC crossover this can be modelled by stopping the RG running at a nonzero infrared scale $k_\mathrm{f} > 0$, which is well below all physical scales of the system due to density, temperature, and scattering length. The dependence of observables computed from the FRG on k_f is a subtle question because it can be either due to physics or due to the truncation. It is know that unphysical infrared scale dependencies appear in the FB_0-truncation when applied to nonrelativistic bosons at zero temperature for $d < 3$. Since we partially recover a bosonic system in d spatial dimensions, the infrared or Goldstone sector is dominated by the same set of flow equations. It is thus important to leverage the ansatz for the effective action to a FB-truncation including the quadratic frequency V_ϕ-term. We have found in computations not presented in this thesis that the inclusion of V_ϕ does indeed remove the unphysical k_f-dependence of the zero temperature gap. However, the infrared scale dependence of the critical temperature persists.

The FB-truncation with q^2-opt regulator violates the nonrelativistic vacuum hierarchy which ensures that the fermion propagator and four-fermion coupling are

not renormalized in vacuum. The same is true for any truncation employing the Q-exp regulator. This is not problematic in the sense that the boson and fermion mass terms can still be fine-tuned to yield the scattering length or binding energy in vacuum. However, the correct result for the dimer propagator coefficients A_ϕ, S_ϕ, and V_ϕ is not recovered for $k \to 0$ in those cases with unphysical vacuum contributions, see Table 6.1. We attribute this to a failure to accurately describe the vacuum even with fine-tuning of the mass terms. This may result in an additional error on the scattering length.

The improper account for the dimer propagator can be seen as a breakdown of the mediation of fermionic vacuum interactions by the s-channel boson. In fact, the u-channel or particle-hole ('box') diagram does not vanish in vacuum for those cases, and thus successively spoils the proper account for fermionic interactions during the flow. With a correct dynamical bosonization procedure during the flow, this contribution can be subtracted at each scale, thereby resulting in a truncation which respects the vacuum hierarchy and resolves the correct dimer propagator. From this point of view, the c_ϕ-dependence of results with the Q-exp regulator can partially be seen as a parametrization of the running of the box diagram. It is very likely that the 2D BCS-BEC crossover at zero temperature can be captured accurately by means of a FB-truncation where the correct vacuum scaling is obtained from dynamical bosonization. It will also be interesting to study the BCS-BEC crossover in continuous dimension.

Besides the theoretical approach to fermion pairing in 3D and 2D we also looked at the 2D system from an experimental perspective. The realization of the 2D BCS-BEC crossover using ^{6}Li by the Jochim group at PI Heidelberg offers many opportunities to investigate the thermodynamics and phase structure of the system. From a new $T/4$-imaging technique it is possible to obtain the momentum distribution in a clean way after expansion in a harmonic potential. This can be understood easily from a classical picture, but has been derived in this thesis with quantum field theoretical techniques as well. From an enhanced occupation of low momentum modes we have defined the condensed phase of the system, which allowed to extract the experimental phase diagram of the 2D BCS-BEC crossover. It agrees well with the expected form on the bosonic side of the resonance and possesses a maximum at $\log(k_\mathrm{F}a) \approx 1$. On the atomic side of the resonance no condensation is observed for $\log(k_\mathrm{F}a) \geq 2$, thus complicating a comparison to theory in this regime. For the measurement of the phase diagram an accurate determination of T, T_F, and a from the experimental data was crucial.

The experimental data immediately opens up several directions of future research. By applying the local density approximation to the in-situ density profiles we can map out the equation of state in the 2D BCS-BEC crossover. The relevant techniques have partially been developed in this thesis for the in-situ thermometry, and thus are ready for application. Of course, this allows for a comparison of FRG-predictions for the phase diagram and the equation of state with experiment. Another interesting question concerns the nature of the quasi-long range

order in the system which can be observed from a power law decay of phase correlations. The latter can be obtained from the Fourier transform of the momentum distribution. Furthermore, the bosonic side of the resonance realizes a strongly coupled Bose gas, and thus facilitates the comparison with results for the momentum distribution of 2D bosons from the FRG. Here we can build on earlier works for purely bosonic systems.

In this thesis we made important steps towards the understanding of fermion pairing in the BCS-BEC crossover in 3D and 2D. Our analysis provides insights into the merits and shortcomings of different FRG-approaches to the system. For the first time, we included the additional parameters of spin-imbalance, $\delta\mu$, and two dimensions, $d = 2$, in the FRG-description of the BCS-BEC crossover. The experimental phase diagram of the balanced 2D BCS-BEC crossover has been extracted in close collaboration with experiment.

Danksagung

An der Entstehung dieser Dissertation waren viele Personen unterstützend beteiligt. Hier nutze ich die Gelegenheit mich dafür zu bedanken.

Großer Dank geht an Christof Wetterich, der diese Arbeit durch zahllose physikalische Beiträge, wertvolle Einsichten und umfangreiche organisatorische Unterstützung ermöglicht hat. Es bereitet mir stets große Freude mit ihm zu diskutieren und seine offene und kreative Herangehensweise an physikalische Probleme ist beeindruckend und immer sehr motivierend zugleich. Ich schätze in großem Maß die Freiräume die er mir für meine Forschung gegeben hat und auch damit den Charakter dieser Arbeit entscheidend geprägt hat.

Ebenso entscheidend dafür war die Zusammenarbeit mit Jan Martin Pawlowski, dem ich an dieser Stelle herzlich für unermüdliche wissenschaftliche und organisatorische Unterstützung danke. Seine physikalischen Erkenntnisse sind immer eine große Bereicherung und an den lebhaften Diskussionen mit ihm beteilige ich mich stets mit Freude. Viele Projekte die zu dieser Arbeit beigetragen haben wurden durch ihn initiiert, wofür ich ihm sehr danke.

Für viele wichtige Beiträge zu dieser Arbeit danke ich Sebastian Diehl. Von seiner Unterstützung und der Zusammenarbeit mit ihm habe ich in allen Stadien meiner Promotion sehr profitiert und daraus viele wertvolle physikalische Einsichten gewonnen. Insbesondere danke ich ihm herzlich für die Möglichkeit drei Monate in Innsbruck mit ihm und seiner Gruppe in einem interessanten Umfeld zu arbeiten.

Für die freundliche Übernahme der Zweitbegutachtung und sein Interesse an der Arbeit bedanke ich mich bei Manfred Salmhofer. Es war für mich ein großer Gewinn am Meeting des FOR 723 in Wien, 2014, teilzunehmen. Für die Organisation des Treffens und die Möglichkeit dort meine Arbeit vorstellen zu können danke ich ihm und Sabine Andergassen herzlich.

Die Arbeit am ITP Heidelberg schätze ich sowohl vom wissenschaftlichen als auch menschlichen Standpunkt sehr. Entscheidend zu diesem angenehmen Arbeitsklima tragen Eduard Thommes, die Damen des Sekretariats, Werner Wetzel und Elmar Bittner bei, deren kompetente Hilfe bei organisatorischen Problemen, aber auch aufopferungsvollen Beiträge im Hintergrund unersetzlich sind. Dafür bedanke ich mich an dieser Stelle sehr bei ihnen.

Das einmalige Forschungsumfeld am ITP resultiert zudem zum großen Teil aus der Begeisterung seiner Mitglieder. Für erkenntnisreiche und unterhaltsame Diskussionen danke ich hier herzlich meinen Kollegen Conrad Albrecht, Youness Ayaita, Joschka Beyer, Nicolai Christiansen, Laura Classen, Tilman Enss, Leonard Fister, Simon Friederich, Lisa Marie Haas, Michael Haas, Tina Katharina Herbst, Naseemuddin Khan, Sören Lammers, Mario Mitter, Sergej Moroz, Dorival Goncalves Netto, Timo Reckling, Fabian Rennecke, Andreas Rodigast, Michael Scherer, David Schnoerr, Nils Strodthoff, Daniel Spielmann, Maik Weber und Sebastian Wetzel.

Für sehr interessante Zusammenarbeit und Einblicke in die experimentelle Perspektive auf ultrakalte Atome bedanke ich mich herzlich bei Selim Jochim und seiner Arbeitsgruppe, d.h. Luca Bayha, Andrea Bergschneider, Dhruv Kedar, Vincent Klinkhamer, Thomas Lompe, Simon Murmann, Puneet Murthy, Mathias Neidig, Martin Ries, Andre Wenz und Gerhard Zürn. Aus unseren oft langen Diskussionen habe ich viele neue Erkenntnisse gewonnen, die auch wesentlich meine theoretische Arbeit beeinflusst haben. Ich freue mich sehr auf die weitere Zusammenarbeit an nachfolgenden Projekten. Inbesondere danke ich Martin Ries für hilfreiche Kommentare zum experimentellen Teil dieser Dissertation.

Während meiner Promotion hatte ich das Glück mit zahlreichen Physikern außerhalb Heidelbergs zu forschen. Für interessante und wertvolle Zusammenarbeit danke ich hier herzlich Jens Braun, Michael Buchhold, Liang He, Stefan Floerchinger, Jamir Marino, Dietrich Roscher, Lukas Sieberer und Lorenz von Smekal.

Für finanzielle Unterstützung bedanke ich mich bei der Landesgraduiertenförderung Baden-Württemberg, der Heidelberg Graduate School for Fundamental Physics, der Helmholtz Alliance HA216/EMMI, der DFG Forschergruppe FOR 723 und dem ERC Advanced Grant No. 290623.

Meinen Eltern Albrecht und Sylvia Böttcher, sowie Eva und Tim Friebertshäuser danke ich herzlich für ihre Unterstützung in allen Belangen während meiner Promotion.

Bibliography

Alford, M. G., Schmitt, A., Rajagopal, K., and Schäfer, T. (2008). Color superconductivity in dense quark matter. *Rev.Mod.Phys.*, 80:1455–1515.

Altland, A. and Simons, B. (2010). *Condensed Matter Field Theory*. Cambridge University Press.

Anderson, E. R., Bogner, S. K., Furnstahl, R. J., and Perry, R. J. (2010). Operator evolution via the similarity renormalization group: The deuteron. *Phys. Rev. C*, 82:054001.

Anderson, M. H., Ensher, J. R., Matthews, M. R., Wieman, C. E., and Cornell, E. A. (1995). Observation of Bose-Einstein Condensation in a Dilute Atomic Vapor. *Science*, 269(5221):198–201.

Andrews, M. R., Townsend, C. G., Miesner, H.-J., Durfee, D. S., Kurn, D. M., and Ketterle, W. (1997). Observation of Interference Between Two Bose Condensates. *Science*, 275(5300):637–641.

Banerjee, D., Bögli, M., Dalmonte, M., Rico, E., Stebler, P., Wiese, U.-J., and Zoller, P. (2013). Atomic Quantum Simulation of U(N) and SU(N) Non-Abelian Lattice Gauge Theories. *Phys. Rev. Lett.*, 110:125303.

Baranov, M. A. (2008). Theoretical progress in many-body physics with ultracold dipolar gases. *Physics Reports*, 464:71–111.

Baranov, M. A., Dalmonte, M., Pupillo, G., and Zoller, P. (2012). Condensed Matter Theory of Dipolar Quantum Gases. *Chemical Reviews*, 112(9):5012–5061.

Barth, M. and Zwerger, W. (2011). Tan relations in one dimension. *Annals of Physics*, 326(10):2544 – 2565.

Bartosch, L., Kopietz, P., and Ferraz, A. (2009). Renormalization of the BCS-BEC crossover by order-parameter fluctuations. *Phys. Rev. B*, 80:104514.

Bauer, M., Parish, M. M., and Enss, T. (2014). Universal Equation of State and Pseudogap in the Two-Dimensional Fermi Gas. *Phys. Rev. Lett.*, 112:135302.

Bedaque, P. F., Caldas, H., and Rupak, G. (2003). Phase Separation in Asymmetrical Fermion Superfluids. *Phys. Rev. Lett.*, 91:247002.

Benitez, F., Blaizot, J.-P., Chaté, H., Delamotte, B., Méndez-Galain, R., and Wschebor, N. (2012). Nonperturbative renormalization group preserving full-momentum dependence: Implementation and quantitative evaluation. *Phys. Rev. E*, 85:026707.

Berezinskii, V. L. (1972). Destruction of Long-range Order in One-dimensional and Two-dimensional Systems Possessing a Continuous Symmetry Group. II. Quantum Systems. *Soviet Journal of Experimental and Theoretical Physics*, 34:610.

Berges, J., Borsányi, S., and Wetterich, C. (2004). Prethermalization. *Phys. Rev. Lett.*, 93:142002.

Berges, J., Tetradis, N., and Wetterich, C. (2002). Nonperturbative renormalization flow in quantum field theory and statistical physics. *Phys.Rept.*, 363:223–386.

Bertaina, G. and Giorgini, S. (2011). BCS-BEC Crossover in a Two-Dimensional Fermi Gas. *Phys. Rev. Lett.*, 106:110403.

Birse, M. C., Krippa, B., McGovern, J. A., and Walet, N. R. (2005). Pairing in many-fermion systems: an exact renormalisation group treatment. *Physics Letters B*, 605(3-4):287 – 294.

Birse, M. C., Krippa, B., and Walet, N. R. (2011). Convergence of a renormalization-group approach to dimer-dimer scattering. *Phys. Rev. A*, 83:023621.

Bloch, I., Dalibard, J., and Zwerger, W. (2008). Many-body physics with ultracold gases. *Rev. Mod. Phys.*, 80:885–964.

Boettcher, I., Braun, J., Herbst, T., Pawlowski, J., Roscher, D., and Wetterich, C. (2014a). Phase structure of spin-imbalanced unitary Fermi gases. *e-print arXiv:1409.5070*.

Boettcher, I., Diehl, S., Pawlowski, J. M., and Wetterich, C. (2013). Tan contact and universal high momentum behavior of the fermion propagator in the BCS-BEC crossover. *Phys. Rev. A*, 87:023606.

Boettcher, I., Herbst, T., Pawlowski, J., Strodthoff, N., von Smekal, L., and Wetterich, C. (2014b). Sarma phase in relativistic and non-relativistic systems. *e-print arXiv:1409.5232*.

Boettcher, I., Pawlowski, J. M., and Diehl, S. (2012). Ultracold atoms and the Functional Renormalization Group. *Nuclear Physics B - Proceedings Supplements*, 228(0):63 – 135.

Boettcher, I., Pawlowski, J. M., and Wetterich, C. (2014c). Critical temperature and superfluid gap of the unitary Fermi gas from functional renormalization. *Phys. Rev. A*, 89:053630.

Bogner, S. K. and Roscher, D. (2012). High-momentum tails from low-momentum effective theories. *Phys. Rev. C*, 86:064304.

Braaten, E. (2012). Universal Relations for Fermions with Large Scattering Length. *Lect.Notes Phys.*, 836:193–231.

Braaten, E. and Hammer, H.-W. (2006). Universality in few-body systems with large scattering length. *Phys.Rept.*, 428:259–390.

Braaten, E., Kang, D., and Platter, L. (2008). Exact Relations for a Strongly-interacting Fermi Gas near a Feshbach Resonance. *Phys. Rev. A*, 78:053606.

Braaten, E. and Platter, L. (2008). Exact Relations for a Strongly Interacting Fermi Gas from the Operator Product Expansion. *Phys. Rev. Lett.*, 100:205301.

Braun, J., Diehl, S., and Scherer, M. M. (2011). Finite-size and particle-number effects in an ultracold Fermi gas at unitarity. *Phys. Rev. A*, 84(6):063616.

Braun, J., Drut, J. E., Jahn, T., Pospiech, M., and Roscher, D. (2014). Phases of spin- and mass-imbalanced ultracold Fermi gases in harmonic traps. *Phys. Rev. A*, 89:053613.

Braun, J., Klein, B., and Pirner, H. (2005). Influence of quark boundary conditions on the pion mass in finite volume. *Phys. Rev.*, D72:034017.

Braun, J., Klein, B., and Schaefer, B.-J. (2012). On the Phase Structure of QCD in a Finite Volume. *Phys. Lett.*, B713:216–223.

Braun, J. and Roscher, D. (in prep. 2014). The Unitary Fermi Gas with spin- and mass-imbalance.

Bulgac, A., Drut, J. E., and Magierski, P. (2008). Quantum Monte Carlo simulations of the BCS-BEC crossover at finite temperature. *Phys. Rev. A*, 78:023625.

Bulgac, A. and Forbes, M. M. (2007). Zero-temperature thermodynamics of asymmetric Fermi gases at unitarity. *Phys. Rev. A*, 75:031605.

Burovski, E., Prokof'ev, N., Svistunov, B., and Troyer, M. (2006). Critical Temperature and Thermodynamics of Attractive Fermions at Unitarity. *Phys. Rev. Lett.*, 96:160402.

Calabrese, P. and Cardy, J. (2006). Time Dependence of Correlation Functions Following a Quantum Quench. *Phys. Rev. Lett.*, 96:136801.

Canet, L., Chaté, H., Delamotte, B., and Wschebor, N. (2010). Nonperturbative Renormalization Group for the Kardar-Parisi-Zhang Equation. *Phys. Rev. Lett.*, 104:150601.

Canet, L., Chaté, H., Delamotte, B., and Wschebor, N. (2011). Nonperturbative renormalization group for the Kardar-Parisi-Zhang equation: General framework and first applications. *Phys. Rev. E*, 84:061128.

Canet, L., Delamotte, B., Mouhanna, D., and Vidal, J. (2003). Optimization of the derivative expansion in the nonperturbative renormalization group. *Phys. Rev. D*, 67:065004.

Carlson, J., Chang, S.-Y., Pandharipande, V. R., and Schmidt, K. E. (2003). Superfluid Fermi Gases with Large Scattering Length. *Phys. Rev. Lett.*, 91:050401.

Carlson, J., Gandolfi, S., Schmidt, K. E., and Zhang, S. (2011). Auxiliary-field quantum Monte Carlo method for strongly paired fermions. *Phys. Rev. A*, 84:061602.

Carlson, J. and Reddy, S. (2005). Asymmetric Two-Component Fermion Systems in Strong Coupling. *Phys. Rev. Lett.*, 95:060401.

Carlson, J. and Reddy, S. (2008). Superfluid Pairing Gap in Strong Coupling. *Phys. Rev. Lett.*, 100:150403.

Carr, L. D. and Ye, J. (2009). Focus on Cold and Ultracold Molecules. *New Journal of Physics*, 11(5):055009.

Celi, A., Massignan, P., Ruseckas, J., Goldman, N., Spielman, I. B., Juzeliunas, G., and Lewenstein, M. (2014). Synthetic Gauge Fields in Synthetic Dimensions. *Phys. Rev. Lett.*, 112:043001.

Chandrasekhar, B. S. (1962). A note on the maximum critical field of high field superconductors. *Applied Physics Letters*, 1(1).

Chevy, F. (2006). Universal phase diagram of a strongly interacting Fermi gas with unbalanced spin populations. *Phys. Rev. A*, 74:063628.

Chin, C., Grimm, R., Julienne, P., and Tiesinga, E. (2010). Feshbach resonances in ultracold gases. *Rev. Mod. Phys.*, 82:1225–1286.

Clogston, A. M. (1962). Upper Limit for the Critical Field in Hard Superconductors. *Phys. Rev. Lett.*, 9:266–267.

Cramer, M., Dawson, C. M., Eisert, J., and Osborne, T. J. (2008). Exact Relaxation in a Class of Nonequilibrium Quantum Lattice Systems. *Phys. Rev. Lett.*, 100:030602.

Daley, A. J. (2011). Quantum Computing and Quantum Simulation with Group-II Atoms. *Quantum Information Processing*, 10:865–884.

Dalfovo, F., Giorgini, S., Pitaevskii, L. P., and Stringari, S. (1999). Theory of Bose-Einstein condensation in trapped gases. *Rev. Mod. Phys.*, 71:463–512.

Dalla Torre, E. G., Demler, E., Giamarchi, T., and Altman, E. (2010). Quantum critical states and phase transitions in the presence of non equilibrium noise. *Nature Physics*, 6:806.

Davis, K. B., Mewes, M. O., Andrews, M. R., van Druten, N. J., Durfee, D. S., Kurn, D. M., and Ketterle, W. (1995). Bose-Einstein Condensation in a Gas of Sodium Atoms. *Phys. Rev. Lett.*, 75:3969–3973.

Dean, D. J. and Hjorth-Jensen, M. (2003). Pairing in nuclear systems: from neutron stars to finite nuclei. *Rev. Mod. Phys.*, 75:607–656.

Delamotte, B. (2012). An Introduction to the nonperturbative renormalization group. *Lect.Notes Phys.*, 852:49–132.

Diehl, S., Floerchinger, S., Gies, H., Pawlowkski, J., and Wetterich, C. (2010a). Functional renormalization group approach to the BCS-BEC crossover. *Annalen der Physik*, 522(9):615–656.

Diehl, S., Gies, H., Pawlowski, J. M., and Wetterich, C. (2007a). Flow equations for the BCS-BEC crossover. *Phys. Rev. A*, 76:021602.

Diehl, S., Gies, H., Pawlowski, J. M., and Wetterich, C. (2007b). Renormalization flow and universality for ultracold fermionic atoms. *Phys. Rev. A*, 76:053627.

Diehl, S., Krahl, H. C., and Scherer, M. (2008a). Three-body scattering from nonperturbative flow equations. *Phys. Rev. C*, 78:034001.

Diehl, S., Micheli, A., Kantian, A., Kraus, B., Büchler, H., and Zoller, P. (2008b). Quantum states and phases in driven open quantum systems with cold atoms. *Nature Physics*, 4:878.

Diehl, S., Tomadin, A., Micheli, A., Fazio, R., and Zoller, P. (2010b). Dynamical Phase Transitions and Instabilities in Open Atomic Many-Body Systems. *Phys. Rev. Lett.*, 105:015702.

Diehl, S. and Wetterich, C. (2006). Universality in phase transitions for ultracold fermionic atoms. *Phys. Rev. A*, 73:033615.

Diehl, S. and Wetterich, C. (2007). Functional integral for ultracold fermionic atoms. *Nuclear Physics B*, 770(3):206 – 272.

Drechsler, M. and Zwerger, W. (1992). Crossover from BCS-superconductivity to Bose-condensation. *Annalen der Physik*, 504(1):15–23.

Drut, J. E., Lähde, T. A., and Ten, T. (2011). Momentum Distribution and Contact of the Unitary Fermi Gas. *Phys. Rev. Lett.*, 106:205302.

Dupuis, N. (2009a). Infrared behavior and spectral function of a Bose superfluid at zero temperature. *Phys. Rev. A*, 80:043627.

Dupuis, N. (2009b). Unified Picture of Superfluidity: From Bogoliubov's Approximation to Popov's Hydrodynamic Theory. *Phys. Rev. Lett.*, 102:190401.

Eagles, D. M. (1969). Possible Pairing without Superconductivity at Low Carrier Concentrations in Bulk and Thin-Film Superconducting Semiconductors. *Phys. Rev.*, 186:456–463.

Efimov, V. (1970). Energy levels arising form the resonant two-body forces in a three-body system. *Phys.Lett.*, B33:563–564.

Efimov, V. (1973). Energy levels of three resonantly interacting particles. *Nuclear Physics A*, 210(1):157 – 188.

Engelbrecht, J. R. and Randeria, M. (1990). New collective mode and corrections to fermi-liquid theory in two dimensions. *Phys. Rev. Lett.*, 65:1032–1035.

Engelbrecht, J. R. and Randeria, M. (1992). Low-density repulsive fermi gas in two dimensions: Bound-pair excitations and fermi-liquid behavior. *Phys. Rev. B*, 45:12419–12434.

Enss, T., Haussmann, R., and Zwerger, W. (2011). Viscosity and scale invariance in the unitary Fermi gas. *Annals of Physics*, 326(3):770 – 796.

Ferlaino, F., Zenesini, A., Berninger, M., Huang, B., Nägerl, H., and Grimm, R. (2011). Efimov Resonances in Ultracold Quantum Gases. *Few-Body Systems*, 51:113–133.

Feynman, R. (1982). Simulating physics with computers. *Int. J. Theor. Phys.*, 21:467.

Fischer, A. M. and Parish, M. M. (2014). Quasi-two-dimensional Fermi gases at finite temperature. *e-print arXiv:1408.0476*.

Fister, L. and Pawlowski, J. M. (2011). Yang-Mills correlation functions at finite temperature. *e-print arXiv:1112.5440*.

Floerchinger, S. (2012). Analytic Continuation of Functional Renormalization Group Equations. *JHEP*, 1205:021.

Floerchinger, S. (2014). Few-body hierarchy in non-relativistic functional renormalization group equations and a decoupling theorem. *Nuclear Physics A*, 927:119–133.

Floerchinger, S., Scherer, M., Diehl, S., and Wetterich, C. (2008). Particle-hole fluctuations in BCS-BEC crossover. *Phys. Rev. B*, 78:174528.

Floerchinger, S., Scherer, M. M., and Wetterich, C. (2010). Modified Fermi sphere, pairing gap, and critical temperature for the BCS-BEC crossover. *Phys. Rev. A*, 81:063619.

Floerchinger, S. and Wetterich, C. (2008). Functional renormalization for Bose-Einstein Condensation. *Phys.Rev.*, A77:053603.

Fölling, S., Widera, A., Müller, T., Gerbier, F., and Bloch, I. (2006). Formation of Spatial Shell Structure in the Superfluid to Mott Insulator Transition. *Phys. Rev. Lett.*, 97:060403.

Fröhlich, J. and Spencer, T. (1981). The Kosterlitz-Thouless transition in two-dimensional abelian spin systems and the Coulomb gas. *Communications in Mathematical Physics*, 81(4):527–602.

Fulde, P. and Ferrell, R. A. (1964). Superconductivity in a Strong Spin-Exchange Field. *Phys. Rev.*, 135:A550–A563.

Gasenzer, T., Berges, J., Schmidt, M. G., and Seco, M. (2005). Nonperturbative dynamical many-body theory of a Bose-Einstein condensate. *Phys. Rev. A*, 72:063604.

Gersdorff, G. v. and Wetterich, C. (2001). Nonperturbative renormalization flow and essential scaling for the Kosterlitz-Thouless transition. *Phys. Rev. B*, 64:054513.

Gezerlis, A., Pethick, C., and Schwenk, A. (2014). Pairing and superfluidity of nucleons in neutron stars. *e-print arXiv:1406.6109*.

Gies, H. (2012). Introduction to the functional RG and applications to gauge theories. *Lect.Notes Phys.*, 852:287–348.

Giorgini, S., Pitaevskii, L. P., and Stringari, S. (2008). Theory of ultracold atomic Fermi gases. *Rev. Mod. Phys.*, 80:1215–1274.

Goldman, N., Juzeliunas, G., Ohberg, P., and Spielman, I. B. (2013). Light-induced gauge fields for ultracold atoms. *e-print arXiv:1308.6533*.

Goldstone, J. (1961). Field theories with Superconductor solutions. *Il Nuovo Cimento*, 19(1):154–164.

Gorshkov, A. V., Hermele, M., Gurarie, V., Xu, C., Julienne, P. S., Ye, J., Zoller, P., Demler, E., Lukin, M. D., and Rey, A. M. (2010). Two-orbital SU(N) magnetism with ultracold alkaline-earth atoms. *Nature Physics*, 6:289–295.

Goulko, O. and Wingate, M. (2010). Thermodynamics of balanced and slightly spin-imbalanced Fermi gases at unitarity. *Phys. Rev. A*, 82:053621.

Gräter, M. and Wetterich, C. (1995). Kosterlitz-Thouless Phase Transition in the Two Dimensional Linear Sigma Model. *Phys. Rev. Lett.*, 75:378–381.

Greiner, M., Mandel, O., Hänsch, T. W., and Bloch, I. (2002). Collapse and revival of the matter wave field of a Bose-Einstein condensate. *Nature*, 419:51–54.

Grimm, R., Weidemüller, M., and Ovchinnikov, Y. B. (2000). Optical Dipole Traps for Neutral Atoms. *Advances in Atomic Molecular and Optical Physics*, 42:95–170.

Gubbels, K., Romans, M., and Stoof, H. (2006). Sarma Phase in Trapped Unbalanced Fermi Gases. *Phys.Rev.Lett.*, 97:210402.

Gubbels, K. and Stoof, H. (2013). Imbalanced Fermi gases at unitarity. *Phys.Rept.*, 525:255–313.

Gubbels, K. B. and Stoof, H. T. C. (2008). Renormalization Group Theory for the Imbalanced Fermi Gas. *Phys. Rev. Lett.*, 100:140407.

Gupta, S., Hadzibabic, Z., Zwierlein, M. W., Stan, C. A., Dieckmann, K., Schunck, C. H., van Kempen, E. G. M., Verhaar, B. J., and Ketterle, W. (2003). Radio-Frequency Spectroscopy of Ultracold Fermions. *Science*, 300(5626):1723–1726.

Gurarie, V. and Radzihovsky, L. (2007). Resonantly paired fermionic superfluids. *Annals of Physics*, 322(1):2 – 119. January Special Issue 2007.

Haussmann, R. (1993). Crossover from BCS superconductivity to Bose-Einstein condensation: A self-consistent theory. *Z. Phys. B*, 91:291–308.

Haussmann, R. (1994). Properties of a Fermi liquid at the superfluid transition in the crossover region between BCS superconductivity and Bose-Einstein condensation. *Phys. Rev. B*, 49:12975–12983.

Haussmann, R., Rantner, W., Cerrito, S., and Zwerger, W. (2007). Thermodynamics of the BCS-BEC crossover. *Phys. Rev. A*, 75:023610.

Ho, T.-L. (2004). Universal Thermodynamics of Degenerate Quantum Gases in the Unitarity Limit. *Phys. Rev. Lett.*, 92:090402.

Ho, T.-L. and Zhou, Q. (2010). Obtaining the phase diagram and thermodynamic quantities of bulk systems from the densities of trapped gases. *Nature Physics*, 6:131–134.

Hofferberth, S., Lesanovsky, I., Fischer, B., Schumm, T., and Schmiedmayer, J. (2007). Non-equilibrium coherence dynamics in one-dimensional Bose gases. *Nature*, 449:324–327.

Hohenberg, P. C. (1967). Existence of Long-Range Order in One and Two Dimensions. *Phys. Rev.*, 158:383–386.

Holland, M., Kokkelmans, S. J. J. M. F., Chiofalo, M. L., and Walser, R. (2001). Resonance Superfluidity in a Quantum Degenerate Fermi Gas. *Phys. Rev. Lett.*, 87:120406.

Horikoshi, M., Nakajima, S., Ueda, M., and Mukaiyama, T. (2010). Measurement of Universal Thermodynamic Functions for a Unitary Fermi Gas. *Science*, 327(5964):442–445.

Hu, H., Liu, X.-J., and Drummond, P. D. (2010). Static structure factor of a strongly correlated Fermi gas at large momenta. *Europhysics Letters*, 91(2):20005.

Hu, H., Liu, X.-J., and Drummond, P. D. (2011). Universal contact of strongly interacting fermions at finite temperatures. *New Journal of Physics*, 13(3):035007.

Husemann, C., Giering, K.-U., and Salmhofer, M. (2012). Frequency-dependent vertex functions of the (t,t') Hubbard model at weak coupling. *Phys. Rev. B*, 85:075121.

Iskin, M. and de Melo, C. A. R. S. (2009). Evolution from BCS to Berezinskii-Kosterlitz-Thouless Superfluidity in One-Dimensional Optical Lattices. *Phys. Rev. Lett.*, 103:165301.

Jaksch, D. and Zoller, P. (2005). The cold atom Hubbard toolbox. *Annals of Physics*, 315(1):52 – 79. Special Issue.

Jakubczyk, P., Dupuis, N., and Delamotte, B. (2014). Revisiting the nonperturbative renormalization-group approach to the Kosterlitz-Thouless transition. *e-print arXiv:1409.1374*.

Jakubczyk, P., Metzner, W., and Yamase, H. (2009). Turning a First Order Quantum Phase Transition Continuous by Fluctuations: General Flow Equations and Application to d-Wave Pomeranchuk Instability. *Phys. Rev. Lett.*, 103:220602.

José, J. V., Kadanoff, L. P., Kirkpatrick, S., and Nelson, D. R. (1977). Renormalization, vortices, and symmetry-breaking perturbations in the two-dimensional planar model. *Phys. Rev. B*, 16:1217–1241.

Kadanoff, L. P. (1966). Scaling Laws For Ising Models Near T(c). *Physics*, 2:263.

Kamikado, K., Strodthoff, N., von Smekal, L., and Wambach, J. (2013). Fluctuations in the quark-meson model for QCD with isospin chemical potential. *Phys.Lett.*, B718:1044–1053.

Ketterle, W., Durfee, D., and Stamper-Kurn, D. (1999). Making, probing and understanding Bose-Einstein condensates. *Proceedings of the International School of Physics "Enrico Fermi", Course CXL, edited by M. Inguscio, S. Stringari and C.E. Wieman*, pages 67–176.

Kloss, T., Canet, L., and Wschebor, N. (2012). Nonperturbative renormalization group for the stationary Kardar-Parisi-Zhang equation: Scaling functions and amplitude ratios in 1+1, 2+1, and 3+1 dimensions. *Phys. Rev. E*, 86:051124.

Kohstall, C., Zaccanti, M., Jag, M., Trenkwalder, A., Massignan, P., Bruun, G. M., Schreck, F., and Grimm, R. (2012). Metastability and coherence of repulsive polarons in a strongly interacting Fermi mixture. *Nature*, 485:615–618.

Kollath, C., Läuchli, A. M., and Altman, E. (2007). Quench Dynamics and Nonequilibrium Phase Diagram of the Bose-Hubbard Model. *Phys. Rev. Lett.*, 98:180601.

Kopietz, P., Bartosch, L., and Schütz, F. (2010). *Introduction to the Functional Renormalization Group*. Springer, Berlin.

Kosterlitz, J. and Thouless, D. (1973). Ordering, metastability and phase transitions in two-dimensional systems. *J.Phys.*, C6:1181–1203.

Krahl, H. and Wetterich, C. (2007). Functional renormalization group for d-wave superconductivity in Hubbard type models. *Phys.Lett.*, A367:263–267.

Krahl, H. C., Friederich, S., and Wetterich, C. (2009). Incommensurate antiferromagnetic fluctuations in the two-dimensional Hubbard model. *Phys. Rev. B*, 80:014436.

Krippa, B., Walet, N. R., and Birse, M. C. (2010). Renormalization group, dimer-dimer scattering, and three-body forces. *Phys. Rev. A*, 81:043628.

Krüger, T., Hebeler, K., and Schwenk, A. (2014). To which densities is spin-polarized neutron matter a weakly interacting Fermi gas? *e-print arXiv:1408.4168*.

Ku, M. J. H., Sommer, A. T., Cheuk, L. W., and Zwierlein, M. W. (2012). Revealing the Superfluid Lambda Transition in the Universal Thermodynamics of a Unitary Fermi Gas. *Science*, 335(6068):563–567.

Kuhnle, E. D., Hoinka, S., Dyke, P., Hu, H., Hannaford, P., and Vale, C. J. (2011). Temperature Dependence of the Universal Contact Parameter in a Unitary Fermi Gas. *Phys. Rev. Lett.*, 106:170402.

Kuhnle, E. D., Hu, H., Liu, X.-J., Dyke, P., Mark, M., Drummond, P. D., Hannaford, P., and Vale, C. J. (2010). Universal Behavior of Pair Correlations in a Strongly Interacting Fermi Gas. *Phys. Rev. Lett.*, 105:070402.

Larkin, A. and Ovchinnikov, Y. (1964). Nonuniform state of superconductors. *Zh.Eksp.Teor.Fiz.*, 47:1136–1146.

Latorre, J. I. and Morris, T. R. (2000). Exact scheme independence. *Journal of High Energy Physics*, 2000(11):004.

Lee, T. D., Huang, K., and Yang, C. N. (1957). Eigenvalues and Eigenfunctions of a Bose System of Hard Spheres and Its Low-Temperature Properties. *Phys. Rev.*, 106:1135–1145.

Lee, T. D. and Yang, C. N. (1958). Low-Temperature Behavior of a Dilute Bose System of Hard Spheres. I. Equilibrium Properties. *Phys. Rev.*, 112:1419–1429.

Leggett, A. (1980). Diatomic Molecules and Cooper Pairs. *in* Modern Trends in the Theory of Condensed Matter*, edited by by A. Pekalski and R. Przystawa (Springer-Verlag, Berlin)*, 115:13.

Levinsen, J. and Parish, M. M. (2014). Strongly interacting two-dimensional Fermi gases. *e-print arXiv:1408.2737*.

Lewenstein, M., Sanpera, A., Ahufinger, V., Damski, B., De, A. S., and Sen, U. (2006). Ultracold atomic gases in optical lattices: mimicking condensed matter physics and beyond. *Advances in Physics*, 56:135.

Liao, S.-B., Polonyi, J., and Strickland, M. (2000). Optimization of renormalization group flow. *Nuclear Physics B*, 567(3):493 – 514.

Litim, D. F. (2000). Optimization of the exact renormalization group. *Phys. Lett.*, B486:92–99.

Litim, D. F. (2001a). Mind the gap. *Int. J. Mod. Phys.*, A16:2081–2088.

Litim, D. F. (2001b). Optimised renormalisation group flows. *Phys. Rev.*, D64:105007.

Litim, D. F. (2002). Critical exponents from optimized renormalization group flows. *Nucl.Phys.*, B631:128–158.

Litim, D. F. and Pawlowski, J. M. (2002). Completeness and consistency of renormalisation group flows. *Phys. Rev.*, D66:025030.

Litim, D. F. and Pawlowski, J. M. (2006). Non-perturbative thermal flows and resummations. *JHEP*, 0611:026.

Litim, D. F., Pawlowski, J. M., and Vergara, L. (2006). Convexity of the effective action from functional flows. *e-print arXiv:hep-th/0602140*.

Liu, W. V. and Wilczek, F. (2003). Interior Gap Superfluidity. *Phys. Rev. Lett.*, 90:047002.

Liu, W. V., Wilczek, F., and Zoller, P. (2004). Spin-dependent Hubbard model and a quantum phase transition in cold atoms. *Phys. Rev. A*, 70:033603.

Lobo, C., Recati, A., Giorgini, S., and Stringari, S. (2006). Normal State of a Polarized Fermi Gas at Unitarity. *Phys. Rev. Lett.*, 97:200403.

Loktev, V. M., Quick, R. M., and Sharapov, S. G. (2001). Phase fluctuations and pseudogap phenomena. *Physics Reports*, 349(1):1 – 123.

Lombardo, U. and Schulze, H. (2001). Superfluidity in neutron star matter. *Lect.Notes Phys.*, 578:30–53.

Makhalov, V., Martiyanov, K., and Turlapov, A. (2014). Ground-State Pressure of Quasi-2D Fermi and Bose Gases. *Phys. Rev. Lett.*, 112:045301.

Mermin, N. D. and Wagner, H. (1966). Absence of Ferromagnetism or Antiferromagnetism in One- or Two-Dimensional Isotropic Heisenberg Models. *Phys. Rev. Lett.*, 17:1133–1136.

Metzner, W., Salmhofer, M., Honerkamp, C., Meden, V., and Schönhammer, K. (2012). Functional renormalization group approach to correlated fermion systems. *Rev. Mod. Phys.*, 84:299–352.

Morgan, S. A., Lee, M. D., and Burnett, K. (2002). Off-shell T matrices in one, two, and three dimensions. *Phys. Rev. A*, 65:022706.

Murthy, P. A., Kedar, D., Lompe, T., Neidig, M., Ries, M. G., Wenz, A. N., Zürn, G., and Jochim, S. (2014). Matter wave Fourier optics with a strongly interacting two-dimensional Fermi gas. *e-print arXiv:1408.4680*.

Nambu, Y. (1960). Quasi-Particles and Gauge Invariance in the Theory of Superconductivity. *Phys. Rev.*, 117:648–663.

Nascimbène, S., Navon, N., Jiang, K. J., Chevy, F., and Salomon, C. (2010). Exploring the thermodynamics of a universal Fermi gas. *Nature*, 463:1057–1060.

Navon, N., Nascimbène, S., Chevy, F., and Salomon, C. (2010). The Equation of State of a Low-Temperature Fermi Gas with Tunable Interactions. *Science*, 328(5979):729–732.

Navon, N., Nascimbène, S., Leyronas, X., Chevy, F., and Salomon, C. (2013). Condensation energy of a spin-1/2 strongly interacting Fermi gas. *Phys. Rev. A*, 88:063614.

Negele, J. W. and Orland, H. (1998). *Quantum Many-Particle Systems*. Westview Press.

Nikolić, P. and Sachdev, S. (2007). Renormalization-group fixed points, universal phase diagram, and 1/N expansion for quantum liquids with interactions near the unitarity limit. *Phys. Rev. A*, 75:033608.

Nishida, Y. (2012). Probing strongly interacting atomic gases with energetic atoms. *Phys. Rev. A*, 85:053643.

Nussinov, Z. and Nussinov, S. (2006). Triviality of the BCS-BEC crossover in extended dimensions: Implications for the ground state energy. *Phys. Rev. A*, 74:053622.

Page, D., Lattimer, J. M., Prakash, M., and Steiner, A. W. (2013). Stellar Superfluids. *e-print arXiv:1302.6626*.

Palestini, F., Perali, A., Pieri, P., and Strinati, G. C. (2010). Temperature and coupling dependence of the universal contact intensity for an ultracold Fermi gas. *Phys. Rev. A*, 82:021605.

Parish, M. M., Marchetti, F. M., Lamacraft, A., and Simons, B. D. (2007). Finite-temperature phase diagram of a polarized Fermi condensate. *Nature Physics*, 3:124–128.

Parish, M. M., Marchetti, F. M., Lamacraft, A., and Simons, B. D. (2007). Polarized Fermi Condensates with Unequal Masses: Tuning the Tricritical Point. *Phys. Rev. Lett.*, 98:160402.

Partridge, G. B., Strecker, K. E., Kamar, R. I., Jack, M. W., and Hulet, R. G. (2005). Molecular Probe of Pairing in the BEC-BCS Crossover. *Phys. Rev. Lett.*, 95:020404.

Pawlowski, J. M. (2007). Aspects of the functional renormalisation group. *Annals Phys.*, 322:2831–2915.

Pethick, C. J. and Smith, H. (2002). *Bose-Einstein Condensation in Dilute Gases*. Cambridge University Press.

Petrov, D. S., Baranov, M. A., and Shlyapnikov, G. V. (2003). Superfluid transition in quasi-two-dimensional Fermi gases. *Phys. Rev. A*, 67:031601.

Petrov, D. S., Salomon, C., and Shlyapnikov, G. V. (2004). Weakly Bound Dimers of Fermionic Atoms. *Phys. Rev. Lett.*, 93:090404.

Petrov, D. S. and Shlyapnikov, G. V. (2001). Interatomic collisions in a tightly confined Bose gas. *Phys. Rev. A*, 64:012706.

Pilati, S. and Giorgini, S. (2008). Phase Separation in a Polarized Fermi Gas at Zero Temperature. *Phys. Rev. Lett.*, 100:030401.

Pitaevskii, L. and Stringari, S. (2003). *Bose-Einstein Condensation*. Oxford University Press.

Prokof'ev, N., Ruebenacker, O., and Svistunov, B. (2001). Critical Point of a Weakly Interacting Two-Dimensional Bose Gas. *Phys. Rev. Lett.*, 87:270402.

Prokof'ev, N. and Svistunov, B. (2002). Two-dimensional weakly interacting Bose gas in the fluctuation region. *Phys. Rev. A*, 66:043608.

Prokof'ev, N. and Svistunov, B. (2008). Fermi-polaron problem: Diagrammatic Monte Carlo method for divergent sign-alternating series. *Phys. Rev. B*, 77:020408.

Punk, M. and Zwerger, W. (2007). Theory of rf-Spectroscopy of Strongly Interacting Fermions. *Phys. Rev. Lett.*, 99:170404.

Radzihovsky, L. and Sheehy, D. E. (2010). Imbalanced Feshbach-resonant Fermi gases. *Reports on Progress in Physics*, 73(7):076501.

Randeria, M., Duan, J.-M., and Shieh, L.-Y. (1989). Bound states, Cooper pairing, and Bose condensation in two dimensions. *Phys. Rev. Lett.*, 62:981–984.

Randeria, M. and Taylor, E. (2014). Crossover from Bardeen-Cooper-Schrieffer to Bose-Einstein Condensation and the Unitary Fermi Gas. *Annual Review of Condensed Matter Physics*, 5(1):209–232.

Ries, M. G., Wenz, A. N., Zürn, G., Bayha, L., Boettcher, I., Kedar, D., Murthy, P. A., Neidig, M., Lompe, T., and Jochim, S. (submitted (2014)). Observation of pair condensation in a strongly interacting two-dimensional Fermi gas. *e-print arXiv:1409.5373*.

Rigol, M., Dunjko, V., and Olshanii, M. (2008). Thermalization and its mechanism for generic isolated quantum systems. *Nature*, 452:854–858.

Ringwald, A. and Wetterich, C. (1990). Average Action for the N Component ϕ^4 Theory. *Nucl.Phys.*, B334:506.

Sadler, L. E., Higbie, J. M., Leslie, S. R., Vengalattore, M., and Stamper-Kurn, D. M. (2006). Spontaneous symmetry breaking in a quenched ferromagnetic spinor Bose-Einstein condensate. *Nature*, 443:312–315.

Saffman, M., Walker, T. G., and Mølmer, K. (2010). Quantum information with Rydberg atoms. *Rev. Mod. Phys.*, 82:2313–2363.

Sagi, Y., Drake, T. E., Paudel, R., and Jin, D. S. (2012). Measurement of the Homogeneous Contact of a Unitary Fermi Gas. *Phys. Rev. Lett.*, 109:220402.

Salmhofer, M. (2007). Dynamical adjustment of propagators in Renormalization Group flows. *Annalen der Physik*, 16(3):171–206.

Sarma, G. (1963). On the influence of a uniform exchange field acting on the spins of the conduction electrons in a superconductor. *Journal of Physics and Chemistry of Solids*, 24(8):1029 – 1032.

Schaefer, B.-J. and Wambach, J. (2005). The Phase diagram of the quark meson model. *Nucl. Phys.*, A757:479–492.

Schaefer, B.-J. and Wambach, J. (2008). Renormalization group approach towards the QCD phase diagram. *Phys. Part. Nucl.*, 39:1025–1032.

Schirotzek, A., Shin, Y.-i., Schunck, C. H., and Ketterle, W. (2008). Determination of the Superfluid Gap in Atomic Fermi Gases by Quasiparticle Spectroscopy. *Phys. Rev. Lett.*, 101:140403.

Schmidt, R. and Enss, T. (2011). Excitation spectra and rf response near the polaron-to-molecule transition from the functional renormalization group. *Phys. Rev. A*, 83:063620.

Schneider, W. and Randeria, M. (2010). Universal short-distance structure of the single-particle spectral function of dilute Fermi gases. *Phys. Rev. A*, 81:021601.

Schnoerr, D., Boettcher, I., Pawlowski, J. M., and Wetterich, C. (2013). Error estimates and specification parameters for functional renormalization. *Annals Phys.*, 334:83–99.

Serwane, F., Zürn, G., Lompe, T., Ottenstein, T. B., Wenz, A. N., and Jochim, S. (2011). Deterministic Preparation of a Tunable Few-Fermion System. *Science*, 332(6027):336–338.

Sheehy, D. E. and Radzihovsky, L. (2006). BEC-BCS Crossover in "Magnetized" Feshbach-Resonantly Paired Superfluids. *Phys. Rev. Lett.*, 96:060401.

Sinner, A., Hasselmann, N., and Kopietz, P. (2009). Spectral Function and Quasiparticle Damping of Interacting Bosons in Two Dimensions. *Phys. Rev. Lett.*, 102:120601.

Sinner, A., Hasselmann, N., and Kopietz, P. (2010). Functional renormalization-group approach to interacting bosons at zero temperature. *Phys. Rev. A*, 82:063632.

Son, D. T. and Thompson, E. G. (2010). Short-distance and short-time structure of a unitary Fermi gas. *Phys. Rev. A*, 81:063634.

Stewart, J. T., Gaebler, J. P., Drake, T. E., and Jin, D. S. (2010). Verification of Universal Relations in a Strongly Interacting Fermi Gas. *Phys. Rev. Lett.*, 104:235301.

Strack, l. and Jakubczyk, P. (2014). Fluctuations of Imbalanced Fermionic Superfluids in Two Dimensions Induce Continuous Quantum Phase Transitions and Non-Fermi-Liquid Behavior. *Phys. Rev. X*, 4:021012.

Strack, P., Gersch, R., and Metzner, W. (2008). Renormalization group flow for fermionic superfluids at zero temperature. *Phys. Rev. B*, 78:014522.

Symanzik, K. (1970). Small distance behavior in field theory and power counting. *Commun.Math.Phys.*, 18:227–246.

Tan, S. (2008a). Energetics of a strongly correlated Fermi gas. *Annals of Physics*, 323(12):2952 – 2970.

Tan, S. (2008b). Generalized virial theorem and pressure relation for a strongly correlated Fermi gas. *Annals of Physics*, 323(12):2987 – 2990.

Tan, S. (2008c). Large momentum part of a strongly correlated Fermi gas. *Annals of Physics*, 323(12):2971 – 2986.

Taylor, E. and Randeria, M. (2010). Viscosity of strongly interacting quantum fluids: Spectral functions and sum rules. *Phys. Rev. A*, 81:053610.

Thies, M. and Urlichs, K. (2003). Revised phase diagram of the Gross-Neveu model. *Phys. Rev. D*, 67:125015.

Thomas, J. E., Kinast, J., and Turlapov, A. (2005). Virial Theorem and Universality in a Unitary Fermi Gas. *Phys. Rev. Lett.*, 95:120402.

Valiente, M., Zinner, N. T., and Mølmer, K. (2011). Universal relations for the two-dimensional spin-1/2 Fermi gas with contact interactions. *Phys. Rev. A*, 84:063626.

Verstraete, F., Wolf, M. M., and Cirac, J. I. (2009). Quantum computation and quantum-state engineering driven by dissipation. *Nature Physics*, 5:633.

Viverit, L., Giorgini, S., Pitaevskii, L., and Stringari, S. (2004). Momentum distribution of a trapped Fermi gas with large scattering length. *Phys. Rev. A*, 69:013607.

Wenz, A. N., Zürn, G., Murmann, S., Brouzos, I., Lompe, T., and Jochim, S. (2013). From Few to Many: Observing the Formation of a Fermi Sea One Atom at a Time. *Science*, 342(6157):457–460.

Werner, F. and Castin, Y. (2012). General relations for quantum gases in two and three dimensions: Two-component fermions. *Phys. Rev. A*, 86:013626.

Werner, F., Tarruell, L., and Castin, Y. (2009). Number of closed-channel molecules in the BEC-BCS crossover. *Eur. Phys. J. B*, 68:401.

Wetterich, C. (1993). Exact evolution equation for the effective potential. *Phys. Lett.*, B301:90–94.

Wetterich, C. (2008). Functional renormalization for quantum phase transitions with nonrelativistic bosons. *Phys. Rev. B*, 77:064504.

Wilson, K. G. (1971a). Renormalization group and critical phenomena. 1. Renormalization group and the Kadanoff scaling picture. *Phys. Rev.*, B4:3174–3183.

Wilson, K. G. (1971b). Renormalization group and critical phenomena. 2. Phase space cell analysis of critical behavior. *Phys. Rev.*, B4:3184–3205.

Wu, S.-T. and Yip, S. (2003). Superfluidity in the interior-gap states. *Phys. Rev. A*, 67:053603.

Ye, J., Kimble, H. J., and Katori, H. (2008). Quantum State Engineering and Precision Metrology Using State-Insensitive Light Traps. *Science*, 320:1734–1738.

Yu, Z., Bruun, G. M., and Baym, G. (2009). Short-range correlations and entropy in ultracold-atom Fermi gases. *Phys. Rev. A*, 80:023615.

Zhang, S. and Leggett, A. J. (2009). Universal properties of the ultracold Fermi gas. *Phys. Rev. A*, 79:023601.

Zinn-Justin, J. (1993). *Quantum Field Theory and Critical Phenomena*. Oxford University Press, Oxford.

Zürn, G., Lompe, T., Wenz, A. N., Jochim, S., Julienne, P. S., and Hutson, J. M. (2013). Precise Characterization of Li-6 Feshbach Resonances Using Trap-Sideband-Resolved RF Spectroscopy of Weakly Bound Molecules. *Phys. Rev. Lett.*, 110:135301.

Zwerger, W. (2012). *The BCS-BEC Crossover and the Unitary Fermi Gas*. Springer, Berlin. Editor W. Zwerger.